POSITION ESTIMATION IN SWITCHED RELUCTANCE MOTOR DRIVES USING THE FIRST SWITCHING HARMONICS OF PHASE VOLTAGE AND CURRENT

By

Keunsoo Ha

Dissertation submitted to the faculty of the Virginia Polytechnic Institute and State University in partial fulfillment of the requirements for the degree of

Doctor of Philosophy

In

Electrical and Computer Engineering

APPROVED:

Dr. Krishnan Ramu, Committee Chair

Dr. Jamie De La Reelopez

Dr. Douglas K. Lindner

Dr. Daniel J. Stilwell

Dr. Werner E. Kohler

June 26, 2008

Blacksburg, Virginia

Keywords: Switched Reluctance Motor, Flux-linkage Estimation, Position Estimation, First Switching Harmonic, FFT, Fourier series, Low-cost Drive, High Efficiency, Acoustic Noise

POSITION ESTIMATION IN SWITCHED RELUCTANCE MOTOR DRIVES USING THE FIRST SWITCHING HARMONICS OF PHASE VOLTAGE AND CURRENT

By

Keunsoo Ha

Prof. Krishnan Ramu, Chairman

The Bradley Department of Electrical and Computer Engineering

ABSTRACT

Position estimation using only active phase voltage and current is presented to perform high accuracy position sensorless control of a SRM drive. By extracting the amplitude of the first switching harmonic terms of phase voltage and current for a PWM period through Fourier analysis, flux-linkage and position are estimated without external hardware circuitry such as a modulator and demodulator, resulting in increasing cost, as well as large position estimation error produced when the motional back emf is ignored near zero speed. Hence the proposed position estimation scheme covers the entire speed range including the standstill under various loads and it has high resolution information depending on switching frequency. Fourier series and Fast Fourier transform are employed to decompose the phase voltage and current into its first switching harmonic. A two-phase SRM drive system, consisting of an asymmetrical converter and a conventional closed-loop PI current controller, is utilized to validate the performance of the proposed position estimation scheme in comprehensive operating conditions. The estimated values very closely track the actual values in dynamic simulations and experiments. It is shown that the proposed position estimation scheme using Fourier analysis is sufficiently accurate and works satisfactorily at various operating points.

This research also proposes an accurate self-inductance measurement method. In general, when applying circulating currents within the body of a ferromagnetic material under conditions of a time varying magnetic flux, the effects of eddy current losses and resistance changes due to

heating decrease the magnetic field strength and thereby the reduced magnetic field decreases the magnetic flux-linkage of SRM. These losses make a challenge to the measurement of magnetic characteristics of SRM. These motives lead to propose a measurement methodology based on 60 Hz sinusoidal excitation using a variable AC power supply, which provides an alternative to time domain integration approaches for self-inductance or flux-linkage measurement as well as eliminates error arising from thermal and eddy currents effects. The validation of the proposed method is verified with the correlation between the measurement and FEA results of flux-linkage.

Furthermore, this research proposes the solutions for low cost and high efficiency drive systems, consisting of a split AC converter and a two-phase SRM. Its performance is analyzed and verified with experiments at the rated speed under various loads. It is believed that this drive system combined with the proposed position estimation scheme using Fourier analysis is a strong contender to be a low cost motor drive system with single switch per phase having comparable efficiency and acoustic noise level as an asymmetric drive system.

ACKNOWLEDGEMENTS

I would like to thank my advisor, Prof. Krishnan Ramu for his invaluable advice on this dissertation, his continued encouragement and support during the completion of this research, and his careful review of the results. He is very enthusiastic and energetic as well as a creative person, seeking high quality works. His ceaseless guidance and incomparable advice helped me in staying on the right track and accomplishing this research. Thanks to him I could win two paper awards from IEEE and successfully finish this dissertation. I would like to owe him lots of gratefulness.

I also would like to thank Dr. Jamie De La Reelopez, Dr. Dr. Douglas K. Lindner, Dr. Daniel J. Stilwell, and Dr. Werner E. Kohler for their assistance and concerns. Their generous encouragement and support throughout the work has been a great source of inspiration. My colleagues in the Center for Rapid Transit Systems deserve my sincere thanks for their kind help in developing a low-cost and high efficiency drive system: Prof. SeokGyu Oh, Cheewoo Lee, Jaehyuck Kim, Nimal Lobo, Ethan Swint, and Dr. Hongsun Lim. Especially I would like to thank Prof. Seokgyu Oh, Cheewoo Lee, and Jaehyuck Kim who substantially contributed to the development and measurement of the drive system. I am grateful to Nimal Lobo and Ethan Swint for his assistance with proofreading this dissertation. Furthermore, I wish thank to my senior members, Prof. Jinwoo Ahn, Prof. Hyeungyeul Yang, Prof. Eunghyuck Lee, Prof. Youngjoong Kim, Dr. Kyouwoong Kim, and Kyehun Lee, for helping me to get through difficult times and accomplish goals. I am also thankful to Panaphase Technologies, LLC. and DeltaGee for their permission to use their proprietary machine to implement the position estimation scheme presented in this dissertation.

Most of all, I would like to express deep gratitude to my parents, brother, and sister who have provided endless encouragement and support. Especially I owe my loving thanks to my wife Hoon Kim, my daughters Yurie and Yujie. They have lost a lot and sacrifice themselves for my research abroad. Without their encouragement and sincere understanding it would have been impossible for me to accomplish this work.

TABLE OF CONTENTS

LIST OF FIGURES

LIST OF TABLES

CHAPTER 1 INTRODUCTION

Switched reluctance motor (SRM) drive technology has been developed over the last three decades and is widely considered as an alternative to conventional electrical machines like induction and BLDC machines in emerging industrial applications. SRM have a simple configuration and winding design which results in lower cost than classical machines for the same power [1]. Moreover, lower cost converter topologies applied to the machine as well as the control strategy adopted to insure variable speed operation makes SRMs very attractive in variable speed motor applications.

In SRM drives, it is necessary to have rotor position information to determine turn-on and turn-off angles to excite and commutate the phase windings. Usually, optical encoders, resolvers, or hall-effect sensors mounted on the shaft are used to obtain rotor position information. These external mechanical sensors, however, have several drawbacks even though they provide high resolution position information. Position sensors are usually expensive and not feasible in very low cost applications. They need to be properly aligned to the rotor shaft in order to avoid mechanical problems. The cable for these position sensors need to be properly shielded in order to avoid signal failures due to the external disturbances such as EMI. When the motor is connected to a PWM converter and is operated through long cables to get position information, the signals containing position information may get attenuated or corrupted due to the external disturbances. These EMI and temperature effects reduce the reliability of the system. In order to avoid these drawbacks, this research proposes a new approach to estimating rotor position in SRM drives.

Current research has focused on estimation rotor position without position sensors and a large number of position estimation algorithms have been proposed for position sensorless operation of SRMs. Research on sensorless operation of SRM drives is reviewed in the following section. The problems to be solved will be defined after the review, and the objective of this research will be summarized.

1.1 Previous Research

Research on sensorless rotor position estimation methods is broadly classified into four categories: 1) Active phase voltage and current measurement, where rotor position information is obtained from the terminal measurements of active phase voltage or current and associated computations, 2) Mutual voltage measurement, where the mutually induced voltage in an inactive phase due to the phase current in an active phase contains rotor position information, 3) External signal injection, where low-magnitude, high-frequency signals are injected into an inactive phase to determine the position by calculating phase inductance variation information, 4) Intelligent control methods, such as artificial neural networks, fuzzy control, and neuro-fuzzy control fall under this category and they have significantly larger computational requirements due to their complexity and having a large number of fuzzy rules even though they are not model dependent. Fig 1.1 summarizes the various sensorless estimation algorithms

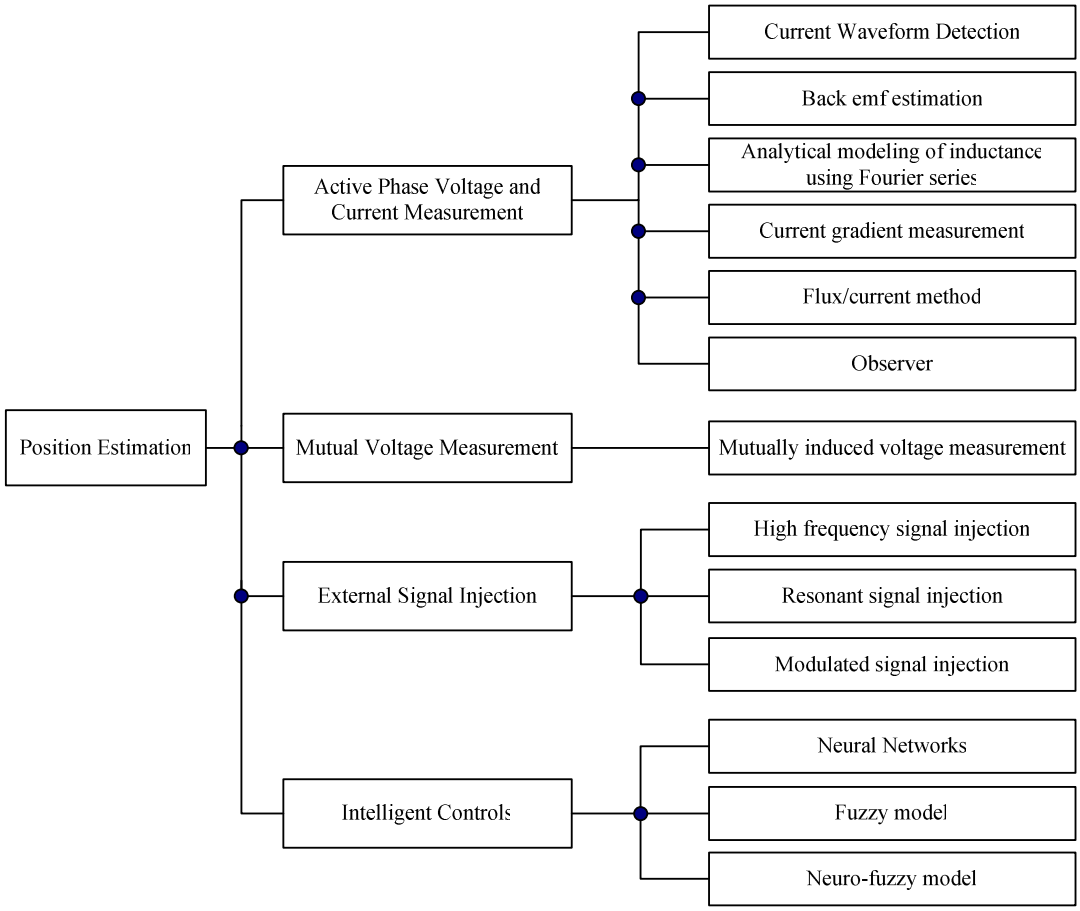

Fig 1.1 Classification of position estimation techniques

1) Active-phase voltage and current measurement

a) Current waveform detection

Acarnley et al. [2] first proposed a rotor position detection method for SRM by monitoring the active phase current waveform. The fundamental idea behind this technique is that the rotor position can be obtained from the incremental inductance ($\delta\lambda / \delta i$) in (1.1) if the motional back emf and voltage drop in the phase winding can be neglected.

$$\frac{di}{dt} = \frac{v_{ph} - i_{ph}R - \frac{\partial \lambda}{\partial \theta}\frac{d\theta}{dt}}{\frac{\partial \lambda}{\partial i}} \tag{1.1}$$

The incremental inductance is reflected in phase current rise and fall times of chopper drives. Thus rotor position can be detected by monitoring the phase current rise and fall times. This method is useful at zero speed where there is no the motional back emf since it detects the rate of change of phase current. This method, unfortunately, did not estimate the motional back emf and could not effectively compensate for its influence on the phase current rise and fall times. At high speeds, the motional back emf becomes so significant that the phase current is not allowed to chop and it is difficult to correlate the phase current rise and fall times with the rotor position.

In order to overcome this back emf effect, S.K. Panda et al. [3-6] carried out detailed mathematical analysis and experiments for position estimation using the current rise and fall times in an inactive phase. If a diagnostic current of small magnitude is applied to the inactive phase, the current rise and fall times in the inactive phase are measured for position detection. By comparing the current rise or fall time with the time selected to switch off the phase current, referred as the detect time, the rotor position is estimated. The detect time is set to a value corresponding to a position to maximize the motor torque. Therefore, due to the low level of diagnostic current, the influence of back emf is minimized even at high speeds. This method is applied to a four-phase and three-phase SRM. However, negative torque can be generated due to the diagnostic current pulse applied to the inactive phase and it requires extra hardware such as counters and comparators to generate the phase current commutation signal. In addition, by varying the detect time, it is possible to commutate the phase current at an inappropriate rotor position so that no negative torque is generated and the torque-speed characteristics of the SRM can be altered by the detect time for the same current. Table 1.1 summarizes the merits and demerits of the position estimation methods using current waveform detection technique.

Table 1.1 Comparison of the position estimation method using current waveform detection

Reference No.	Merits	Demerits
[2]	a. Useful method even at zero speed	a. Disregard the back emf at high speeds
[3-6]	a. Minimize the back emf effect even at high speeds	a. Negative torque generation b. External hardware such as counter and comparator

b) Back emf estimation

In order to suppress large estimation errors when the motional back emf is ignored, Ehsani et al. [7-9] proposed the method of online motional back emf estimation based on the ratio of the rising time to the falling time during a current chopping cycle. Assuming that the motional back emf does not change during the chopping cycle, the back emf, e, can be estimated as,

$$e = \frac{\gamma - 1}{\gamma + 1} v_{bus} - R\left(i_c + \frac{\Delta I}{2} \right) \tag{1.2}$$

where γ is the ratio of the rising time to the falling time during a chopping cycle, i_c is the reference current during a chopping cycle, and ΔI is the swinging range of current waveform during a chopping cycle. Substituting equation (1.2) into the phase voltage equation of the SRM and solving the equation for incremental inductance in equation (1.1), position information can be derived from the relationship between the calculated motional back emf and the incremental inductance of the analytical model for SRM. However, this method still neglected the motional back emf near zero speed since it is very small (noise level magnitude) compared to the DC bus voltage and as a result, the rotor position cannot be estimated near zero. Moreover, this method requires an accurate analytical inductance model for high resolution position estimation. Table 1.2 summarizes the merits and demerits of the position estimation methods using the back emf estimation technique.

Table 1.2 Comparison of the position estimation method using back emf estimation

Reference No.	Merits	Demerits
[7-9]	a. Online back emf estimation based on phase current waveform b. Reduction of large estimation error due to the ignorance of back emf	a. Back emf still exists near zero speed b. Still large estimation error near zero speed c. An accurate analytical inductance model for high resolution estimation

c) Analytical modeling of inductance using Fourier series

Suresh et al. [10], Hongwei et al. [11], Fahimi et al. [12-14], and Salmasi et. al. [15] achieved sensorless control of SRMs using active phase voltage and current measurement. The sensorless scheme relies on the dynamic model of the SRM. Active phase currents are measured and using these measurements, the dynamic equations representing the inductance model of the active phases are solved to obtain rotor position information. The inductance is a periodic function of rotor position and the variation of self-inductance with respect to the rotor position can be represented by Fourier series [16]. Considering the first three components in the Fourier series development, the self-inductance can be given as,

$$L(i,\theta) = \sum_{n=0}^{2} L_n(i)\cos(nN_r\theta + \varphi_n) \quad , \quad n = 0,1,2 \tag{1.3}$$

where n is the harmonic number and N_r is the number of rotor poles. Assuming the self-inductance is maximum at $\theta = 0$ and minimum at $\theta = \pi / N_r$, $\varphi_0 = \varphi_1 = \varphi_2 = 0$. The self-inductance of the active phase is represented by,

$$L(i,\theta) = L_0(i) + L_1(i)\cos N_r\theta + L_2(i)\cos 2N_r\theta \tag{1.4}$$

The three coefficients of equation (1.4) are derived by the expressions of the self-inductance at aligned, midpoint, and unaligned positions, shown below.

$$L_0 = \frac{1}{2}\left[\frac{1}{2}(L_a + L_u) + L_m\right] \tag{1.5}$$

$$L_1 = \frac{1}{2}(L_a - L_u) \tag{1.6}$$

$$L_2 = \frac{1}{2}\left[\frac{1}{2}(L_a + L_u) - L_m\right] \tag{1.7}$$

where L_a is the inductance at aligned position, L_m is the midpoint position inductance, and L_u is the inductance at unaligned position. These inductances are given by polynomial functions.

$$L_a = L(\theta = 0) = \sum_{n=0}^{n=k} a_n i^n \tag{1.8}$$

$$L_m = L(\theta = \frac{\pi}{2N_r}) = \sum_{n=0}^{n=k} b_n i^n \tag{1.9}$$

$$L_u = L(\theta = \frac{\pi}{N_r}) \tag{1.10}$$

where k is the order of approximation. The coefficients, a_n and b_n are determined by curve fitting so equations (1.8) and (1.9) fit inductance profiles obtained from experiments or finite element analysis (FEA). This ensures the accuracy of the inductance profile. Neglecting the mutual inductance between phases, the phase voltage differential equation for the active phase is given by,

$$v = Ri + \left(L(i,\theta) + i\frac{\partial L(i,\theta)}{\partial i} \right) \cdot \frac{di}{dt} + i\omega \frac{\partial L(i,\theta)}{\partial \theta} \tag{1.11}$$

where v is the phase voltage applied to the stator winding, R is the phase resistance, and ω is the rotor speed. Substituting the self-inductance given by equation (1.4) into equation (1.11) yields,

$$\begin{aligned} v = Ri + &\left\{ \left(L_0(i) + i\frac{\partial L_0(i)}{\partial i} \right) + \left(L_1(i) + i\frac{\partial L_1(i)}{\partial i} \right) \cos N_r\theta + \left(L_2(i) + i\frac{\partial L_2(i)}{\partial i} \right) \cos 2N_r\theta \right\} \frac{di}{dt} \\ &+ \left\{ -N_r L_1(i) \sin N_r\theta - N_r L_1(i) \sin N_r\theta \right\} i\omega \end{aligned} \tag{1.12}$$

Once the phase current is measured and the estimated rotor speed is known, three coefficients L_0, L_1, and L_2 in equation (1.4) can be computed and then equation (1.12) is numerically solved to estimate rotor position. The main advantage of this method is that it does not require additional hardware and look-up tables of $\lambda - i - \theta$ characteristics. However, if the modeling error is significant the numerical inductance model and experiments do not match well, hence the accuracy of the position estimation depends on the accuracy of modeling the SRM. In case of the SRM with non-uniform air gap, there may be some discrepancy between the inductance profiles. Table 1.3 summarizes the merits and demerits of the position estimation methods using an analytical inductance modeling using Fourier series.

Table 1.3 Comparison of the position estimation method using an analytical inductance model

Reference No.	Merits	Demerits
[10-16]	a. No external hardware b. No magnetization look-up table	a. An accurate analytical inductance model for high accuracy estimation b. Not useful for the SRM with non-uniform air gap

d) Flux/current method

With the knowledge of the relationship between phase current and flux-linkage, the rotor position can be estimated using a look-up table of $\lambda - i - \theta$ characteristics. The flux/current method was first proposed by Hedland [17] and a similar method was later proposed by Lyons et al. [18]. Flux-linkage can be obtained by open loop integration of $(v_{ph} - i_{ph}R)$ as given below,

$$\hat{\lambda} = \int (v_{ph} - i_{ph}R)dt \tag{1.13}$$

The block diagram of this scheme is shown in Fig 1.2.

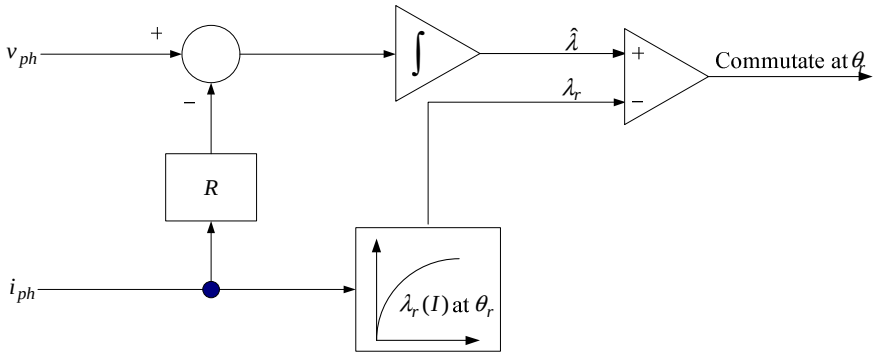

Fig 1.2 Block diagram of flux/current method

In this scheme, rotor position is identified by comparing the estimated flux-linkage with the reference flux-linkage obtained from a stored table of flux-linkage and current vs. rotor position. Lyons et al. [18] extended the work by using a three-dimensional table to find the reference flux-linkage as a function of current and position for a multi-phase motor. The calculation and the look-up table can be implemented using a microcontroller or dedicated hardware circuitry. Panda et al. [19] proposed a self-measured flux/current characteristics by the controller without any mechanical arrangement to lock the rotor. This flux/current method is simple and effective, but has large estimation error in low and zero speed regions due to flux integration errors from improper resistance measurement and error in the sampled current, and demands a high-memory digital signal processor to store a good resolution look-up table. Table 1.4 summarizes the merits and demerits of the position estimation methods using flux/current method.

Table 1.4 Comparison of the position estimation method using flux/current method

Reference No.	Merits	Demerits
[17-19]	a. Simple computation of flux-linkage by integration of $(v_{ph} - i_{ph}R)$	a. Large estimation error due to improper resistance measurement b. High resolution magnetization table for high resolution estimation

e) Current gradient measurement

Gallegos-Lopez et al. [20] proposed a method to use the change of the derivative of the phase current to detect the position where a rotor pole and a stator pole start overlapping. Fig 1.3 shows the derivation of the phase current and its relationship to rotor position [20, 21]. When the phase inductance starts to increase at θ_0 where a rotor pole and a stator pole begin to overlap, the gradient of the phase current, $\frac{di_f}{dt}$, decreases or become zero as shown in Fig 1.3. Therefore, by monitoring the gradient of the phase current assuming constant speed, rotor position can be detected with a sensorless pulse given by a zero-crossing detector.

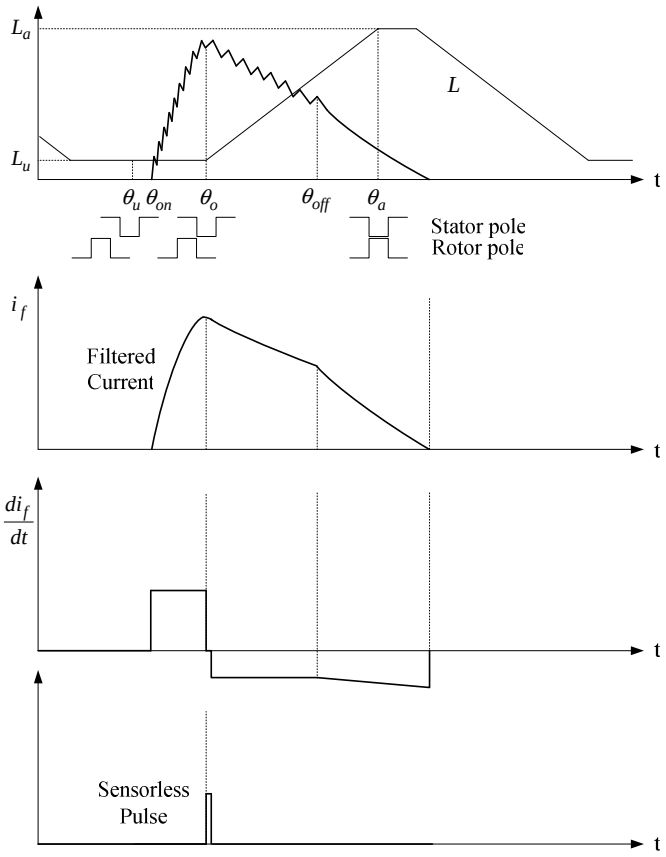

Fig 1.3 Derivation of current gradient and its relationship to rotor position

Even though there is one sensorless pulse signal for each phase conduction cycle that provides absolute position information, relative position information is generated by multiplying the frequency of the zero current gradients by 32 with phase-locked-loop (PLL) techniques. Therefore, a resolution of 32 pulses during the sensorless pulses shown in Fig 1.3 can be

obtained, which is used to generate phase the current commutation pulse. The major advantage of this method is that it does not require voltage transducers. It is realizable with simple hardware and thus lends itself to low-cost applications. In addition, it needs no priori knowledge of the magnetization characteristics. However, the drawback of this method is that the current gradient signals are not applicable at the time of starting; therefore, a separate starting procedure has to be incorporated. It needs a plateau in the inductance profile to start to energizing a phase. Table 1.5 summarizes the merits and demerits of the position estimation methods using the current gradient measurement technique.

Table 1.5 Comparison of the position estimation method using current gradient measurement

Reference No.	Merits	Demerits
[20-21]	b. Realization with simple hardware c. Low-cost applications d. No priori knowledge of magnetic characteristics is required	a. Not available at standstill b. Needs a separate startup procedure c. Needs the plateau in inductance profile to start to energize a phase

f) Observer

Lumsdaine and Lang [22] proposed model-based estimator such as state observer to determine the rotor position of the SRM. In this observer-based state estimation scheme, the dynamics of the motor are modeled in state space while a mathematical model runs in parallel with the physical machine as shown in Fig 1.4.

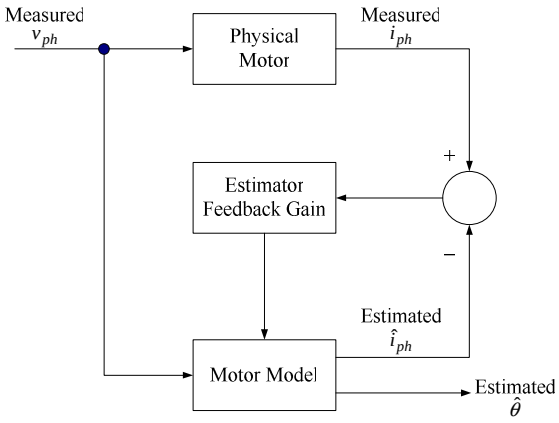

Fig 1.4 State-observer-based system

The model has the same inputs as the physical machine and the difference between its outputs and the measured outputs of the real machine are used to force the estimated variables to converge to the actual values. This method requires neither an additional diagnostic pulse nor has

any inherent speed limitations. The state observer method, however, has a complex implementation since it requires substantial real-time computations and needs knowledge of load parameters as well as an accurate machine dynamic model. The needs for the computational simplicity and robust stability properties prompted the study of sliding mode observer. Briefly, the sliding mode observer estimates rotor position and velocity from phase current and voltage measurement.

Husain et al. [23] first presented a sliding-mode-observer-based rotor position estimation scheme for the SRM. The estimated rotor position obtained from the observer is used for the commutation of the machine phases. However, the results presented in this paper were based on computer simulation of a linear magnetic model for the SRM. The discrete time implementation using sliding mode observer was presented by McCann et al. [24]. An error correction term is computed based on the difference of the motor flux computed from the mathematical model and that derived from motor measurements. A block diagram of the sliding-mode-observer-based motor drive is shown in Fig 1.5.

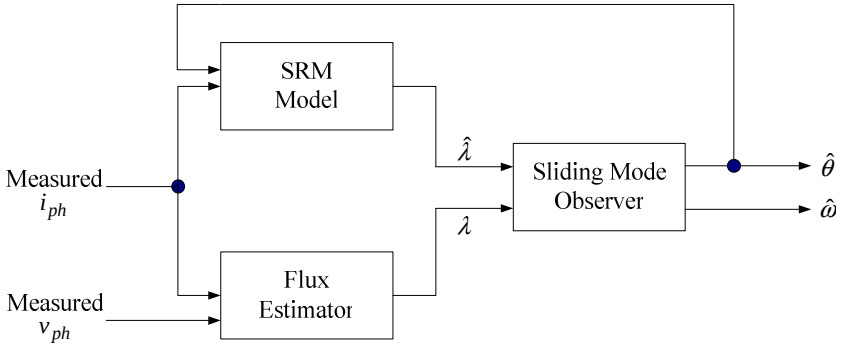

Fig 1.5 Sliding-mode-observer-based system

The method in [24] considered the convergence of the observer when there is an initial position error and when there is a flux observer error. Depending on the initial position error, the sliding surface could be different and consequently be reflected in the position estimation as a lag or lead between actual and estimated position. The estimated position converges after approximately 35 ms for the worst case when the initial error is $180°$. Although there is a large error between flux observer and true motor flux, there is no significant impact on the position and velocity estimations, demonstrating the robustness of sliding observer toward parameter variations and nonlinearity in machine modeling.

Based on the sliding mode observer, Husain et al. [25] presented a four-quadrant sensorless controller over wide speed range including zero speed. To avoid the unobservability at zero speed with no phase current, a high frequency bipolar speed is commanded, which dithered the motor to allow the successful operation of the observer at zero speed. However, this may obviously result in some rotor hesitation problem and the reference current in regulating the phase current has the lower limit to continuously maintain the observability of the sliding mode observer. Table 1.6 summarizes the merits and demerits of the observer-based position estimation methods.

Table 1.6 Comparison of the position estimation method using observer

Reference No.	Merits	Demerits
[22]	e. No additional diagnostic pulses f. No speed limitations	a. Load parameters are required b. Accurate dynamic model is required
[23]	a. First presented the sliding-mode-observer-based estimation scheme	a. Only simulation verification
[24]	a. Hardware implementation using sliding mode observer	a. Long convergence time of the estimated rotor position in large initial position error
[25]	a. Four-quadrant sensorless control including zero speed b. Successful operation of the observer at zero speed by applying high frequency bipolar speed command	a. Rotor hesitation problem at standstill b. Limitation of the reference current command for consecutive operation of the sliding mode observer

2) Mutual voltage measurement

a) Mutually induced voltage measurement

Husain and Ehsani [26] proposed a sensorless method by measuring a mutually induced voltage of an inactive phase of SRM. When a phase current is regulated by PWM or hysteresis control, the mutually induced voltage in an adjacent phase is given by,

$$\begin{aligned} v_m &= \frac{d\lambda_m}{dt} \\ &= M(\theta)\frac{di}{dt} + i\frac{dM}{d\theta}\omega \end{aligned} \tag{1.14}$$

where $\lambda_m = M(\theta)\cdot i$ and $M(\theta)$ is the mutual inductance. When the positive voltage is applied to the phase, the phase voltage equation of SRM is governed by the equation,

$$V = iR + \frac{d\lambda}{dt} + v_m \tag{1.15}$$

where λ is the flux-linkage, v_m is the mutual voltage, and R is the phase resistance. Neglecting the mutual voltage since the applied voltage is larger, equation (1.15) can be rewritten by,

$$V = iR + L(\theta)\frac{di}{dt} + i\frac{dL}{dt} \tag{1.16}$$

where L is the self-inductance of a stator winding. Replacing $\frac{d\theta}{dt}$ by ω in equation (1.16), the current gradient when the positive voltage is applied becomes,

$$\frac{di}{dt} = \frac{1}{L(\theta)}\left(V - i\frac{dL}{d\theta}\omega - iR\right) \tag{1.17}$$

Substituting equation (1.17) into equation (1.14), the mutually induced voltage while the positive voltage is applied to the adjacent phase, v_{m1}, is derived.

$$v_{m1} = \frac{M(\theta)}{L(\theta)}V - \frac{M(\theta)}{L(\theta)}i\frac{dL}{d\theta}\omega - iR\frac{M(\theta)}{L(\theta)} + i\frac{dM}{d\theta}\omega \tag{1.18}$$

Similarly when the zero voltage is applied to the phase, the phase voltage equation is,

$$0 = iR + \frac{d\lambda}{dt} \tag{1.19}$$

Equation (1.19) can be rewritten as,

$$0 = iR + L(\theta)\frac{di}{dt} + i\frac{dL}{dt} \tag{1.20}$$

The current gradient when the zero voltage is applied is given by,

$$\frac{di}{dt} = -\frac{1}{L(\theta)}\left(i\frac{dL}{d\theta}\omega + iR\right) \tag{1.21}$$

Substituting equation (1.21) into equation (1.14), the mutually induced voltage while the zero voltage is applied to the adjacent phase, v_{m2}, can be derived as,

$$v_{m2} = -\frac{M(\theta)}{L(\theta)}i\frac{dL}{d\theta}\omega - iR\frac{M(\theta)}{L(\theta)} + i\frac{dM}{d\theta}\omega \tag{1.22}$$

From these mutually induced voltages, the rotor position can be estimated from the calibrated conversion tables for various currents and speeds. This is an effective way to estimate the shaft position of the SRM because it provides a clear relationship between the induced voltage and rotor position. This method, however, requires a synchronizing signal to detect whether the energized winding is operated in a conduction mode or a freewheeling mode. A sample and hold

circuit are needed to capture any one of the mutual voltages in conduction mode and freewheeling mode. Moreover, a three-dimensional table is required for accessing the data.

Tian-Hua et al. [27, 28] proposed a position estimation method to overcome the above discussed disadvantages. In [27], the commutation angle of the SRM is easily determined by applying a rectifying and a passive filter to eliminate the high frequency harmonics of the induced voltage. In [28], a position estimation method using the slope of phase current was proposed in the single pulse operation. The slope of phase current changes from a positive value to a negative value as the self-inductance increases. As a result, the rotor position is estimated from the slope of phase current in the single pulse operation mode. However, this method can be applied only in the hard chopping strategy, not in the soft chopping. Moreover, it requires external circuitry such as rectifying circuit and passive filter. Table 1.7 summarizes the merits and demerits of the position estimation methods using mutual voltage measurement.

Table 1.7 Comparison of the position estimation method using mutual voltage measurement

Reference No.	Merits	Demerits
[26]	a. Estimation scheme with direct measurement of an internal signal, mutually induced voltage	a. Sample and hold (S/H) circuit to capture the mutually induced voltage b. Synchronization trigger signals to control S/H circuit with PWM signals c. Useful only in high frequency PWM operation mode
[27-28]	a. Design rectifying circuit and passive filter to smooth the mutually induced voltages b. Applicable even in single pulse operation mode	a. Applicable only in hard chopping PWM mode b. External hardware such as rectifying circuit and passive filter

3) External signal injection

a) High frequency signal injection

Another way to obtain rotor position information is to detect the phase current waveform of an inactive or unexcited phase with high frequency diagnostic signals and determine the rotor position by calculating the phase inductance variation. If a voltage pulse is applied to a non-conducting phase for a short duration of time, the phase inductance remains unsaturated and the current amplitude is small assuming that the motional back emf and phase winding resistance voltage drop can be neglected. For low current levels, the phase voltage equation of SRM can be written as,

$$V = iR + L(\theta)\frac{di}{dt} + i\omega\frac{dL(\theta)}{d\theta} \tag{1.23}$$

If the voltage is applied for a short period of time, equation (1.23) can be approximated as,

$$V = L(\theta)\frac{\Delta i}{\Delta t} \quad \Rightarrow \quad L(\theta) = V\frac{\Delta t}{\Delta i} \tag{1.24}$$

The rotor position can then be estimated from a mapping of inductance to rotor position information. The main limitation of this method is the inter-phase coupling effect which is particularly severe when the active phase is undergoing high frequency chopping for current regulation. Eddy currents also affect the accuracy of position sensing.

Dunlop et al. [29] first investigated the effects of mutual coupling in his implemented scheme of measuring the change in the diagnostic current over a fixed sampling period. Harris et al. [30] also used a similar technique and mentioned the problems of inter-phase coupling and eddy current effects in detail. Another drawback of injecting a diagnostic pulse from the main converter is that their magnitude could be significant, and hence can generate negative torque.

MacMinn et al. [31] also later implemented the conventional high frequency signal injection method with power MOSFET transistors integrated with current sensing devices to eliminate Hall-effect or resistive current sensors.

The flux sensing method proposed by Mvungi et al. [32, 33] is based on applying diagnostic pulses to an idle phase which is not being used for torque production and integrating the voltage across the phase to obtain the phase flux. So as to minimize mutual coupling effects, the phase used for diagnostic sampling is the one farthest from the excited phase. The rotor position is then obtained from the motor flux-angle-current characteristics data. Either flux or current is kept constant during diagnostic sampling and the other variable is obtained as a function of the rotor position. This method appears to have potential for position estimation at higher speeds, but an accurate knowledge of phase winding resistance is required for high resolution position estimation.

Guo et al. [34, 35] proposed a single pulse injecting method for impressed pulses to overcome this negative torque. While the conventional injecting timing for impressed voltage pulses use the end of exciting signal, this method injects voltage pulses at the end of negative phase voltage signal, which is coincident with the end of tail current generated after commutating the excited phase. The extracted current pulses are passed through a low-pass filter

and then compared with the appropriate threshold to determine the excitation time of each phase. However, this method requires external circuitry for injecting the impressed voltage pulse. Also, it might need to be waiting for the sensing pulse to decrement to negligible levels not to generate negative torque before the next pulse can be applied. The rotor might move a considerable distance during that period; therefore, the rotor position resolution will decrease. In order to eliminate the effect of eddy currents after the diagnostic pulse is injected, few microseconds have to elapse and consequently, longer sensing pulses are required. All these factors limit the resolution at high speeds with this method of position sensing.

E. Kayikci et al. [36] proposed a load invariant position estimation method based on the high frequency signal injection method. A high frequency rotating vector voltage is superimposed on the main excitation voltage and it induces high frequency currents whose magnitude varies with rotor position. Therefore, the high frequency carrier current vector contains the rotor position that is dependent on the inductance. The high frequency rotating current vector, i^{s}_{qds-c}, is given in equation (1.25), as was derived in [37].

$$i^{s}_{qds-c} = I_p \cdot e^{j(\omega t-\pi/2)} + \left[I_{n1} e^{-jP_r\theta_r} + I_{n2} e^{j2P_r\theta_r} \right] \cdot e^{-j(\omega t-\pi/2)} \tag{1.25}$$

It is comprised of a positive sequence carrier current, the first term of the right side of equation (1.25), which contains no position information, and a negative sequence carrier current, the second term of the right side of equation (1.25), which contains position information. A band-pass filter is used to extract negative sequence carrier current including position information from the stator rotating current vector, i^{n}_{qds-n}. Finally, the extracted signal is transformed back to the negative carrier frame to be fed into the tracking observer [37]. The extraction the position is dependent on the saliency information from high frequency rotating current vector and is illustrated in Fig 1.6.

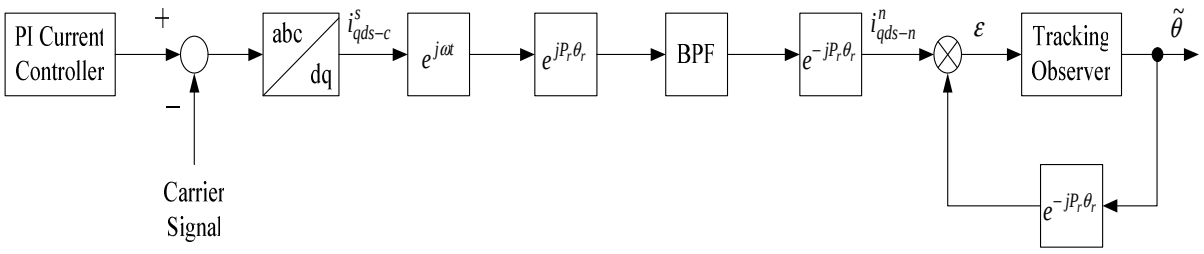

Fig 1.6 The extraction of position from high frequency rotating current vector

This method does not require additional hardware to inject high frequency sinusoidal voltage signals and is less sensitive to parameter variations. However, it does not considered the saturation effect on position estimation at high current levels and at rated load. Inductance variations due to the saturation will result in additional saliencies, which will degrade the accuracy of the estimated position. Table 1.8 summarizes the merits and demerits of the position estimation methods using high frequency signal injection.

Table 1.8 Comparison of the position estimation method using high frequency signal injection

Reference No.	Merits	Demerits
[29-30]	a. Investigation of the mutual coupling and eddy current effects on estimation performance	a. External circuitry for injecting voltage pulses b. Negative torque generation c. Low variation of the measuring current signal with rotor position
[31]	a. Implementation of conventional high frequency signal injection method b. Elimination Hall-effect or resistive current sensor by using power MOSFET transistors integrated with current sensing devices	a. External circuitry for injecting voltage pulses b. Negative torque generation c. Distortion of the current pulses by mutual coupling and eddy current effects d. Low variation of the measuring current signal with rotor position
[32-33]	a. Flux-linkage variation sensing method to avoid the back emf effect b. Injection of voltage pulses into the one opposite to the excited phase to minimize the mutual coupling effects	a. External circuitry for injecting voltage pulses b. Negative torque generation c. Distortion of the current pulses by mutual coupling and eddy current effects d. Low variation of the measuring current signal with rotor position
[34-35]	a. Injection of voltage pulses into one inactive phase b. Elimination of the negative torque by injecting voltage pulses at the end of negative phase voltage signal	a. External circuitry for injecting voltage pulses b. Position information might be lost during the time for sensing pulse to decrement to negligible levels c. Distortion of the current pulses by mutual coupling and eddy current effects d. Low variation of the measuring current signal with rotor position
[36-37]	a. No additional high frequency sinusoidal voltage signal injection b. Less sensitive to parameter errors	a. Disregard of saturation effect at high current b. Degrade the accuracy of the estimated rotor position at high current

b) Resonant signal injection

The main disadvantages of the classical modulation-based position estimation method using carrier injection lies in the small variation of the measurement signal with the rotor position especially under high frequency and low magnetic field levels. In order to increase this variation, Laurent et al. [38] proposed the method to increase the resolution of the measured impedance by designing a resonance at the unaligned position by selecting a capacitor to be connected in series with the machine phase. The resonant circuit is supplied with a high frequency sinusoidal current generator. The resonant capacitor value is determined so as to obtain as,

$$L_u \cdot C \cdot \omega_c^2 = 1 \tag{1.26}$$

where L_u is the minimum inductance at unaligned position and ω_c is the carrier frequency. By measuring the voltage UIc in Fig 1.7, a particular rotor position can be detected by a synchronous demodulation technique based on the extraction of the UIc maximal amplitude.

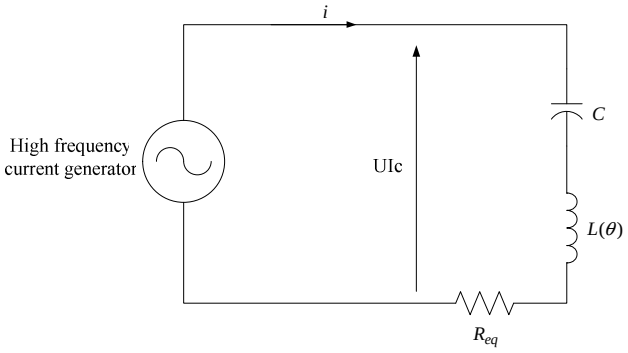

Fig 1.7 Block diagram of resonance circuit method

The impedance of the resonant circuit from Fig 1.7 is determined by,

$$Z(s) = \frac{1}{Cs} + L(\theta)s + R_{eq} = \frac{1 + L(\theta)Cs^2}{Cs} + R_{eq} \tag{1.27}$$

Note that at the unaligned position, the measured impedance equals the equivalent resistance of the circuit, whereas at the aligned position the impedance will be represented as the equivalent resistance, the differential inductance between the aligned and unaligned position, and carrier frequency. This increases the resolution of the impedance and the equivalent inductance variations and consequently improves the measurement resolution. However, a major problem of this method lies in the fact that it needs to scan all phases which are about to be energized to determine the rotor position. As soon as the unaligned position is found, the drive signal is

provided to supply the power for the actual scanned phase while other phases are scanned at the same time. Table 1.9 summarizes the merits and demerits of the position estimation methods using resonant signal injection.

Table 1.9 Comparison of the position estimation method using resonant signal injection

Reference No.	Merits	Demerits
[38]	a. Increase the variation of demodulated voltage signal by resonant circuit b. Enhancement the accuracy of the estimated position	a. External circuitry such as high frequency signal generator and capacitor b. Distortion of the demodulated voltage signal by mutual coupling effect c. Scan all phases to determine rotor position as well as exciting phase

c) Modulated signal injection

Several alternative sensorless techniques based on modulation schemes have been developed in order to eliminate above mentioned drawbacks of high frequency or resonant signal injection-based methods for position estimation. The block diagram of the modulation-based techniques is shown in Fig 1.8.

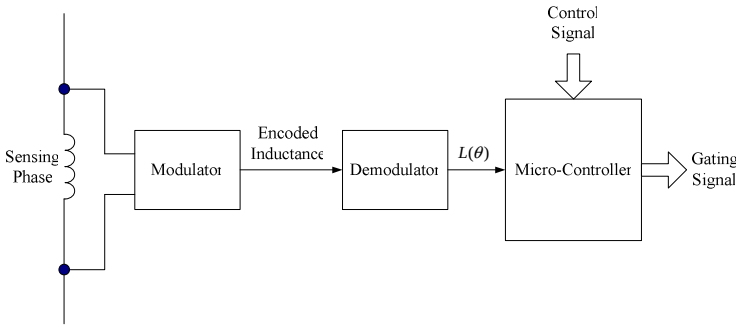

Fig 1.8 Block diagram of modulation-based system

In the frequency modulation (FM) based technique proposed by Ehsani et al. [39-41], an FM encoder generates a signal containing inductance variation information of the SRM. A simple L-T converter which maintains a linear relationship between inductance and time was used. The time period T of the FM signal can be written as,

$$T = K_1 L = \frac{1}{f} \tag{1.28}$$

where K_1 is a proportional constant and L is the phase inductance. The encoded signal of the phase inductance is then converted into a voltage by using F-V (frequency to voltage) converter.

Because the phase inductance depends on the rotor position, the rotor position is estimated from the output voltage of the F-V converter. The FM technique does not need an extra sinusoidal source and it can oscillate itself under DC voltage excitation [42]. However, position estimation methods by using FM encoders require analog circuitry that converts a phase inductance into frequency as well as the control circuit to convert the encoded signal into the voltage fed to the microcontroller. Moreover, the threshold value to determine the commutation angle affects the accuracy of the estimated position.

The phase modulation (PM) and the amplitude modulation (AM) techniques proposed by Ehsani et al. [43, 44] are based on the phase and amplitude variations, respectively, of the phase current due to the time varying inductance when a sinusoidal voltage is applied to the phase winding in series with a resistance. The current flowing through the circuit in response to the alternating voltage is a function of the magnetic circuit impedance. Since the phase inductance is varying periodically, phase angle between the current and applied voltage also varies in a periodic manner.

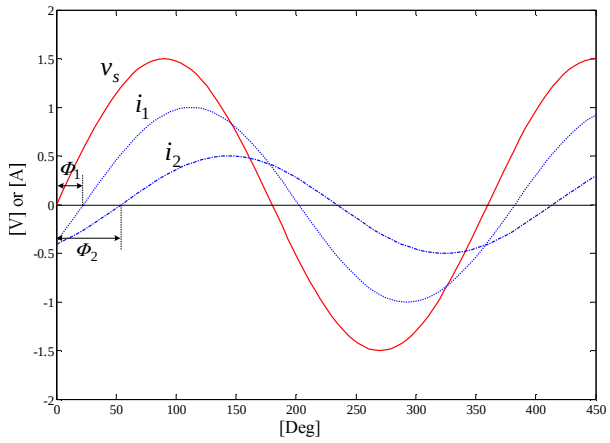

Fig 1.9 Basic waveforms corresponding to $L_{\min}$ and $L_{\max}$ in AM/PM method

Fig 1.9 shows the input sinusoidal voltage and the current waveforms i_1 and i_2 corresponding to the minimum and maximum phase inductances, respectively [43]. Angles Φ_1 and Φ_2 are the corresponding phase angles by which the phase current lags the input voltage. Furthermore, the current has the maximum peak in the i_1 waveform and the minimum peak in the i_2 waveform. The PM encoder technique measures the instantaneous phase angle on a continuous basis, while the AM encoder technique measures the peak current. The sinusoidal carrier voltage

signal is chosen to have a frequency which is much higher than the frequency of phase inductance variation. The transient variation of the current phase or amplitude will contain information about the motor winding inductance. The main contribution is the verification of the effect of frequency of the sensing signal injected into an inactive phase on the performance of the sensorless scheme. As the frequency increases, the maximum inductance at the aligned position diminishes, while the minimum inductance at the unaligned position does not vary appreciably. By measuring the inductance at a different frequency, 4.5 kHz is chosen in [44] as the frequency of the sensing signal and its performance is verified over a wide speed range with different loads. However, it requires external hardware such as a sine wave generator, a demodulator, and an optical isolator to separate the phase winding from the sensing circuit. Furthermore, the sensing signal in an active phase can be corrupted due to its mutual coupling with adjacent active phases, resulting in a deteriorating of the performance of the sensorless scheme.

The modified AM encoder technique proposed by Suresh at el. [45-47] was implemented for sensorless control of SRMs over wide speed range. The amplitude of the modulated current signal depends on the inductance of the sensing phase and hence the rotor position. A demodulator detects the envelope of the modulated current signal and converts it into an output voltage. The output voltage of the demodulator is connected to one of the inputs to a comparator, the other input being a fixed dc threshold voltage corresponding to a particular inductance value at a particular rotor position. Therefore, the comparator output changes at fixed intervals and generates an index pulse every particular rotor position. Intermediate rotor positions between two consecutive index pulses are estimated using linear interpolation of the time count in the microcontroller. The main advantage of this method over the conventional AM method is that the dc threshold at one of the comparator inputs can be fixed which results in simpler hardware and the resolution of estimated position can be enhanced if the internal timer clock of micro-controller is very high. However, this method imposes the lower limit on the speed operation, which is determined by the timer overflow. This is because if the time window between two consecutive index pulses is too large for the timer to count, then the timer will overflow, resulting in malfunctioning of the sensorless scheme. Moreover, the time span of two consecutive index pulses during transient speed changes will produce position error due to the usage of linear interpolation between the index pulses.

Bishop et al. [48] proposed another modified AM method to make the system less expensive and more robust by injecting only the positive portion of lower magnitude sinusoidal source voltage for amplitude modulation. This method increases the peak voltage and current level of the sinusoidal signal that will improve the signal-to-noise ratio (SNR) of the modulated signal. Furthermore, this method allows the AM encoder technique to be used on switching topologies other than ones with two switches per phase. However, it still requires external hardware such as a sinusoidal wave generator and an envelope detector for the modulated signal.

Brosse.A et al. [49] presented the sensorless control at low speed and standstill based on signal power evaluation, which is basically the AM method. The modulation signal with the frequency of 600 Hz is injected into the machine by converter. If the back emf is neglected and the resistive voltage drop is neglected at low speeds, saturation does not occur and the self-inductance depends on only rotor position. The phase voltage is simplified as,

$$v(t) = L(\theta)\frac{di}{dt} \tag{1.29}$$

The amplitude of the phase voltage is very sensitive to the noise and thus it is averaged through the power of the phase voltage. It is defined as,

$$p = \frac{1}{T}\int_{-T/2}^{T/2} v^2(t)dt \tag{1.30}$$

As the phase voltage depends on rotor position, the power of the phase voltage depends on rotor position as well. It is measured and stored in a lookup table to give the relationship between power and rotor position. Therefore, the measured power of the modulated voltage signal is compared to the signal power stored in a lookup table for different rotor positions. The difference between measured and stored signal power drives a tracking observer [37]. This approach is illustrated in Fig 1.10.

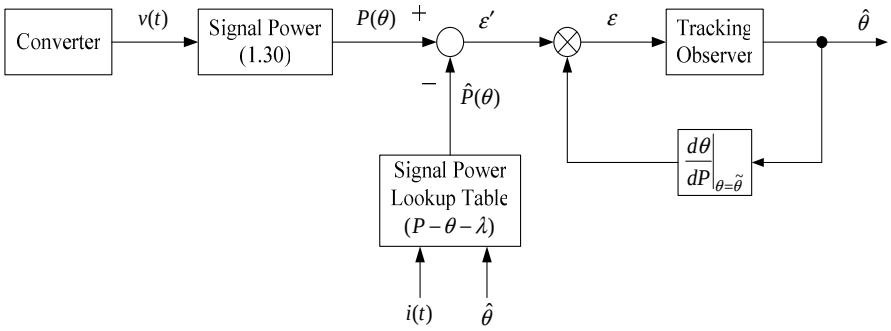

Fig 1.10 The position estimation method using signal power evaluation

This method requires no additional hardware to inject the modulation signal into the stator winding. The modulation signal is generated through the converter itself. However, this method has a couple of disadvantages. The first is the generation of negative torque. The modulation signal is injected in the negative torque region when controlling a phase for positive torque. Another problem is the delay of the commanded torque. This means the commanded torque should be delayed for a short time so that the energized phase can be modulated and the modulated phase can be energized when there is a sudden change in the sign of the commanded torque.

Table 1.10 Comparison of the position estimation method using modulated signal injection

Reference No.	Merits	Demerits
[39-42]	a. FM-based position estimation scheme b. No additional high frequency sinusoidal signal source c. Generation of frequency encoded signal by -.L/T converter [39-41] -.Wien bridge oscillation circuit [42]	a. External hardware such as frequency encoder and decoder b. Position resolution dependent on the frequency of FM signal
[43]	a. Present and implement PM and AM based position estimation schemes	a. External hardware such as sinusoidal signal generator and demodulator
[44]	a. AM-based position estimation scheme b. Verification of the high frequency effect of sensing signals on the inductance variation	a. External hardware such as sinusoidal signal generator and demodulator b. Distortion of the sensing signal by mutual coupling effect with adjacent phases
[45-47]	a. Modified AM-based position estimation scheme b. Simple hardware by using a fixed dc value compatible with the sensing signal c. Increase the resolution of estimated position by using a high frequency timer clock	a. External hardware such as sinusoidal signal generator and demodulator b. Lower limitation of speed operation according to the timer overflow c. Position error during transient speed changes
[48]	a. Modified AM-based position estimation scheme b. Injection of only positive portion of sinusoidal voltage source c. Improvement of SNR of the modulated signal	a. External hardware such as sinusoidal signal generator and demodulator
[49]	a. Modified AM-based position estimation scheme b. Position estimation based on signal power evaluation c. No additional hardware to inject the modulation signal	a. Negative torque generation due to the modulation signal injected into the negative torque region b. Delay of the commanded torque at a change in the sign of the commanded torque

The modulation encoding techniques for rotor position estimation are based on extracting the periodically varying phase inductance by applying a high frequency carrier signal. The carrier frequency is higher compared to the signal containing the phase inductance information. The encoded inductance information is decoded using suitable demodulation circuitry. However, the associated penalty is the need for external hardware circuitry, which adds cost and complexity to the drive system. When the high frequency signal is injected into one of the phases, the effective self inductance reduces considerably due to the high frequency behavior of the magnetic laminations. As a result, in order to have a reasonable resolution and good variation inductance with rotor position, the frequency of the sensing signal should be chosen optimally.

4) Intelligent control methods

Most recent literature on intelligent control methods uses artificial neural networks and fuzzy control in SRM control. The block diagram of these intelligent control methods are generally illustrated as Fig 1.11.

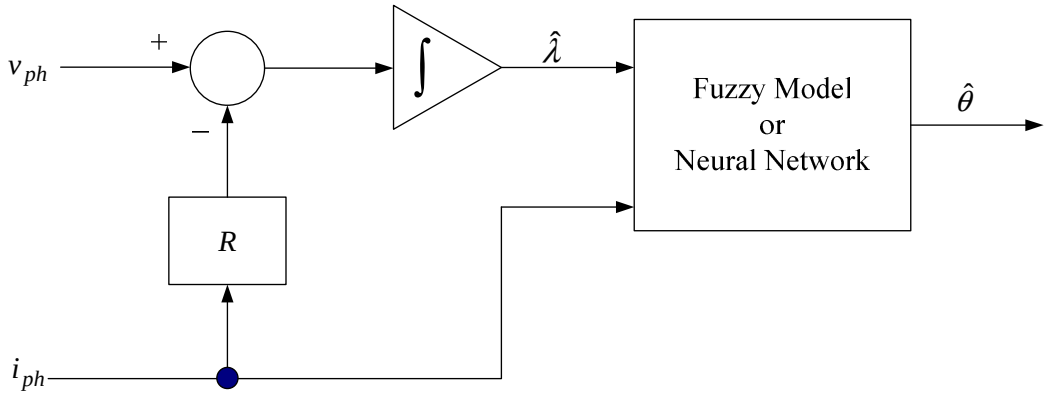

Fig 1.11 The basic scheme of intelligent control methods

Fuzzy models or neural network controllers provide rotor position information required by conventional SRM drive. In general, intelligent control methods are not model dependent, even though they learn from off-line simulation and experimental results consisting of input and output data sets. Therefore, the estimation has freedom from dependencies of parameters and disturbances. However, the number of computations is large compared to other methods and many fuzzy rules are necessary for dynamic mapping of flux linkage vs. current vs. rotor position relationships, even though operation with the estimated position from these intelligent controllers has been shown to be satisfactory.

a) Neural networks

Bellini et al. [50] used a neural network for system identification control purposes. A feed-forward type of neural network is used to identify the dynamic states of an SRM. Its inputs are the dwell angle and the state variables, consisting of phase current, flux-linkage, rotor position and speed. Its outputs are the state variables at the next time step. Naturally, rotor position along with speed is the output of the neural network. The size of training data set is 570 points for each input and the training of the two layer neural network is performed with 8 hidden neurons. It successfully proved by simulation that neural networks can be used in a closed loop system as a position and speed estimator. However, it requires a large number of computations for the training of the neural network to match the defined training data set.

Reay et al. [51, 52] proposed the enhanced position estimation algorithm at low speeds assuming the inductance is substantially varying as a sinusoidal function of rotor position and rotor pole numbers. This method makes use of the neural network in order to learn rotor position as a function of currents resulting from diagnostic voltage pulses injected into inactive phases. This eliminates the requirement of a priori knowledge about the magnetic characteristics of the SRM. However, this method requires external hardware to inject diagnostic voltage pulses into inactive phases, resulting in negative torque generation.

Mese et al. [53] proposed an approach to the sensorless control of an SRM using two neural networks; one for position estimation and the other for flux linkage estimation. The flux linkage is estimated from the estimated rotor position along with the phase current, and the error between the real and estimated flux linkages reflects the difference between the real and estimated rotor position. The flux linkage error is used to correct the estimated rotor position. This process effectively decreased the systematic errors in the position estimation and overcame the localization problem around the aligned and unaligned positions by using at least three phase's information. However, significantly large memory requirement and multiple layers with many hidden neurons per layer are necessary for optimum training of the neural network. In regards to neural networks, most of the computational effort is due to the large number of neurons in hidden layers with 15 to 20 neurons.

Hudson et al. [54, 55] proposed an approach to decrease the computational effort significantly by inserting a pre-processor in the neural network, generating a third input to the

neural network that is the product of the phase current and flux-linkage. The proposed neural network structure is shown in Fig 1.12.

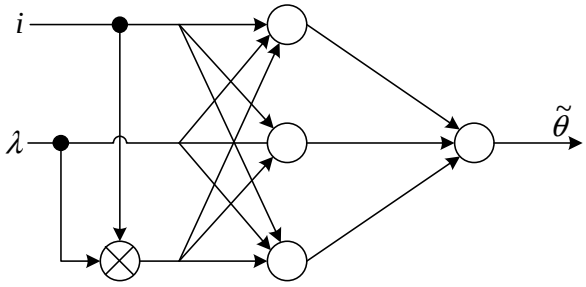

Fig 1.12 The position estimation method using minimal neural network

However, this method has the disadvantage that the accuracy of the estimated rotor position is highly dependent on the accuracy of the estimated flux-linkage. Table 1.11 summarizes the merits and demerits of the position estimation method using neural networks.

Table 1.11 Comparison of the position estimation method using neural networks

Reference No.	Merits	Demerits
[50]	a. Verification of neural network-based position estimation scheme by simulation	a. A large number of computations for the training of neural network to match the defined training data set
[51-52]	a. Enhancement of the accuracy of estimated position at low speeds by combining the diagnostic voltage pulse injection method with the neural network b. No prior knowledge of magnetic characteristics	a. External hardware for injecting diagnostic voltage pulses into inactive phases b. Negative torque generation
[53]	a. Sensorless control using two neural networks; one for position estimation and the other for flux-linkage estimation b. Correction of the estimated position error by using flux-linkage error	a. Significant large memory and computations by using two neural networks
[54-55]	a. Minimization of neural network with no hidden layer and a pre-processor with the product of flux-linkage and phase current	a. High dependence of the estimated position on the estimated flux-linkage

b) Fuzzy model

Cheok et al. [56-59] developed fuzzy logic-based rotor position algorithm for SRMs. In this method, the flux-linkage and phase current values are inputs to the fuzzy logic system. The inputs were assigned to some fuzzy set with triangular membership functions and passed through

the fuzzy rule base whose output is a certain rotor position value. In order to discard the flux-linkage measurement error which affects position estimation error, the predicted values of rotor position and flux-linkage by the fuzzy logic predictor are used in conjunction with the measured values of flux-linkage from integration and rotor position from the fuzzy system output. Therefore the fuzzy predictors forecast with very good accuracy at steady speeds. Optimal phase selector places weights on the estimated rotor positions when more than one phase is excited. The proposed method is shown in Fig 1.13.

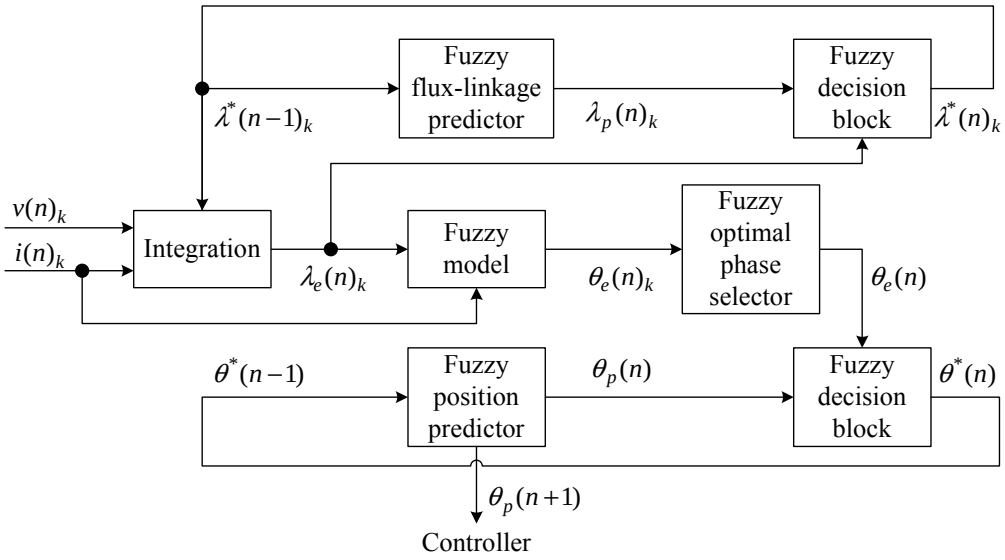

Fig 1.13 The position estimation method with fuzzy logic estimation and prediction blocks

From Fig 1.13, v_k, i_k, and λ_k are voltage, current, and flux-linkage of each phase, respectively, θ_k is position resulted from excited phases. The subscripts e and p indicate the estimated and predicted values respectively, and the superscript $*$ indicates weighted values. However, during transients the fuzzy predictors may not perform as well due to the learning period required with new events and the implementation was complex due to the use of fuzzy logic learning rules in real time and a very large number of fuzzy rules for the input data.

A simplified fuzzy logic algorithm was presented in software by Eyguesier et al. [60]. It combined the well tried flux-current lookup table method with a basic fuzzy logic system and a prediction of the rotor position by linear interpolation. The estimation is better when the rotor is not near the aligned and unaligned positions, and when the current is high. Therefore, the fuzzy logic block puts a weight of confidence in each of estimation and prediction. The prediction gives the rotor position at the next sampling time and it is refreshed by linear interpolation with

10 previous positions at a sampling rate of 10 kHz. The predicted values are compared with the estimated values and then the value being closest to the actual position is sent to the micro controller. However, confidence in predicted values will be low under transient speeds. Therefore, the reliability of the predicted position varies with operating conditions and the quality of the previous position data. Table 1.12 summarizes the merits and demerits of the position estimation method using fuzzy model.

Table 1.12 Comparison of the position estimation method using fuzzy model

Reference No.	Merits	Demerits
[56-59]	a. Prediction of flux-linkage and position to minimize measurement errors and flux-linkage integration errors b. Good accuracy of estimated rotor position at steady speeds	a. Too complex to implement due to many fuzzy rules b. Large number of fuzzy sets
[60]	a. Simplified fuzzy logic algorithm based on the combination of flux-linkage lookup table with a fuzzy predictor	a. Low confidence in predicted position values during transient speeds

c) Neuro-fuzzy model

A large number of fuzzy sets and fuzzy rules are necessary to ensure an accurate fuzzy model. To extract and optimize fuzzy rules, the adaptive neuro-fuzzy inference system (ANFIS) was proposed by Zhongfang et al. [61, 62]. The estimated rotor position will have error due to the imperfect modeling around the aligned and unaligned regions as well as the noise in the feedback signals. To overcome these problems and improve the estimation accuracy, the parameters of membership functions are iteratively adjusted to give a minimum modeling error using gradient descent and least squares methods. However, the performance of the proposed sensorless position estimation scheme was evaluated during open loop control with different turn-on and turn-off angles, dc link voltage, as well as current hysteresis reference. Despite using open loop control, the overall execution time of the implemented software routine of the proposed method is large and the sampling frequency is low, resulting in difficulties during the real time implementation.

S. Paramasivam et al. [63] proposed position estimation methods using an artificial neural network and adaptive neuro-fuzzy system with the calculation of flux-linkage and compared the performance between two estimators. The rotor position is estimated with two inputs consisting

of flux-linkage and phase current. However, in order to form a very efficient mapping between two inputs and one output, a large off-line training data set is required before getting into implementation of the neural network-based position estimator. The implementation of the neuro-fuzzy-based position estimator required 5 layers, 20 membership functions, and 400 fuzzy rules to have high accuracy position estimation. Table 1.13 summarizes the merits and demerits of the position estimation method using neuro-fuzzy model.

Table 1.13 Comparison of the position estimation method using neuro-fuzzy model

Reference No.	Merits	Demerits
[61-62]	a. Adjustment of membership functions to minimize a modeling error by using gradient descent and least squares methods	a. Not verified in closed loop system b. Hard to implement in real-time due to large execution time of the proposed method
[63]	a. Comparison of neural network and neuro-fuzzy-based position estimation methods	a. Large off-line training data set to achieve high accuracy of estimated position in neuro-fuzzy-based estimator – 5 layers, 20 membership functions, 400 fuzzy rules

1.2 Objectives for This Research

Existing position estimation methods have been reviewed. All methods use instantaneous phase inductance or flux-linkage variation information in some way to detect the rotor position. The methods have been broadly classified into four major groups.

One approach is the method to estimate position information based on terminal measurements of active phase voltage or current and associated computations. The method of monitoring the slope of phase current varying with incremental inductance [2-6], the motional back emf method [7-9], the dynamic model-based method using Fourier series [10-16], the flux-linkage/current method [17-19], the derivative of phase current method [20-21], and the observer-based method [22-25] fall under this category. Most of methods do not require additional hardware and rely on the machine characteristics for estimating rotor position. The terminal measurements of active phase voltage and current are employed as inputs for an estimator to obtain the rotor position. The most sophisticated one is the observer-based method, but it is computationally complex and needs an exact model of the motor and the load. The flux/current method are computationally simpler than observer-based methods and they may produce large estimation error near zero speed if the motional back emf is neglected and the

improper measurement of the resistance of the stator winding will lead to an erroneous estimation due to change in resistance caused by heating or measurement error.

Second approach is to estimate position information from direct measurement of an internal signal [26-28], mutually induced voltage in an active phase in chopping drives. This is possible since the mutually induced voltage can be represented as a function of the rotor position and current. However, the main disadvantage of this method is the mutually induced voltage is very small in magnitude and appears across the inactive phase. Thereby it is difficult to extract rotor position information by capturing the mutually induced voltage. Furthermore, it requires external circuitry such as rectifying circuit and passive filter in [26-28] as well as sample and hold (S/H) circuit to detect the mutually induced voltage.

Third approach is to inject low-level and high-frequency signals into an inactive phase to obtain phase inductance variation which is then mapped to position information. High frequency signal injection method [29-37], resonant circuit-based method [38], modulated signal injection method [39-49] belong to this category. The phase inductance in the inactive phase varies between aligned and unaligned position and therefore position information can be easily determined from phase inductance information. However, these methods are susceptible to interference from the excitation currents in other phases. Besides, they may produce negative torque and extra hardware circuitry is needed for most estimation methods. The maximum inductance value can be varied by increasing the frequency of the injecting pulse due to the diminution of magnetic material permeability. At high speeds, the excitation waveform occupies a major part of the phase period. Under this operating condition, the duration available for test signal injection is restricted and hence these methods are more suitable for low speed operation.

Fourth approach is the position estimation method by intelligent control using neural network [50-55], fuzzy model [56-60], and neuro-fuzzy model [61-63]. These methods are not dependent on accurate prior knowledge of the magnetic characteristics of the motor, thus having a freedom from dependencies of parameters and disturbances. However, a large number of computations for the training of the neural network to match the defined training data set and many fuzzy rules are required to have high accuracy of estimated position. Hence these methods are not the preferred approach for simpler implementations in industrial applications.

After reviewing literature relating to the sensorless position estimation of SRMs, it is evident that position estimation in SRM drives requires additional work to overcome

disadvantages of the discussed methods before a reliable and commercially applicable method is fully developed.

Prof. R. Krishnan and M. Wellner [64] proposed a new position estimation method to give a reasonable solution to the problems of reviewed publications: back emf effect near zero speed, increase of drive costs with additional hardware except for measurements of active phase voltage and current, flux-linkage measurement error from improper resistance measurement, accurate inductance model for high accuracy estimation, and speed limitation by negative torque generation. In the method, position information in a PWM period is estimated by using the first switching harmonic phase voltage and current computed by Fourier series. Assuming the resistance of the stator winding is much smaller than inductive reactance in an equivalent circuit for one phase of the SRM, inductive reactance can be represented as the ratio of magnitudes of the first switching harmonic phase voltage and current. Dividing inductive reactance by the switching frequency, phase inductance can be obtained and therefore rotor position is estimated from the relation between phase inductance and rotor position at a given current. However, if a stator winding is driven by regulated DC current with a small variation ΔI , phase inductance can be expressed as the ratio of change in flux-linkage to the corresponding change in phase current and is given as,

$$L = \frac{\Delta \lambda}{\Delta I} \tag{1.31}$$

where $\Delta \lambda$ is the variation of flux-linkage established by the variation in phase current ΔI . As SRMs operate in the saturated region or with high current, the nonlinear effect of saturation significantly diminishes phase inductance given by (1.31) and thereby the rate of change of phase inductance with respect to rotor position also diminishes. Thus the accuracy of the estimated rotor position will be degraded in saturated region or at high current.

The various methods for sensorless position estimation suggested in literature have their own merits and demerits depending on their principles of operation. Ideally, it is desirable to have a position estimation scheme, which uses only terminal measurements and does not require additional hardware and does not lead to an erroneous estimation due to the motional back emf effect near zero speed and improper measurement of the resistance of stator winding. In addition, it is desired to have reliable operation over entire speed and torque range while maintaining high resolution and accuracy even at saturated operating points.

This research proposes a new approach to all these requirements for position estimation in the SRM. The rotor position is estimated by using the first switching harmonic components of phase voltage and current through Fourier analysis, consisting of Fourier series and fast Fourier transform. The proposed method differs from [64] in that the rotor position is estimated from a unique flux-linkage value estimated by an incremental inductance at a given phase current with taking into account of the variation of phase current due to the saturation effect. ***The objectives of this research*** are:

1) to propose a novel robust position estimation algorithm independent of the motional back emf effect near zero speed, resistance change of the winding due to heating, and doesn't require external hardware circuitry such as a modulator and a demodulator;

2) to analyze and verify the proposed position estimation algorithm using Fourier series and fast Fourier transform through dynamic simulations and experiments with various loads;

3) to realize the proposed position estimation algorithm for a two-phase 6/3 SRM using a DSP-based control system under various loads;

4) to propose offline inductance measurement eliminating the eddy current effect generated by PWM switching, based on 60 Hz sinusoidal excitation using AC power supply;

5) to propose a low cost and high efficiency drive system with lower acoustic noise.

This dissertation is organized as follows. In Chapter 2, an accurate measurement method of magnetic characteristics of the SRM using AC excitation is presented. It eliminates the effect of thermal resistance change and eddy currents. With the proposed method, the accuracy of estimated rotor position can be improved due to the reduction of magnetic characteristic errors generated from thermal resistance changes and eddy current effects. However, this AC steady-state-based measurement method cannot be used during machine operation since the topology of the measurement is different from the converter for SRM drives. Hence a new method of the magnetic characterization in SRM drives is required and proposed. It decomposes active phase voltage and current in a PWM period into their first switching harmonic components. Chapter 3 describes how to compute the magnetic characteristics of the SRM during normal operation and Chapter 4 presents how to effectively estimate the rotor position with the computed magnetic characteristics. In order to validate the proposed position estimation method, comprehensive sets of dynamic simulations and experiments under various loads are performed and analyzed in Chapter 5 and 6, respectively. Chapter 7 presents a split AC drive system with low acoustic noise.

This drive system combined with the proposed position estimation method will make a strong solution for low-cost variable speed drive system application. Concluding remarks including contributions of the work are given in Chapter 8.

CHAPTER 2 FLUX-LINKAGE MEASUREMENT USING AC EXCITATION

2.1 Introduction

SRM drives offer advantages in many applications due to their constructional simplicity, energy efficiency, and wide speed range. SRMs are mechanically simple and robust due to their lack of windings and brushes on the rotor [65]. The design, evaluation, and control of SRMs require detailed knowledge of the flux-linkage characteristics of the stator windings as a function of rotor position and excitation current. However, SRM drives are very difficult to model and simulate by analytical methods because of their inherent nonlinearity and complex magnetization characteristics. For a fixed supply voltage, phase current is dependent on the flux-linkage or inductance at given rotor position. Furthermore, SRMs are commonly operated during magnetic saturation and their excitation waveforms are non-sinusoidal. Hence, precise measurement of the magnetic flux-linkage characteristics is important to verify machine design and for accurately predicting the performance of SRM drives.

Generally, it is possible to calculate the magnetization curves without resorting to experimental measurements by using finite element analysis (FEA) [66-68]. However, the accuracy of FEA depends on the size of the elements used and in addition, it is difficult to model non-linear effects because they are computationally complex. Due to the inherent limitations of FEA, experimental measurements are an important part of the design process, prototyping, and production line verification of SRM drives.

A common method to obtain the motor's magnetization characteristics is to measure the voltage and current waveforms in the stator winding and use the waveforms to calculate the stator flux-linkage. In this method, a voltage is applied to the phase winding and the terminal voltage and current are measured. The flux-linkage can be found by taking the time integral of the difference between the applied phase voltage and the voltage drop across the stator phase resistance. In most integration techniques, the general practice is to apply a voltage pulse to the stator winding by clamping the rotor to a know position. The current rises up to a steady state level, and then the voltage is turned off, de-energizing the stator winding. Throughout this time,

integration takes place to determine the instantaneous flux-linkage as a function of current and position.

Prof. R. Krishnan et al. [69] described and compared various methods to measure the inductance of the SRM. Three approaches to implement the proposed method are described and compared. One of them is the direct measurement of flux-linkage by hardware integration of the winding voltage. Others are the indirect measurement of flux-linkage by the measurement of rising current at constant voltage or the measurement of decaying current when the stator winding is de-energized. However, the direct method requires an elaborate hardware circuit including op-amps for integration and the measurement accuracy is affected by the temperature sensitivity and offsets in the hardware circuit. In the indirect method, there is a difficulty in maintaining the voltage across the stator winding continuously throughout the measurement.

Recently, digital methods using a personal computer or data acquisition system have been presented to acquire the voltage and current waveforms, and thereafter integrate and plot the flux-linkage. Data acquisition system proposed in [70] measures the flux-linkage characteristics by integration of $\left(v_{ph} - i_{ph}R\right)$ with voltage and current recorded in digital storage oscilloscope (DSO). However, it has the difficulty in accurate synchronization of the trigger signal to excite a winding with the trigger signal for sampling data in DSO. This produces numerical integration errors. Furthermore, the variation of the resistance of the stator winding due to thermal effects leads to a drift in flux-linkage characteristics. This measurement is not fully automated in terms of controlling phase current during the test. Therefore, improved digital methods [71-73] have been published by constructing a PC-based digital integration system with controlling phase current.

An off-line PC-based measurement scheme with appropriate data acquisition system employing choppers for measuring the inductance of SRM was proposed in [71]. This method conducts the measurement under condition closer to normal operation since the chopper circuit for the measurement setup is similar to the SRM converter. However, this method requires several hardware interface circuits including the chopper circuit consisting of two transistors and two diodes, the base driver circuit, and the control circuit as well as the integration routine in software. The main advantage in [72] is that set of lead acid batteries is used to excite the stator winding. Due to very low source resistance, battery regulation is better than rectifying ac

voltage with capacitor filters. However, two or more batteries are required in series, depending on the resistance of the stator winding and the peak current required during the test.

In [73], a fully automated and user friendly experimental method for measuring the magnetization characteristics of the SRM was proposed. The proposed measurement method is based on the graphical programming environment, LabVIEW software. However, thermal resistance changes are neglected during the test. The pervious methods have not taken into account impact on flux-linkage by thermally induced resistance changes and eddy current effects. Circulating eddy currents in motor laminations produce power losses in the machine and decrease the magnetic field strength. The reduced magnetic field diminishes the magnetic inductance or flux-linkage and thereby the torque output of the machine diminishes. Furthermore, as current flows through the stator windings, the resistance of the phase winding increases. At the same time, heat is transferred from the phase windings into the stator laminations, causing a temperature rise in the stator and electrical resistance of the stator windings. Due to the complexity of these nonlinear effects, it is necessary to develop a fully automated experimental environment for accurately measuring the flux-linkage characteristics of the SRM.

The proposed method in this research is based on analysis in the frequency domain of AC equivalent circuit by using a variable AC power supply. Instead of chopping the dc power supply, the measurement system can be more simplified and the chopper for adjusting the DC power supply becomes superfluous. This simplified and automated method measures the magnetic characteristics of SRM drives using reconfigurable FPGA hardware programmed graphically with National Instruments LabVIEW. The FPGA-based measurement system provides advantages in the measurement and control of electric machines due to the timing, triggering, and custom logic capabilities of the reconfigurable chipset. A measurement methodology based on 60 Hz sinusoidal excitation using a variable AC power supply is developed which provides an alternative to time domain integration approaches for magnetic characterization. An automated software environment provides the ability to accurately measure voltage and current waveforms, perform sensor calibration, acquire rotor angular position, and eliminate error from thermal and eddy currents effects. The measured flux-linkage profile is correlated with FEA results for validation of the proposed method.

2.2 Measurement of Eddy Currents

Eddy current losses are generated due to the existence of circulating currents within the body of a ferromagnetic material under conditions of a time varying magnetic flux. Circulating eddy currents in motor laminations produce power losses in the machine and decrease the field strength. The reduced magnetic field decreases the magnetic inductance and thereby the torque output of the machine. The magnitude of the eddy current effect can be measured by taking the difference between the measured input power and the copper losses while running the motor at rated voltage and frequency under no-load conditions. We assume that the power dissipation effects from windage losses due to air resistance and friction losses due to mechanical friction in the machine bearings are negligible. Per phase equivalent circuit of SRM with ac excitation is shown in Fig 2.1.

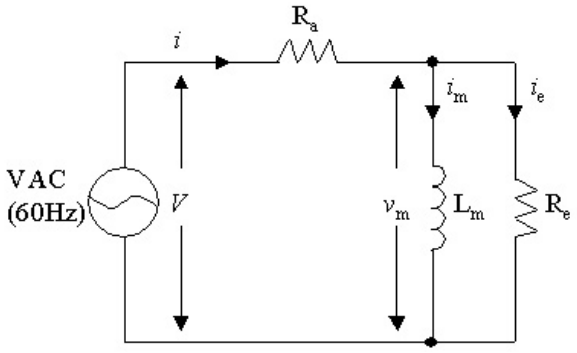

Fig 2.1 Equivalent circuit with the eddy current

In this figure, V is the RMS input voltage, v_m is the reactive voltage in the phase inductance of the stator winding, i is the current in the phase resistance of the stator winding, i_m is the reactive current in the phase inductance of the stator winding, i_e is the eddy current through the eddy current paths, R_a is the AC phase resistance in the stator winding, R_e is the eddy current-flowing resistance and L_m is the phase inductance of the stator winding. In terms of the equivalent circuit, the resistance of the eddy current paths at very low frequencies is very high compared with the reactance and all the current flows through the inductance providing magnetization in the machine [74]. The power relationship in the Fig 2.1 is given by,

$$P = P_{R_a} + P_{R_e} = I^2 \cdot R_a + I_e{}^2 \cdot R_e \tag{2.1}$$

$$P_{R_e} = P - P_{R_a} \tag{2.2}$$

where P is the total real power input (W), P_{R_a} is the copper loss (W), and P_{R_e} is the eddy current loss (W). Since using an AC single phase supply to measure inductance, the machine will have not only eddy current losses but also hysteresis losses. They are obtained by subtracting the copper losses from the total losses. However, hysteresis losses are much less than those of the eddy currents. (Hysteresis loss is 17% of the total core losses and in fact 83% of the losses are due to the eddy currents [75].) Therefore, the hysteresis losses are neglected in this research. A reactive voltage and an eddy current loss (P_{R_e}) are also represented as,

$$v_m = v - i \cdot R_a \ , \ P_{R_e} = \frac{{V_m}^2}{R_e} \tag{2.3}$$

where V_m is the RMS value of v_m. Based on the above equation, the eddy current-flowing resistor is obtained as following,

$$R_e = \frac{{V_m}^2}{P_{R_e}} \tag{2.4}$$

From the Ohm's law, the eddy current is obtained and then the current in the stator winding is calculated as below.

$$i_e = \frac{v_m}{R_e} \tag{2.5}$$

$$i_m = i - i_e \tag{6.6}$$

Self-inductance is obtained by dividing the RMS phase inductance voltage, V_m by the product of the angular frequency and RMS phase inductance current, I_m.

$$L_m = \frac{V_m}{\omega I_m} \tag{2.7}$$

Flux-linkage is obtained from the self-inductance calculated in equation (2.7) and the RMS value of the phase current as,

$$\lambda_m = L_m I_m \tag{2.8}$$

2.3 Measurement of Resistance Change Due to Heating

The change in resistance of the phase winding due to temperature has to be integrated for accurate flux-linkage measurements. Improper value of resistance can lead to drift in flux-

linkage characteristics. Measurements are made with sufficient time gap between measurements so that the temperature effects are minimized. Resistor values for copper at any temperature other than the standard temperature (usually specified at 20 Celsius) are measured through the following formula [76].

$$R = R_{ref}\,[1+\alpha\cdot(T-T_{ref})] \tag{2.9}$$

where, R is the resistance at temperature "T", R_{ref} is the resistance at reference temperature T_{ref}, α is 0.004041, which is the temperature coefficient of resistance for copper, T is the temperature in degree Celsius.

2.4 Experiments

2.4.1 Experimental Setup

The systems for measuring the flux-linkage of the SRM consists of two-phase SR machine with 4 stator poles and 6 rotor poles, a rotor clamping and disk, several CompactRIO devices, an interface drive circuit between AC power supply and the CompactRIO devices, LabVIEW 7.1, PXI-7831R reconfigurable I/O device using the LabVIEW FPGA Module. Fig 2.2 shows the completed experimental measurement setup for flux-linkage profile of the SRM. Clamping and disk are used to fix the rotor position to a given angle and to lock the disk coupled with the machine shaft through an attached clamp.

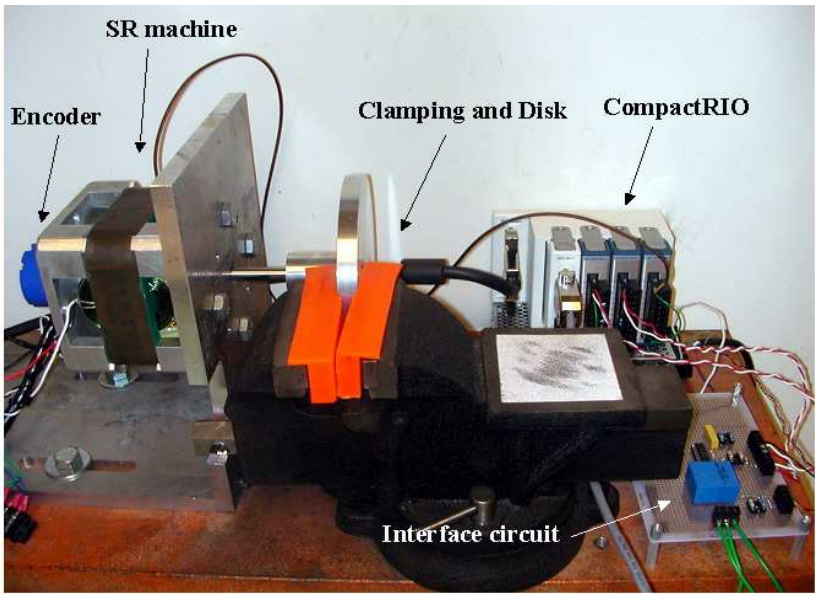

Fig 2.2 The measurement system for flux-linkage profile of SRM
- Photo taken by Keunsoo Ha on May in 2005

AC power supply is connected to the interface circuit through a single-phase transformer as shown in Fig 2.3. The applied AC power supply is adjusted at every measuring rotor position so that the maximum reactive peak current reached during the test do not exceed approximately the rated machine current of 8A.

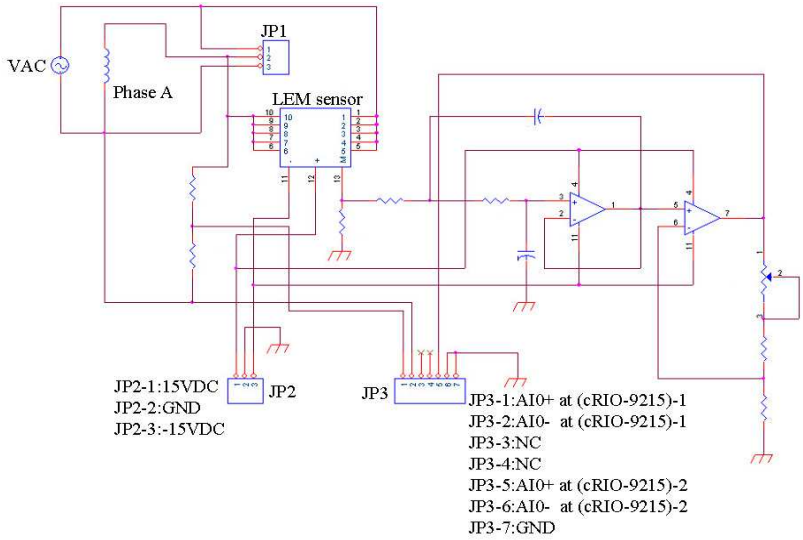

Fig 2.3 Interface circuit for measurement phase voltage and current

Power supply ($\pm 15V$) is connected through JP2 in order to operate the current sensor and op-amp. Two optically isolated cRIO-9215 modules (4-channel /$\pm 10V$, 16-bit simultaneous analog input modules) are used so that the phase voltage and the current are isolated and cannot share the same ground. The phase voltage is measured through one analog input module (cRIO-9215, JP3-1 and JP3-2) by the mode of sensing floating differential signals. To keep the voltage within the common-mode range of the module, the negative lead of the signal is connected to the COM of the cRIO-9215 through $1M\Omega$. The phase current is measured through another analog input module (cRIO-9215, JP3-5 and JP3-6). The current sensor signal is amplified through a non-inverting amplifier circuit as shown in Fig 2.3 and then converted to a voltage. The converted voltage signal is connected to the cRIO-9215 in a referenced single-ended mode.

From Fig 2.4, RMS values for phase current and phase voltage of the stator winding are measured by LEM current sensor (LA25-NP) with a second order low pass filter and an amplifier and the voltage attenuator, respectively. The actual resistance variation due to the temperature changes is measured by a cRIO-9211 (4-channel thermocouple input module) with a J-type thermocouple. A quadrature encoder is used to obtain the rotor position and detect any

variations in rotor position after clamping. The encoder signals are acquired using a cRIO-9411 (6-channel differential digital input module). A LabVIEW FPGA application for decoding the encoder signals is downloaded into the PXI-7831R FPGA module. This reconfigurable FPGA I/O module is also used to collect the voltage, current, and temperature of the stator winding. The measurement data is also then passed to a Windows host application for computing the flux-linkage.

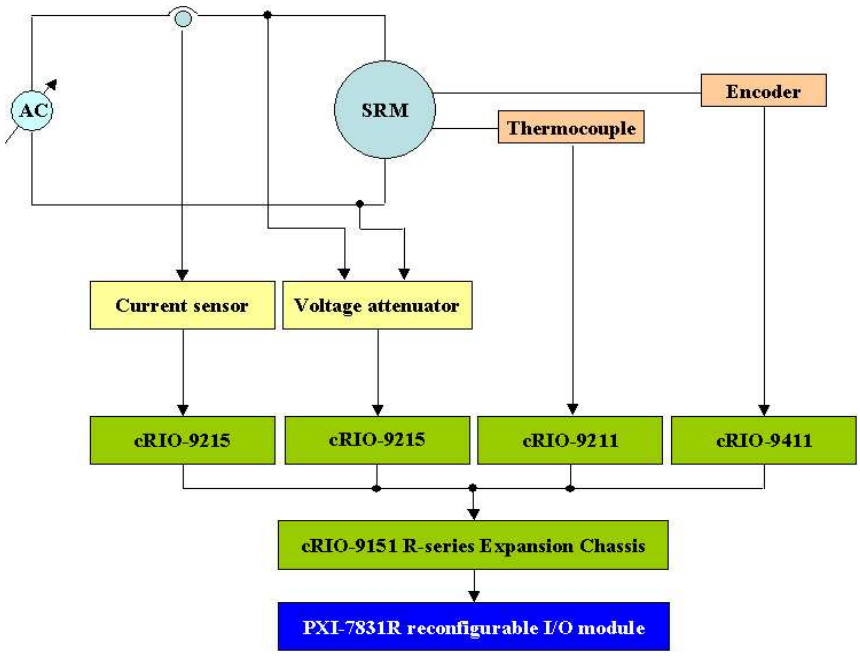

Fig 2.4 Block diagram for experimental measurement system

The real-time based system initiates the measurement of the flux-linkage of the SRM and the following steps are performed.

i) An offset error adjustment of the current sensor and voltage of the stator winding by calibration process is performed.

ii) The rotor position is reset and fixed every two mechanical degrees by clamping device. The rotor position is obtained from the encoder and it is online monitored by running the LabVIEW software program.

iii) The stator winding is excited by AC power supply, which is adjusted so that the stator current can rise up to a desired steady state current value.

iv) Phase voltage, phase current, and resistance of the stator winding due to temperature raises are measured and then real input power, copper loss, and the eddy current loss are calculated.

v) Flux-linkage is calculated by multiplying the self-inductance and reactive current in the phase inductance. These calculated flux-linkage, phase current, and position are automatically stored onto the disk drive.

Based on the above steps, the detailed flowchart for the execution of the proposed method performed on the LabVIEW environment is given in Fig 2.5.

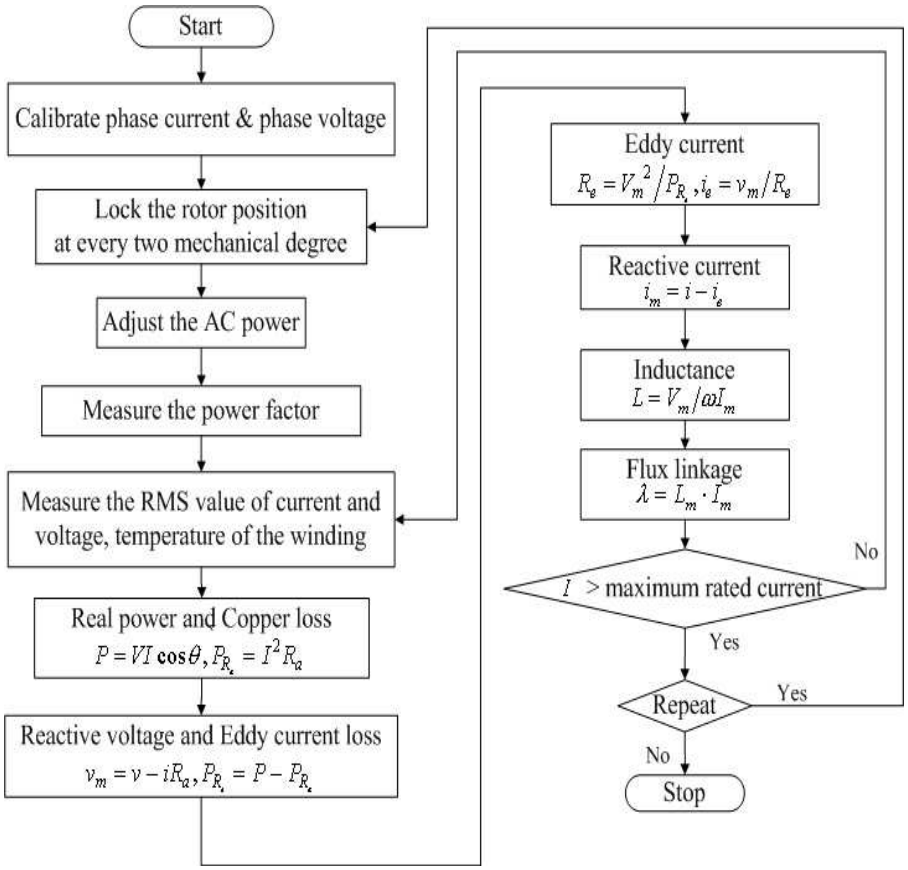

Fig 2.5 The flow chart for the measurement of flux-linkage

The LabVIEW environment is based on the concept of virtual instruments (VIs), which can be defined as layers of software and hardware, added to a personal computer, in such a way that the computer acts as a custom-designed instrument. The VIs is consisted of two elements, which are a front panel and a block diagram. The front panel is a graphical user interface used for data presentation and control inputs. The layer behind the front panel is called the block diagram and is essentially the program that implements the user-defined analysis, acquisition, and control. The developed front panel in this paper is shown in Fig 2.6 and it allows the user to enter the resistance of the motor, supply power frequency, etc. and displays the rotor position,

calibration data, and the measurement data including the phase current, the phase voltage, the eddy current losses, the resistance value due to the temperature raises, the flux-linkage, etc.

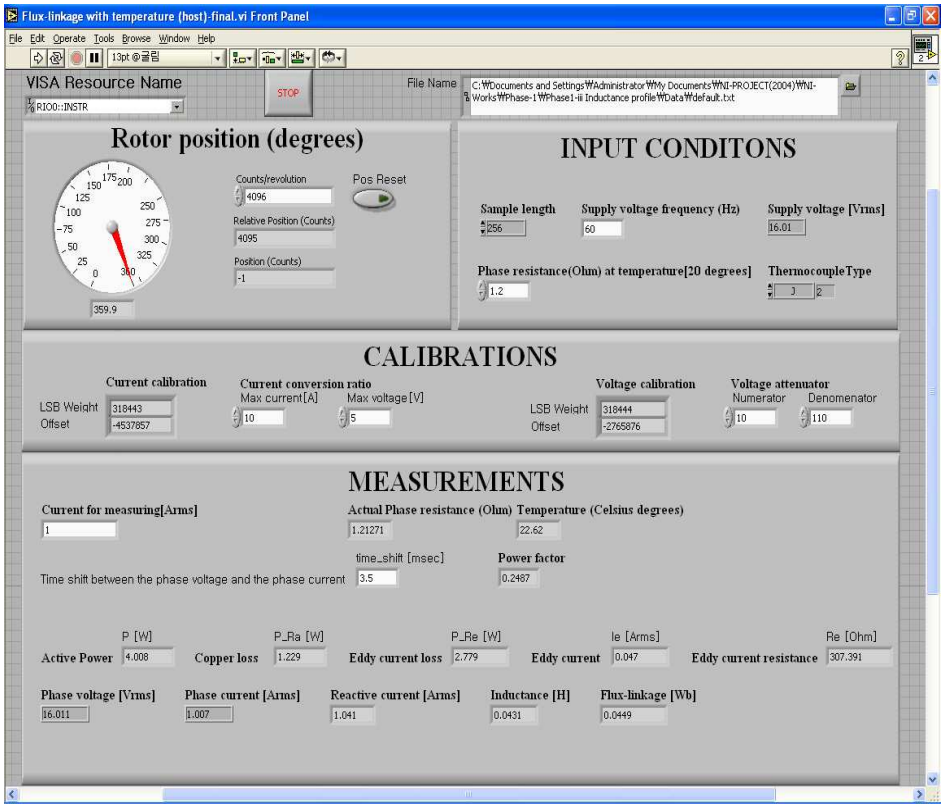

Fig 2.6 The front panel for the measurement of flux-linkage

The encoder used in the test has the resolution of 4,096 counts per revolution and the rotor position is represented as an absolute position and relative position. The temperature of the stator winding is measured by a J-type thermocouple and used to calculate the actual resistance. The power and eddy current is calculated by the principle in section 2.2. The power factor can be measured by checking the time shift between the phase voltage and the phase current. It can be used in calculating the active power and the reactive power. The phase voltage and current is acquired at a sampling rate of 65 μs. This provides 256 samples per 60 Hz cycle. To increase the reliability of the calculated RMS values, the duration of the acquisition should include at least three 60 Hz cycles. The measured voltage and the current are used to calculate the flux-linkage. The flux-linkage value vs. phase current vs. position is displayed and is automatically stored on the computer disk.

2.4.2 Experimental Results

Experiments to measure the flux-linkage vs. current characteristics are performed every two degrees. The rotor position is automatically saved and appended to a file at the end of each test. As the tested SRM has 4 stator poles and 6 rotor poles and is designed with curved stator poles for self-starting, there is asymmetry between the positive and negative slope of the flux-linkage. Experimental results from the proposed method are given in Fig 2.7 and Fig 2.8.

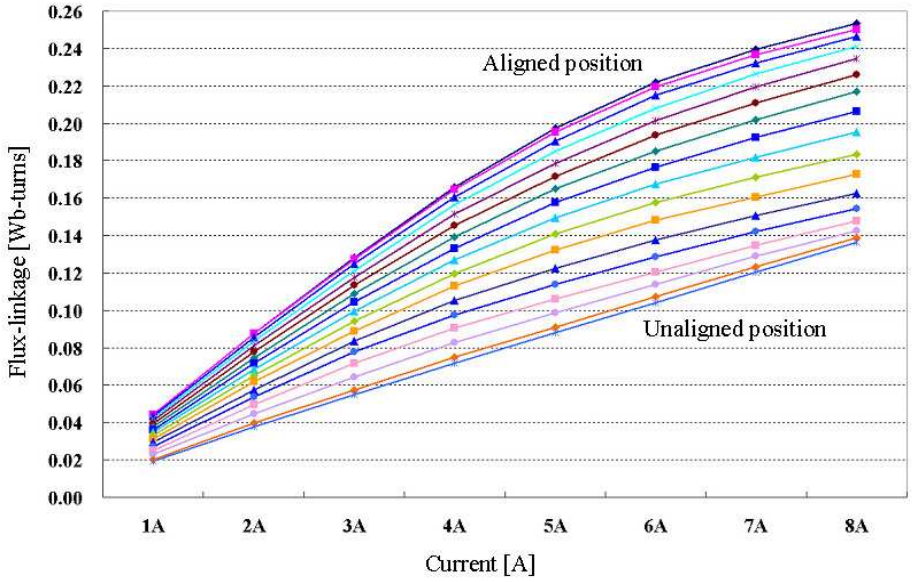

Fig 2.7 Experimentally measured flux-linkage vs. current for 0 to 30 degrees at steps of 2 degrees

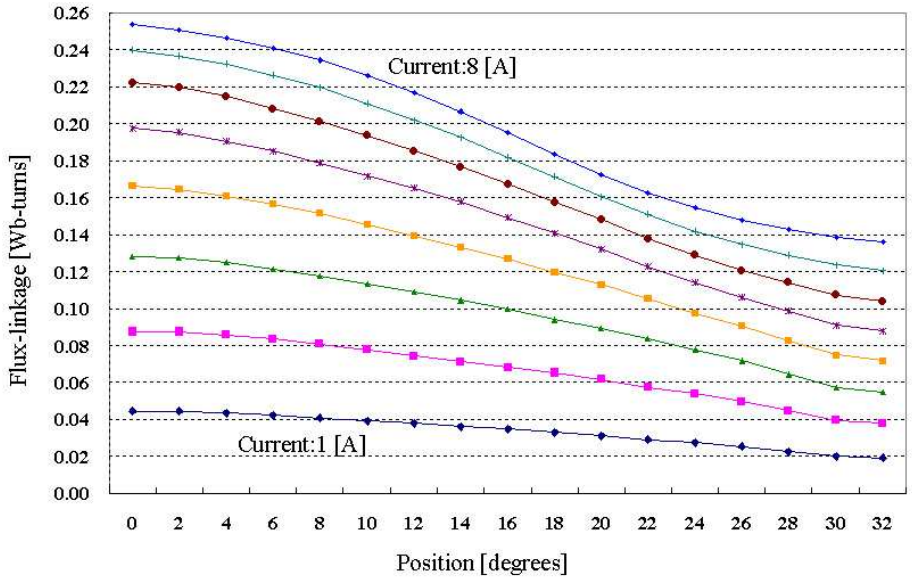

Fig 2.8 Experimentally measured flux-linkage vs. position

These figures illustrate the flux-linkage vs. the current and the flux-linkage vs. position. A number of measurements were performed and the flux-linkage characteristics were plotted to portray a set of magnetization characteristics. From Figs 2.7 and 2.8, the magnetizing curves are very smooth and it can be noticed that the curves are denser near aligned position than at unaligned position. Flux-linkage curves were linear at the fully unaligned position, but nonlinear around the fully aligned position, as expected. In these results, we can observe saturation with currents greater than 7 A.

2.4.3 Evaluation

For available two phases 4/6 SRM, experimental measurements are performed in order to compare flux-linkages to simulation results given by FEA even though FEA method has a variation depending on the elements used. The measured and finite element results of the motor from the unaligned to aligned position with a step of two degrees in the rotor position are shown in Fig 2.9.

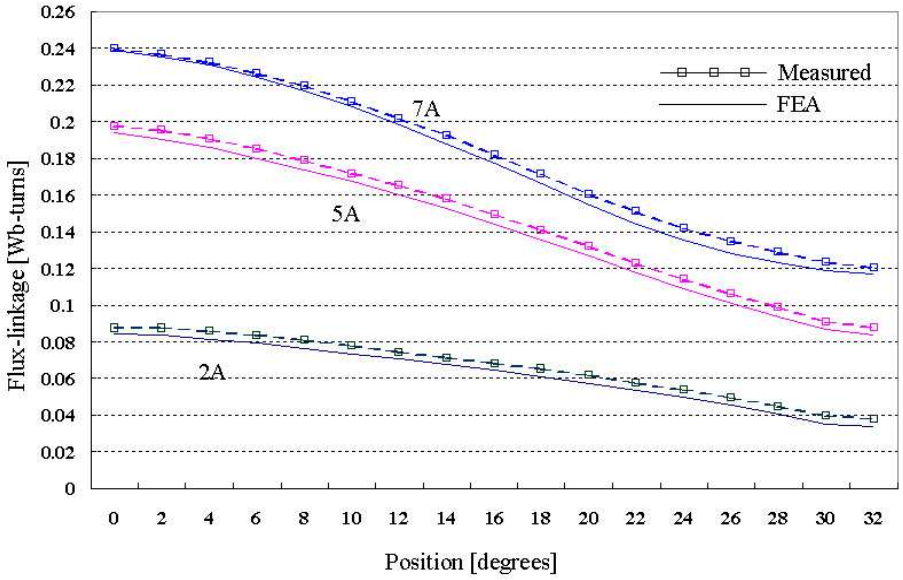

Fig 2.9 Comparison of the flux-linkage at various current levels

From 2.9, there is high correlation in the aligned region, but small discrepancies occur since it may be attributed to the clamping action being not strong enough to hold the rotor through the torque, attempting to align the rotor with the nearest stator pole when current is applied. Further,

the steel manufacturers provide the inexact B-H characteristics and to a smaller degree, the magnetic properties of the core material can be distorted due to the punching process.

Table 2.1 shows a comparison of the flux-linkage by measurement and finite element analysis methods at discrete points to evaluate the correlation between the results.

Table 2.1 Comparison of the measured flux-linkage

Current (A)	Position (Degree)	Measured	FEA	Error
		[Wb-turns]	[Wb-turns]	[%]
2	0	0.087496	0.084159	3.81
	10	0.077822	0.076428	5.34
	20	0.061711	0.057124	7.43
	30	0.039639	0.035425	10.63
5	0	0.197373	0.195733	1.65
	10	0.171717	0.169498	2.55
	20	0.132155	0.129321	4.20
	30	0.091079	0.088792	4.90
7	0	0.239582	0.239278	0.44
	10	0.210998	0.209278	1.51
	20	0.160824	0.157634	3.64
	30	0.123702	0.120856	4.22

In the aligned position, both the analytical and finite element results are close to the measured flux-linkage with approximately 4% error. The maximum error is approximately 11% and the error reduces as the current increases in the winding. It can be seen from Table 2.1 that the magnetic characteristics from the proposed experimental method have satisfactory results. The closeness of the values suggests that a high confidence can be placed on the results obtained by the real-time measurement method.

In order to evaluate the eddy current effects on flux-linkage, the eddy current is measured using the proposed method in this research. The effect of the eddy current on the flux-linkage at the unaligned position is illustrated in Fig 2.10.

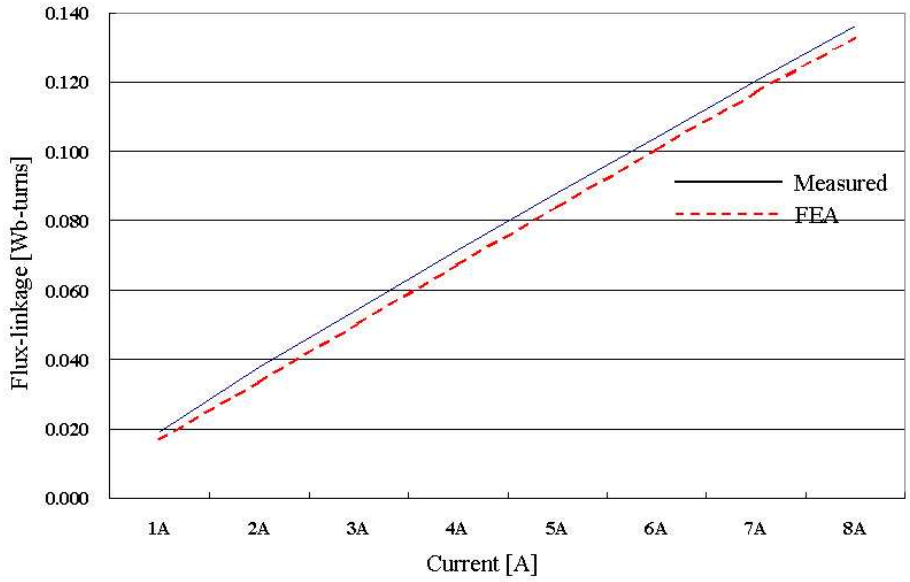

(a) Measured (without eddy current) and FEA (with eddy current)

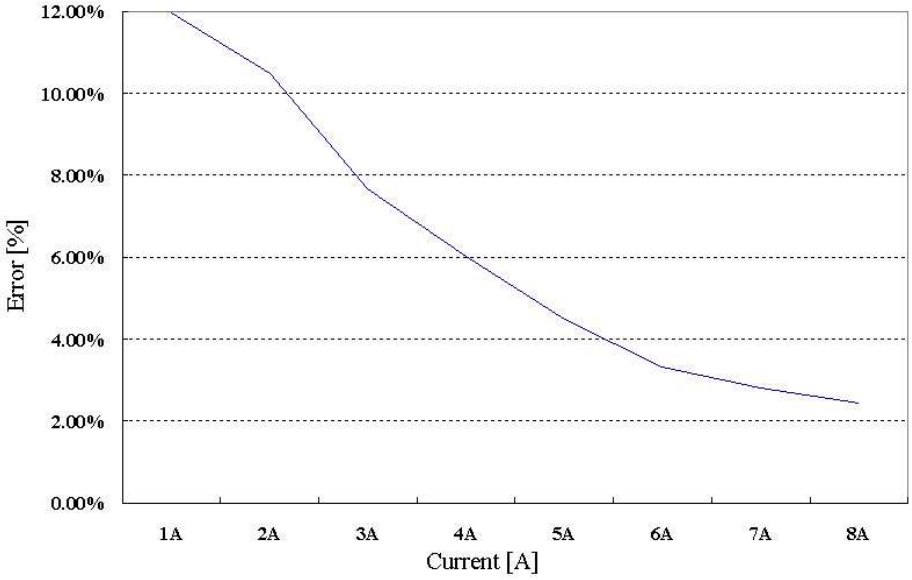

(b) Percentage error with the eddy current

Fig 2.10 Effect of the eddy current on the flux-linkage under the unaligned position

From Fig 2.10(a), the measured data represents the information without the eddy current, that is to say, the eddy current is eliminated from the real current of the stator winding, and the FEA represents the information with eddy current. Fig 2.10(b) gives the percentage error for different currents at the unaligned position. The error reduces as the current increases in the stator winding. The maximum error is found to be approximately 12% at 1A. In spite of using laminated core to

reduce the undesirable eddy current effect, time varying current applied to the stator winding produces an eddy current in the core in the direction canceling the original magnetic field. This results in a reduction in the flux-linkage or self-inductance.

2.5 Conclusions

In this chapter, an automated method to measure flux-linkage of the SRM has been proposed and it has eliminated error from thermal resistance changes and eddy current effects. The measured flux-linkage has been compared with FEA results for validation of the proposed method. The following are believed to be original contributions of this chapter:

1) A method of magnetic characterization of the SRM using ac excitation independent of eddy current effects and without the use of a dc chopper has been proposed.
2) The proposed method has been experimentally verified and correlated with FEA of a prototype SRM.
3) Excellent correlation between the proposed method of measurement and finite element analysis results has validated the proposed approach.
4) The proposed method has taken into consideration the variation of resistance in the winding during measurements.
5) For a flexible measurement environment and user-friendliness of the measurement system, a LabVIEW environment has been developed. This greatly facilitated the experimental measurement.

CHAPTER 3 COMPUTATION OF FLUX-LINKAGE BASED ON THE FIRST SWITCHING HARMONICS OF PHASE VOLTAGE AND CURRENT USING FOURIER ANALYSIS

3.1 Introduction

The general principle behind most sensorless schemes reviewed in Chapter 1 is that, if one can measure flux-linkage or inductance together with phase current, then the rotor position can be determined from the magnetic characteristics of the SRM. The accuracy of rotor position information can be determined from an accurate measurement of flux-linkage or inductance. Hence, in the previous chapter, the automated method to measure flux-linkage of the SRM was proposed. With the proposed method, the accuracy of estimated rotor position can be improved due to the reduction of magnetic characteristic errors generated from thermal resistance changes and eddy current effects.

However, the flux-linkage measured by this AC steady-state measurement method cannot be used during machine operation since the circuit topology of the measurement system is different from the converter in normal SRM drives. In SRM drives, the current flowing into the stator winding is regulated by switching on or off power devices which connect each phase to a DC power supply. Therefore, a new method of magnetic characterization in SRM drives for this type of control is required and it is proposed and developed in this chapter.

The SRM control at a constant switching frequency in the converter causes to have harmonic components in phase voltage and current besides dc components. With harmonic analysis in frequency domain, harmonic frequency components of phase voltage and current can be obtained. If the fundamental frequency in harmonic spectrum of the phase voltage and current is to the switching frequency, it is shown that the magnetic characteristics of the SRM drives can be computed based on the decomposed first switching harmonic components of phase voltage and current. Assuming the resistance of the stator winding is much smaller than inductive reactance in an equivalent circuit for one phase of the SRM, inductive reactance can be represented as the ratio of magnitudes of the first switching harmonic phase voltage and current.

Dividing the inductive reactance by the switching frequency, phase inductance can be obtained and flux-linkage can be obtained from the multiplication of phase inductance and current. Hence rotor position information can be estimated from the relationship between flux-linkage and rotor position at a phase current measured in SRM drives.

If the SRM is controlled at a constant switching frequency, which is reflected in phase voltage and current, we can assume that phase voltage and current are continuous and periodic with the switching frequency and thereby they can be decomposed into their frequency components consisting of magnitude and phase angle. For the decomposition of phase voltage and current in frequency domain, Fourier series and fast Fourier transform (FFT) are selected. In harmonic analysis of phase voltage and current, dc component is ignored since the first switching frequency component is only of interest in the sampled phase voltage and current.

A procedure to extract the first switching harmonic components of phase voltage and current in a PWM period is presented in this chapter. In a method using Fourier series, the first switching harmonic component of phase current is computed with the help of the slope of phase current during turn-ON and turn-OFF times, assuming the gradients of phase current are linear in a PWM period. Higher slope of phase current in the hardware implementation leads to easier computations for flux-linkage or inductance in a PWM period. Thus the hard chopping method, one of methods in PWM control strategies, is selected in order to obtain a higher slope in the phase current.

On the other hand, in a method using FFT, phase voltage and current are sampled at a constant rate, at least two times the switching frequency, in order to ensure that all relevant information is contained in sampled signals. An anti-aliasing filter eliminates distortions in the signal, resulting in sufficient attenuation at frequencies above the switching frequency. With these considerations of the sampling rate and anti-aliasing filter, the sampling rate and sample size for FFT computation are presented. A procedure to compute the flux-linkage based on the decomposed first switching harmonic components of phase voltage and current is presented in this chapter.

3.2 Fourier Series Development

The decomposition of phase voltage and current into their first switching frequency components based on Fourier series is described in this section. It was originally reported by Prof. R. Krishnan and M. Wellner [64]. The SRM is controlled at a constant switching frequency and assuming phase voltage and current are continuous and periodic with the switching frequency, they are decomposed into a weighted sum of sinusoidal functions. The first harmonic components of phase voltage and current are utilized to compute the inductance or flux-linkage.

3.2.1 General Form of Fourier Series

The Fourier series is a mathematical tool used for analyzing an arbitrary periodic function by decomposing it into a weighted sum of much simpler sinusoidal component functions. If $f(t)$ is continuous and periodic with T, $f(t)$ is expressed as sum of harmonic sine waves and a dc value as,

$$f(t) = \frac{a_0}{2} + \sum_{n=1}^{\infty} [a_n \cos(\omega_n t) + b_n \sin(\omega_n t)] \tag{3.1}$$

where, for any non-negative integer *n*:

$\omega_n = n\frac{2\pi}{T}$, is the nth harmonic of the function of $f(t)$

$a_n = \frac{2}{T} \cdot \int_0^T f(t) \cdot \cos(\omega_n t) dt$, are the even Fourier coefficients of $f(t)$, and

$b_n = \frac{2}{T} \cdot \int_0^T f(t) \cdot \sin(\omega_n t) dt$, are the odd Fourier coefficients of $f(t)$

Given a periodic signal $f(t)$, straightforward calculations in trigonometric form can be used to find the amplitude and phase angle in the Fourier series development as,

$$f(t) = \sum_{n=0}^{\infty} c_n \cdot \sin(\omega_n t + \varphi_n) \tag{3.2}$$

Periodic function $f(t)$ is decomposed into the following various forms as,

DC term: $c_0 \cdot \sin(\varphi_0)$

Fundamental or first harmonic term: $c_1 \cdot \sin(\omega t + \varphi_1)$

n-*th* harmonic term: $c_n \cdot \sin(\omega_n t + \varphi_n)$

If the first harmonic term in equation (3.1) is represented as $g(t)$, it is expressed as,

$$g(t) = a_1 \cos(\omega_1 t) + b_1 \sin(\omega_1 t) \tag{3.3}$$

Comparing the first harmonic term in equation (3.2) with equation (3.3), we can represent the phase angle and amplitude of the first harmonic term of a periodic function $f(t)$ as,

$$\varphi_1 = \tan^{-1}(\frac{a_1}{b_1}) \tag{3.4}$$

$$c_1 = \sqrt{a_1^2 + b_1^2} \tag{3.5}$$

Based on equations (3.4) and (3.5), we can compute the amplitude and phase angle of the first switching harmonic term in phase voltage and current, if $f(t)$ is replaced with the phase voltage and current, respectively.

3.2.2 Computation of the First Switching Harmonics of Phase Voltage and Current

3.2.2.1 First Switching Harmonic of Phase Voltage

In hard chopping PWM current control mode, the resulting phase voltage waveform in SRM drives is shown in Fig 3.1. T is a PWM period, inverse of chopping frequency, and d is the ratio of turn-on time to a PWM period, referred as the duty cycle.

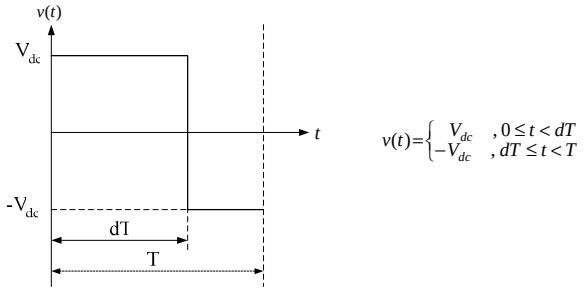

Fig 3.1 Phase voltage characteristic during one PWM period

A dc value in phase voltage is of no concern since we are only interested in the first harmonic term in phase voltage. The first harmonic of phase voltage is given by,

$$v_{a1} = \frac{2}{T} \cdot \int_0^T v(t) \cdot \cos(\omega t) dt \tag{3.6}$$

$$v_{b1} = \frac{2}{T} \cdot \int_0^T v(t) \cdot \sin(\omega t) dt \tag{3.7}$$

By substituting $v(t)$ in Fig 3.1 into equation (3.6), the coefficient of the cosine part in the first switching harmonic of phase voltage can be expressed as,

$$v_{a1} = \frac{2}{T} \cdot \left\{ \int_0^{dT} V_{dc} \cdot \cos(\omega t) dt + \int_{dT}^{T} (-V_{dc}) \cdot \cos(\omega t) dt \right\} = \frac{2 \cdot V_{dc}}{\pi} \cdot \sin(2\pi d) \tag{3.8}$$

By substituting $v(t)$ in Fig 3.1 into equation (3.7), the coefficient of the sine part in the first switching harmonic of phase voltage can be expressed as,

$$v_{b1} = \frac{2}{T} \cdot \left\{ \int_0^{dT} V_{dc} \cdot \sin(\omega t) dt + \int_{dT}^{T} (-V_{dc}) \cdot \sin(\omega t) dt \right\} = \frac{2 \cdot V_{dc}}{\pi} \cdot \{1 - \cos(2\pi d)\} \tag{3.9}$$

From equations (3.8) and (3.9), the phase angle and amplitude of the first switching harmonic of phase voltage can be expressed as,

$$v_{\varphi 1} = \tan^{-1}\left(\frac{v_{a1}}{v_{b1}}\right) \tag{3.10}$$

$$v_{c1} = \sqrt{v_{a1}^2 + v_{b1}^2} \tag{3.11}$$

Consequently, $v_1(t)$ the first switching harmonic function of phase voltage in trigonometric form can be represented as equation (3.12) and it contains the amplitude and phase angle as,

$$v_1(t) = v_{c1} \cdot \sin(\omega t + v_{\varphi 1}) \tag{3.12}$$

3.2.2.2 First Switching Harmonic of Phase Current

By the phase voltage applied to the stator winding, phase current increases when the phase voltage is positive and decreases when the phase voltage is negative. This phase current waveform during one PWM period is shown in Fig. 3.2. The gradient of phase current is linear. It is very important that the current may have different values at the beginning and end of a PWM cycle.

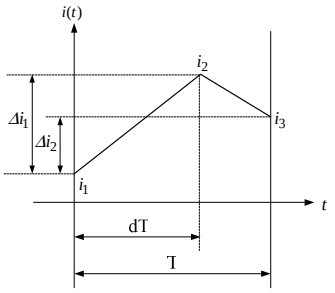

$$i(t) = \begin{cases} \frac{\Delta i_1}{dT} t & , 0 \le t < dT \\ i_0 - \frac{\Delta i}{(1-d)T} t & , dT \le t < T \end{cases}$$

$$\Delta i = \Delta i_1 - \Delta i_2$$

, where

$$i_0 = \Delta i_1 + \Delta i \frac{d}{1-d}$$

Fig 3.2 Phase current characteristic during one PWM period

The first switching harmonic of phase current can be computed as,

$$i_{a1} = \frac{2}{T} \cdot \int_0^T i(t) \cdot \cos(\omega t) dt \tag{3.13}$$

$$i_{b1} = \frac{2}{T} \cdot \int_0^T i(t) \cdot \sin(\omega t) dt \tag{3.14}$$

By substituting $i(t)$ in Fig 3.2 into equation (3.13), the coefficient of the cosine part in the first switching harmonic of phase current can be expressed as,

$$\begin{aligned} i_{a1} &= \frac{2}{T} \cdot \left\{ \int_0^{dT} \frac{\Delta i_1}{dT} t \cdot \cos(\omega t) dt + \int_{dT}^T (i_0 - \frac{\Delta i}{(1-d)T} t) \cdot \cos(\omega t) dt \right\} \\ &= \frac{\Delta i_1 - d \cdot \Delta i_2}{d \cdot (1-d) \cdot 2\pi^2} \cdot \{\cos(2\pi d) + 2\pi d \cdot \sin(2\pi d) - 1\} - \frac{i_0}{\pi} \cdot \sin(2\pi d) \end{aligned} \tag{3.15}$$

By substituting $i(t)$ in Fig 3.2 into equation (3.14), the coefficient of the sine part in the first switching harmonic of phase current can be expressed as,

$$\begin{aligned} i_{b1} &= \frac{2}{T} \cdot \left\{ \int_0^{dT} \frac{\Delta i_1}{dT} t \cdot \sin(\omega t) dt + \int_{dT}^T (i_0 - \frac{\Delta i}{(1-d)T} t) \cdot \sin(\omega t) dt \right\} \\ &= \frac{\Delta i_1}{d \cdot 2\pi^2} \cdot \{\sin(2\pi d) - 2\pi d \cdot \cos(2\pi d)\} - \frac{i_0}{\pi} \cdot \{1 - \cos(2\pi d)\} \\ &\quad + \frac{\Delta i}{(1-d) \cdot \pi} \cdot \left\{ 1 + \frac{\sin(2\pi d)}{2\pi} - d \cdot \cos(2\pi d) \right\} \end{aligned} \tag{3.16}$$

From equations (3.15) and (3.16), the phase angle and amplitude of the first switching harmonic of phase current can be expressed as,

$$i_{\varphi 1} = \tan^{-1}(\frac{i_{a1}}{i_{b1}}) \tag{3.17}$$

$$i_{c1} = \sqrt{i_{a1}^2 + i_{b1}^2} \tag{3.18}$$

Consequently, $i_1(t)$ the first switching harmonic function of phase current in trigonometric form can be represented as equation (3.19) and it contains the amplitude and phase angle as,

$$i_1(t) = i_{c1} \cdot \sin(\omega t + i_{\varphi 1}) \tag{3.19}$$

3.2.2.3 Phase Difference

The trigonometric form of the first switching harmonic of phase voltage and current in equations (3.12) and (3.19) can be transformed into a phasor form as,

$$P\{v_1(t)\} = P\{v_{c1} \cdot \sin(\omega t + v_{\varphi 1})\} = v_{c1} e^{jv_{\varphi 1}} \tag{3.20}$$

$$P\{i_1(t)\} = P\{i_{c1} \cdot \sin(\omega t + i_{\varphi 1})\} = i_{c1} e^{ji_{\varphi 1}} \tag{3.21}$$

where $P\{\ \}$ denotes phasor transform operator. Phase difference between two instantaneous phase angles is defined as,

$$\varphi = \left| v_{\varphi 1} - i_{\varphi 1} \right| \tag{3.22}$$

3.3 Fast Fourier Transform Development

Because the analog waveform consists of an infinite number of contiguous points, the representation of all their values is a practical impossibility. Thus the analog values have to be sampled at regular intervals and the sample values are then converted to a digital binary representation. Provided the number of samples recorded per second is high enough the waveform will be adequately represented. The theoretically necessary sampling rate is called the Nyquist rate and is $2f_{\max}$ where $f_{\max}$ is the frequency of the highest frequency sinusoidal component in the signal of the significant amplitude. In this section, phase voltage and current waveform will be sampled at regular time intervals and the values of a time series will be transformed into the frequency domain.

3.3.1 Discrete Fourier Transform

Assume that a waveform has been sampled at certain regular time interval T to produce the sample sequence $\{x(nT)\} = x(0), x(t), \cdots, x[(N-1)T]$ of N sample values, where n is the sample number from $n = 0$ to $n = N-1$. The data values $x(nT)$ will be read only when representing values of a time series such as a voltage waveform. The DFT of $x(nT)$ is then defined as the sequence of complex values $\{X(k\Omega)\} = X(0), X(\Omega), \cdots, X[(N-1)\Omega]$ in the frequency domain, where Ω is the first harmonic frequency given by $\Omega = 2\pi / NT$. N-complex DFT values in the frequency domain, $X(k)$, are understood to represent $X(k\Omega)$ and they are given by,

$$X(k) = \sum_{n=0}^{N-1} x(nT) e^{-jk\Omega nT} \quad , \quad k = 0, 1, \cdots, N-1 \tag{3.23}$$

In this equation, k represents the harmonic of the transform component and the upper and lower indices in the summation reflect the fact that $x(nT) = 0$ outside the range $0 \le n \le N-1$. $X(k)$ have real and imaginary components in general so that for the k-th harmonic

$$X(k) = R(k) + jI(k) \tag{3.24}$$

and

$$|X(k)| = [R(k)^2 + I(k)^2]^{1/2} \tag{3.25}$$

and $X(k)$ has the associated phase angle

$$\Phi(k) = \tan^{-1}[I(k)/R(k)] \tag{3.26}$$

3.3.2 Fast Fourier Transform

In this section, it will be shown how the computational redundancy inherent in the DFT is used to reduce the number of different calculations necessary, thereby speeding up the computation. The drawback of using DFT for practical applications is its intensive computational requirement. To compute each $X(k)$ defined in equation (3.23), for each value of k, direct computation of $X(k)$ involves N complex multiplications ($4N$ real multiplications) and $N-1$ complex addition ($4N-2$ real additions). Therefore for computing N samples of $X(k)$ for $k = 0,1,\cdots,N-1$, N^2 complex multiplications and $N(N-1)$ complex additions are required. The DFT defined in equation (3.23) can be re-written as,

$$X(k) = \sum_{n=0}^{N-1} x(nT) e^{-j2\pi nk/N} \quad , \quad k = 0,1,\cdots,N-1 \tag{3.27}$$

Also, the factor $e^{-j2\pi/N}$ will be written as W_N, thus

$$W_N = e^{-j2\pi/N} \tag{3.28}$$

so that equation (3.27) becomes,

$$X(k) = \sum_{n=0}^{N-1} x(nT) W_N^{kn} \quad , \quad k = 0,1,\cdots,N-1 \tag{3.29}$$

where

$$W_N^{kn} = e^{-j(2\pi/N)kn} = \cos\left(\frac{2\pi kn}{N}\right) - j\sin\left(\frac{2\pi kn}{N}\right) \quad , \quad n,k = 0,1,\cdots,N-1 \tag{3.30}$$

The parameter W_N^{kn} is called the twiddle factors of the DFT. The twiddle factors have the symmetry property,

$$W_N^{k+N/2} = -W_N^k \quad , \quad k = 0,1,\cdots,N/2-1 \tag{3.31}$$

the periodicity property,

$$W_N^{k+N} = W_N^k \quad , \quad k = 0,1,\cdots,N/2-1 \tag{3.32}$$

and the useful relationship to reduce the redundancy of the DFT.

$$W_N^2 = W_{N/2} \tag{3.33}$$

By reducing these redundancies, a very efficient algorithm called the Fast Fourier Transform (FFT) can be derived.

3.3.2.1 Decimation-In-Time Fast Fourier Transform

In exploiting the computation redundancy expressed by equations (3.31), (3.32), and (3.33), the data sequence is divided into two equal sequences, one of even-numbered data, and one of odd-numbered data. For the sequences to be of equal length, they must all contain an even number of data. If the original sequence consists of an odd number of data, then an augmenting zero should be added to render the number of data even. The terms in the even sequence may be designated as x_{2n} with $n=0$ to $n=N/2-1$ while those in the odd sequence become x_{2n+1}. Then equation (3.29) may be rewritten as,

$$\begin{aligned} X(k) &= \sum_{n=0}^{N/2-1} x_{2n} W_N^{2nk} + \sum_{n=0}^{N/2-1} x_{2n+1} W_N^{(2n+1)k} \\ &= \sum_{n=0}^{N/2-1} x_{2n} W_N^{2nk} + W_N^k \sum_{n=0}^{N/2-1} x_{2n+1} W_N^{2nk} \quad , \quad k = 0,1,\cdots,N-1 \end{aligned} \tag{3.34}$$

Equation (3.33) gives $W_N^{2nk} = W_{N/2}^{nk}$ so that equation (3.34) becomes,

$$X(k) = \sum_{n=0}^{N/2-1} x_{2n} W_{N/2}^{2nk} + W_N^k \sum_{n=0}^{N/2-1} x_{2n+1} W_{N/2}^{nk} \quad , \quad k = 0,1,\cdots,N-1 \tag{3.35}$$

Equation (3.35) may be written as,

$$X(k) = X_{11}(k) + W_N^k X_{12}(k) \quad , \quad k = 0,1,\cdots,N-1 \tag{3.36}$$

On comparison of equation (3.36) with equation (3.29), it is seen that $X_{11}(k)$ is indeed the DFT of the even sequence, while $X_{12}(k)$ is that of the odd sequence. Therefore, the DFT, $X(k)$ can

be expressed in terms of two DFTs: $X_{11}(k)$ and $X_{12}(k)$. The twiddle factor $W_{N/2}^{k}$ occurring in both $X_{11}(k)$ and $X_{12}(k)$ needs calculation once only. Thus N-point DFT is converted into two DFTs each of $N/2$ points. This process is then repeated until $X(k)$ is decomposed into $N/2$ DFTs, each of two points, both of which are initial sampled data. Thus, in practice, the initial data is reordered and the $N/2$ two-point DFTs are calculated by taking the data in pairs. These DFT outputs are suitably combined in fours to provide $N/4$ four-point DFTs which are computed and approximately combined to produce $N/8$ eight-point DFTs which are computed, and so on until the final N-point DFT, $X(k)$, is obtained. At each stage common factors which are powers of W_N are incorporated to reduce the number of complex calculations. Thus the total number of complex multiplications is reduced to $(N/2)\log_2 N$. Each butterfly contains two complex additions so the number of complex additions becomes $N\log_2 N$. Fig 3.3 represents the computation of ($N=8$)-point DFT. We can see that the computation is performed in three stages, beginning with the computations of 4($N/2$) two-point DFTs, then 2($N/4$) four-point DFTs, and finally, 1($N/8$) eight-point DFT.

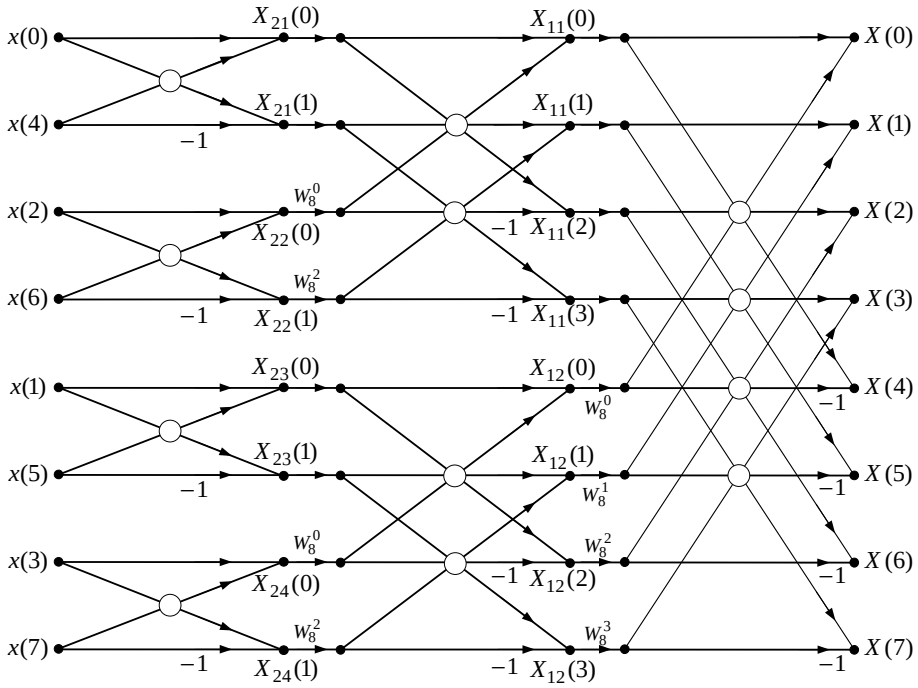

Fig 3.3 8-point Decimation-in-time FFT algorithm

3.3.2.2 Decimation-In-Frequency Fast Fourier Transform

In previous section, Decimation-in-time FFT can be obtained by repeatedly dividing an initial DFT of the form equation (3.29) into two transforms, one consisting of the even number terms and one of the odd number terms, until the initial transform was reduce to two-point DFTs of the initial data. An alternative approach, called the Decimation-in-frequency FFT, is to separate the initial transform into two transforms, one containing the first half of data and the other containing the second half of the data. Then it separates the frequency term $X(k)$ into even and odd samples of k. The N-point DFT can be split into two summations, one of which involves the sum over the first $N/2$ data samples and the second sum involves the last $N/2$ data points. Then, equation (3.29) can be rewritten as,

$$\begin{aligned} X(k) &= \sum_{n=0}^{N/2-1} x(n)W_N^{kn} + \sum_{n=N/2}^{N-1} x(n)W_N^{kn} \\ &= \sum_{n=0}^{N/2-1} x(n)W_N^{kn} + W_N^{Nk/2} \sum_{n=0}^{N/2-1} x(n+\frac{N}{2})W_N^{kn} \quad , \quad k = 0,1,\cdots,N-1 \end{aligned} \tag{3.37}$$

Since $W_N^{Nk/2} = (-1)^k$, equation (3.37) can be written as,

$$X(k) = \sum_{n=0}^{N/2-1} \left[x(n) + (-1)^k x(n+\frac{N}{2}) \right] W_N^{kn} \quad , \quad k = 0,1,\cdots,N-1 \tag{3.38}$$

The even numbered DFT coefficients are given by,

$$X(2k) = \sum_{n=0}^{N/2-1} \left[x(n) + x(n+\frac{N}{2}) \right] W_N^{kn} \quad , \quad k = 0,1,\cdots,N/2-1 \tag{3.39}$$

and the odd numbered DFT coefficients are given by,

$$X(2k+1) = \sum_{n=0}^{N/2-1} \left[x(n) - x(n+\frac{N}{2}) \right] W_N^{kn} \quad , \quad k = 0,1,\cdots,N/2-1 \tag{3.40}$$

This process of decomposition is repeated until the last stage consists of two-point DFTs. The decomposition and symmetry relationships are reversed from the Decimation-in-time FFT algorithm. The bit-reversal occurs at the output instead of the input and the order of the output samples $X(k)$ will rearranged as shown in Fig 3.4. Consequently, the computation of the N-point DFT by the Decimation-in-frequency FFT requires $(N/2)\log_2 N$ complex multiplications and $N\log_2 N$ complex additions, just as in the Decimation-in-time FFT algorithm. The 8-point Decimation-in-frequency FFT is given in Fig 3.4.

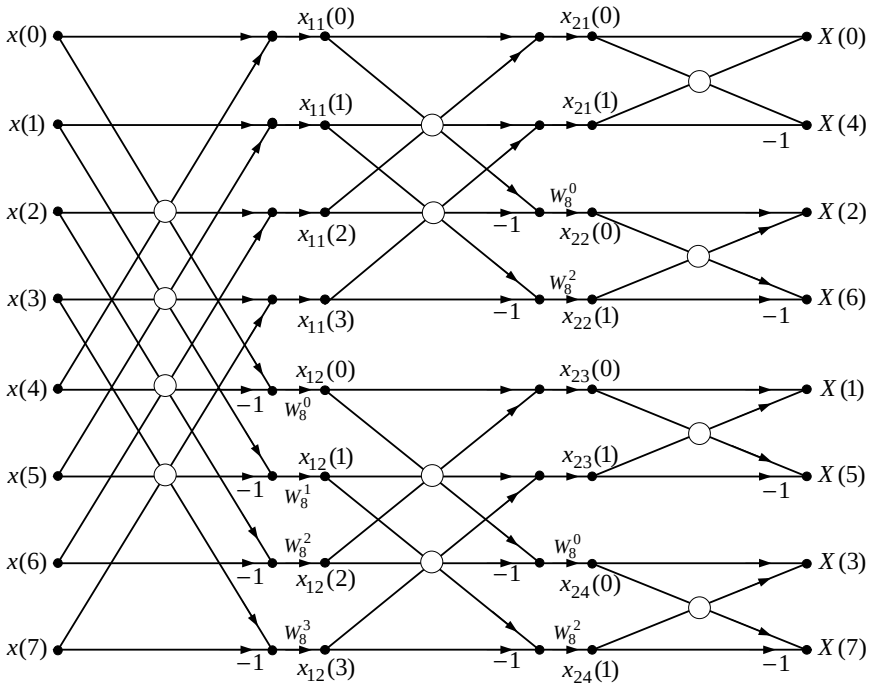

Fig 3.4 8-point Decimation-in-frequency FFT algorithm

3.3.2.3 Comparison of DIT and DIF Algorithms

For the Decimation-in-time FFT algorithm, it is important to note that, if the input signal data are placed in bit-reversed order before beginning the FFT computations, the outputs of each butterfly throughout the computation can be placed in the same memory locations from which the inputs were fetched, resulting in an in-place algorithm that requires no extra memory to perform the FFT. For the Decimation-in-frequency FFT algorithm, it is important to note that, if the input data are in order before beginning the FFT computations, the outputs of each butterfly throughout the computation can be placed in bit-reversed order memory locations from which the inputs were fetched, resulting in an in-place algorithm that requires no extra memory to perform the FFT. The number of complex multiplications required for both algorithms is the same. In this research, only the first switching harmonic components of input signals, phase voltage and current, are required for the computation of flux-linkage of the SRM and thereby the sampled input signals do not need to be placed in bit-reversed order. Hence the Decimation-in-frequency FFT algorithm is going to be used for the computation of the first switching harmonic components of phase voltage and current.

3.3.3 Computation of the First Switching Harmonics of Phase Voltage and Current

The FFT computation in real-time DSP system, in which C28x DSP system will be implemented, uses radix-2 decimation-in-time and in-place FFT algorithm. N -point FFT can be computed with data sampling at the rate of at least Nyquist frequency.

3.3.3.1 Sampling

Sampling is the acquisition of a continuous analog signal at discrete time intervals and is a fundamental concept in real-time signal processing. Therefore, the rate at which an analog signal should be sampled to ensure that all the relevant information contained in the signal is captured or retained by sampling. If highest frequency component in a signal is $f_{\max}$, then the signal should be sampled as the rate of at least $2f_{\max}$ for the samples to describe the signal completely:

$$F_s \geq 2f_{\max} \tag{3.41}$$

where F_s is the sampling frequency. Thus, if the switching frequency at PWM operation is 5 kHz, then to preserve or capture all required information in the phase voltage and current, it should be sampled at 10 kHz or more. Sampling at less than the rate specified by the Nyquist sampling theorem leads to a folding over or aliasing effects so that the original signal cannot be recovered if we were to convert to the sampled data back to analog.

In practice, aliasing is always present because of noise and the existence of signal energy outside of the band of interest. The problem then is deciding the level of aliasing that is acceptable and then designing a suitable anti-aliasing filter and choosing an appropriate sampling frequency to achieve this. In order to reduce the effects of aliasing, sharp cutoff anti-aliasing filters are normally used to limit the band of the signal or the sampling frequency is increased so as to widen the separation between the signal and high frequency spectra. Ideally, anti-aliasing filter should remove all frequency components above the fold-over frequency, which is the half the sampling frequency. However, the practical response of the anti-aliasing filter introduces an amplitude distortion into the signal as it is not flat in the pass-band. Also, the signal components greater than the stop-band frequency will be attenuated, but those between the cutoff and stop-band frequency, which is called the transition width, will have their amplitudes reduced monotonically. The anti-aliasing filter should provide sufficient attenuation at frequencies above

the Nyquist frequency. Because of the non-ideal response of practical filters, the effective Nyquist frequency is taken as the stop-band frequency. In specifying the anti-aliasing filter, it is useful to take the ADC resolution requirements into account. Thus a filter would be designed to attenuate the frequencies above the Nyquist frequency to a level not detectable by the ADC, for example to less than the quantization noise level. Thus, for a system using a B-bit linear ADC, the minimum stop-band attenuation would typically be,

$$A_{\min} = 20\log(\sqrt{1.5} \times 2^{B+1}) \tag{3.42}$$

where B is the number of bits in the ADC and $A_{\min}$ is the minimum stop-band attenuation in low-pass filter. The values of $A_{\min}$ for 10-bit and 12-bit ADC resolutions are 68 dB and 80 dB, respectively.

The use of an analog filter at the front-end of a DSP system also introduces other constraints such as phase distortion that the phase response is not linear with frequency, so that the components of the desired signal will be shifted in phase or delayed by amounts which are not in proportion to their frequencies. The amount of distortion depends on the characteristics of the filter including how steep its roll-off is. Generally, the steeper the roll-off meaning the narrower the transition width, the worse the phase distortion introduced by the filters, and the more difficult it is to achieve a good match in amplitude and group delay between channels in a multi-channel system. In order to minimize the phase distortion in the anti-aliasing filters, over-sampling has been introduced in real-time signal processing, so that the transition width is wider and the phase distortion can be reduced. Over-sampling combined with additional digital signal processing leads to an improved signal-to-noise ratio. When using higher sample rates, the noise power is spread over a wider range of frequencies. Therefore the effective noise power density at the band of interest is lower at higher sampling rates and this leads to an enhancement of the signal-to-noise ratio.

Assuming that each phase of SRM can be independently driven with 10 kHz PWM method and phase voltage and current of SRM are sampled and acquired with 12-bit ADC real-time DSP system, the band of interest frequencies extends from 0 to 5 kHz and the first switching harmonic frequency is 5 kHz. The anti-aliasing filter should attenuate the levels of frequencies in the stop-band to less than quantization noise level for the ADC, which is 80 dB in 12-bit ADC real-time DSP system, so that they are not detectable by ADC. The third-order Butterworth filter can be used because it has the flattest pass-band region, so that it has the least

attenuation over the desired frequency range. Choosing the folding frequency, $F_s/2$ as the effective stop-band frequency, then the minimum sampling frequency can be computed as,

$$\begin{aligned} -A_{\min} &= 20\log(|H(f)|) \\ &= 20\log\left(1\Big/\left[1+\left(\frac{f}{f_c}\right)^6\right]^{1/2}\right) \end{aligned} \tag{3.43}$$

where $A_{\min}$ is the minimum stop-band attenuation, 80 dB for 12-bit ADC resolutions, $H(f)$ and f_c are the gain and cutoff frequency of the third-order Butterworth anti-aliasing filter, f is the folding frequency, $F_s/2$. From equation (3.43), we have $f > 107.7\,kHz = F_s/2$. Thus the sampling frequency should be greater than $215.4\,kHz$. Letting $F_s = 250\,kHz$, the aliasing level at 5 kHz can be obtained as,

$$\frac{1}{\left[1+\left(\frac{f-F_s}{f_c}\right)^6\right]^{1/2}} = \frac{1}{\left[1+\left(\frac{5-250}{5}\right)^6\right]^{1/2}} = 8.5\times10^{-6} \tag{3.44}$$

The level of aliasing error relative to the signal level at 5 kHz can obtained as,

$$\frac{8.5\times10^{-6}}{0.7071}\times100 = 0.0012\,[\%] \tag{3.45}$$

3.3.3.2 First Switching Harmonics of Phase Voltage and Current

The FFT routines accept complex-valued inputs; therefore the number of memory locations required is $2N$ for N-point FFT. To use the available complex FFT program for real-valued signals, we have to set the imaginary parts to zero. The complex multiplication of N-point FFT has the form which requires four real multiplications and two real additions.

$$(a+jb)(c+jd) = (ac-bd)+j(bc+ad) \tag{3.46}$$

The number of multiplications and the storage requirements can be reduced if the signal has special properties. For example, if the input signal is real, only $N/2$ samples from $X(0)$ to $X(N/2)$ need to be computed due to the complex conjugate property. If the input sequence is purely real valued, then

$$X(-k) = X^*(k) = X(N-k) \quad , \quad k = 0,1,\cdots,N-1 \tag{3.47}$$

where $X^*(k)$ is the complex conjugate of $X(k)$. It has the equivalent meaning as,

$$X(M+k) = X^*(M-k) \quad , \quad k = 0,1,\cdots,M \tag{3.48}$$

where $M = N/2$ if N is even, or $M = (N-1)/2$ if N is odd. This property shows that the first $(M+1)$ DFT coefficients from $k = 0$ to M are independent. Hence, the FFT for N-point real valued sequence requires $N+2$ memory locations to compute the FFT, which is highly preferable in contrast to the FFT that consumes $2N$ locations for N-point real valued sequence.

By using equation (3.30), N-point FFT computation represented as equation (3.29) can be expanded as,

$$\begin{aligned} X(k) &= \sum_{n=0}^{N-1} x(nT) W_N^{kn} \\ &= \sum_{n=0}^{N-1} x(nT) \cdot \left(\cos\left(\frac{2\pi kn}{N} \right) - j \sin\left(\frac{2\pi kn}{N} \right) \right) \quad , \quad k = 0,1,\cdots,N-1 \end{aligned} \tag{3.49}$$

By twiddle factors, the output sequence of N-pint FFT computation can be divided into real and imaginary parts in equation (3.49). In most FFT programs developed for general-purpose computers, the computation of twiddle factors is embedded in the program and the twiddle factors only need to be computed once during the program initialization stage. In the implementation of FFT algorithm on DSP controller, it is preferable to tabulate the values of twiddle factors so that they can be looked up during the computation of FFT. Hence, twiddle factors are initialized in memory as SIN and COS values. Storing twiddle factors would require N locations, which is $N/2$ samples containing half cycle of SIN and $N/2$ samples containing half cycle of COS. In this research, the first harmonic of input functions, phase voltage and current in this research, are only needed for FFT computation and thus the first harmonic component of equation (3.49) can be expressed as,

$$\begin{aligned} X(1) = x(0) &+ x(1) \cdot \left(\cos\left(\frac{2\pi k}{N} \right) - j \sin\left(\frac{2\pi k}{N} \right) \right) + x(2) \cdot \left(\cos\left(\frac{2\pi k}{N} \cdot 2 \right) - j \sin\left(\frac{2\pi k}{N} \cdot 2 \right) \right) \\ &\vdots \\ &+ x(N-2) \cdot \left(\cos\left(\frac{2\pi k}{N} \cdot (N-2) \right) - j \sin\left(\frac{2\pi k}{N} \cdot (N-2) \right) \right) \\ &+ x(N-1) \cdot \left(\cos\left(\frac{2\pi k}{N} \cdot (N-1) \right) - j \sin\left(\frac{2\pi k}{N} \cdot (N-1) \right) \right) \end{aligned} \tag{3.50}$$

Real and imaginary parts of the first harmonic of input function can be divided into equations (3.51) and (3.52) and consequently to compute the first harmonic of N-point FFT, it requires $N/2$ multiplications and $N+1$ additions for real part and $N/2$ multiplications and $N-1$ additions for imaginary part.

$$\begin{aligned}\mathrm{Re}\{X(1)\} &= x(0) - x\left(\frac{N}{2}\right) + \left(x(1)+x(N-1)\right)\cdot\cos\left(\frac{2\pi}{N}\right) + \left(x(2)+x(N-2)\right)\cdot\cos\left(\frac{2\pi}{N}\cdot 2\right) \\ &\quad\vdots \\ &\quad + \left(x\left(\frac{N}{2}-2\right)+x\left(\frac{N}{2}+2\right)\right)\cdot\cos\left(\frac{2\pi}{N}\cdot\left(\frac{N}{2}-2\right)\right) \\ &\quad + \left(x\left(\frac{N}{2}-1\right)+x\left(\frac{N}{2}+1\right)\right)\cdot\cos\left(\frac{2\pi}{N}\cdot\left(\frac{N}{2}-1\right)\right)\end{aligned} \tag{3.51}$$

$$\begin{aligned}\mathrm{Im}\{X(1)\} &= \left(-x(1)+x(N-1)\right)\cdot\sin\left(\frac{2\pi}{N}\right) + \left(-x(2)+x(N-2)\right)\cdot\sin\left(\frac{2\pi}{N}\cdot 2\right) \\ &\quad\vdots \\ &\quad + \left(-x\left(\frac{N}{2}-2\right)+x\left(\frac{N}{2}+2\right)\right)\cdot\sin\left(\frac{2\pi}{N}\cdot\left(\frac{N}{2}-2\right)\right) \\ &\quad + \left(-x\left(\frac{N}{2}-1\right)+x\left(\frac{N}{2}+1\right)\right)\cdot\sin\left(\frac{2\pi}{N}\cdot\left(\frac{N}{2}-1\right)\right)\end{aligned} \tag{3.52}$$

Hence N locations are required to store the above twiddle factors: $N/2$ samples containing half cycle of SIN function and samples containing half cycle of COS function. These SIN and COS values are saved into a memory of DSP controller to compute the first harmonic of input function.

In this research, the SRM is controlled at the switching frequency of 5 kHz and phase voltage and current are sampled at the rate of 250 kHz to reduce the aliasing effect in sampling, where the size of FFT (N) is 50 samples and the first harmonic frequency is given by 5 kHz. Hence 25 values of SIN and 25 values of COS are initialized into a memory of DSP controller. If the sampled sequence of phase voltage is represented as $\{v(n)\} = v(0), v(1), \cdots, v[(N-1)]$ of N sample values, N point FFT values of phase voltage in frequency domain are represented as $\{V(k)\} = V(0), V(1), \cdots, V[(N-1)]$, where k is the harmonic number. Hence the first harmonic component in the FFT computation of phase voltage is represented as $V(1)$ and real and imaginary components of $V(1)$ are obtained from equations (3.51) and (3.52). Therefore, the

amplitude and phase angle of the first harmonic component of phase voltage, $V(1)$, can be expressed as,

$$v_{c1} = \sqrt{\left(\mathrm{Re}\{V(1)\}\right)^2 + \left(\mathrm{Im}\{V(1)\}\right)^2} \tag{3.53}$$

$$v_{\varphi 1} = \tan^{-1}\left(\frac{\mathrm{Im}\{V(1)\}}{\mathrm{Re}\{V(1)\}}\right) \tag{3.54}$$

where $V(1)$ is the first harmonic component in the FFT computation of phase voltage and $\mathrm{Re}\{V(1)\}$ and $\mathrm{Im}\{V(1)\}$ are the real and imaginary part of $V(1)$, respectively. Similarly, if the sampled sequence of phase current is represented as $\{i(n)\} = i(0), i(1), \cdots, i[(N-1)]$ of N sample values, N point FFT values of phase current in the frequency domain are represented as $\{I(k)\} = I(0), I(1), \cdots, I[(N-1)]$, where k is the harmonic number. Hence the first harmonic component in the FFT computation of phase current is represented as $I(1)$ and real and imaginary components of $I(1)$ are obtained from equations (3.51) and (3.52). Therefore, the amplitude and phase angle of the first harmonic component of phase current, $I(1)$, can be expressed as,

$$i_{c1} = \sqrt{\left(\mathrm{Re}\{I(1)\}\right)^2 + \left(\mathrm{Im}\{I(1)\}\right)^2} \tag{3.55}$$

$$i_{\varphi 1} = \tan^{-1}\left(\frac{\mathrm{Im}\{I(1)\}}{\mathrm{Re}\{I(1)\}}\right) \tag{3.56}$$

where $I(1)$ is the first harmonic component in the FFT computation of phase current and $\mathrm{Re}\{I(1)\}$ and $\mathrm{Im}\{I(1)\}$ are the real and imaginary part of $I(1)$, respectively.

3.3.3.3 Phase Difference

Given phase angles of the first switching harmonic of phase voltage and current in a PWM period, phase difference between two instantaneous phase angles in a PWM period can be defined as equation (3.57) and it gives a value in radians that varies from $-\pi$ to π.

$$\varphi = \left| v_{\varphi 1} - i_{\varphi 1} \right| \tag{3.57}$$

3.4 Computation of Flux-Linkage

For most doubly salient motors with windings concentrated on stator teeth or poles, the mutual coupling between phases is small and the voltage equation for one phase winding of SRM can written in terms of the current and flux-linkage for that phase as,

$$v(t) = R \cdot i + \frac{\partial \lambda}{\partial t} \tag{3.53}$$

where v is the terminal voltage, i is the phase current, R is the phase resistance, and λ is the flux-linkage linked by the stator winding. In a doubly salient configuration of SRM, the flux-linkage is a function of the rotor position and phase current. Thus, equation (3.53) can be expanded as,

$$v(t) = R \cdot i + \frac{\partial \lambda}{\partial i}\frac{di}{dt} + \frac{\partial \lambda}{\partial \theta}\frac{d\theta}{dt} \tag{3.54}$$

where $\frac{\partial \lambda}{\partial i}$ is the incremental inductance and the third term on the right side of (3.54) is a back emf generated from the variation of the rotor position. The flux-linkage can be described as the multiplication of the phase current and inductance of the stator winding, which is a function of the rotor position and phase current. Thus, by neglecting the mutual inductance between phases, the differential equation governing the dynamics of the SRM can be expressed as,

$$\begin{aligned} v(t) &= R \cdot i + L\frac{di}{dt} + i\frac{\partial L}{\partial i}\frac{di}{dt} + i\frac{\partial L}{\partial \theta}\frac{d\theta}{dt} \\ &= \left(R + \frac{\partial L}{\partial \theta}\frac{d\theta}{dt} \right) \cdot i + \left(L + i\frac{\partial L}{\partial i} \right) \cdot \frac{di}{dt} \end{aligned} \tag{3.55}$$

Neglecting the nonlinear effects of the saturation in equation (3.55), an applied voltage being equal to the sum of the resistive voltage drop, inductive voltage drop, and induced back emf, respectively, is given as,

$$v(t) = R \cdot i + L \cdot \frac{di}{dt} + i \cdot \omega_m \cdot \frac{dL}{d\theta} \tag{3.56}$$

where ω_m is the rotor speed and L is the inductance dependent on the rotor position and phase current. The induced back emf is defined as,

$$e(t) = i \cdot \omega_m \cdot \frac{dL}{d\theta} \tag{3.57}$$

where $\frac{dL}{d\theta}$ can be defined as a back emf constant similar to that of the dc series excited machine. The back emf constant is dependent on operating point and can be obtained with constant current at the point. Using the phase voltage dynamic equation including the induced back emf expression, the equivalent circuit for one phase of the SRM is derived and shown in Fig 3.5.

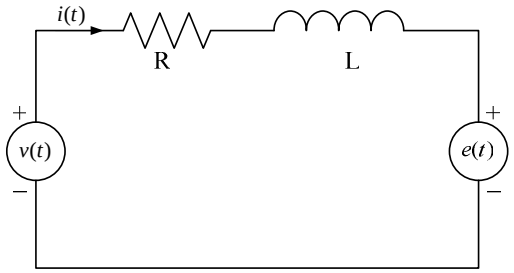

Fig 3.5 The single-phase equivalent circuit of SRM

The voltage equation, then, is given by,

$$v(t) - e(t) = R \cdot i + L \cdot \frac{di}{dt} \tag{3.58}$$

If the SRM is driven by PWM current control strategy and the voltage source is periodic function with the fixed chopping frequency f_s, the equivalent circuit of the SRM is represented by simple resistor and inductor circuit in Fig 3.6.

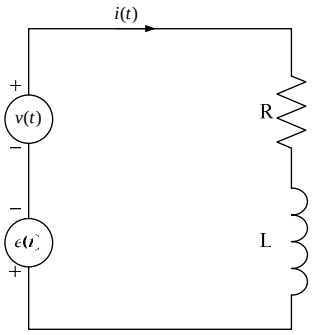

Fig 3.6 The simplified equivalent circuit of SRM

Assuming the resistance of the stator winding is much smaller than the inductive reactance since the chopping frequency is usually in the range of 5 to 20 kHz, the equivalent circuit of SRM is simplified into purely inductive circuit and the inductive reactance is expressed as,

$$X_L = \omega \cdot L = \frac{v_{c1}}{i_{c1}} \tag{3.59}$$

where $\omega = \frac{2 \cdot \pi}{T_s}$ is the fundamental frequency of the voltage source, v_{c1} is the amplitude of the first switching harmonic phase voltage, i_{c1} is the amplitude of the first harmonic phase current, and T_s is the reciprocal of switching frequency of PWM signal applied to the stator winding. Finally, the inductance of SRM is estimated by using the first switching harmonic of phase voltage and current and the inductive reactance in the simplified equivalent circuit of the SRM.

$$L = \frac{v_{c1}}{i_{c1}} \cdot \frac{T_s}{2 \cdot \pi} \tag{3.60}$$

Therefore, by multiplying equation (3.60) by the average phase current in a PWM period, flux-linkage is obtained as,

$$\lambda = L \cdot I \tag{3.61}$$

where I is the average phase current flowing into the stator winding for a PWM period. The flow chart for computing the flux-linkage in a PWM period is represented in Fig 3.8.

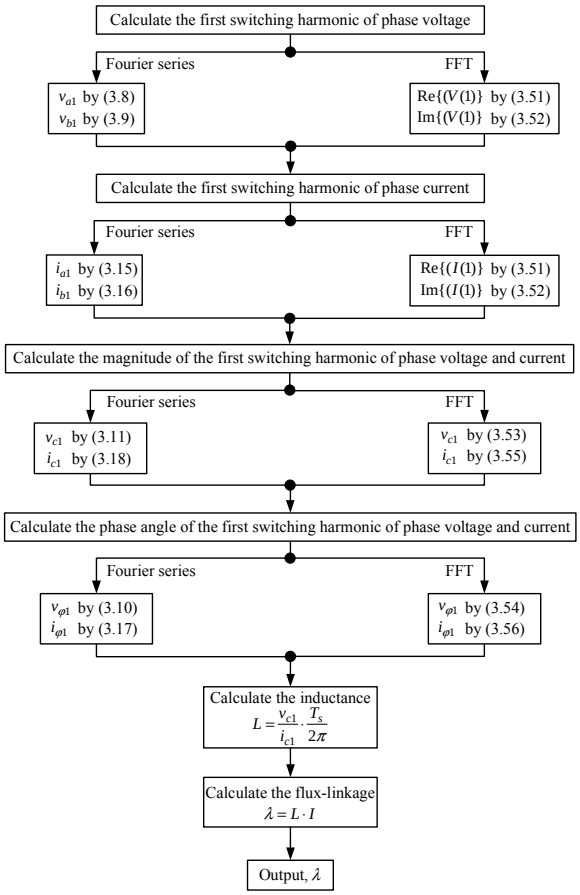

Fig 3.7 The flow chart for computing the flux-linkage in a PWM period

3.5 Conclusions

In this chapter, a new method of magnetic characterization in SRM drives for PWM current control has been proposed based on harmonic frequency analysis in frequency domain. The following are believed to be original contributions of this chapter:

1) A new method of magnetic characterization in SRM drives for PWM current control under hard chopping has been proposed.
2) The proposed method used the first switching harmonic components of phase voltage and current in a PWM period.
3) For the computation of the first switching harmonic components of phase voltage and current, the decompositions of phase voltage and current into their first switching frequency components through Fourier series and FFT have been proposed.
4) The magnetic characterization of the SRM by the proposed method is used for rotor position estimation with given phase current.

CHAPTER 4 ESTIMATION ALGORITHM

4.1 Introduction

Position estimation without a mechanical position sensor is considered to be desirable due to the compactness in weight and volume, lower cost due to elimination of the mechanical assembly and mounting associated with a rotor position sensor. The driving factor behind sensorless operation of any electrical drive including that of SRMs is the quest for low-cost drives having high performance. A comprehensive review of the sensorless position estimation methods for SRMs was discussed in Chapter 1. Depending on the technique adopted, the position estimation methods were classified into four major groups.

References [2-25] used terminal measurements of active phase voltage or current and associated computations to estimate the rotor position. Most methods do not need any hardware for sensing signals except for phase voltage and current. In addition, they do not need any probing pulses. However, they may produce large estimation errors near zero speed if the motional back emf is neglected and improper measurement of the winding resistance will lead to an erroneous estimation.

References [26-28] estimated rotor position by using mutually induced voltage in an inactive phase in the chopping mode. Mutually induced voltage is very small in magnitude and appears across the inactive phase, therefore it is difficult to extract rotor position information by capturing the mutually induced voltage.

References [29-49] used low-level and high-frequency signals injected into an inactive phase to obtain phase inductance variation which is then mapped to position information. However, the injected signals in these methods need to be low to minimize negative torque, avoid inter-phase coupling effects, and minimize the volume and cost of external injection circuitry.

References [50-63] used intelligent control methods, consisting of fuzzy models and artificial neural network controllers. These methods are not dependent on the magnetic characteristics of the motor, thus independent of parameter variations and disturbances. However, a large number of computations for the training of the neural network and many fuzzy rules are required to have high accuracy position estimation.

With a review of previous literature relating to the sensorless position estimation of the SRM, a robust position estimation technique to overcome these detrimental effects will be necessary and a novel position estimation method for SRM drives is presented in this chapter.

If flux-linkage is measured together with phase current, rotor position information is determined from the relationship between flux-linkage and rotor position at given phase current. In Chapter 3, a new measurement method of flux-linkage in SRM drives based on the decomposed first switching harmonic components of phase voltage and current in a PWM period has been proposed. Phase inductance of the SRM is estimated by using the first switching harmonic components of phase voltage and current and the inductive reactance in the simplified equivalent circuit of the SRM. Flux-linkage of the SRM is easily obtained by the multiplication of phase inductance and the average phase current in a PWM period.

However, if phase current flowing through a stator winding is controlled by regulated dc current with a small variation ΔI, phase inductance can be expressed as the ratio of change in flux-linkage to the corresponding change in phase current and is given as,

$$L = \frac{\Delta\lambda}{\Delta I} \tag{4.1}$$

where $\Delta\lambda$ is the variation of flux-linkage established by the applied phase current and ΔI is the variation of phase current at regulating active phase current. A typical flux-linkage curve with respect to phase current of the SRM is illustrated in Fig 4.1.

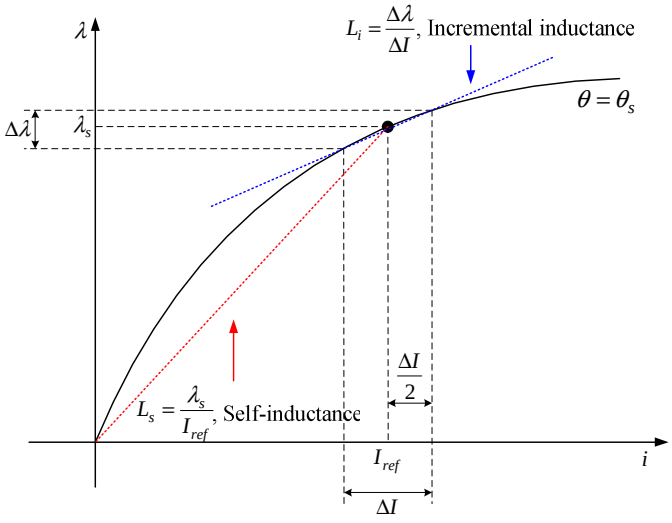

Fig 4.1 Typical flux-linkage vs. phase current characteristics of the SRM

From Fig 4.1, I_{ref} is the regulated phase current value, θ_s is the current rotor position, λ_s is the flux-linkage at (I_{ref}, θ_s), ΔI is the current band in regulating phase current, and $\Delta\lambda$ is the flux-linkage band when phase current is controlled between $I_{ref} - \frac{\Delta I}{2}$ and $I_{ref} + \frac{\Delta I}{2}$. Self-inductance L_s which can be referred as apparent or static inductance [77, 78], is defined as the slope of the straight line from the origin through the actual operating point on the magnetizing curve. Incremental inductance L_i, which can be referred as dynamic inductance [77, 78], is defined as the ratio of change in flux-linkage to the corresponding change in phase current at the operating point on the magnetizing curve.

Obviously, it can be noted from Fig 4.1 that the self-inductance is equal or very close to the incremental inductance when the magnetic material is not saturated. However, both self and incremental inductance will gradually decrease as the material becomes saturated. Hence incremental inductance is significantly less than the corresponding self-inductance. Similarly, at the rated phase current, incremental inductance increases initially up to a certain rotor position similarly to the self-inductance and then decreases as the rotor moves towards aligned position because the iron is saturated at the aligned position or high phase current. Hence even small variations of the incremental inductance at the operating current I_{ref} in saturated region causes an increase in the position error and thus the accuracy of the estimated rotor position will be low. Fig 4.2 shows their characteristics at 2 A, 3 A, and 4 A when phase currents are regulated with a switching frequency of 5 kHz.

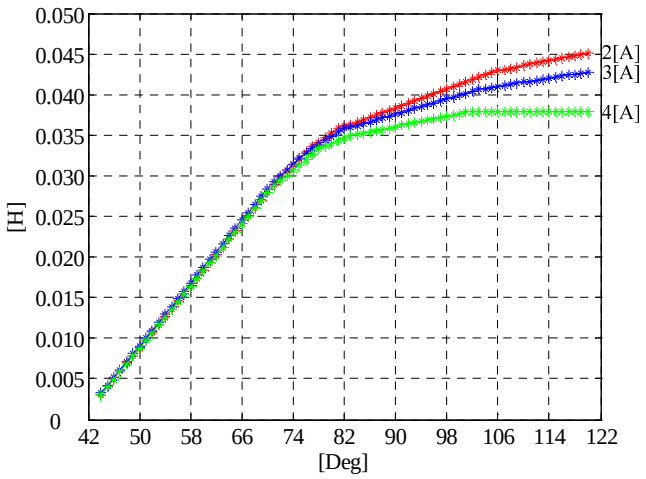

Fig 4.2 Incremental inductance at 2A, 3A, and 4A when the switching frequency is 5 kHz

In addition, the variation of the incremental inductance at constant rotor position produces variation of phase current waveform as the rotor pole moves towards the aligned position as shown in Fig 4.3. It shows the variation of phase current at the unaligned, mid, and aligned positions when the phase current command is 2 A and the switching frequency is 5 kHz.

Fig 4.3 Phase current at the unaligned, midpoint, and aligned position when $i^* = 2A$ and $f_{PWM} = 5kHz$

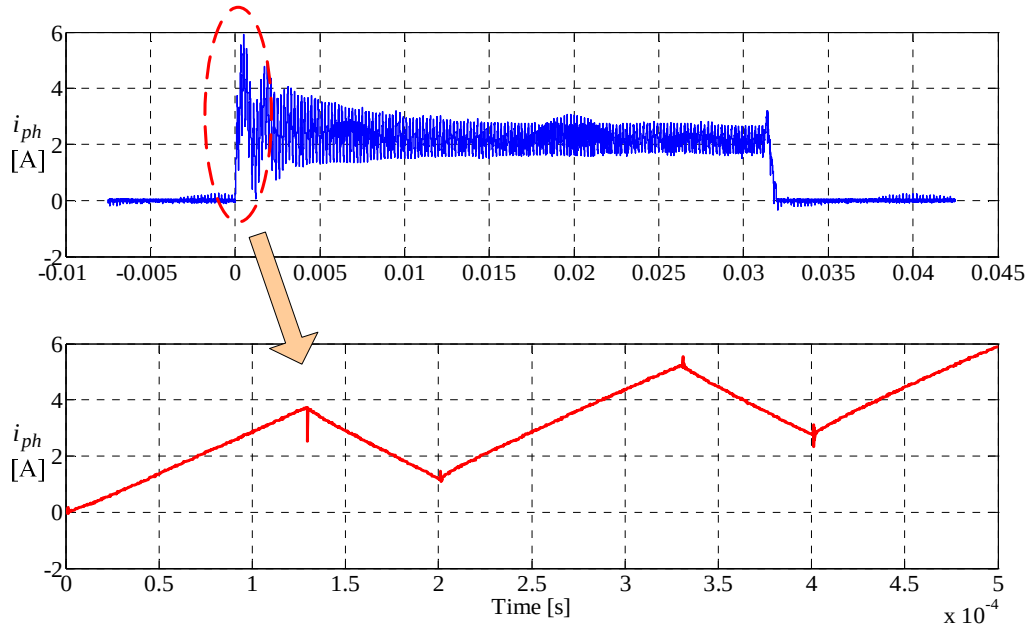

(a) Phase current at the unaligned position

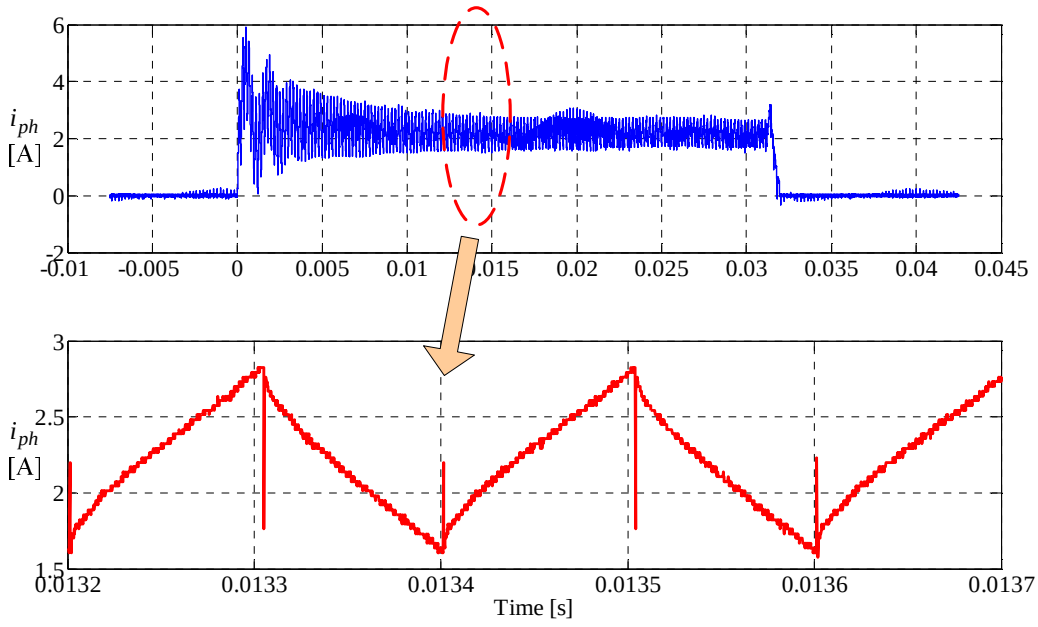

(b) Phase current at the mid position

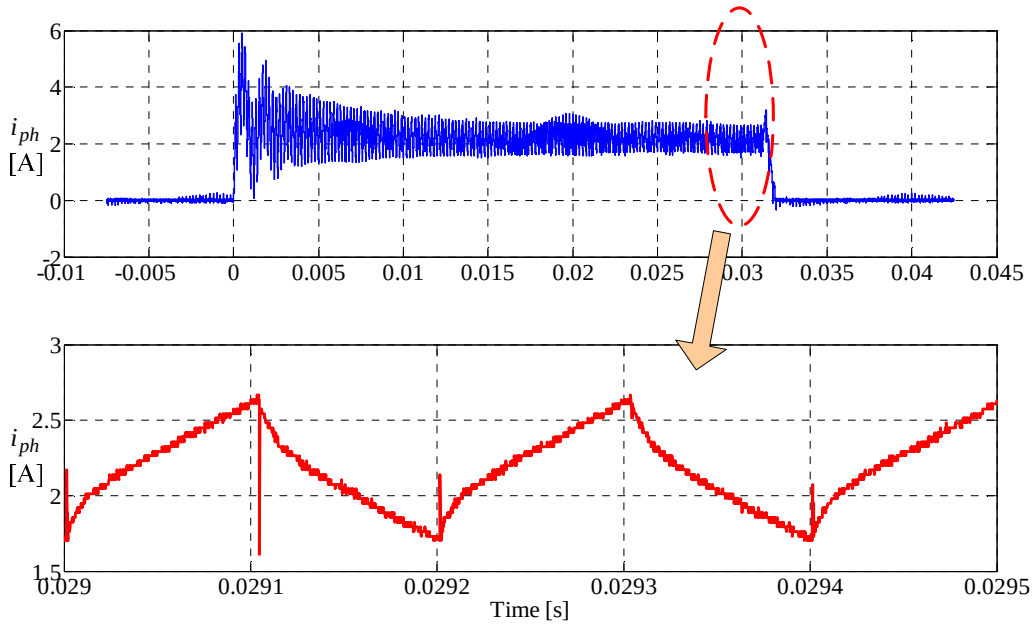

(c) Phase current at the aligned position

In SRMs, flux-linkage is a function of the rotor position and phase current and it can be described as the multiplication of phase current and self-inductance of the stator winding. Neglecting the mutual inductance between phases, the voltage equation for one phase of the SRM is given by,

$$v(t) = R \cdot i + \frac{\partial \lambda}{\partial i}\frac{di}{dt} + \frac{\partial \lambda}{\partial \theta}\frac{d\theta}{dt} \tag{4.3}$$

From equation (4.3), the rate of change of phase current with respect to time can be derives as,

$$\frac{di}{dt} = \frac{v - R \cdot i - \frac{\partial \lambda}{\partial \theta}\frac{d\theta}{dt}}{\frac{\partial \lambda}{\partial i}} \tag{4.4}$$

Considering the nonlinear effects of the saturation, equation (4.4) can be expanded as,

$$\frac{di}{dt} = \frac{v - R \cdot i - i \cdot \frac{\partial L}{\partial \theta}\frac{d\theta}{dt}}{L + i \cdot \frac{\partial L}{\partial i}} \tag{4.5}$$

When a positive voltage is applied to the stator winding during turn ON as the rotor pole is moving towards the aligned position, the rate of change of inductance with respect to phase

current at a constant rotor position is negative and the incremental inductance L_i at constant rotor position in the denominator of equation (4.4) is lower than the self-inductance L.

$$v>0 \quad , \quad \left.\frac{\partial L}{\partial i}\right|_{ON} <0 \quad , \quad L_i = \left.\frac{\partial \lambda}{\partial i}\right|_{ON} < L \tag{4.6}$$

Hence, as the rotor pole is moving towards the aligned position, the rate of change of phase current with respect to time increases during turn ON as shown in Fig 4.3. On the other hand, while a negative or zero voltage is applied to the stator winding during turn OFF as the rotor pole is moving towards the aligned position, the rate of change of inductance with respect to phase current at constant rotor position is negative and the incremental inductance L_i at constant rotor position in the denominator of equation (4.4) is lower than the self-inductance L.

$$v\leq 0 \quad , \quad \left.\frac{\partial L}{\partial i}\right|_{OFF} <0 \quad , \quad L_i = \left.\frac{\partial \lambda}{\partial i}\right|_{OFF} < L \tag{4.7}$$

Hence, as the rotor pole is moving towards the aligned position, the rate of change of phase current with respect to time decreases during turn OFF as shown in Fig 4.3.

Therefore, this incremental inductance or the variation of flux-linkage given by equation (4.1) is not used for estimating the rotor position since the variation of the incremental inductance with respect to rotor position is too small to estimate the rotor position as the rotor moves towards aligned position. This makes it difficult for position estimation being useful in SRM.

In the proposed position estimation method, the rotor position is estimated from the dynamic mapping of flux-linkage or inductance vs. phase current vs. rotor position relationship given by FEA. Therefore, the method to convert the incremental inductance to be compatible with FEA results, self-inductance or flux-linkage, is presented in this chapter. The incremental inductance at a given phase current and rotor position is converted into the flux-linkage in this development. With the estimated flux-linkage, the rotor position is obtained from the relationship between the flux-linkage and rotor position at given phase current.

4.2 Flux-Linkage Estimation

From Fig 4.2, at low current, such as I=2A for a two-phase 6/3 SRM (6 stator poles and 3 rotor poles) being employed in this research, a unique rotor position is defined by the given phase incremental inductance between its unaligned and aligned position. However, at medium or high current, such as I=4A or higher, the phase incremental inductance starts to fall off from

the mid-point of the unaligned and aligned position. It exhibits the same incremental inductance at multiple rotor positions for given phase current. Therefore, the gradient of flux-linkage with respect to phase current increases when low current is applied to the SRM, but it decreases rapidly as phase current reaches its rated value. It leads to multiple rotor position values when estimating rotor position using the incremental inductance and given current for that phase. To solve this problem, several schemes have been published in literature.

Relevant work: Acarnely et al. [2] first suggested the waveform detection method using the variation of the incremental inductance as a function of phase current and rotor position. By monitoring the incremental inductance, the rotor position can be detected indirectly. The variation of incremental inductance is reflected in the phase current rise and fall times. Thus the rotor position can be estimated effectively by monitoring phase current rise and fall times. The current rise and fall times in a PWM cycle can be expressed as in the following,

$$T_r = \frac{\frac{\partial \lambda}{\partial i} \cdot \delta I}{V - R \cdot I - \frac{\partial \lambda}{\partial \theta} \frac{d\theta}{dt}} \tag{4.8}$$

$$T_f = \frac{\frac{\partial \lambda}{\partial i} \cdot (-\delta I)}{-V - R \cdot I - \frac{\partial \lambda}{\partial \theta} \frac{d\theta}{dt}} \tag{4.9}$$

where T_r is current rise time, T_f is current fall time, δI is hysteresis current band, I is average current, V is supply voltage, R is phase winding resistance, $\partial\lambda/\partial I$ is incremental inductance, and $(\partial\lambda/\partial\theta)\cdot(d\theta/dt)$ is motional back emf. During normal operation, the DC supply voltage is much greater than the resistive voltage drop and the motional back emf. Assuming δI is kept constant, the PWM current rise and fall times are then directly proportional to the incremental inductance varying as a function of rotor position and current. Therefore, the possibility of using the current rise and fall times in the active phase for position detection is suggested. However, the main problem of this method is that no account is taken of the back emf influence on the current rise and fall times. In order to overcome this back emf effect, S.K. Panda et al. [3-6] carried out detailed mathematical analysis and experiments for position estimation using the current rise and fall times in an inactive phase. If a diagnostic current of small magnitude is applied to the inactive phase, the current rise and fall times in the inactive phase are measured for position detection. Therefore, the influence of back emf is minimized even at high speeds. This method is

applied to 4-phase and 3-phase SRM. By comparing the PWM current rise or fall time with pre-selected detect time, T_d , rotor position information can be estimated as shown in Fig 4.4 [6].

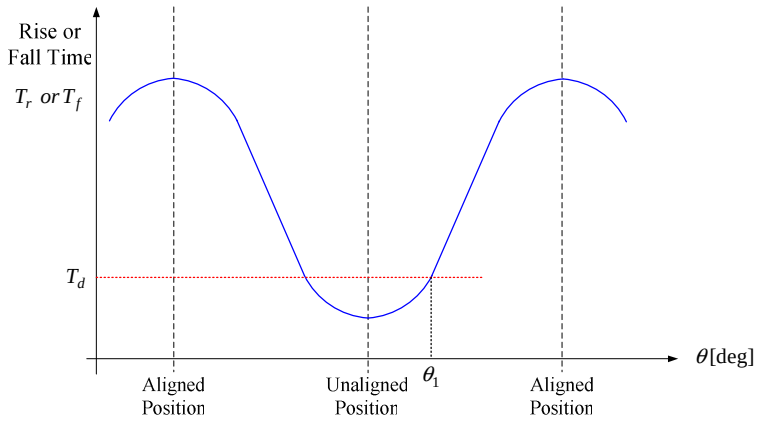

Fig 4.4 PWM current rise or fall time vs. rotor position

When the current rise or fall time falls below the pre-selected detect time, T_d , the phase being excited is commutated and another phase in excitation sequence is to be excited to produce a positive torque. However, the negative torque can be generated due to the diagnostic current pulse applied to the inactive phase and it requires extra hardware to compare the current rise or fall time with the pre-selected detect time. In addition, by varying the pre-selected detect time, T_d , the torque-speed characteristics of the SRM can be altered. In order to overcome the drawback leading to multiple rotor positions in estimating rotor position information using the incremental inductance at medium and high currents, Hongwei et al. [11] used phase incremental inductances of multiple active phases and they have one-to-one relation with the rotor position at any phase current. This method is applied to an 8/6 SRM. The approach is illustrated in Fig 4.5 [11].

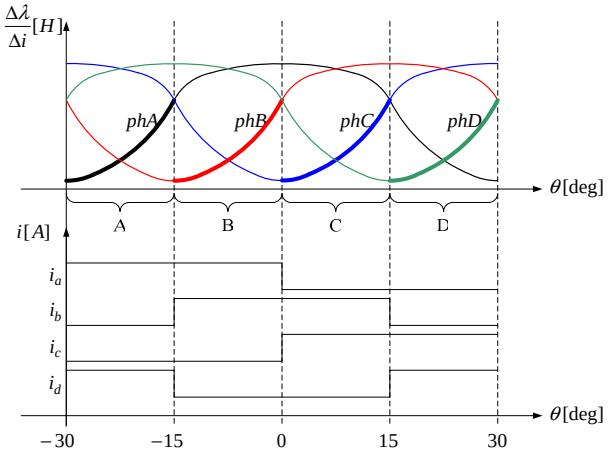

Fig 4.5 The rotor position estimation method using incremental inductances of multiple active phases

As shown in Fig 4.5, when the rotor position is at the region A, $-30° < \theta - 15°$, phase A is active and the rotor position is estimated from the incremental inductance of phase A. On the other hand, when the rotor position is at the region B, $-15° < \theta < 0°$, though phase A is still active, the incremental inductance of phase A loses uniqueness versus rotor position at high or medium currents, and thus it is not used to estimate the rotor position. However, phase B is excited for positive torque production and its incremental inductance has one-to-one relation with the rotor position, and thus it is used to estimate the rotor position. For the 8/6 SRM, the relative position displacement between two phase is $15°$. Thus there exist four phase incremental inductance regions having one-to-one relation with the rotor position and positive torque production, within an electrical cycle of the 8/6 SRM, $60°$. These phase incremental inductance regions are used to estimate the rotor position. Therefore, this method is useful only if phase incremental inductance regions having one-to-one relation with the rotor position and positive torque production consecutively exist within an electrical cycle of the SRM. However, in case of the SRM with non-uniform air gap, this method is impossible to apply because the self-inductance is not symmetrical and in addition, phase incremental inductance regions having one-to-one relation with the rotor position and positive torque production do not consecutively exist within an electrical cycle of the SRM. Therefore, this method is not appropriate for estimating rotor position of the prototype, two-phase 6/3 SRM with a non-uniform air gap.

Proposed approach: In order to overcome these drawbacks such as back emf effect at high speed, negative torque generation due to the diagnostic current pulse into the inactive phase, and the restriction to the SRM with the symmetrical inductance profile, a novel position estimation method using the incremental inductance is proposed. In the proposed position estimation method, the incremental inductance is converted into a flux-linkage or self-inductance to be compatible with FEA results, resulting in estimating an accurate rotor position at the region. Flux-linkage is chosen in this research and this approach is illustrated in Fig 4.6.

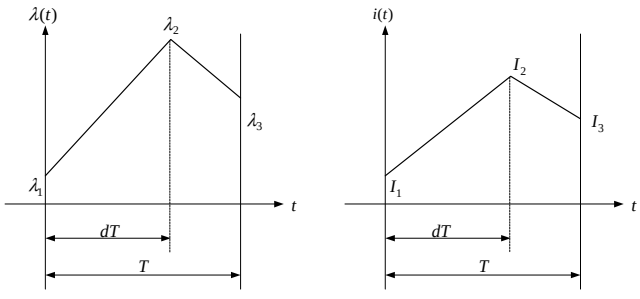

Fig 4.6 Flux-linkage and phase current in a PWM period

The flux-linkage in a PWM period can be drawn on the left side of Fig 4.6, assuming that the ringing and glitches of phase current at the instant of switching are ignored as shown in the right side of Fig 4.6 and the hard chopping PWM current control strategy is chosen for PWM operation. The flux-linkage of the stator winding can be calculated by taking the time integral of the difference between the applied phase voltage and the voltage drop across the stator phase resistance.

Case (i): Turn ON

$$\lambda_2 = \int_0^{dT} (v - Ri)\, dt + \lambda_1 \tag{4.10}$$

$$\lambda_2 - \lambda_1 = \int_0^{dT} (v - Ri)\, dt \tag{4.11}$$

$$\frac{\lambda_2 - \lambda_1}{dT} = \frac{(V_{dc} - R \cdot I_{on}) \cdot dT}{dT} = V_{dc} - R \cdot I_{on} \tag{4.12}$$

Case (ii): Turn OFF

$$\lambda_3 = \int_{dT}^{T} (v - Ri)\, dt + \lambda_2 \tag{4.13}$$

$$\lambda_3 - \lambda_2 = \int_{dT}^{T} (v - Ri)\, dt \tag{4.14}$$

$$\frac{\lambda_3 - \lambda_2}{(1-d)T} = \frac{(-V_{dc} - R \cdot I_{off}) \cdot (1-d)T}{(1-d)T} = -V_{dc} - R \cdot I_{off} \tag{4.15}$$

where V_{dc} is the DC supply voltage, d is the duty cycle, I_{on} is the average current during turn ON time, and I_{off} is the average current during turn OFF time. Assuming that the average currents during turn ON and turn OFF times are close to each other and neglecting the resistive voltage drop compared to the DC supply voltage, the relationships between the slopes of flux-linkage with respect to time during turn ON and turn OFF can be simply expressed as,

$$\left| \frac{\lambda_2 - \lambda_1}{dT} \right| \approx \left| \frac{\lambda_3 - \lambda_2}{(1-d)T} \right| \tag{4.16}$$

Defining “a” as the slope of flux-linkage with respect to time during turn ON,

$$a = \left| \frac{\lambda_2 - \lambda_1}{dT} \right| \tag{4.17}$$

By the definition of incremental inductance, $L_i = \Delta\lambda / \Delta I$, the slope of flux-linkage with respect to time, “a”, can be rewritten as,

$$a = \left| \frac{\lambda_2 - \lambda_1}{dT} \right| = \left| \frac{\Delta\lambda_1}{dT} \right| = \left| \frac{\tilde{L}_i \cdot \Delta I_1}{dT} \right| \tag{4.18}$$

where $\Delta I_1 = I_2 - I_1$ as shown in Fig 4.6. From equations (4.16) and (4.18), the flux-linkage in a PWM period, λ_3, can be represented as the slope of flux-linkage with respect to time during turn ON and the duty cycle applied to the stator winding with DC bus voltage and it is given as,

$$\lambda_3 = -a \cdot (1-2d) \cdot T + \lambda_1 \tag{4.19}$$

Fig 4.7 shows the flux-linkage calculated from the incremental inductance. From Fig 4.7, the measured flux-linkage estimated from the incremental inductance has one-to-one relation with the rotor position at any phase currents and the rotor position can be estimated from the flux-linkage and measured phase current in a PWM period.

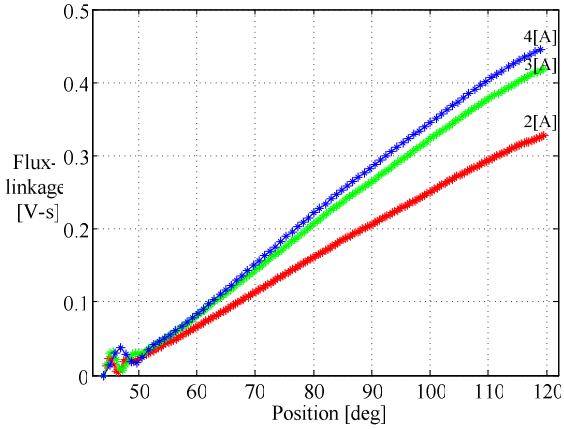

Fig 4.7 Measured flux-linkage estimated from incremental inductance

However, the measured flux-linkage estimated from the incremental inductance is dependent on time as in (4.19) and hence it is varying with respect to the rotor speed as shown in Fig 4.8.

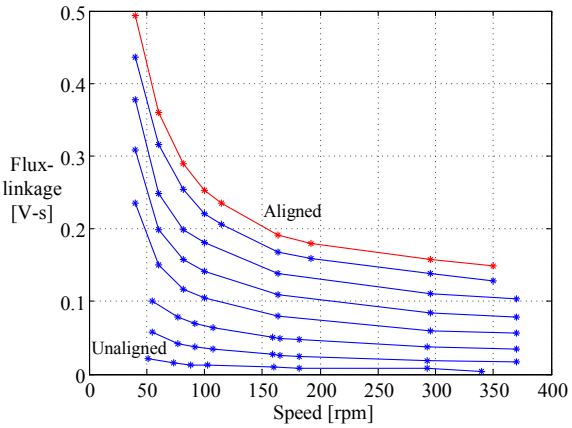

Fig 4.8 Measured flux-linkage estimated from incremental inductance vs. rotor speed at 2A when the switching frequency is 5 kHz

Fig 4.8 shows the variation of the flux-linkage estimated from the unaligned to aligned position according to the variation of the rotor speed. From Fig 4.8, the estimated flux-linkage is larger as the rotor speed is lower, while it decreases significantly as the rotor speed is higher. At the end of each conduction period for each phase, the flux-linkage is to be reset to zero to reduce the error accumulated at the flux-linkage estimation. However, even using a zero initial condition during the flux-linkage estimation, the flux-linkage error accumulated during a phase conduction period never goes to zero. Hence at lower rotor speeds or lower current, the estimated flux-linkage by using the slope of flux-linkage during turn-ON has large errors, leading to increase the position error. It was mainly attributed to the assumption that the phase current and flux-linkage are linearly varying as shown in Fig 4.6.

In contrast to the assumption, phase current is actually non-linear with respect to time due to the saturation effect as the rotor pole moves towards aligned position as shown in Fig 4.3. Moreover, the gradients of phase current during turn-ON and turn-OFF times are steeper as the rotor pole moves towards aligned position due to the decrease of the rate of change of inductance with respect to phase current at constant rotor position. The non-linearity and higher gradient of phase current generated as the rotor pole moves towards aligned position incurs the non-linearity of flux-linkage. Therefore, the non-linearity of phase current and flux-linkage in a PWM period produces a large numerical integration error as the rotor pole moves towards aligned position. In addition, the accumulated flux-linkage error in a conduction period must be larger at lower speed where the phase conduction period is longer.

It should be noted that the estimated flux-linkage in a PWM period depends on the rotor speed as well as the estimated rotor position and measured phase current. However, the flux-linkage estimated from the incremental inductance should be a unique value regardless of the rotor speed and represented as a function of rotor position and phase current in order to be compatible with FEA results every PWM period. Therefore, the flux-linkage estimated from the incremental inductance should be scaled down or up to be a unique value varying as a function of rotor position and phase current regardless of the rotor speed. This approach is illustrated in Fig 4.9.

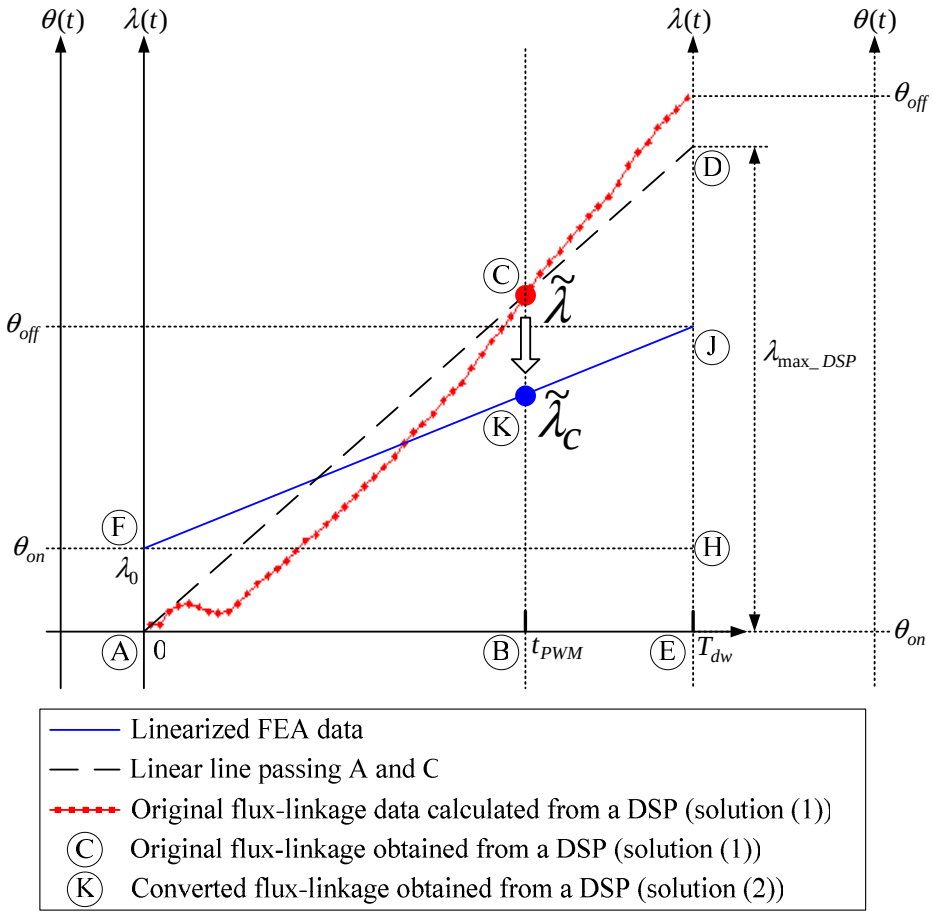

Fig 4.9 Conversion a flux-linkage estimated from an incremental inductance into a unique flux-linkage

If we assume that the variation of the rotor speed is small during phase conduction, the flux-linkage estimated from the incremental inductance, $\tilde{\lambda}$, can be a unique value over phase conduction period, based on the calculations of T_{dw}, $\lambda_{\max\_DSP}$, and $\tilde{\lambda}_c$ given at a certain rotor speed in a PWM period.

a) T_{dw}

By the assumption that the rotor speed is not significantly varying during phase conduction period, T_{dw} corresponding to the conduction time can be derived as,

$$T_{dw} = \frac{\theta_{off} - \theta_{on}}{\tilde{\omega}}, \quad (if\ \omega \neq 0) \tag{4.20}$$

where θ_{off} is the commutation angle where the stator winding is not energized and its unit is radian, θ_{on} is the excitation angle where the stator winding is energized and its unit is radian, $\tilde{\omega}$ is

the rotor speed estimated by the derivative of the estimated rotor position and its unit is rad/s, and T_{dw} is the conduction time with the unit of second.

b) $\lambda_{\max\_DSP}$

It can be seen from Fig 4.9 that a triangle ΔABC is similar to a triangle ΔAED since two pairs of corresponding angles are congruent and if we define $\lambda_{\max\_DSP}$ as the maximum flux-linkage at the instant of T_{dw} commutating a phase, $\lambda_{\max\_DSP}$ can be expressed as equation (4.21) due to the proportionality of the corresponding sides of similar triangles.

$$\lambda_{\max\_DSP} = \frac{T_{dw}}{t_{PWM}} \cdot \tilde{\lambda} \tag{4.21}$$

where t_{PWM} is the time elapsed after exciting a phase, $\tilde{\lambda}$ is the flux-linkage estimated from the incremental inductance before scaling.

c) $\tilde{\lambda}_C$

By using the property of the similarity between a triangle ΔAED and a triangle ΔFHJ, $\lambda_{\max\_FEA}$ can be defined as the maximum flux-linkage given by FEA at (θ_{off}, I), where I is the average current in a PWM period. $\tilde{\lambda}_C$ can then be obtained as equation (4.22) due to the proportionality of the corresponding sides of similar triangles as,

$$\tilde{\lambda}_c = \frac{\lambda_{\max\_FEA} - \lambda_0}{\lambda_{\max\_DSP}} \cdot \tilde{\lambda} + \lambda_0 \tag{4.22}$$

where λ_0 is the flux-linkage given by FEA at (θ_{on}, I), where I is the average current in a PWM period. $\tilde{\lambda}_C$ is the estimated flux-linkage scaled down or up. Consequently, $\tilde{\lambda}_C$ is not varying with respect to the rotor speed and knowing the phase current and the estimated flux-linkage scaled down or up, the rotor position can be estimated using the unique relationship between flux-linkage and position at given phase current. The flow chart for estimating flux-linkage is represented in Fig 4.10.

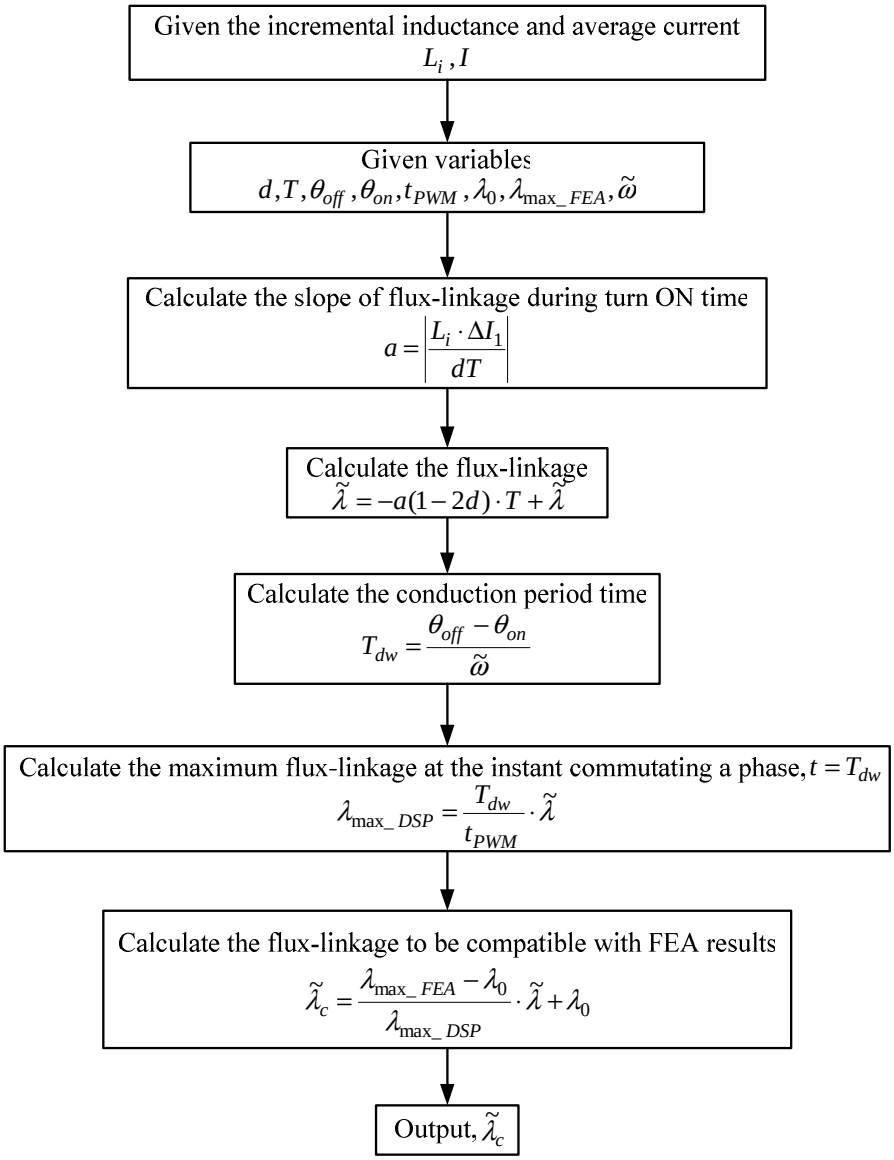

Fig 4.10 The flow chart for flux-linkage estimation

4.3 Position Estimation

The relationship between flux-linkage and rotor position for each excitation current is unique over a phase period regardless of the rotor speed. This particular feature of the SRM is then used to estimate the rotor position from the estimated flux-linkage of a machine phase winding through the stored information of flux-linkage and rotor position for each phase current. Fig 4.11 shows the magnetization characteristic of the two-phase 6/3 SRM used in this research and it is stored in the form of flux-linkage as a function of rotor position and phase current.

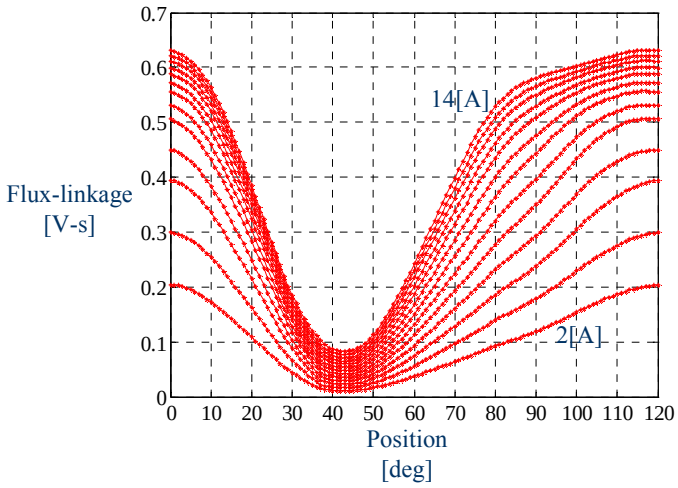

Fig 4.11 Flux-linkage profile for two-phase 6/3 SRM

From Fig 4.11, the flux-linkage starts to saturate from 4A and it is periodic with a period of 120º. If at a given instant, the estimated flux-linkage ($\tilde{\lambda}_C$) and the phase current (i) of particular phase are known, then from the stored flux-linkage characteristics of the SRM, the rotor position ($\tilde{\theta}$) will be found provided it is also known whether the operating mode is motoring or braking. From the motor geometry in this research, it can be found that for the two-phase 6/3 SRM, the relative angular displacement between two phases is 60º because the number of stator and rotor poles are 3 and 6, respectively. It can be observed from the flux-linkage profile of each phase at 2A as shown in Fig 4.12. From Fig 4.12, the SRM starts reliably even the rotor poles are fully aligned to the stator poles and it cannot rotate backward since the region with the positive slope of flux-linkage is longer.

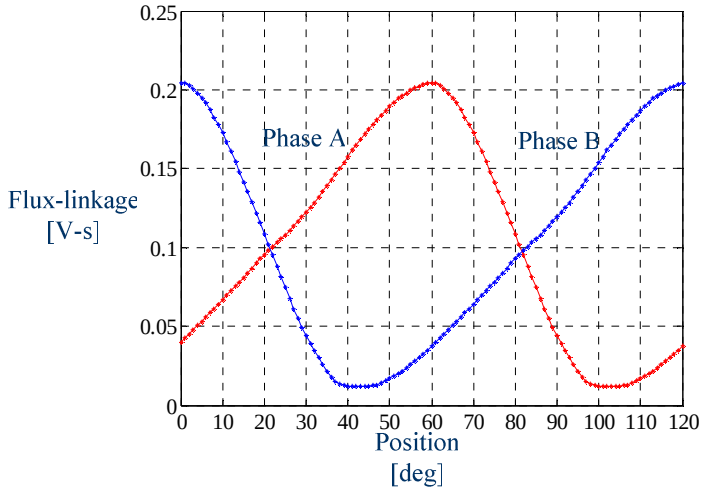

Fig 4.12 Flux-linkage profile of both phases at 2A

If the mechanical angle of the rotor is assumed to be equal to the electrical angle of phase B, the displacement between the mechanical angle of the rotor and the electrical angle of phase A is still 60 º and the relationships between these angles are represented as,

$$\begin{aligned} \theta_A &= \theta_B + 60° = \theta + 60° \\ \theta_B &= \theta \end{aligned} \tag{4.23}$$

where θ_A and θ_B are the electrical angle of phase A and phase B, respectively and θ is the mechanical angle of the rotor. Hence the flux-linkage profile of phase B is stored for easier estimation of the rotor position and the stored flux-linkage profile is two dimensional array with equally spaced phase current for row and rotor position for column. The appropriate new rotor position is estimated from this stored flux-linkage profile at given phase current and it is easily estimated by using the characteristic that the rotor cannot rotate backward. Thus the rotor position is obtained from searching a few forward points of the previously estimated rotor position, instead of searching whole points of the rotor position array in two-dimensional flux-linkage table. In this research, 4 points are selected with consideration of the resolution of estimated rotor position per PWM period at the rated speed. The approach to estimate the rotor position in two-dimensional flux-linkage table is illustrated in Fig 4.13.

Fig 4.13 The position estimation with the estimated flux-linkage at a given current

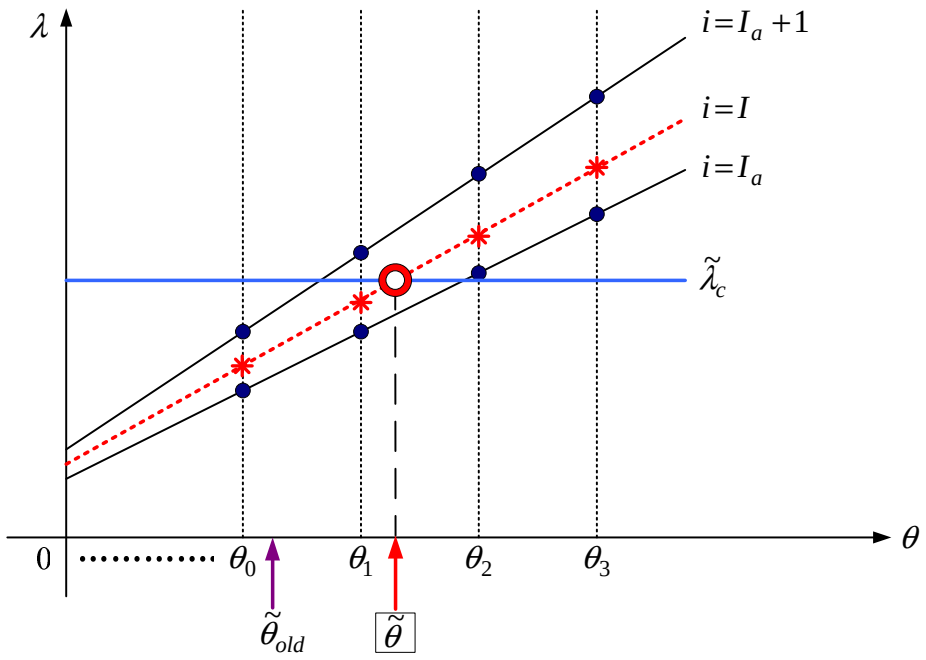

(a) $\tilde{\lambda}_c > \lambda(\theta_1, I)$

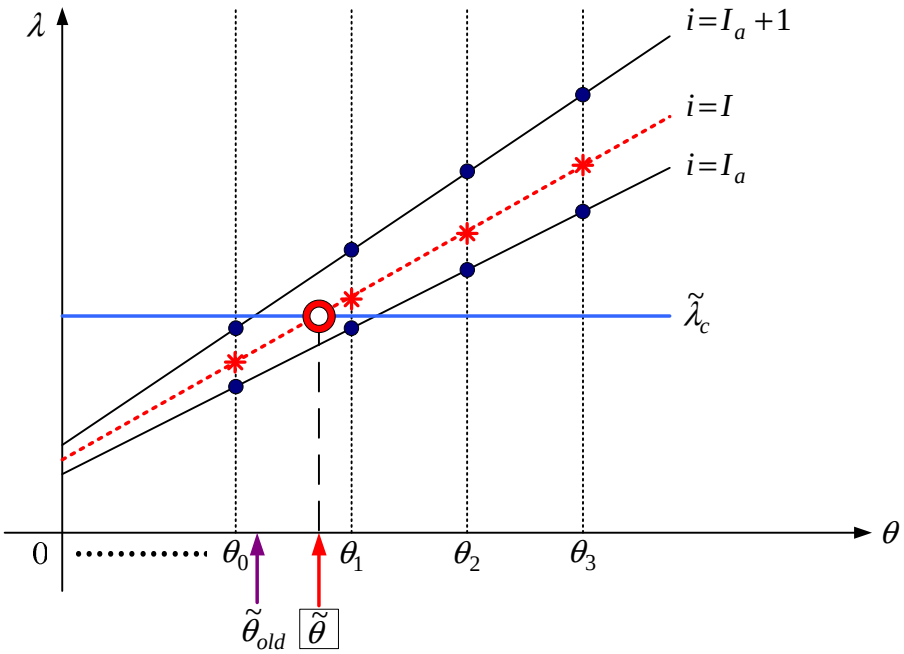

(b) $\tilde{\lambda}_c < \lambda(\theta_1, I)$

From Fig 4.13, I is the measured phase current value at the current PWM cycle, I_a is the closest lower current to the average current and I_a+1 is the next higher current than I_a in the equally spaced current array of the two-dimensional flux-linkage lookup table. Thus I_a and I_a+1 are phase current values surrounding the average current I. '$*$' is the interpolated flux-linkage value between $i=I_a$ and $i=I_a+1$, '$\bullet$' is the flux-linkage value given by FEA, $\tilde{\lambda}_c$ is the estimated flux-linkage at the current PWM cycle, $\tilde{\theta}_{old}$ is the previously estimated rotor position at the previous PWM cycle, $\tilde{\theta}$ is the estimated rotor position at the current PWM cycle, θ_0 is the closest point to the previously estimated rotor position and it is the index of equally spaced rotor position array of the two dimensional flux-linkage table, $\lambda(\theta_1, I)$ is the flux-linkage with the minimal displacement between the estimated flux-linkage and interpolated flux-linkages. With known the previously estimated rotor position and phase current, the linear interpolated flux-linkages between $i=I_a$ and $i=I_a+1$ are obtained by,

$$\lambda(\theta_n, I) = \lambda(\theta_n, I_a) + [\lambda(\theta_n, I_a+1) - \lambda(\theta_n, I_a)] \cdot \left[\frac{I - I_a}{\Delta I}\right] \quad , \quad n = 0,1,2,3 \qquad (4.24)$$

where ΔI is the interval between elements in the current array of the two-dimensional flux-linkage table. Then, the displacement between the estimated flux-linkage and interpolated flux-linkages is computed and the rotor position carrying the minimal distance is obtained. If the estimated flux-linkage is greater than the flux-linkage with the minimal displacement from the estimated flux-linkage as shown in Fig 4.13(a), the new rotor position is estimated by the linear interpolation between $\lambda(\theta_1, I)$ and $\lambda(\theta_2, I)$ along the rotor position dimension as,

$$\tilde{\theta} = \theta_1 + [\theta_2 - \theta_1] \cdot \left[\frac{\tilde{\lambda}_c - \lambda(\theta_1, I)}{\lambda(\theta_2, I) - \lambda(\theta_1, I)} \right] \tag{4.25}$$

On the other hand, in case that the estimated flux-linkage is less than the flux-linkage with the minimal displacement from the estimated flux-linkage as shown in Fig 4.13(b), the new rotor position is estimated by the linear interpolation between $\lambda(\theta_0, I)$ and $\lambda(\theta_1, I)$ along the rotor position dimension as,

$$\tilde{\theta} = \theta_1 - [\theta_1 - \theta_0] \cdot \left[\frac{\lambda(\theta_1, I) - \tilde{\lambda}_c}{\lambda(\theta_1, I) - \lambda(\theta_0, I)} \right] \tag{4.26}$$

However, in saddle regions around unaligned or aligned position, the position having the minimal displacement between the estimated flux-linkage and interpolated flux-linkages may not be appropriate for the new estimated rotor position. That is to say, as shown in Fig 4.14, the position having the minimal displacement, $\tilde{\theta}_{temp1}$, may be far from the previously estimated rotor position, $\tilde{\theta}_{old}$. It may produce large position estimation error in saddle regions.

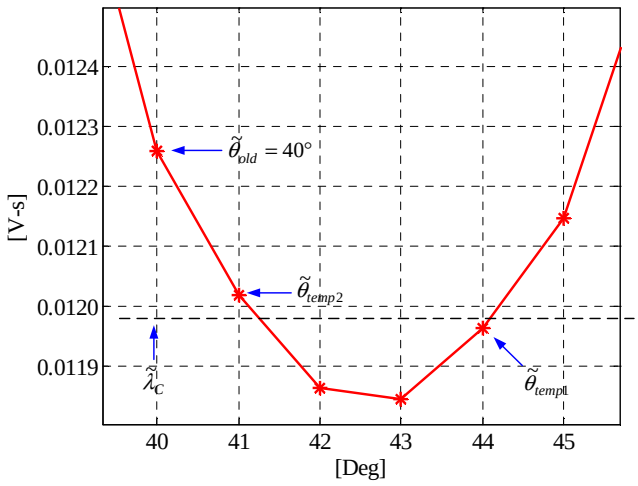

Fig 4.14 The position estimation with the estimated flux-linkage around unaligned position

In order to overcome this detrimental effect, determine two temporary positions, $\tilde{\theta}_{temp1}$ and $\tilde{\theta}_{temp2}$, with the first and second minimal displacement between the estimated flux-linkage and interpolated flux-linkages at a given current and then compare the estimated two temporary positions to the previously estimated rotor position, $\tilde{\theta}_{old}$. The nearest rotor position to the previously estimated rotor position, $\tilde{\theta}_{temp2}$, will be the new estimated rotor position around the unaligned or aligned position, $\tilde{\theta}$. Thus it enhances the accuracy of the estimated rotor position in the work. The flow chart for rotor position estimation is represented in Fig 4.15.

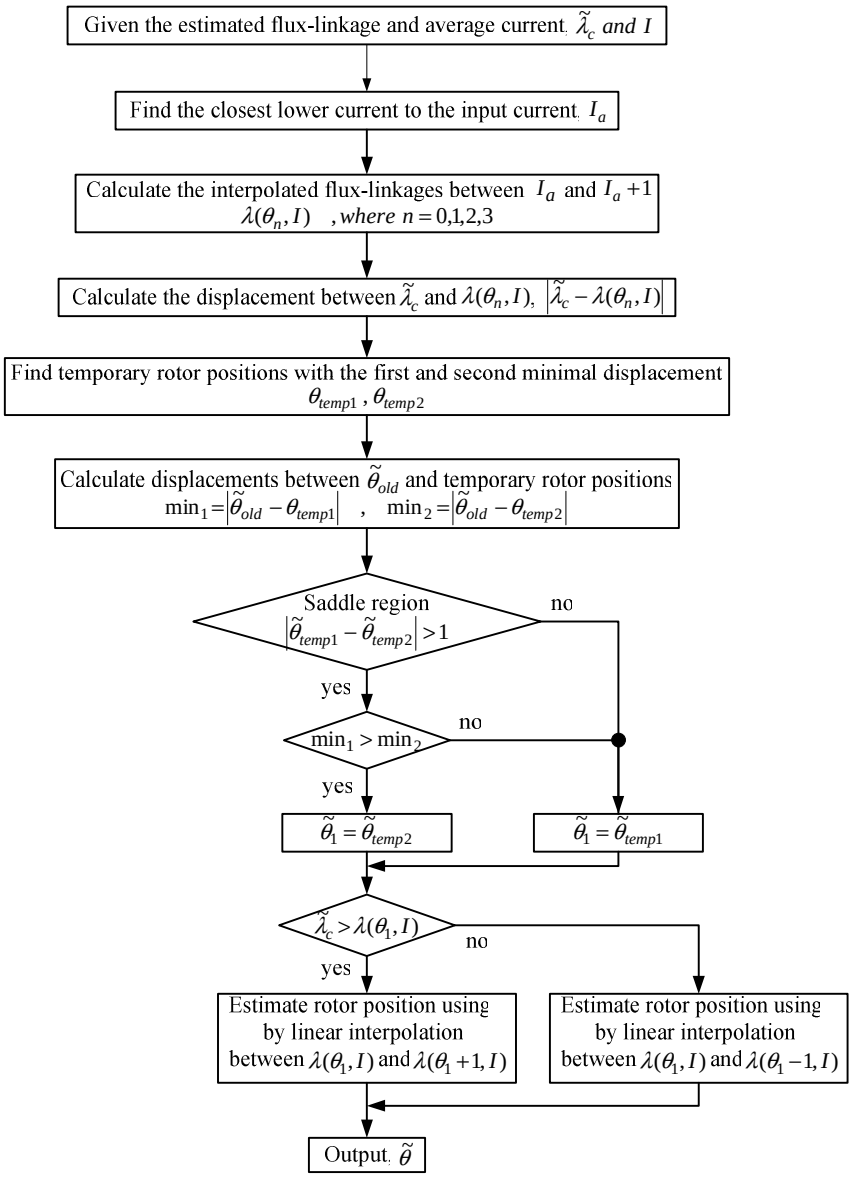

Fig 4.15 The flow chart for rotor position estimation

4.4 Conclusions

If the stator winding is controlled by the average dc current with a small current band, phase inductance is defined as the ratio of change in flux-linkage to the corresponding change in phase current at the operating point on the magnetizing curve $\lambda - i$. The phase inductance for SRM drives is referred to incremental inductance. The incremental inductance or flux-linkage induced from the multiplication of the incremental inductance by phase current is not used for estimating the rotor position in SRM drives since the variation of incremental inductance with respect to rotor position is too small to estimate rotor position in saturated regions or at high currents. Hence, a new method to convert the incremental inductance to be compatible with FEA results has been proposed in this chapter. The incremental inductance at a given phase current and rotor position has been converted into flux-linkage. With the estimated flux-linkage, the rotor position has been determined from the relationship between the flux-linkage and rotor position at a given phase current. The following are believed to be original contributions of this chapter:

1) A new rotor position estimation algorithm irrespective of the motional back emf effect near zero speed and resistance changes of the stator winding due to heating or measurement error, and without additional hardware except for measurements of active phase voltage and current has been proposed.
2) The proposed method depends on the incremental inductance computed using the first switching harmonic phase voltage and current in a PWM period.
3) A method to convert the incremental inductance in SRM drives to be compatible with FEA results regardless of rotor speed has been proposed.
4) The proposed conversion method of the incremental inductance improves the accuracy of estimated rotor position in saturated regions or at high currents.
5) A method to estimate the rotor position in the saddle region such as unaligned or aligned position has been proposed.

CHAPTER 5 DYNAMIC SIMULATIONS FOR POSITION ESTIMATION USING FOURIER ANALYSIS

5.1 Introduction

SRMs are controlled using voltage synchronized with rotor position. The profile of phase current together with the magnetization characteristics defines the electromagnetic torque and hence generates the speed of the motor. Therefore, the motor requires some sort of electronics and control for normal operation in order to generate the proper electromagnetic torque and regulate phase current or speed of the motor. Several power converter topologies for SRM drives are designed, according to the number of motor phases and the desired control algorithm. The particular structure of SRM converters defines the freedom of control for an individual phase.

In this research, an asymmetric converter which has two power switches and two diodes per phase is chosen for the SRM drive since it has good performance compared to other well known converters, even if it increases drive cost but it requires independently control of motor phases [79]. With the asymmetric converter, the verification of the proposed position estimation algorithm is achieved using a novel two-phase SRM with self-starting capability. The novel two-phase SRM has 6 stator poles and 3 rotor poles and it has a flux-reversal-free-stator [80, 81].

This chapter contains dynamic simulations executed at different current commands under various loads to verify the performance of the proposed position estimation method using Fourier analysis. The SRM starts to run from standstill with various loads; 25%, 50%, 75%, and 100% of the rated load which is 4 N·m for the prototype SRM. The simulation procedure is also illustrated with comprehensive sets of SRM operation. The estimated and actual values of the flux-linkage, rotor position, and speed are compared in a PWM period and their results are also analyzed under different operating conditions such as transient startup as well as low and high speed. Voltage drops and switching transients of switching devices and diodes are neglected since they are much smaller than DC-link voltage and mechanical time constant of the motor. Therefore, switching devices and diodes are assumed to be ideal.

5.2 Two-phase SRM and Modeling

Fig 5.1 shows flux lines for a phase in a two-phase 6/3 SRM (6 stator poles and 3 rotor poles) using computer-based FEA [80]. The SRM has one main stator pole and two auxiliary stator poles in each phase. The shape of rotor poles is separated by a uniform and non-uniform air gap. The uniform air gap region is generally formed to minimize reluctance so that inductance can be maximized. The non-uniform air gap region is necessary to keep increasing inductance until the uniform air gap generates inductance up to the maximum. The difference between the air gap in the uniform and non-uniform region is small and does not exceed a few times the minimum air gap as seen from Fig 5.1. This pole shaping is to ensure that the design will not have zero-torque at rotor positions where the stator and rotor poles fully align. Magnetic characteristics of inductance, flux-linkage, and torque are analyzed with FEA and its results are correlated with measurement results as published in [80]. Thus, predicted results from FEA are mainly used for the analysis, dynamic simulations, and experiments in this research.

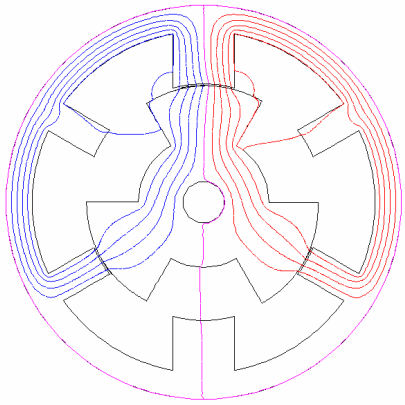

Fig 5.1 Finite element flux pattern of a two-phase 6/3 SRM

Fig 5.2 shows the flux paths and the normal-force diagram of the SRM when stator poles are aligned with rotor poles. In a conventional SRM, the normal forces of one phase are exactly opposite and separated by 180°, thus causing oval deformation of the stator in the process of it being cancelled through the stator and rotor bodies, with the resulting acceleration of the stator. As shown in Fig 5.2, it is seen that the normal forces pull in three different directions and prevent oval deformation of the stator and hence in the mitigation of stator acceleration that invariably leads to reduced acoustic noise [82].

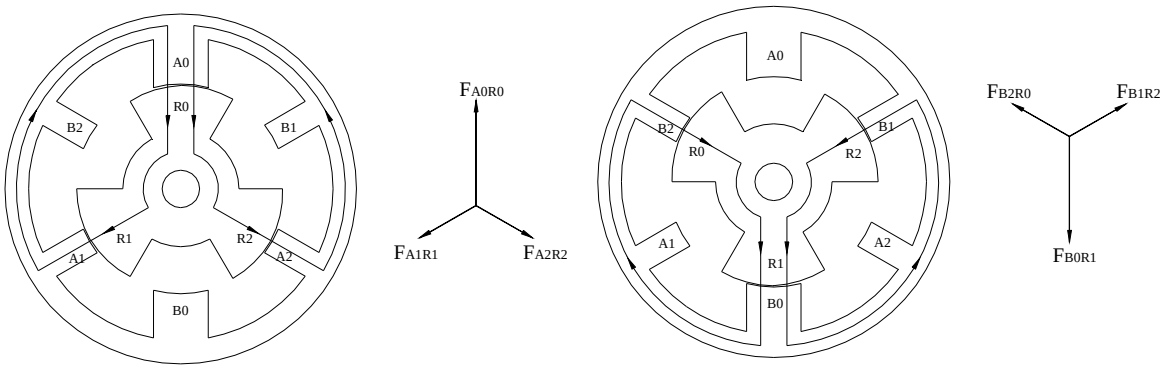

(a) Phase-A windings are excited (b) Phase-B windings are excited

Fig 5.2 Flux path and normal force diagram when poles are aligned

While the rotor rotates, the self-inductance or flux-linkage of each phase varies with rotor position periodically as shown in Fig 5.3. Thus rotor position can be estimated by estimating the self-inductance or flux-linkage with given phase current of a particular phase.

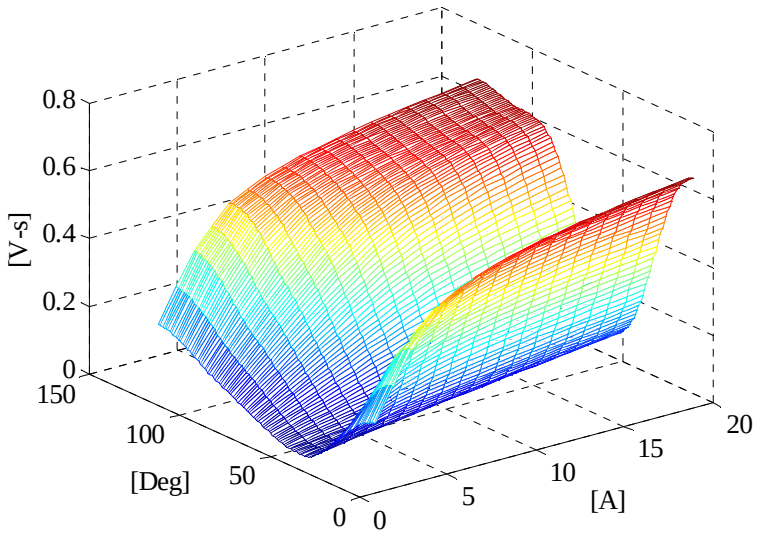

Fig 5.3 The flux-linkage profile at various phase currents and rotor positions

Flux-linkage of the two-phase 6/3 SRM employed in this research is periodic with a period of 120º and an angular displacement between the individual phases is 60º. While the positive slope region of flux-linkage which generates the positive torque is about 70º, the negative torque is generated for 50º corresponding to the negative slope region of flux-linkage. Machine parameters are presented in detail in Appendix B.

Due to the non-uniform air gap design, an accurate analysis of the motor's behavior requires a formal, and relatively complex, mathematical approach. The instantaneous voltage across the terminals of a single phase of an SRM stator winding is related to the flux linked in the winding by Faraday's law,

$$v = R \cdot i + \frac{\partial \lambda}{\partial t} \tag{5.1}$$

where v is the terminal voltage, i is the phase current, R is the resistance of the stator winding, and λ is the flux linked by the winding. Because of the doubly salient construction of SRM in which both the rotor and stator have salient poles and magnetic saturation effects, the flux linked in a phase varies as a function of rotor position and phase current. Thus, equation (5.1) can be expanded as,

$$v = R \cdot i + \frac{\partial \lambda}{\partial i}\frac{di}{dt} + \frac{\partial \lambda}{\partial \theta}\frac{d\theta}{dt} \tag{5.2}$$

where $\frac{\partial \lambda}{\partial i}$ is defined as an incremental inductance, $\frac{\partial \lambda}{\partial \theta}\frac{d\theta}{dt}$ is the instantaneous back emf, and $\frac{d\theta}{dt}$ is the rotor angular velocity. Assuming that the SRM is operated in unsaturated region, where the inductance or flux-linkage is linearly varying with the rotor position for a given phase current, and the mutual effects between two phases are neglected, the torque of a single phase of the SRM can be simply expressed by the product of the derivative of the phase inductance with respect to the rotor position and the square of the phase current.

$$T_e = \frac{1}{2} \cdot i^2 \cdot \frac{dL(\theta, i)}{d\theta} \tag{5.3}$$

5.3 Control and Converter Topology

SRM drives are controlled by synchronizing the excitation of the motor phases with rotor position. From equation (5.3), it is obvious that positive (or motoring) torque is produced when a phase is excited at rotor positions with positive $\frac{dL}{d\theta} > 0$ for that phase, and negative (or braking) torque is produced at rotor positions with negative $\frac{dL}{d\theta} < 0$. Hence a control system is required that determines rotor position and applies the phase-winding excitations at the appropriate instant.

The voltage applied to the motor phases is modulated with a duty cycle to reach the desired current in the excited phase. The instant of commutating the phase currents is linked to the rotor position. Given the desired phase current command, the current controller evaluates the difference between actual and desired phase current command and then calculates an appropriate PWM duty cycle to regulate the phase current. The phase voltage is controlled by the supply voltage chopped with a fixed frequency and a duty cycle. The commutation angle, the energy stored in the stator winding inductance is sent to the voltage source, should be determined to minimize the torque ripple when exciting a phase. The excitation and commutation table for the operation of the two-phase 6/3 SRM is given in Table 5.1.

Table 5.1 Excitation and commutation table

	$T_e^* \geq 0$	$T_e^* < 0$
Phase A	Excitation for $0° \leq \theta < 50°$	Commutation for $0° \leq \theta < 50°$
	Commutation for $50° \leq \theta < 110°$	Excitation for $50° \leq \theta < 110°$
	Excitation for $110° \leq \theta < 120°$	Commutation for $110° \leq \theta < 120°$
Phase B	Commutation for $0° \leq \theta < 50°$	Excitation for $0° \leq \theta < 50°$
	Excitation for $50° \leq \theta < 110°$	Commutation for $50° \leq \theta < 110°$
	Commutation for $110° \leq \theta < 120°$	Excitation for $110° \leq \theta < 120°$

The magnitude of phase current flowing into a stator winding is controlled using a closed control loop with a current feedback. The phase current in a phase winding is directly computed by equation (5.2) and Euler's method to solve the first order differential equation. The actual phase current is compared with a desired value of phase current, forming an error signal. Neglecting the saturation effects, equation (5.2) can be expressed as,

$$\frac{di}{dt} = -\frac{R}{L} i - \frac{1}{L} \cdot \frac{\delta L}{\delta \theta} \cdot \omega_m i + \frac{v}{L} \tag{5.4}$$

The input phase voltage, v, needs to be decoupled to control the phase current, as developed in [83] and it can be expressed as equation (5.5) by defining a new voltage input with the relationship to the old voltage input,

$$v = \bar{v} + \frac{\delta L}{\delta \theta} \cdot \omega_m i \tag{5.5}$$

Substituting equation (5.5) into equation (5.4), equation (5.4) can be simply expressed as,

$$\frac{di}{dt} = -\frac{R}{L}i + \frac{\bar{v}}{L} \tag{5.6}$$

The new voltage input $\bar{v}$ is obtained from a control voltage v_c generated by the PI current controller. The time constant of the converter and the current feedback filter are neglected due to the large electrical time constant of the motor, resulting in the transfer function of converter and current feedback filter are simplified into K_r and H_c, respectively. The closed loop transfer function of the current controller is derived by (5.7), as developed in [21].

$$G_c(s) \cong \frac{1}{H_c} \cdot \frac{\frac{H_c K_r}{L}\left(K_{pc}s + K_{ic}\right)}{s^2 + \frac{H_c K_r K_{pc}}{L}s + \frac{H_c K_c K_{ic}}{L}} \tag{5.7}$$

where K_r is the converter gain, H_c is the feedback gain of the current filter, K_{pc} is the proportional gain, and K_{ic} is the integral gain. For dynamic simulations, phase current is sampled every 200 μs, and the closed control loop and PWM signals are also updated every 200 μs with 1 kHz of the current control loop bandwidth. The damping ratio is 2 and the switching frequency is 5 kHz. The coefficients of the PI controller are determined using the method described in Appendix A. With sampled phase voltage and current for 200 μs, the rotor position is estimated.

The current flowing through the SRM winding is regulated by switching on or off power devices, such as MOSFETs or IGBTs, which connect each SRM phase to a DC bus. The power converter topology is an important issue in SRM control because it largely dictates how the motor can be controlled. There are several converter topologies available and the decision is coming down to trading off the cost of the driver components against having enough control capability such as independent control of phases. In general, an asymmetric converter with two independent power switches and diodes per phase is the most popular converter topology due to its high performance and reliability even at high costs. The configuration of a power converter for two-phase SRMs is illustrated in Fig 5.4.

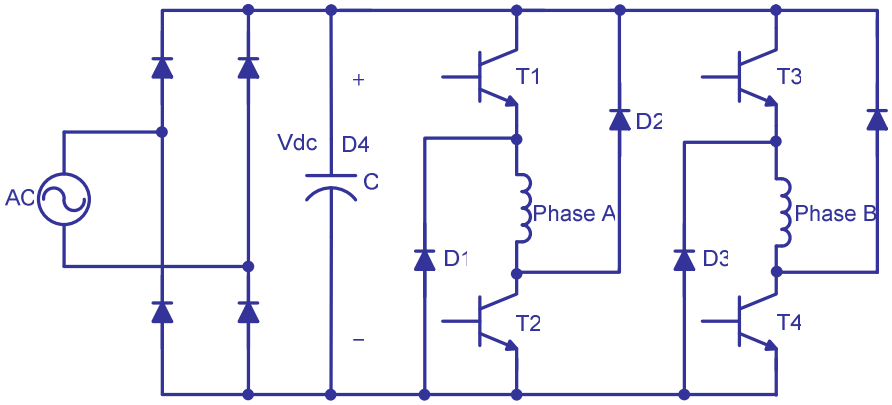

Fig 5.4 The asymmetric converter with two switches and two diodes per phase

From this asymmetric converter, it is possible to control an individual phase independently resulting in great freedom of control [79]. Other power converter topologies [79] share some of the power devices for several phases or have no independent phase control, thus saving on power converter costs, but with these, the motor phases cannot be fully controlled independently. Therefore, the asymmetric converter is attractive for SRM drives. With the asymmetric converter, the SRM is usually controlled by either current control or voltage control. The main advantage of current control over voltage control is that the phase current can be controlled precisely, which means that torque is properly controlled and the reduction of torque ripple or noise is possible. Hence current control is selected for SRM drives. There are two types of current control.

1) Hysteresis current control

The current is controlled between two current levels equal to $I_{ref} \pm \frac{\Delta I}{2}$, where I_{ref} is reference current and $\frac{\Delta I}{2}$ is hysteresis band. The switching frequency is varying in SRM drives. Thus it is inappropriate for the proposed position estimation method.

2) Pulse Width Modulation (PWM) current control

The current is regulated close to I_{ref} using PWM. The switching frequency is fixed in SRM drives, which reflected in phase voltage and current. Because the SRM is controlled at the fixed switching frequency, phase voltage and current are decomposed into their switching harmonic components in frequency domain through Fourier analysis. With PWM current control of the SRM, assuming that each phase of the SRM can be independently controlled, there are two PWM current control strategies except for single pulse operation: Hard chopping mode and soft

chopping mode. In the hard chopping mode, both phase transistors (T_1 and T_2 or T_3 and T_4 in Fig 5.4) are driven by the same pulsed signal: the two transistors are switched on and off at the same time. It increases the current ripple by a large factor. In contrast, in the soft chopping mode, the low side transistors (T_2 and T_4 in Fig 5.4) is left on during phase conduction period and the high side transistors (T_1 and T_3 in Fig 5.4) is chopped according to the pulsed signal. It allows not only control of the current but also a minimization of the current ripple. The differences of the SRM control between two PWM current control strategies are illustrated in Fig 5.5.

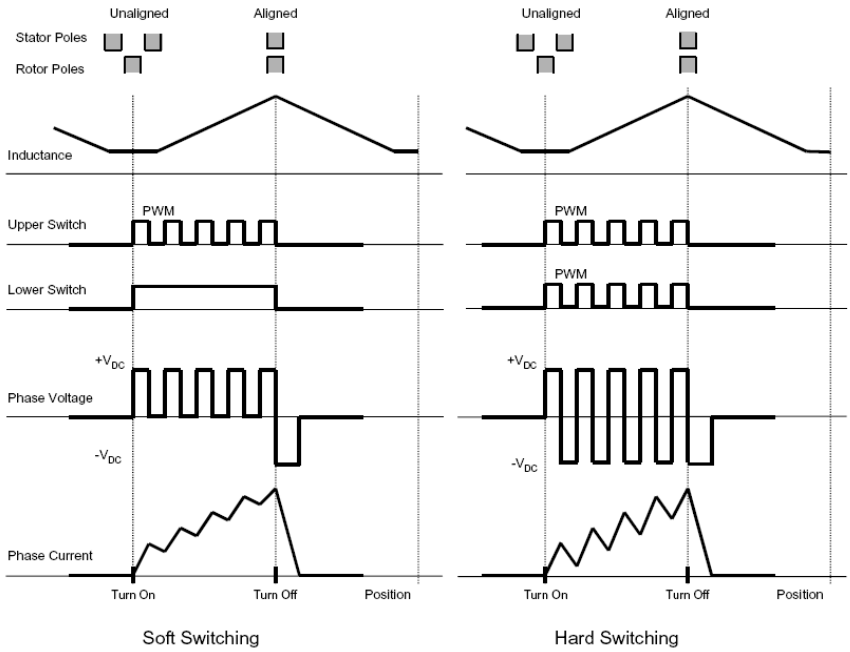

Fig 5.5 SRM drives by soft and hard chopping method

Assuming that the gradient of phase current is linear in a PWM period, the first switching harmonic component of phase current is computed with the helps of slopes of phase current during turn-ON and turn-OFF times. Higher slope of phase current in hardware implementation makes an easy computing of the flux-linkage or inductance in a PWM period. From the aforementioned, PWM current control under hard chopping strategy is chosen since the switching frequency is fixed and it generates more current ripple, which increases the gradient of phase current and makes easy computation of flux-linkage varying as a function of rotor position and phase current. Acoustic noise consideration is ignored in this study.

5.4 Dynamic Simulation Results Using Fourier Series

Position estimation using the first switching harmonics of phase voltage and current decomposed by Fourier series is simulated by using Matlab. Several simulations at different currents commands have been executed to prove the validity of the proposed position estimation algorithm under various loads. For each current command, the estimated and actual values of flux-linkage, rotor position, and speed are presented. Note that no speed control loop is included. In dynamic simulations, the symmetrical PWM method with a fixed frequency (set at 5 kHz) is employed for dynamic current control. The asymmetric bridge converter is designed to apply a phase voltage in hard-chopping mode to increase the rate of the change of phase current for a PWM period. The differential equations governing the operation of the SRM are solved for a given instant of time starting from zero initial conditions with a small simulation integration time step, 1 μs in this research, by using a simple Euler's method for faster computation of the system solution. Individual phase current, flux-linkage, torque, and other mechanical quantities such as the rotor position and speed are easily obtained during simulations and especially the flux-linkage, rotor position, and speed calculated from the differential equations are assigned to the actual values, and then compared to the estimated values. Magnetization data obtained from FEA are stored into a lookup table. The inclusion of saturation limits on PI integrator is embedded in the current controller to provide an anti-windup functionality. The estimated rotor speed is filtered out by using an exponentially weighted moving average filter (EWMAF), which is called the first order IIR filter, at the sample rate of 1 kHz and filter coefficient of 0.95, resulting in increasing the degree of filtering. The reason why this EWMAF is chosen is that the most recent estimated speed is given more emphasis than older values as well as reflects better the state of the process in dynamic control systems.

The simulation includes a precise finite element analysis model of the two-phase 6/3 SRM, which was verified in [80, 81], and the load is applied to the machine from start-up condition. Based on the magnetic characteristics from FEA, discrete data sets of three dimensional relationships between inductance vs. current vs. position and torque vs. current vs. position can be obtained. By using linear interpolation, the inductance and electromagnetic torque for any rotor position and excitation current can be retrieved [21]. Voltage drops and switching transients of power electronic devices are negligible compared to the DC-link voltage

and mechanical time constant of the motor, therefore, the switching devices are assumed to be ideal. The flow chart for dynamic simulations using Fourier series is represented in Fig 5.6.

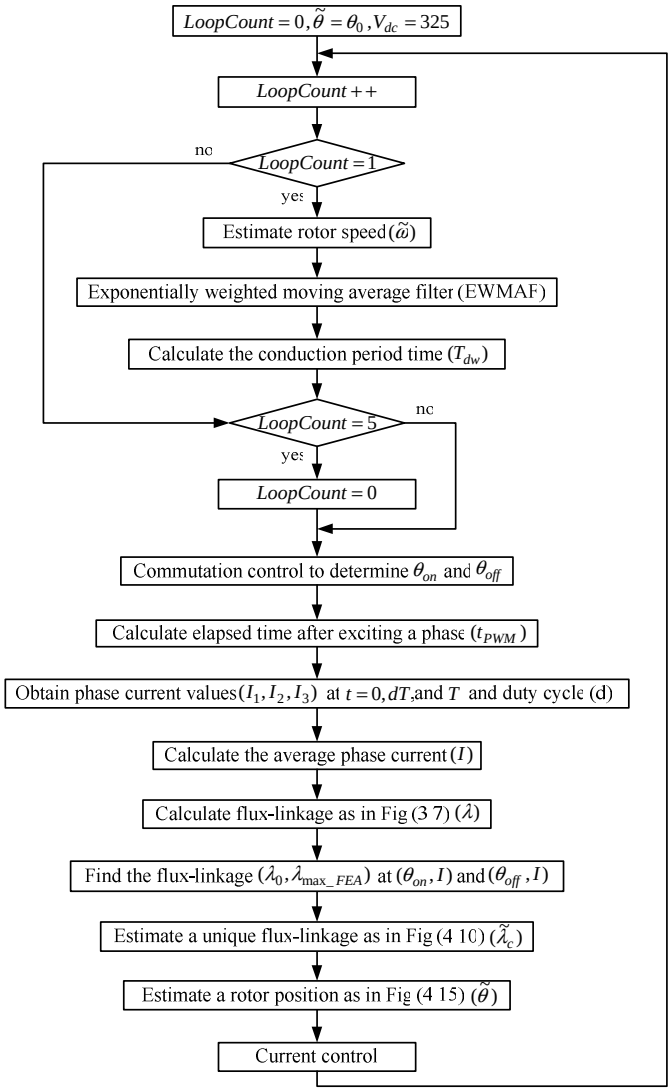

Fig 5.6 The flow chart for dynamic simulations using Fourier series

5.4.1 No Load Test

In order to validate the performance of the proposed position estimation scheme using Fourier series, various dynamic simulations are performed at different phase current commands under no load. The SRM is initially at standstill and no load when a reference current command is applied and it runs with phase current regulation. Note that in these simulations, no speed control loop is included. This test provides the results of the flux-linkage estimated from the

incremental inductance, the rotor position estimated from the estimated flux-linkage and given phase current by looking up the magnetization table, and the rotor speed estimated by the derivative of the estimated rotor position with respect to time. At the rate of 5 kHz, the estimated and actual values of flux-linkage, rotor position, and speed are obtained during 400 PWM cycles at different operating conditions such as transient startup as well as low and high speeds. The average and maximum values of the results obtained during 400 PWM cycles are presented in Table 5.2.

Table 5.2 Simulation results using Fourier series at various current commands under no load

Iref [A]	Average Speed [rpm]	Position Error [deg] $\lvert\Delta\theta\rvert$		Speed Error [rpm] $\lvert\Delta\omega\rvert$		Flux-linkage Error [%] $(\lvert\Delta\lambda\rvert / \lambda_{FEA}) * 100$	
		Average	Maximum	Average	Maximum	Average	Maximum
2	Startup	0.1512	0.8215	0.4704	4.1074	0.7146	3.9870
	240	0.3010	0.4318	0.2358	0.7236	0.7475	1.3655
	324	0.3052	0.4801	0.2284	1.2498	0.8735	1.6931
	549	0.4806	0.6047	0.2617	1.9954	1.2438	2.5176
	710	0.5755	0.7074	0.2632	1.6223	1.4778	3.2030
3	Startup	0.1145	0.8214	0.3403	3.6484	0.5170	3.9870
	499	0.4912	0.9339	0.5703	4.8534	1.2426	5.7667
	699	0.6039	0.9997	0.5585	6.8251	1.5198	5.4455
	965	0.7597	1.1663	0.6639	6.6309	1.8899	5.0435
	1133	0.8445	1.2652	0.8190	7.5480	2.1410	4.7537
4	Startup	0.1101	0.6121	0.3176	2.6195	0.4006	2.5466
	745	0.5852	1.4156	0.4281	6.6002	1.4329	8.8252
	988	0.7352	1.4971	0.5806	11.1191	1.7818	10.5110
	1212	0.8628	1.6168	0.9399	12.0083	2.0590	11.4588
5	Startup	0.0956	0.3739	0.3872	1.9943	0.3712	1.7825
	755	0.6035	1.7581	1.5064	15.5255	1.4951	11.4317
	1137	0.8150	2.2810	2.0330	19.3312	2.0606	11.9124
6	Startup	0.1006	0.2959	0.5355	1.5634	0.3339	1.7818
	890	0.5563	2.1473	0.9885	11.8949	1.4334	12.3796
	1305	0.7813	2.7445	1.5807	17.9467	2.0218	16.0711

Fig 5.7 shows the estimated and actual values plotted at startup when applying the phase current command of 3A under no load. Fig 5.7(a) shows that the estimated flux-linkage is compared with the actual flux-linkage given by FEA simulation results and the absolute values of the percentage errors between them are plotted. From Table 5.2, the average flux-linkage error is approximately 0.51 % and the maximum flux-linkage error is approximately 3.98 %. Based on

the estimated flux-linkage and given phase current, the rotor position is estimated every PWM cycle. Fig 5.7(b) shows the estimated and actual rotor position and the position error between them. From Table 5.2, the average position error is approximately 0.11 deg and the maximum position error is approximately 0.82 deg. Fig 5.76(c) shows the estimated and actual speed and the speed error between them. From Table 5.2, the average speed error is approximately 0.34 rpm and the maximum speed error is approximately 3.64 rpm. It is noted from Fig 5.7 that the flux-linkage error is slightly larger right after startup and it causes the rotor position and speed error to be increased.

Fig 5.7 Simulation results using Fourier series at startup and $I^* = 3A$ under no load

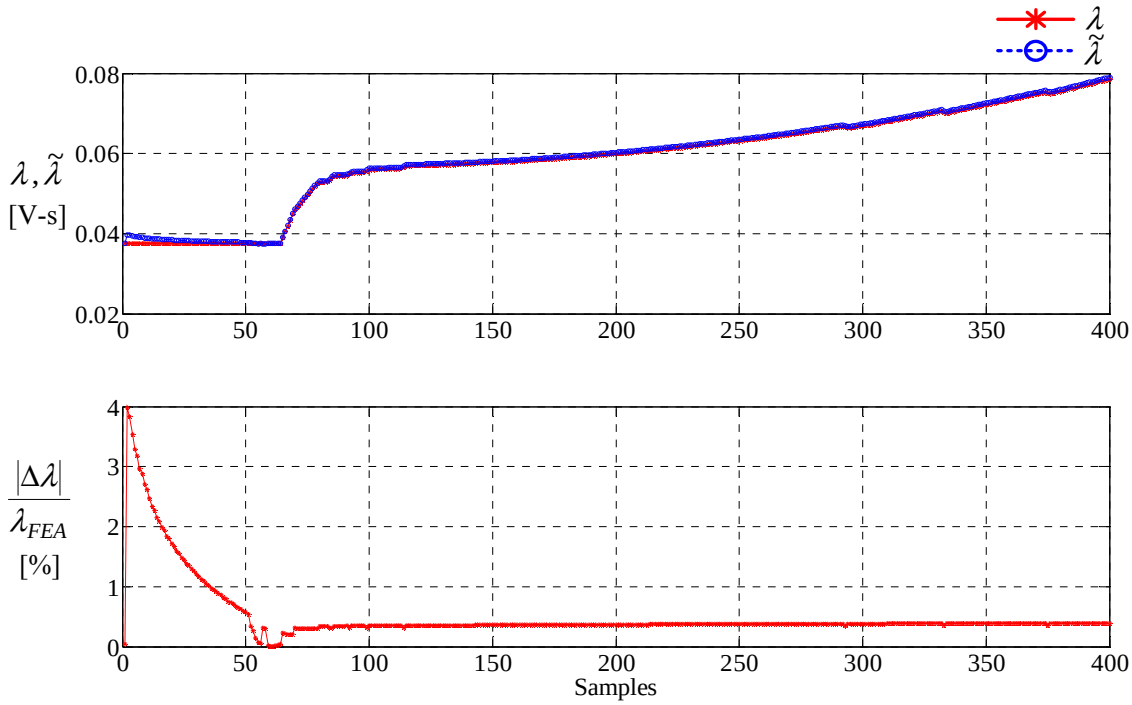

(a) Flux-linkage estimation

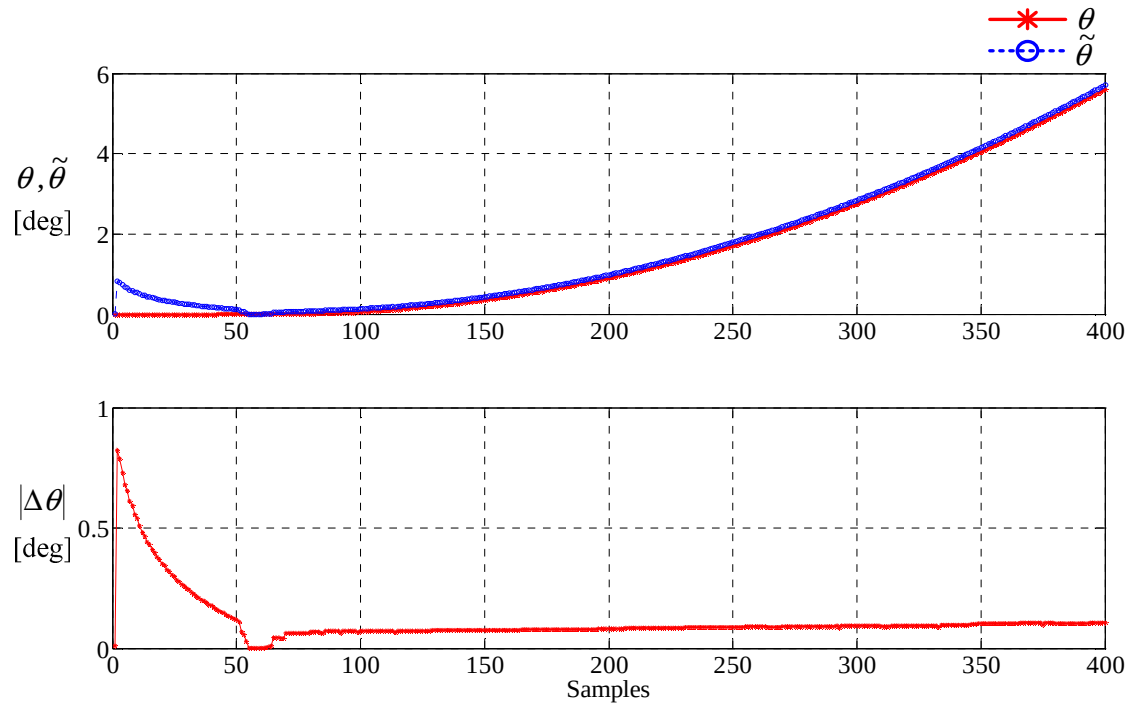

(b) Position estimation

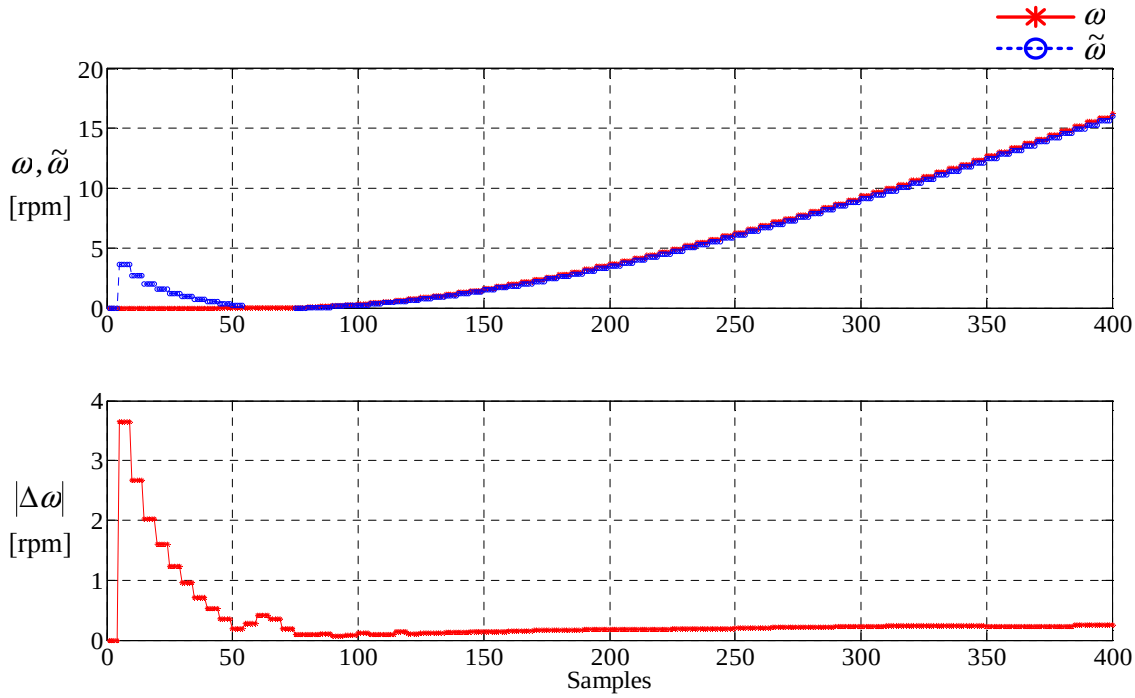

(c) Speed estimation

Fig 5.8 shows the simulation results at high speed when applying the phase current command of 3A under no load. Fig 5.8(a) shows that the estimated flux-linkage is compared with the actual flux-linkage given by FEA at the top and the absolute values of the percentage errors between them are plotted as the error at the bottom. From Table 5.2, the average flux-linkage error is approximately 2.14 % and the maximum flux-linkage error is approximately 4.75 %. Fig 5.8(b) shows the estimated and actual rotor position and the position error between them. From Table 5.2, the average position error is approximately 0.84 deg and the maximum position error is approximately 1.26 deg. Fig 5.8(c) shows the estimated and actual rotor speed and the speed error between them. From Table 5.2, the average speed error is approximately 0.81 rpm and the maximum speed error is approximately 7.54 rpm. From 5.8, the flux-linkage error increases around the unaligned position and it diminishes when the rotor is moving towards aligned position. This results from a higher gradient of phase current around the unaligned position. It increase high frequency components at the expansion of phase current using Fourier series and thereby phase current in a PWM period cannot be satisfactorily represented as the fundamental switching harmonic, resulting in increasing the flux-linkage error around the unaligned position.

Fig 5.8 Simulation results using Fourier series at ω=1133rpm and $I^*=3A$ under no load

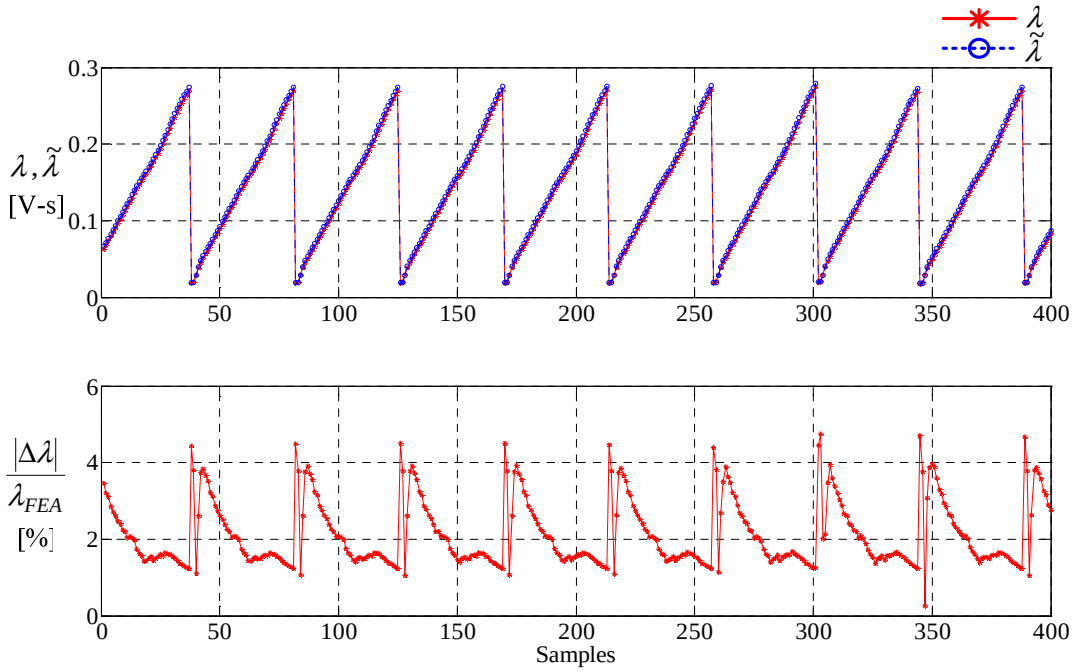

(a) Flux-linkage estimation

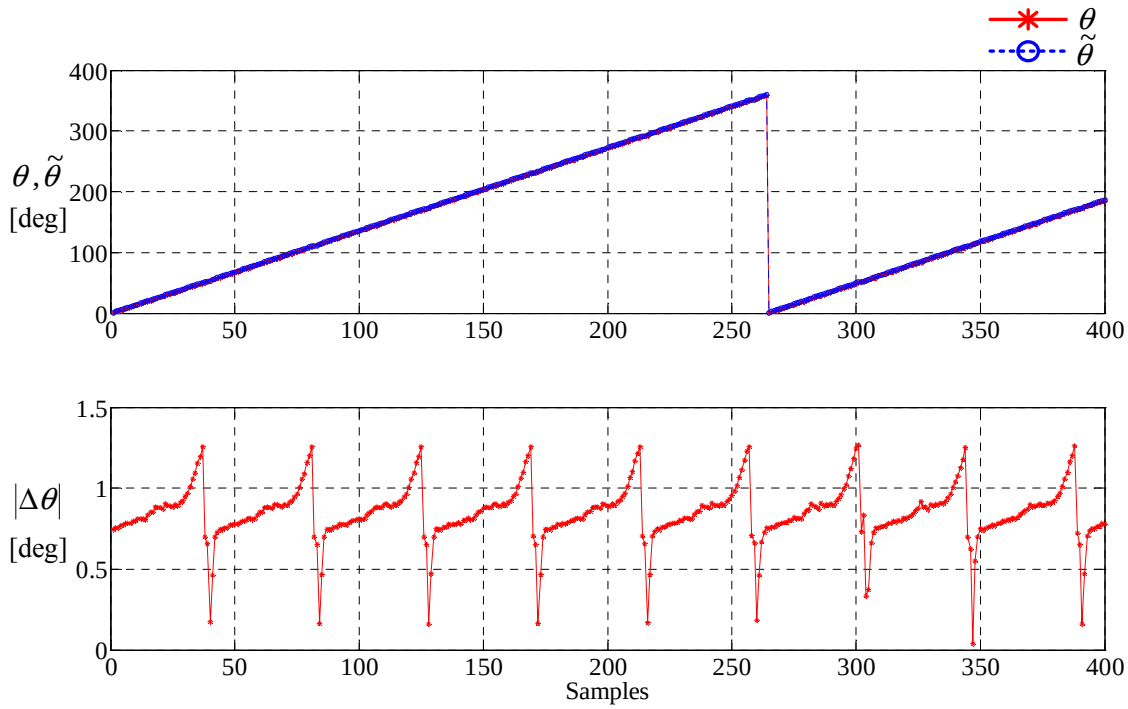

(b) Position estimation

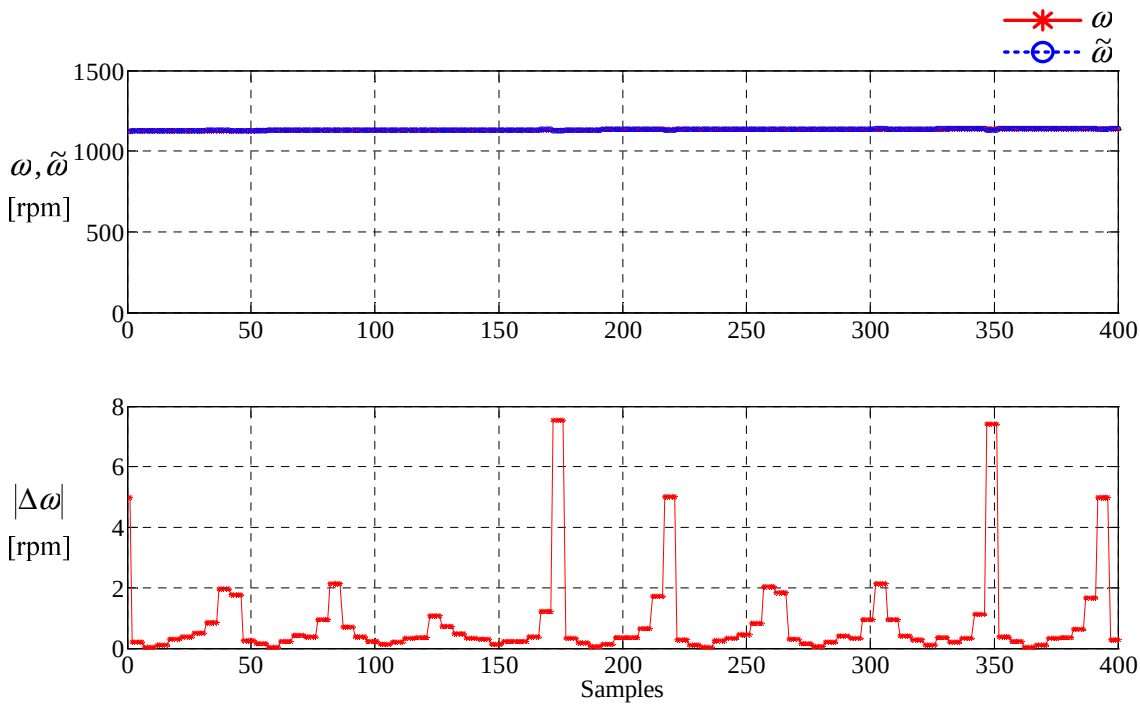

(c) Speed estimation

5.4.2 Load Test

In order to validate the performance of the proposed position estimation algorithm using Fourier series under various loads, various dynamic simulations are performed at different phase current commands. The SRM is initially at standstill with various loads when a phase current command is applied and it runs with phase current regulation. Note that no speed loop is included. The SRM runs at 25%, 50%, 75%, and 100% of full load which is 4 N·m for the prototype. This test provides the results of the flux-linkage estimated from the incremental inductance estimated by the first switching harmonic of phase current and voltage using Fourier series, the rotor position estimated from the estimated flux-linkage and phase current by using a magnetization look-up table, and the rotor speed estimated by the derivative of the estimated rotor position with respect to time. At the rate of 5 kHz, the estimated and actual values of flux-linkage, rotor position, and speed are obtained during 300 PWM cycles at different operating conditions such as transient startup as well as low and high speeds. The average and maximum values of the results obtained during 300 PWM cycles are presented in the following Table 5.3.

Table 5.3 Simulation results using Fourier series at various current commands under various loads

Torque [N·m]	Iref [A]	Average Speed [rpm]	Position Error [deg] $\lvert\Delta\theta\rvert$		Speed Error [rpm] $\lvert\Delta\omega\rvert$		Flux-linkage Error [%] $(\lvert\Delta\lambda\rvert / \lambda_{FEA}) * 100$	
			Average	Maximum	Average	Maximum	Average	Maximum
1	7	894	0.4671	1.4596	2.1607	11.6441	1.5162	11.9308
2	9	884	0.4856	1.2741	3.6077	14.3888	1.4012	11.2256
3	11	852	0.4736	1.6102	2.5794	18.2855	1.3021	15.2236
4	13	778	0.4345	1.6494	2.1741	16.1477	1.1299	13.6541

Fig 5.9 shows the simulation results when applying the phase current command of 9A under half load, 2 N·m. The SRM starts to run from standstill and it is keeping up until the average speed during 300 PWM cycles is 778 rpm. Fig 5.9(a) shows that the estimated flux-linkage is satisfactorily tracking the actual flux-linkage given by FEA and from Table 5.3, the average flux-linkage error is approximately 1.40 % and the maximum flux-linkage error is approximately 11.22 %. Fig 5.9(b) shows the estimated and actual rotor position and the position error between them. From Table 5.3, the average position error is approximately 0.48 deg and the maximum position error is approximately 1.27 deg. Fig 5.9(c) shows that the estimated and actual speed and the speed error between them. From Table 5.3, the average speed error is approximately 3.60 rpm and the maximum speed error is approximately 14.38 rpm. It is noted

form Fig 5.9 that the position error increases right before phase commutation and during phase changeover due to saturation effects.

Fig 5.9 Simulation results at ω=884rpm and I^*=9A under half load, 2 N·m

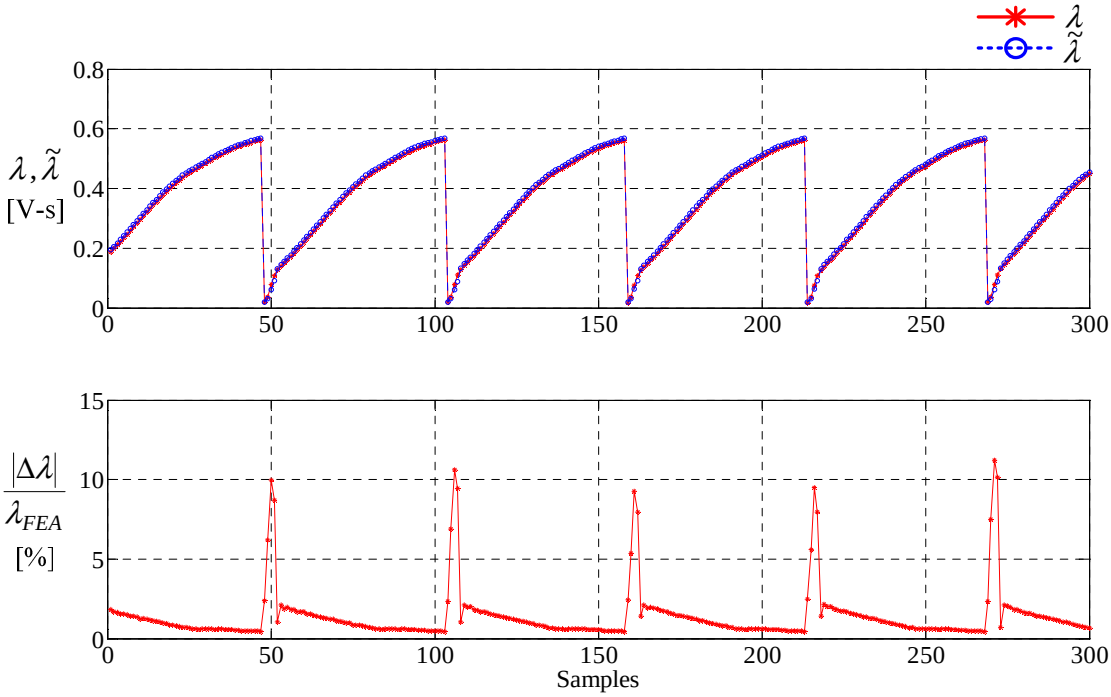

(a) Flux-linkage estimation

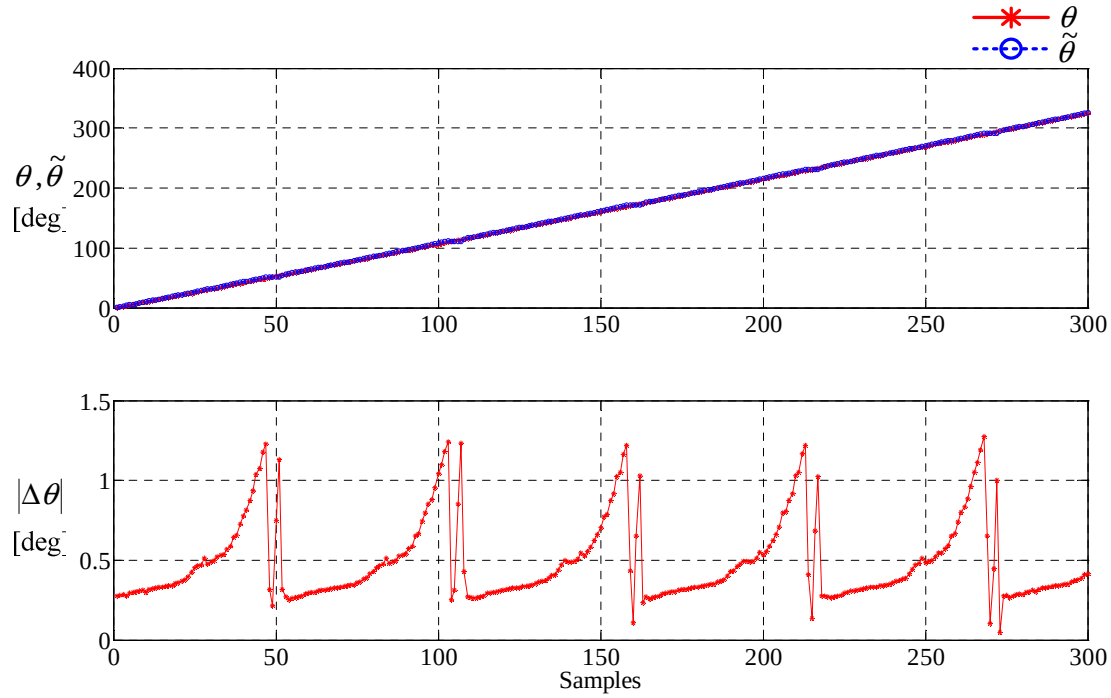

(b) Position estimation

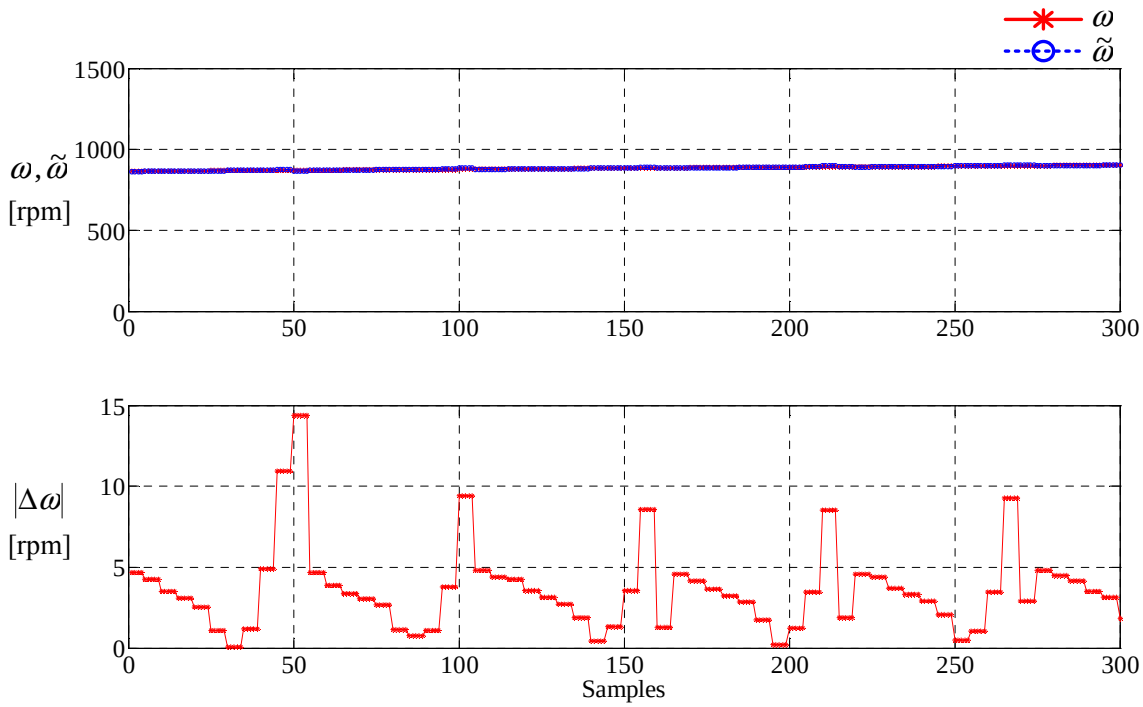

(c) Speed estimation

Fig 5.10 shows the estimated and actual values of flux-linkage, rotor position, and speed when applying the phase current command of 13A under full load, 4 N·m. The SRM starts to run from standstill and it is keeping up until the average speed during 300 PWM cycles is 778 rpm. From Fig 5.10(a), the average flux-linkage error is approximately 1.12 % and the maximum flux-linkage error is approximately 13.65 %. The maximum flux-linkage error is slightly larger than that when applying the phase current of 9A under half load. It resulted from a lot of high frequency components of phase current around the unaligned position due to the higher rate of change of phase current generated when applying high current references. It is shown in Fig 5.10(b) that the estimated and actual rotor position and the position error between them are described. From Table 5.3, the average position error is approximately 0.43 deg and the maximum position error is approximately 1.64 deg. Fig 5.10(c) shows the estimated and actual speed and the speed error between them. From Table 5.3, the average speed error is approximately 2.17 rpm and the maximum speed error is approximately 16.14 rpm. It is noted from Fig 5.10 that the flux-linkage error increases around the unaligned and the position error increases right before phase commutation and during phase changeover as in previous simulations.

Fig 5.10 Simulation results at ω=778rpm and I^*=13A under full load, 4 N·m

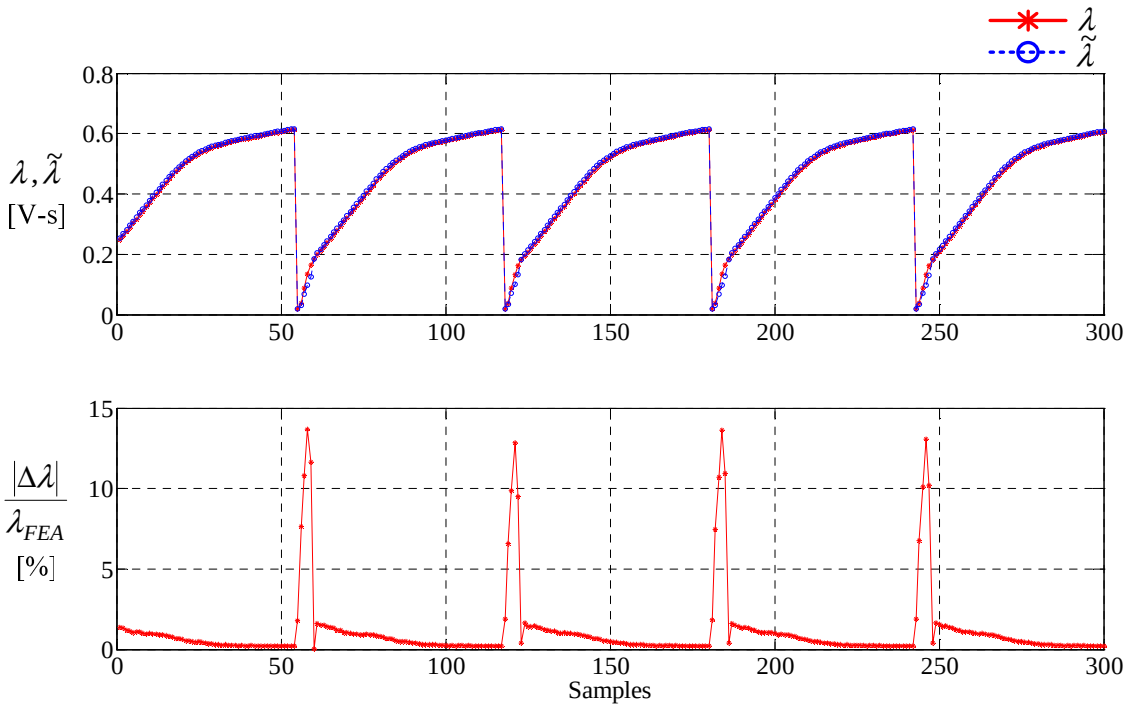

(a) Flux-linkage estimation

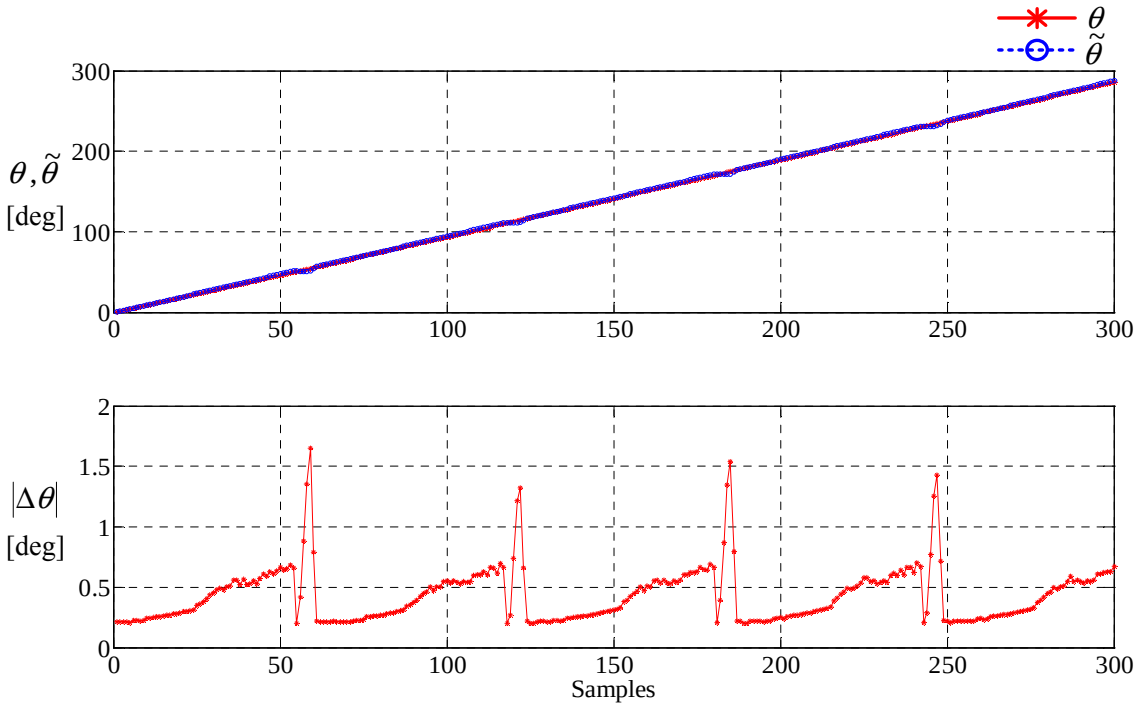

(b) Position estimation

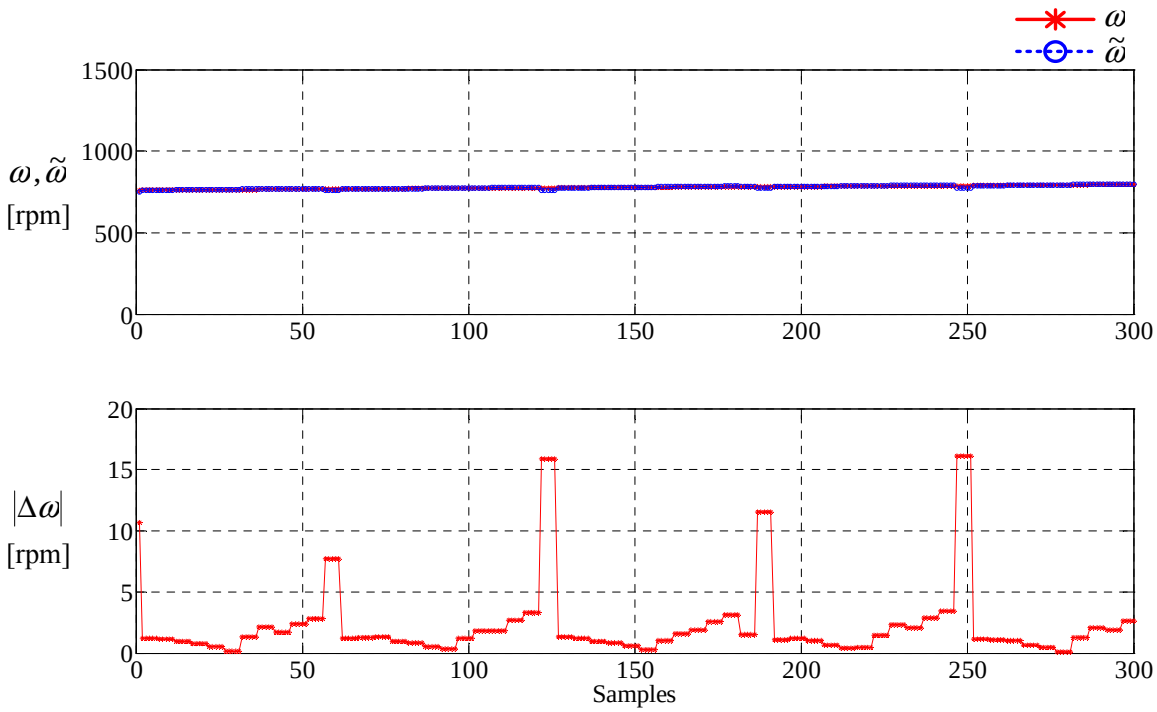

(c) Speed estimation

5.5 Dynamic Simulation Results Using Fast Fourier Transform

Position estimation using the first switching harmonics of phase voltage and current decomposed by FFT is also simulated at different current commands and under various loads. For each current command, the estimated and actual values of flux-linkage, rotor position, and speed are presented. Note that no speed control loop is included and the current command is the only external input of simulations. As mentioned in the previous section, the symmetrical PWM method with a fixed frequency (set at 5 kHz) is employed for dynamic current control. The asymmetric bridge converter under hard chopping mode is employed and it has the integration time step of 1 μs. After taking samples of phase current and voltage at regular time intervals, 1 μs, the FFT computation of a sequence of samples is accomplished to obtain the first switching harmonics of phase voltage and current every PWM cycle through Matlab's FFT function. The magnitudes and phase angles of the first switching harmonics of phase voltage and current are computed every PWM cycle through Matlab's ABS and ANGLE functions and by using them, the incremental inductance and flux-linkage are estimated every PWM cycle. Based on the estimated flux-linkage and phase current, the rotor position is estimated every PWM cycle from the relationship between flux-linkage and rotor position at given phase current. The estimated

rotor speed is filtered out with a EWMAF, referred as the first order IIR filter, at the sample rate of 1 kHz and filter coefficient of 0.95, resulting in increasing the degree of filtering. The EWMAF is chosen so that the most recent estimated speed is given more emphasis than older values as well as reflects better the state of the process in dynamic control systems. Voltage drops and switching transients of power electronic devices are negligible compared to the DC-link voltage and mechanical time constant of the motor, therefore, the switching devices are assumed to be ideal. The flow chart for dynamic simulations using FFT is represented in Fig 5.11.

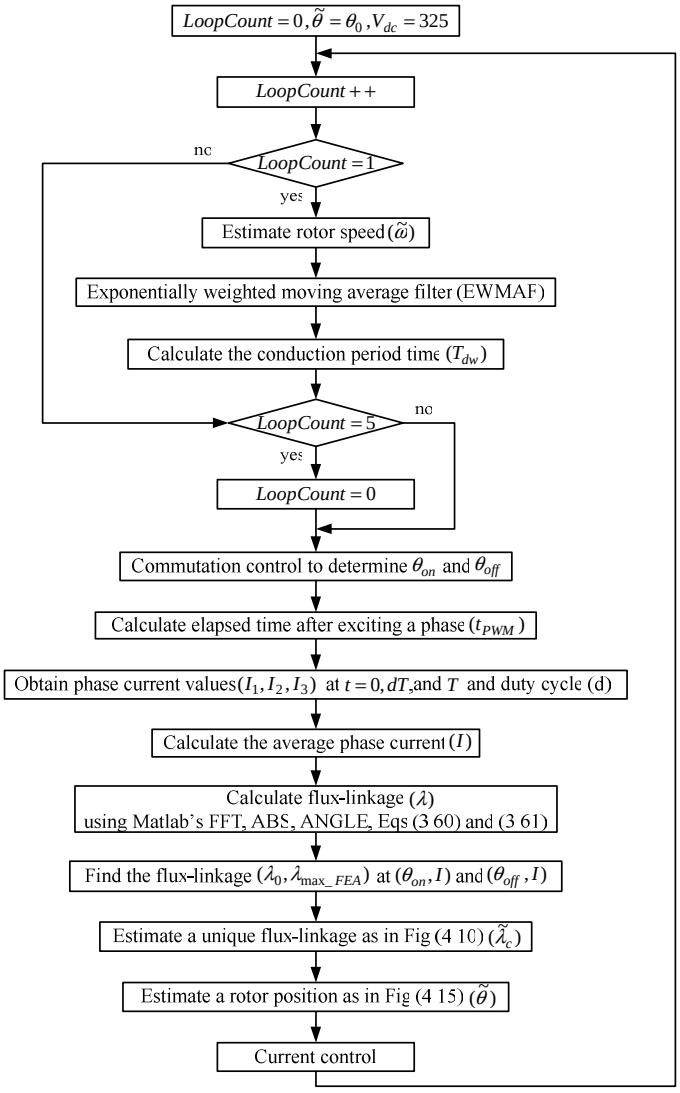

Fig 5.11 The flow chart for dynamic simulations using FFT

5.5.1 No Load Test

In order to validate the performance of the proposed position estimation scheme using FFT under no load, various dynamic simulations are performed at different phase current commands. SRM is initially at standstill with no load when a phase current command is applied and it runs with phase current regulation. Note that no speed loop is included. This test also provides the estimated and actual values of flux-linkage, rotor position, and speed for a PWM period. At the rate of 5 kHz, the estimated and actual values of flux-linkage, rotor position, and speed are obtained during 400 PWM cycles at different operating conditions such as transient startup as well as low and high speeds. The average and maximum values of the results obtained during 400 PWM cycles are presented in the following Table 5.4.

Table 5.4 Simulation results using FFT at various current commands under no load

Iref [A]	Average Speed [rpm]	Position Error [deg] $\lvert\Delta\theta\rvert$		Speed Error [rpm] $\lvert\Delta\omega\rvert$		Flux-linkage Error [%] $(\lvert\Delta\lambda\rvert / \lambda_{FEA}) * 100$	
		Average	Maximum	Average	Maximum	Average	Maximum
2	Startup	0.0062	0.0152	0.0629	0.1621	0.2254	2.3598
	240	0.1352	0.1575	0.1127	0.3303	0.3856	1.0093
	324	0.1863	0.2093	0.1001	0.4978	0.5120	1.3101
	549	0.3178	0.3405	0.0871	1.1982	0.8843	2.1913
	710	0.4113	0.4360	0.0854	0.8430	1.1216	2.8505
3	Startup	0.0031	0.0079	0.1737	0.3078	0.1281	4.6618
	499	0.3239	0.9031	0.3450	3.8829	0.8843	5.5768
	699	0.4356	0.6878	0.3083	5.7373	1.1615	5.1642
	965	0.5879	0.8077	0.3617	6.0887	1.5312	4.6199
	1133	0.6738	0.9088	0.4742	6.2624	1.7816	4.4957
4	Startup	0.0087	0.0209	0.2961	0.5074	0.0891	1.4535
	745	0.4254	1.4360	0.4639	9.6199	1.1340	8.8252
	988	0.5705	1.5611	0.5644	9.7513	1.4838	10.4247
	1212	0.6895	1.6168	0.9029	11.1730	1.7559	10.8173
5	Startup	0.0129	0.0332	0.4631	0.7687	0.0958	1.3158
	755	0.4578	1.8503	1.0923	14.4914	1.2120	11.0586
	1092	0.6407	2.1789	1.1748	16.5782	1.7013	11.6556
6	Startup	0.0126	0.0267	0.6962	1.3550	0.0946	1.9262
	897	0.3986	2.1473	0.9867	10.8062	1.1806	12.3796
	1360	0.6500	2.7719	1.8058	16.3356	1.9374	16.1274

Fig 5.12 shows the estimated and actual values of flux-linkage, rotor position, and speed at startup when applying the phase current command of 3A under no load. Fig 5.12(a) shows the estimated and actual flux-linkage given by FEA and the absolute values of the percentage errors between them. From Table 5.4, the average and maximum flux-linkage errors are approximately 0.11 % and 2.35 %, respectively. Fig 5.12(b) shows the estimated and actual rotor position and the position error between them. From Table 5.4, the average and maximum position errors are close to zero. Fig 5.12(c) shows the estimated and actual speed and the speed error between them. From Table 5.4, the average and maximum speed errors are approximately 0.17 rpm and 0.30 rpm, respectively. It can be noted from Fig 5.12 that the rotor position and speed error is almost zero even if the flux-linkage error is slightly larger right after startup. With known the initial rotor position at standstill, the estimated flux-linkage is lower than the flux-linkage at the initial position and given phase current. Hence the rotor position is estimated as the initial rotor position with the estimated flux-linkage at given phase current by using the characteristic of the prototype SRM that the rotor cannot rotate backward, discussed in Chapter 4.

Fig 5.12 Simulation results using FFT at startup and $I^* = 3A$ under no load

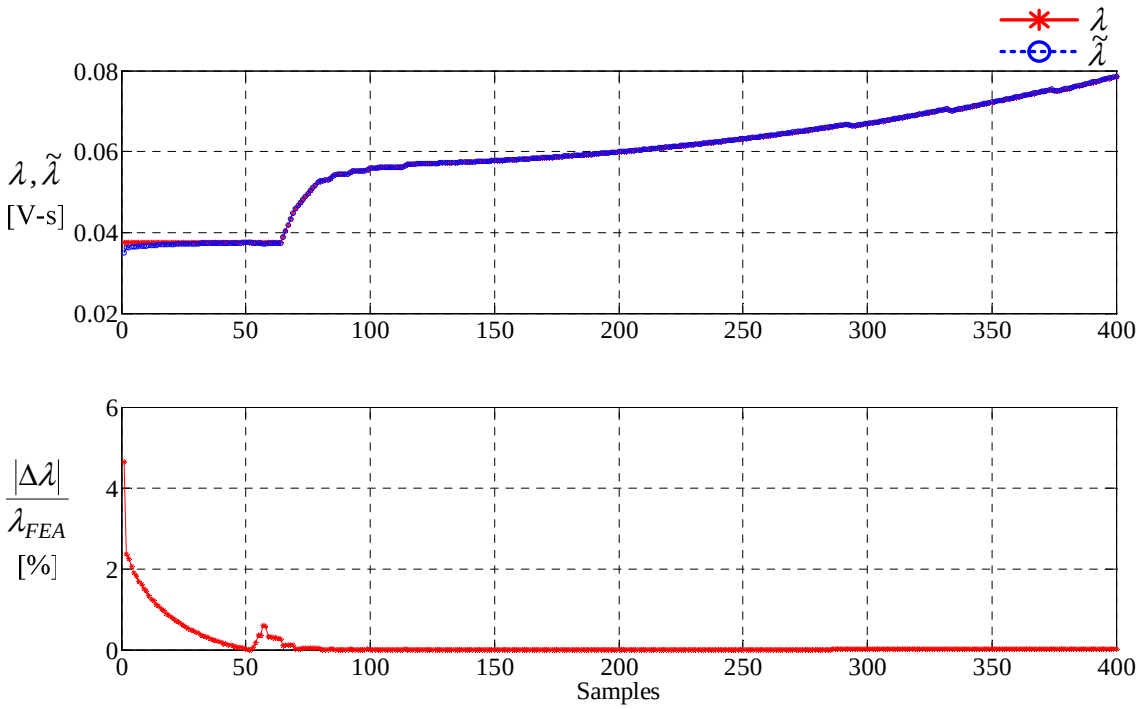

(a) Flux-linkage estimation

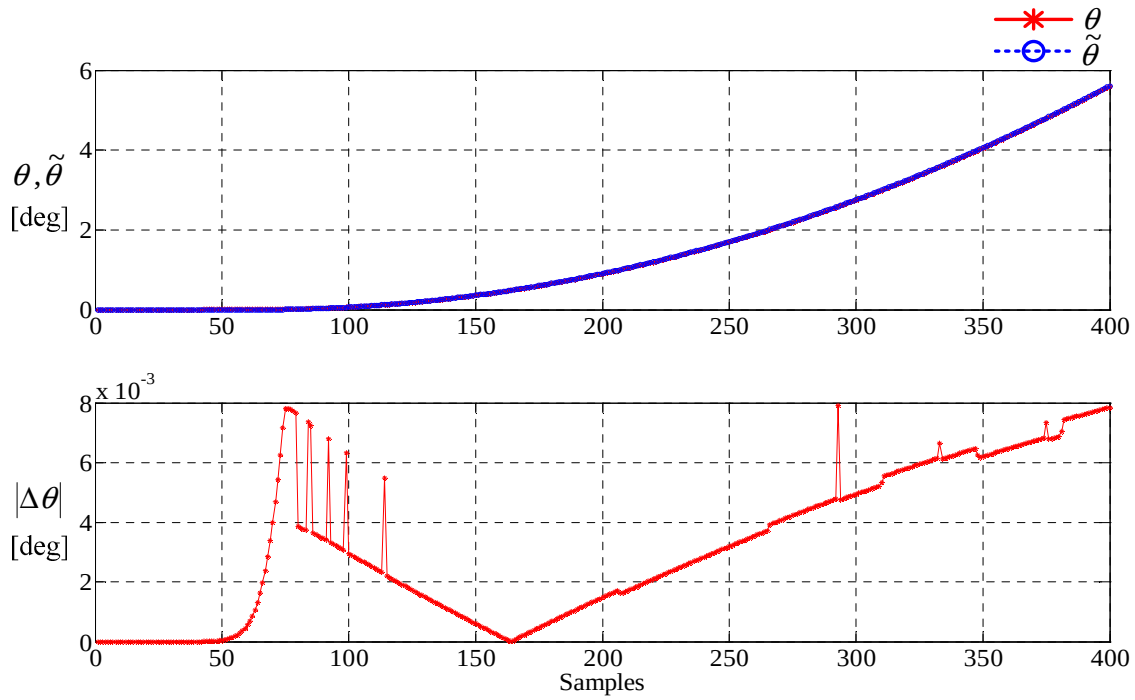

(b) Position estimation

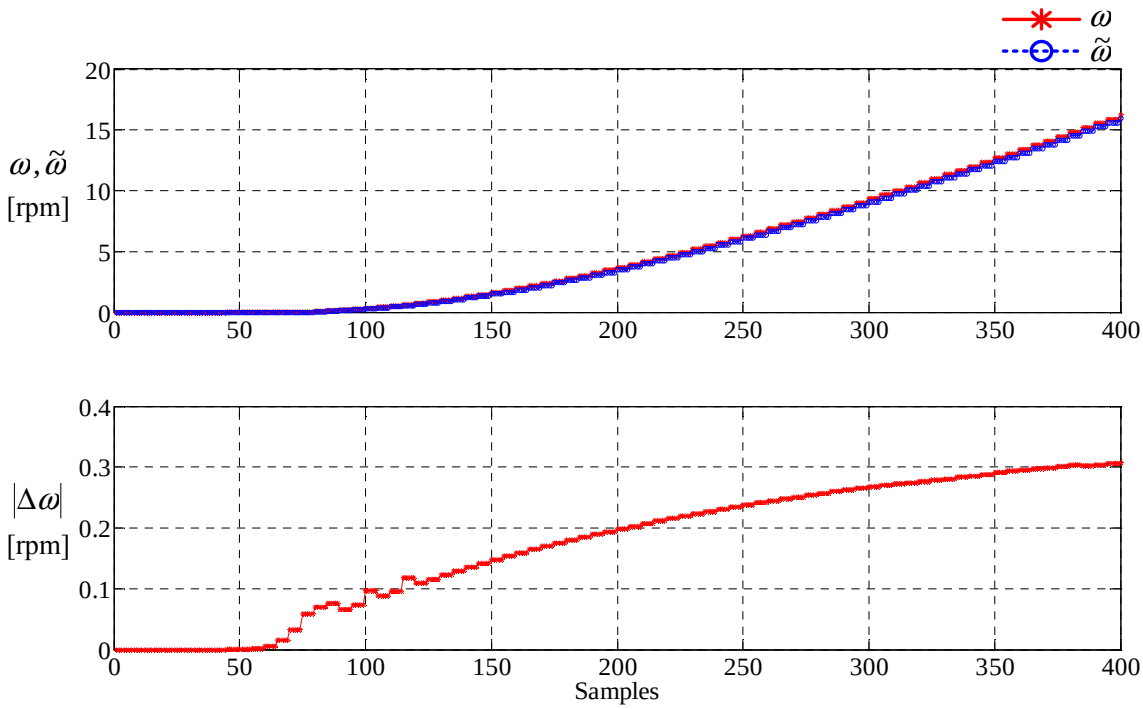

(c) Speed estimation

Fig 5.13 shows the estimated and actual values of flux-linkage, rotor position, and speed at high speed when applying the phase current command of 3A under no load. The SRM starts to run from standstill and it is keeping up until the average speed during 400 PWM cycles is 1133 rpm. Fig 5.13(a) shows the comparison of the estimated and actual flux-linkage given by FEA and the absolute values of the percentage errors between them. From Table 5.4, the average flux-linkage error is approximately 1.78 % and the maximum flux-linkage error is approximately 4.49 %. Based on the estimated flux-linkage and phase current, the rotor position is estimated every PWM cycle. Fig 5.13(b) shows the estimated and actual rotor position and the position error between them. From Table 5.4, the average position error is approximately 0.67 deg and the maximum position error is approximately 0.90 deg. Fig 5.13(c) shows the estimated and actual speed and the speed error between them. From Table 5.4, the average speed error is approximately 0.47 rpm and the maximum speed error is approximately 6.26 rpm. It can be seen from Fig 5.13 that the flux-linkage error increases around the unaligned position and the position error increases right before phase commutation and during phase changeover.

Fig 5.13 Simulation results using FFT at ω=1133rpm and $I^*=3A$ under no load

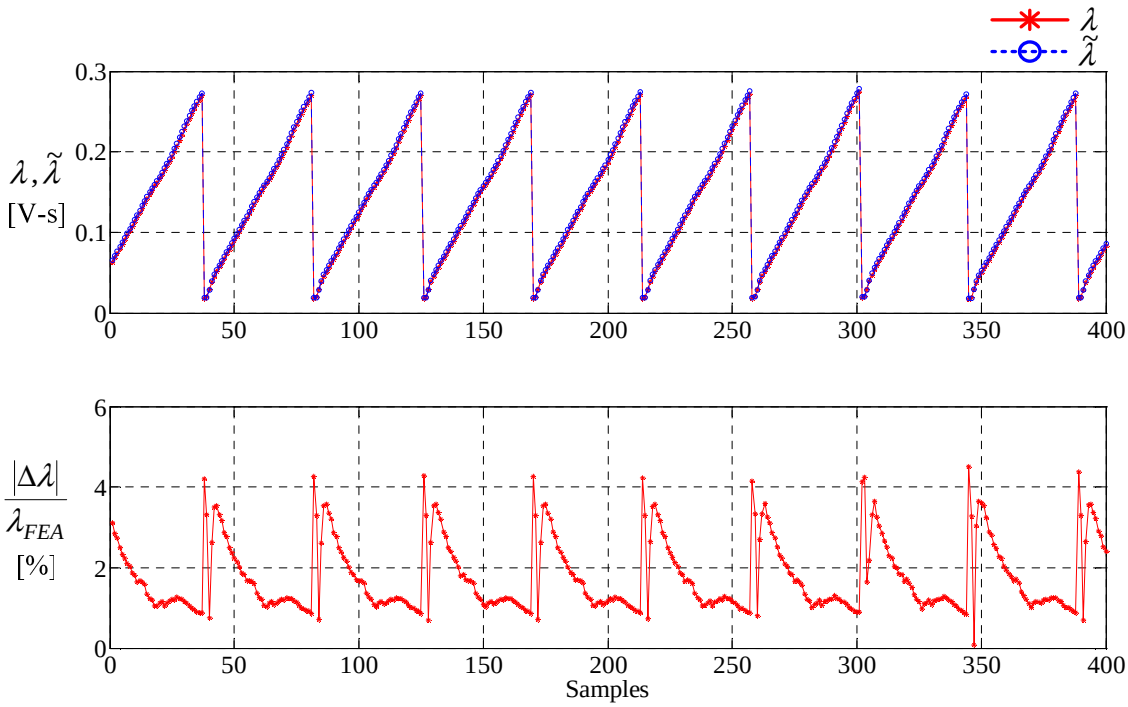

(a) Flux-linkage estimation

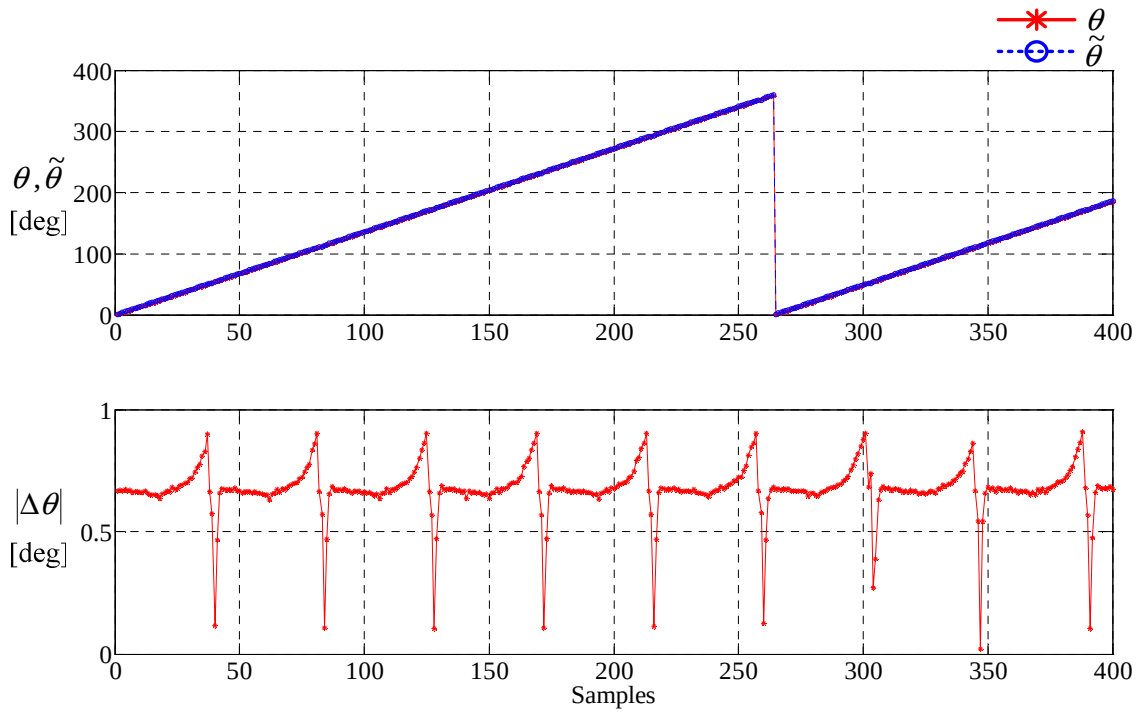

(b) Position estimation

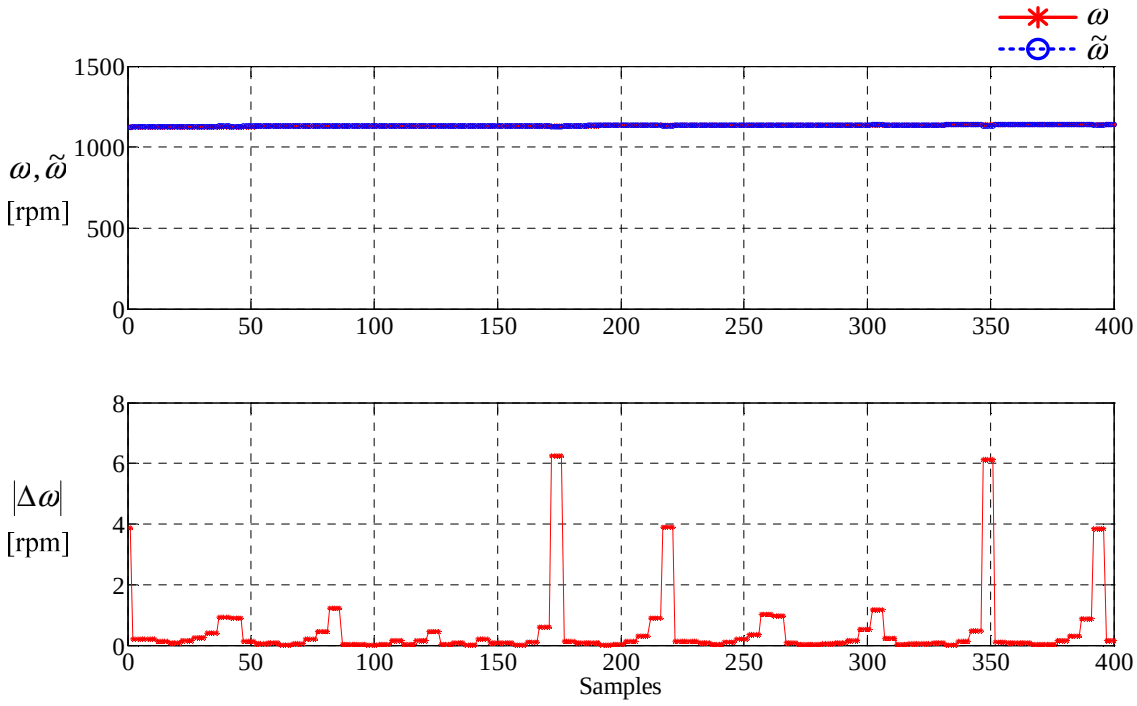

(c) Speed estimation

5.5.2 Load Test

In order to validate the performance of the proposed position estimation algorithm at different phase current commands under various loads, various dynamic simulations are performed. SRM is initially at standstill with various loads when a phase current command is applied and it runs with phase current regulation. Note that no speed loop is included. This test provides the results of the flux-linkage estimated from the incremental inductance estimated by the first switching harmonic of phase current and voltage using FFT, the rotor position estimated from the estimated flux-linkage and phase current by using a magnetization look-up table, and the rotor speed estimated by the derivative of the estimated rotor position with respect to time. At the rate of 5 kHz, the estimated and actual values of flux-linkage, rotor position, and speed are obtained during 300 PWM cycles at different operating conditions such as transient startup as well as low and high speeds. The average and maximum values of the results obtained during 300 PWM cycles are presented in the following Table 5.5. It can be observed from Table 5.5 that the estimated values satisfactorily track the actual values under loads.

Table 5.5 Simulation results using FFT at various current commands under various loads

Torque [N·m]	Iref [A]	Average Speed [rpm]	Position Error [deg] $\lvert\Delta\theta\rvert$		Speed Error [rpm] $\lvert\Delta\omega\rvert$		Flux-linkage Error [%] $(\lvert\Delta\lambda\rvert/\lambda_{FEA})*100$	
			Average	Maximum	Average	Maximum	Average	Maximum
1	7	845	0.3387	1.2054	1.5104	8.4918	1.2123	10.9599
2	9	926	0.3409	1.4029	1.3833	17.1263	1.1833	12.3852
3	11	892	0.2537	1.6964	1.8885	18.4599	1.0794	15.4845
4	13	820	0.1890	1.7476	1.6967	16.9927	1.0091	14.3954

Fig 5.14 shows the estimated and actual values of flux-linkage, rotor position, and speed when applying the phase current command of 9A under half load, 2 N·m. The SRM starts to run from standstill and it is keeping up until the average speed during 300 PWM cycles is 926 rpm. Fig 5.14(a) shows the estimated and actual flux-linkage and the absolute values of the percentage errors between them. From Table 5.5, the average and maximum flux-linkage errors are approximately 1.18 % and 12.38 %, respectively. Fig 5.14(b) shows the estimated and actual rotor position and the position error between them. From Table 5.5, the average and maximum position errors are approximately 0.34 deg and 1.40 deg, respectively. Fig 5.14(c) shows the estimated and actual speed and the speed error between them. From Table 5.5, the average and maximum speed errors are approximately 1.38 rpm and 17.12 rpm, respectively. It is noted form

Fig 5.14 that the position error increases right before phase commutation and during phase changeover due to saturation effects.

Fig 5.14 Simulation results at ω=926rpm and I^*=9A under half load, 2 N·m

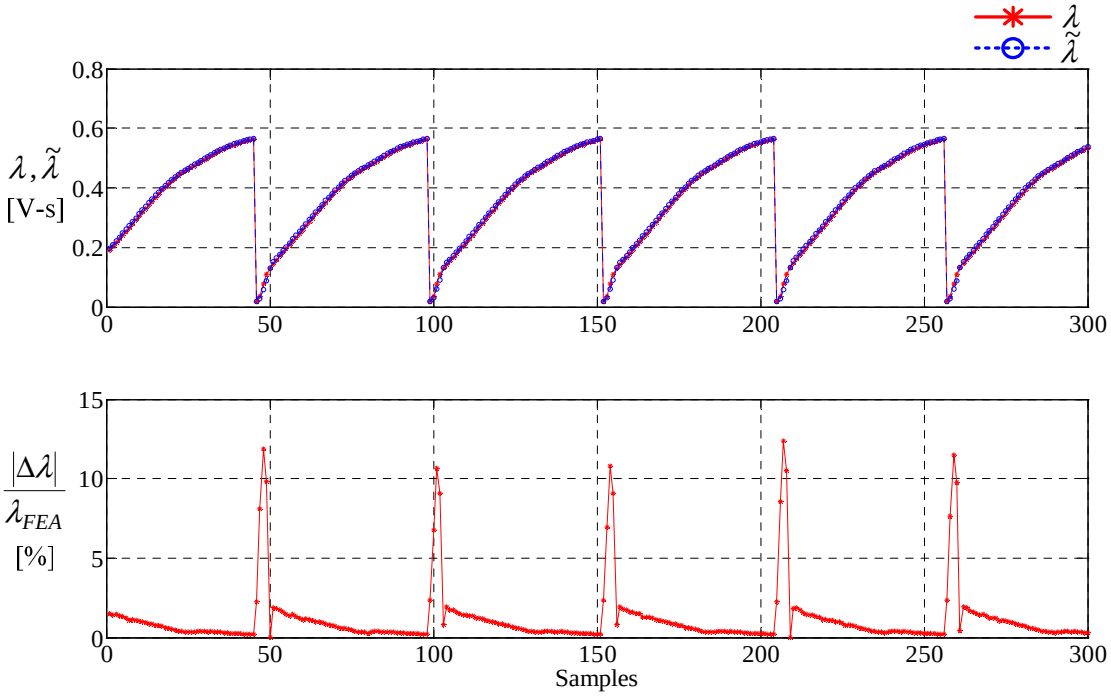

(a) Flux-linkage estimation

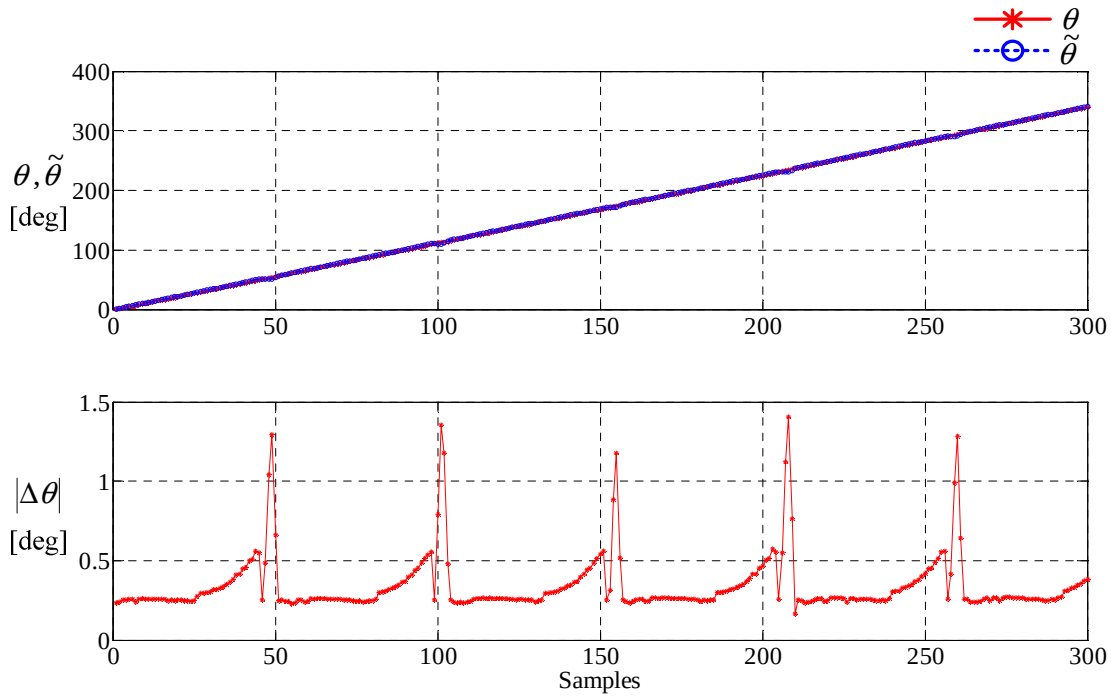

(b) Position estimation

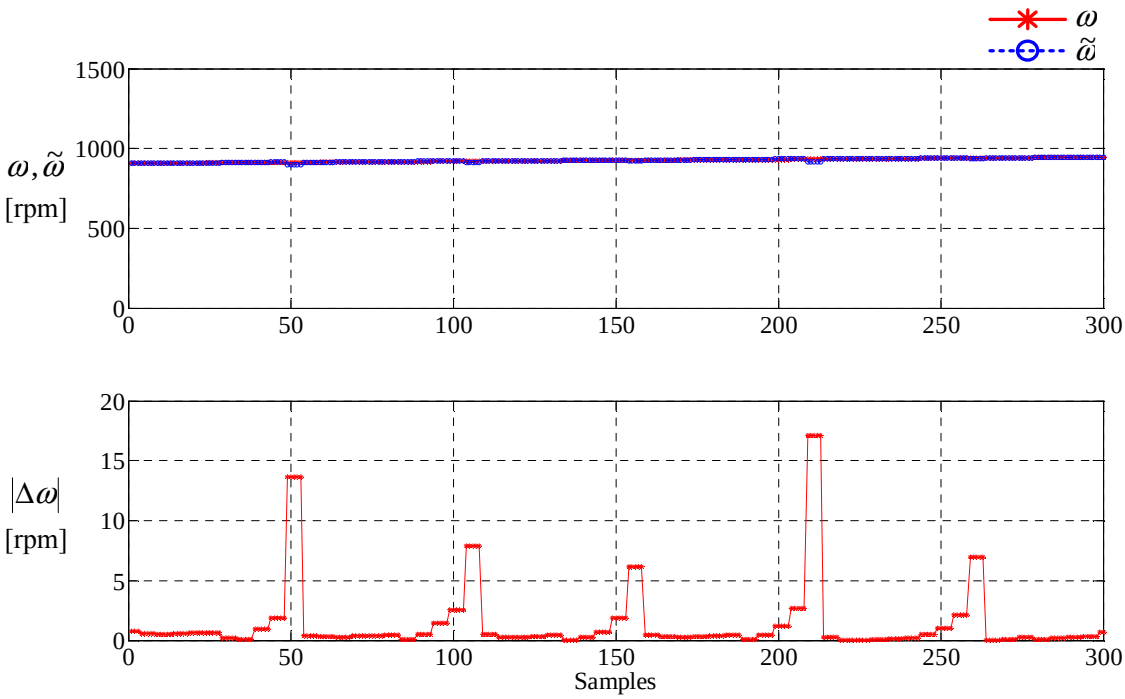

(c) Speed estimation

Fig 5.15 shows the estimated and actual values of flux-linkage, rotor position, and speed when applying the phase current command of 13A under full load, 4 N·m. The SRM starts to run from standstill and it is keeping up until the average speed during 300 PWM cycles is 820 rpm. Fig 5.15(a) shows that the estimated flux-linkage is compared with the actual flux-linkage given by FEA at the top and it shows the absolute values of the percentage errors between them as the error at the bottom. From Table 5.5, the average flux-linkage error is approximately 1.00 % and the maximum flux-linkage error is approximately 14.39 %. The error magnitudes are similar to those in the dynamic simulations using Fourier series. It is shown in Fig 5.15(b) that the estimated and actual rotor position and the position error between them and the average position error is approximately 0.18 deg and the maximum position error is approximately 1.74 deg. Fig 5.15(c) shows that the estimated and actual speed and the speed error between them and the average speed error is approximately 1.69 rpm and the maximum speed error is approximately 16.99 rpm. It can be seen from Fig 5.15 that the flux-linkage error increases around the unaligned position due to the higher gradient of phase current around the unaligned position and the position error increases right before phase commutation and during phase changeover due to the saturation effects.

Fig 5.15 Simulation results at ω=820rpm and I^* =13A under full load, 4 N·m

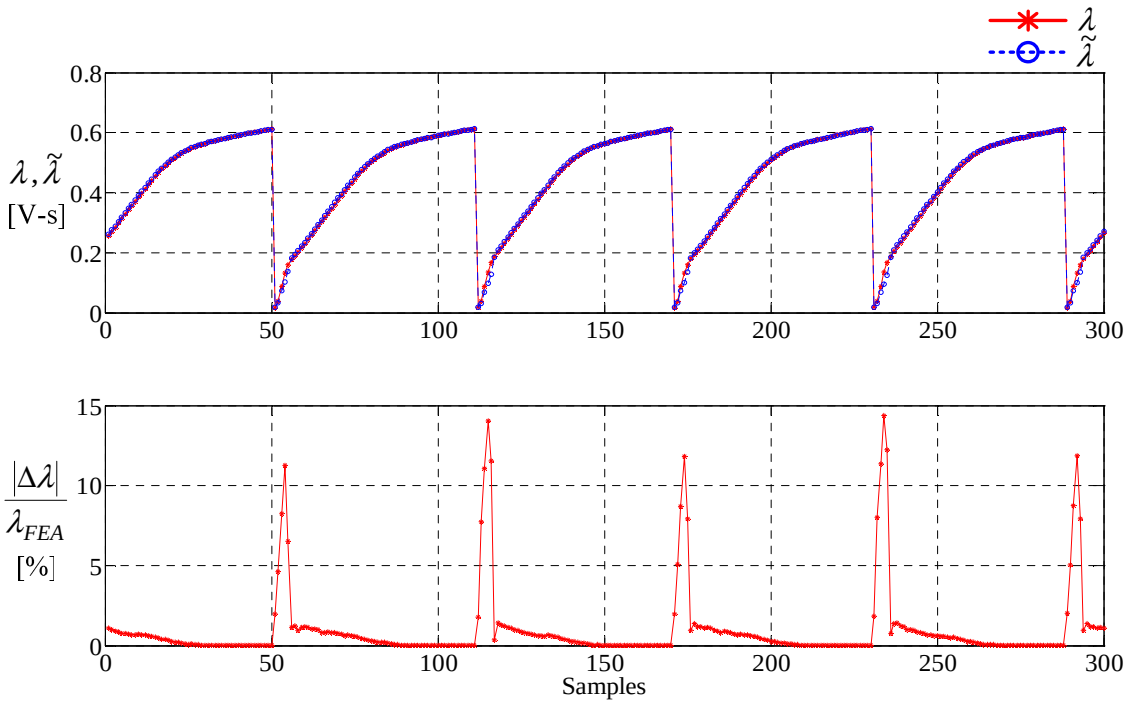

(a) Flux-linkage estimation

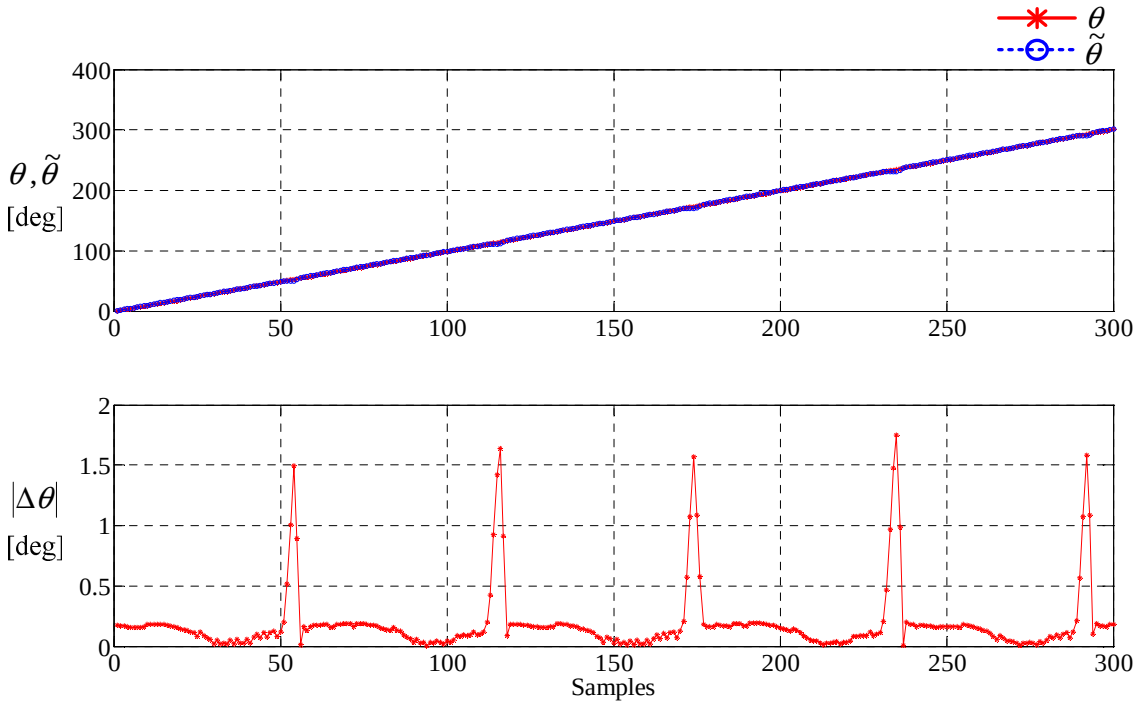

(b) Position estimation

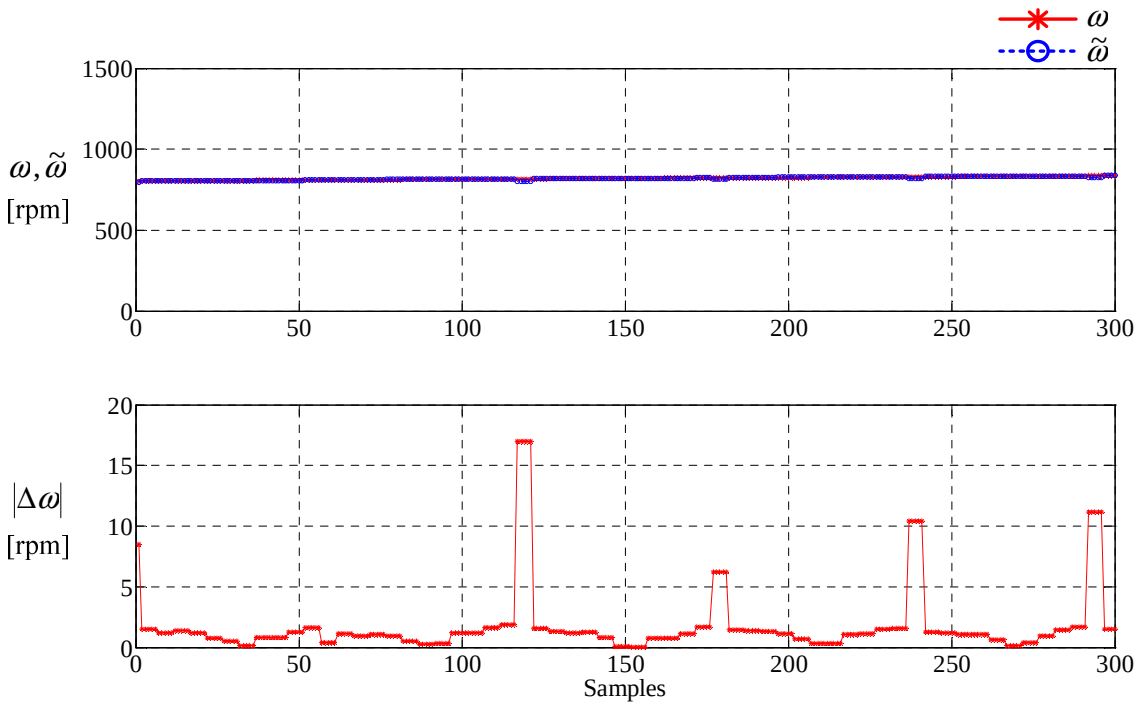

(c) Speed estimation

5.6 Analysis

In order to have a high performance practical position estimation algorithm, it is essential to have reliable characteristics about the accuracy and resolution of the estimated rotor position. In this research, detailed analysis of the proposed position estimation method using Fourier analysis has been carried out from standstill and under various loads in order to estimate these attributes with the dynamic simulation. The SRM has been started up from zero speed at different current commands under various loads and it has run with phase current regulation. The loads of 25%, 50%, 75%, 100% of the rated load, 4 N·m, have been applied to the SRM. Note that in the simulations, no speed control loop is included.

Each phase is turned ON at 50° (mechanical angle) from its unaligned region and turned OFF at 110° (mechanical angle) from its aligned region. Phase voltage and current of the excited phase are used for rotor position estimation during its conduction period. The speed range is defined as: when it is lower than 1,000 rpm, it is referred as low speed, while it is higher than 1,000 rpm, then it is referred as high speed.

On the other hand, at the current command of 2A, the rotor speed does not exceed 800 rpm in the simulations since the positive torque generated during the conduction period is not

enough to increase the rotor speed. Thereby, at the current command of 2A, it is referred as high speed when the rotor speed is higher than 700 rpm.

The simulation results under no load are summarized in Table 5.6.

Table 5.6 Comparisons of simulation results under no load

Iref [A]	Speed [rpm]	**Fourier series**						**Fast Fourier Transform**					
		Position Error [deg]		Speed Error [rpm]		Flux-linkage Error [%]		Position Error [deg]		Speed Error [rpm]		Flux-linkage Error [%]	
		Avg.	Max.	Avg.	Max.	Avg.	Max.	Avg.	Max.	Avg.	Max.	Avg.	Max.
2	Startup	0.15	0.82	0.47	4.10	0.71	3.98	0.01	0.02	0.06	0.16	0.22	2.35
	Low	0.36	0.50	0.24	1.32	0.95	1.85	0.21	0.23	0.10	0.67	0.60	1.50
	High	0.57	0.70	0.26	1.62	1.47	3.20	0.41	0.43	0.08	0.84	1.12	2.85
3	Startup	0.11	0.82	0.34	3.64	0.51	3.98	0.01	0.02	0.17	0.30	0.12	4.66
	Low	0.61	1.03	0.59	6.10	1.55	5.41	0.45	0.80	0.34	5.24	1.20	5.12
	High	0.84	1.26	0.81	7.54	2.14	4.75	0.67	0.91	0.47	6.26	1.78	4.49
4	Startup	0.11	0.61	0.31	2.61	0.40	2.54	0.01	0.02	0.29	0.50	0.08	1.45
	Low	0.66	1.45	0.50	8.85	1.60	9.66	0.50	1.50	0.51	9.69	1.30	9.62
	High	0.86	1.61	0.93	12.00	2.05	11.45	0.69	1.62	0.90	11.17	1.76	10.82
5	Startup	0.09	0.37	0.38	1.99	0.37	1.78	0.01	0.03	0.46	0.76	0.09	1.31
	Low	0.60	1.75	1.50	15.52	1.49	11.43	0.46	1.85	1.09	14.49	1.21	11.06
	High	0.81	2.28	2.03	19.33	2.06	11.91	0.64	2.18	1.17	16.58	1.70	11.66
6	Startup	0.10	0.29	0.53	1.56	0.33	1.78	0.01	0.02	0.69	1.35	0.10	1.92
	Low	0.55	2.14	0.98	11.89	1.43	12.37	0.40	2.15	0.99	10.81	1.18	12.38
	High	0.78	2.74	1.58	17.94	2.02	16.07	0.65	2.77	1.81	16.34	1.94	16.13

Table 5.6 shows the average and maximum errors of flux-linkage, rotor position, and speed obtained during 400 PWM cycles at transient startup and low and high speeds. The maximum errors of flux-linkage, rotor position, and speed are approximately 16 %, 3 deg, and 19 rpm, respectively. The speed tolerance with the maximum speed error is approximately 2 %.

Table 5.7 shows the summary of the simulation results executed at different current commands under various loads, where the average and maximum values of flux-linkage, rotor position, and speed obtained during 300 PWM cycles are presented. The average actual rotor speed obtained during 300 PWM cycles is approximately 850 rpm. Table 5.7 shows that the maximum errors of flux-linkage, rotor position and speed are approximately 15 %, 2 deg, and 18 rpm, respectively. The speed tolerance with the maximum speed error is approximately 2 %.

Table 5.7 Comparisons of simulation results under various loads

Torque [N·m]	Iref [A]	**Fourier series**						**Fast Fourier Transform**					
		Position Error [deg]		Speed Error [rpm]		Flux-linkage Error [%]		Position Error [deg]		Speed Error [rpm]		Flux-linkage Error [%]	
		Avg.	Max.	Avg.	Max.	Avg.	Max.	Avg.	Max.	Avg.	Max.	Avg.	Max.
1	7	0.46	1.45	2.16	11.64	1.51	11.93	0.33	1.20	1.51	8.49	1.21	10.95
2	9	0.48	1.27	3.60	14.38	1.40	11.22	0.34	1.40	1.38	17.12	1.18	12.38
3	11	0.47	1.61	2.57	18.28	1.30	15.22	0.25	1.69	1.88	18.45	1.07	15.48
4	13	0.43	1.64	2.17	16.14	1.12	13.65	0.18	1.74	1.69	16.99	1.00	14.39

It is demonstrated in these simulations that the proposed position estimation algorithm is reliably fulfilled at startup and low and high speeds under various loads. It is capable of providing an accurate position estimation to overcome the disadvantages of requiring position sensors.

It should be noted from Figs 5.7 to 5.10 and from Figs 5.10 to 5.12 that the error between estimated and actual values of flux-linkage, rotor position, and speed increases around the unaligned position or right before phase commutation. The maximum absolute average percentage error between the estimated and actual flux-linkages is approximately 16 %, but the significant differences occur at the beginning of the phase conduction period, namely, around the unaligned position, which yields inaccurate results for the position and speed estimation. It can be observed that the error between estimated and actual flux-linkages gives relatively accurate results as the rotor pole is moving towards the aligned position.

As shown in Fig 5.3, the rate of change of flux-linkage with respect to the position around the unaligned position is lower than that around the aligned position, thus the phase voltage applied to the winding is greater and the rate of change of phase current in the unaligned position is eventually greater, assuming the speed is constant during operation. As the rate of change of phase current is higher, the high frequency components at phase current in a PWM period increase and thus phase current in a PWM period cannot be satisfactorily represented as the fundamental switching frequency component. Consequently, the flux-linkage error around the unaligned position is larger than the flux-linkage error around the aligned position.

On the other hand, the error between estimated and actual position is slightly larger right before phase current commutation and during phase changeover due to saturation effects. The rotor position can be estimated using the estimated flux-linkage and phase current in a PWM period. Indeed, the magnetic material of the machine saturates for different current levels and

thereby the slope of inductance or flux-linkage can be varying with respect to the magnitude of the excitation current. That is to say, the rate of change of inductance with respect to phase current is not zero in saturated region and thus varies with respect to the rotor position and the magnitude of phase current.

On the other hand, in unsaturated region, the rate of change of inductance with respect to phase current is almost zero and thereby the slope of inductance or flux-linkage is closely constant with respect to the position regardless of the magnitude of phase current. Hence the estimated position can be altered in saturated region according to the phase current value selected from the triangular current waveform in a PWM period. Therefore, in this research, the average value of phase current in a PWM period is employed to reduce the position error being able to be generated due to the saturation effect.

In the proposed position estimation method using Fourier analysis, the rotor position is estimated with the measurement of active phase voltage and current in a PWM period. This means that the resolution of the estimated rotor position is directly susceptible to the PWM period, which is the reciprocal of PWM switching frequency. Assuming that the variation of the rotor speed is small in a phase conduction period, the resolution of the estimated rotor position per PWM period increases as the PWM period decreases. That is to say, the resolution of the estimated rotor position is proportional to the PWM switching frequency.

In addition, the rotor speed affects the resolution of estimated rotor position. Assuming that phase conduction period is not varying regardless of the rotor speed, the number of PWM pulses during phase conduction period must be diminished as the rotor speed increases. While the rotor speed diminishes, the number of PWM pulses during phase conduction period must be increased. Assuming that phase conduction period is 60° and PWM switching frequency is 5 kHz, phase conduction period time at 1000 rpm can be obtained as,

$$\frac{1}{1000[rev/\min]\times\frac{1}{60}[\min/\sec]\times 6[conduction/rev]}=\frac{1}{100}[\sec/conduction] \tag{5.8}$$

The number of PWM pulses per conduction period can be obtained by dividing the conduction period by PWM period and it can be obtained as,

$$\frac{1}{100}[\sec/conduction]/200[\mu\sec/PWM]=50[PWM/condcution] \tag{5.9}$$

where 50 PWM pulses can be obtained for a conduction period if the PWM switching frequency is 5 kHz. Thereby, the resolution of the estimated rotor position in a PWM period can be calculated as,

$$60[^\circ / condcution] / 50[PWM / condcution] = 1.2[^\circ / PWM] \tag{5.10}$$

Consequently, the estimated rotor position has theoretical resolution of 1.2° per PWM period while the rotor speed is 1000 rpm. With this relation between the resolution of the estimated rotor position and speed, the resolution of the estimated rotor position per PWM period decreases according to the increase of the rotor speed and it becomes 3.6° at the rated speed of 3,000 rpm for the prototype SRM.

5.7 Conclusions

In this chapter, verification of the proposed position estimation algorithm has been achieved using a novel two-phase SRM with 6 stator poles and 3 rotor poles and having a flux-reversal-free-stator [80, 81]. Detailed analysis of the proposed position estimation method has been carried out from standstill and under various loads in order to estimate these attributes with the dynamic simulation. The symmetrical PWM method with a fixed frequency (5 kHz) is employed for dynamic current control. The inclusion of saturation limits on the PI integrator is embedded in the current controller to provide an anti-windup functionality. The estimated rotor speed is filtered out by an exponentially weighted moving average filter (EWMAF). The SRM has been operated from zero speed at different current commands under various loads and has run with phase current regulation. The loads of 25%, 50%, 75%, and 100% of the rated load, 4 N·m, have been applied to the SRM. The following are believed to be original contributions of this chapter:

1) Position estimation by *Fourier series* development of phase voltage and current waveforms for a PWM cycle has been analyzed and validated through dynamic simulations at different current commands and under various loads.
2) Position estimation by *FFT* development of phase voltage and current waveforms for a PWM cycle has been analyzed and validated through dynamic simulations at different current commands and under various loads.
3) Excellent correlation of dynamic simulation results by using between Fourier series and FFT has confirmed the validity of the proposed position estimation method.

4) The proposed position estimation method has successfully performed under different operating conditions such as transient startup and low and high speeds.

It is demonstrated in these simulations that the proposed position estimation algorithm is reliable at startup and low and high speeds under various loads. It is capable of providing an accurate position estimation to overcome the disadvantages of position sensors.

CHAPTER 6 EXPERIMENTAL EVALUATION OF POSITION ESTIMATION USING FOURIER ANALYSIS

6.1 Introduction

In the previous chapter, the performance of the proposed position estimation method was verified with comprehensive dynamic simulations under different current commands and various loads. Experimental evaluation of the proposed position estimation method is performed in this chapter. Comprehensive sets of experiments are executed with different current commands under various loads. The SRM is operated at standstill with various loads; 25%, 50%, 75%, and 100% of the rated load, 4 N·m. The estimated and actual values of the flux-linkage, rotor position and speed are compared in a PWM period. Experimental results are analyzed and correlation between dynamic simulations and experiments is provided.

6.2 Experimental Setup

The implementation of the proposed estimation algorithm using Fourier analysis is accomplished by a classical asymmetric bridge converter. A 16-bit DSP controller of Texas Instruments is employed in order to control the converter. The proposed position estimation algorithm is implemented in C-language in the DSP controller. The magnetization profile of flux-linkage vs. position vs. phase current is stored into a SARAM (single-access RAM) for a faster access and it is used with measured phase current for estimating the rotor position every PWM cycle.

Phase current and DC bus voltage from which an average phase voltage is calculated with a PWM duty cycle are fed to the DSP through a multi-channel ADC with 12-bit resolution and 80 ns conversion rate. These signals are sampled to calculate the first switching harmonic of phase voltage and current. For measuring phase current in the position estimation scheme using Fourier series, 6 points are sampled in a PWM cycle and then phase current values at the instant of turn-on and turn-off of switching devices are calculated by using a linear least squares (LLS) fitting algorithm.

On the other hand, in the position estimation scheme using FFT, 50 points are sampled at a sampling rate of 250 kHz in a PWM cycle and they are used for calculating the first switching harmonic of phase voltage and current. 3-phase AC power supply is fed to a full-bridge rectifier and the full voltage across the DC link capacitor is 325 V. The duty ratio of PWM chopper is controlled by a PI current controller with anti-windup functionality. Gains of the PI controller are calculated in Appendix A. A rotary encoder with the resolution of 1024 [pulses/rev] is coupled to the rotor shaft and the actual rotor position is provided using this encoder. It is used for evaluating the accuracy of the estimated rotor position.

The accuracy of the estimated rotor position in experiments is also compared with the simulation results in order to evaluate the correlation between them. 2.2 hp, two-phase 6/3 SRM is loaded using a separately excited DC generator coupled to its shaft and different loads are set by changing a load resistance through sliding a knob of a rheostat. The experimental SRM drive system is shown in Fig 6.1.

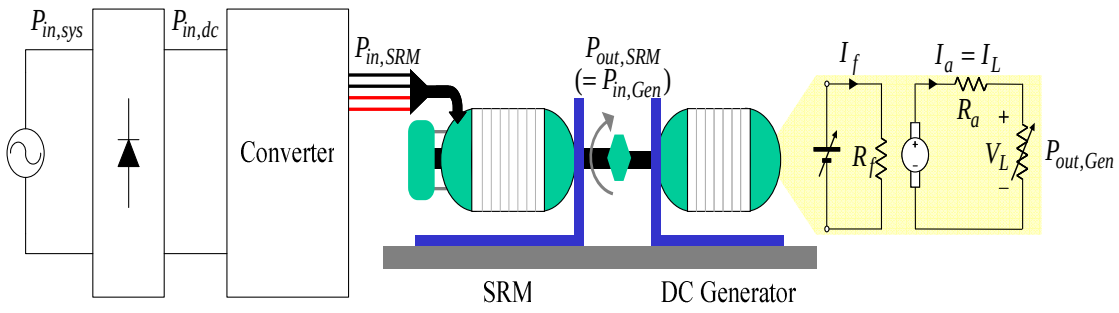

Fig 6.1 Experimental setup

6.3 Experimental Evaluation of Fourier Series-Based Algorithm

To evaluate the performance of the proposed position estimation method using Fourier series, several experiments at different currents commands have been executed under various loads. For each current command, the estimated and actual values of flux-linkage, rotor position, and speed are presented in the following subsections. Note that no speed control loop is included. In experiments, the asymmetrical PWM method with a fixed frequency (set at 5 kHz) is employed for dynamic current control. The inclusion of saturation limits on the PI integrator is embedded in the current control loop to provide an anti-windup functionality. The asymmetric bridge converter is employed to apply a phase voltage in a hard-chopping mode to increase the

rate of the change of phase current in a PWM period. 6 samples of phase current and 6 samples of DC bus voltage are taken with the same ADC trigger signals. From the sampled DC bus voltage and the duty cycle provided from the current control loop, average DC bus voltages during turn ON and turn OFF times are calculated. Hence, accurate DC bus voltages in a PWM period can be obtained.

From the sampled phase current and LLS fitting algorithm, the slopes of phase current during turn ON and turn OFF times are calculated and thereafter three phase current values at $t = 0$, dT, and T are calculated, where d is the PWM duty cycle and T is the PWM period. Based on these average DC bus voltages and three phase current values in a PWM period, the flux-linkage is estimated. Discrete magnetic data sets of three dimensional relationships between flux-linkage vs. current vs. position are obtained from FEA and flux-linkage values are stored into the two dimensional lookup table with phase current for row and rotor position for column.

By using linear interpolation in the two-dimensional flux-linkage lookup table with the estimated flux-linkage and average phase current, the rotor position is estimated. The rotor speed estimated by the derivative of the estimated rotor position is filtered out by using an exponentially weighted moving average filter (EWMAF), which is called the first order IIR filter, at the sample rate of 1 kHz and filter coefficient of 0.9, resulting in increasing the degree of filtering. The EWMAF is chosen because the most recent estimated speed is given more emphasis than older values as well as reflects better the state of the process in dynamic control systems. Different loads are applied to the SRM from startup by using a separately excited DC generator. The flow chart for experiments using Fourier series is represented in Fig 6.2.

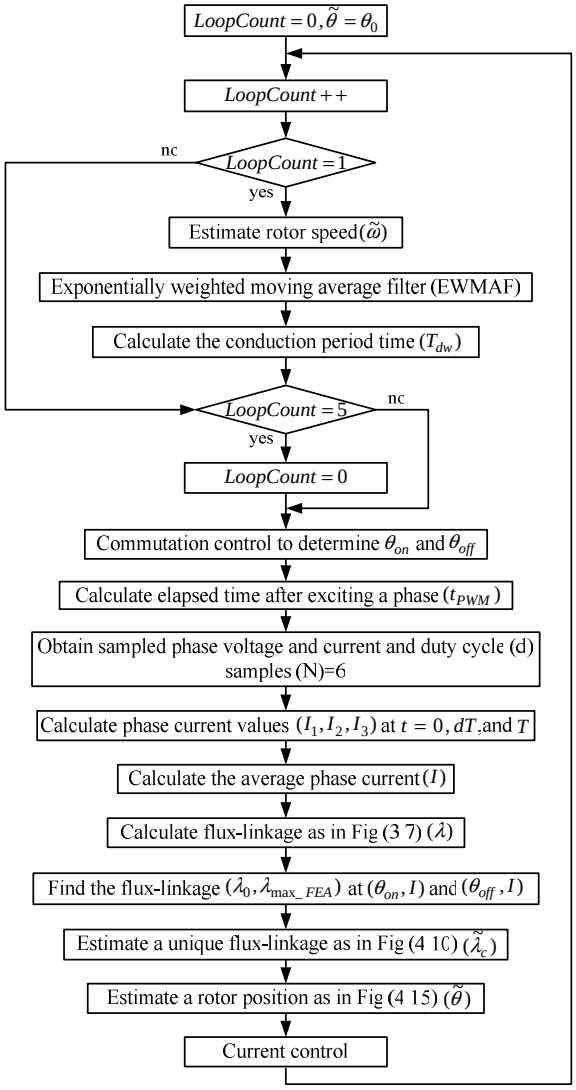

Fig 6.2 The flow chart for experiments using Fourier series

6.3.1 No Load Test

With the experimental setup described in Fig 6.1, the proposed position estimation scheme using Fourier series is performed at different phase current commands under no load. The SRM is initially at standstill with no load when a phase current command is applied to the SRM and it runs with phase current regulation. Note that no speed control loop is included. This test provides the results of the flux-linkage estimated from the incremental inductance, the rotor position estimated from the estimated flux-linkage and given phase current by looking up the magnetization table, and the rotor speed estimated by the derivative of the estimated rotor position with respect to time. At the rate of 5 kHz, the estimated and actual values of flux-

linkage, rotor position, and speed are obtained during 400 PWM cycles at different operating conditions such as transient startup as well as low and high speeds. The number of PWM cycles is determined by the available memory space of the DSP controller [84]. The average and maximum values of the results obtained during 400 PWM cycles are summarized in Table 6.1.

Table 6.1 Experimental results using Fourier series at various current commands under no load

Iref [A]	Average Speed [rpm]	Position Error [deg] $\lvert\Delta\theta\rvert$		Speed Error [rpm] $\lvert\Delta\omega\rvert$		Flux-linkage Error [%] $(\lvert\Delta\lambda\rvert / \lambda_{FEA}) * 100$	
		Average	Maximum	Average	Maximum	Average	Maximum
2	Startup	0.1150	0.4785	0.9509	3.4737	0.6788	2.5683
	230	0.1201	0.4020	1.6594	5.4490	0.3974	3.6676
	308	0.1632	0.5493	1.8519	9.0424	0.5267	4.5747
	566	0.2257	1.3379	3.0344	10.7069	1.1366	11.5844
	757	0.4174	2.0176	4.1957	18.3642	1.9383	16.2753
3	Startup	0.2625	0.5711	1.2683	3.5708	1.3729	2.8413
	475	0.2705	0.9742	2.8452	15.5190	0.9234	8.9759
	660	0.2679	1.4980	3.3973	15.3150	1.4834	11.8887
	921	0.4897	1.2801	5.0940	15.7720	2.3991	14.9209
	1111	0.5336	1.6401	6.1007	29.7714	2.3791	16.8226
4	Startup	0.5351	1.0048	2.1523	5.5742	2.4448	4.2587
	683	0.2450	2.0015	3.7208	17.5003	1.0060	17.7031
	951	0.2950	1.3446	4.5094	23.4027	1.4075	15.3196
	1156	0.4131	1.6866	6.5342	21.7721	2.0583	17.3868
5	Startup	0.7518	1.2863	2.9198	6.4981	2.9743	5.1924
	702	0.3037	0.8128	4.4372	18.6855	1.2576	11.3145
	1051	0.4081	1.4386	5.4785	17.1675	1.9649	16.8606
6	Startup	0.8171	1.4228	3.4317	8.4019	3.0109	5.8137
	854	0.4195	1.2017	6.1064	22.7399	1.8164	13.3203
	1266	0.5488	1.9037	6.8371	23.6163	2.7170	18.6364

Fig 6.3 shows the estimated and actual values of flux-linkage, rotor position and speed at startup when applying the phase current command of 3A under no load. These values are obtained every PWM period. The rotor position set to zero at the aligned position. Fig 6.3(a) shows the estimated and actual flux-linkage and the absolute values of the percentage errors between them. From Table 6.1, the average flux-linkage error is approximately 1.37 % and the maximum flux-linkage error is approximately 2.84 %. Fig 6.3(b) shows the estimated and actual position error and the position error between them. From Table 6.1, the average position error is approximately 0.26 deg and the maximum position error is approximately 0.57 deg. Fig 6.3(c) shows the estimated and actual rotor speed and the error between them. From Table 6.1, the average speed error is approximately 1.26 rpm and the maximum speed error is approximately

3.57 rpm. It can be observed that the proposed position estimation scheme using Fourier series works reliably at startup under no load.

Fig 6.3 Experimental results using Fourier series at startup and $I^* = 3A$ under no load

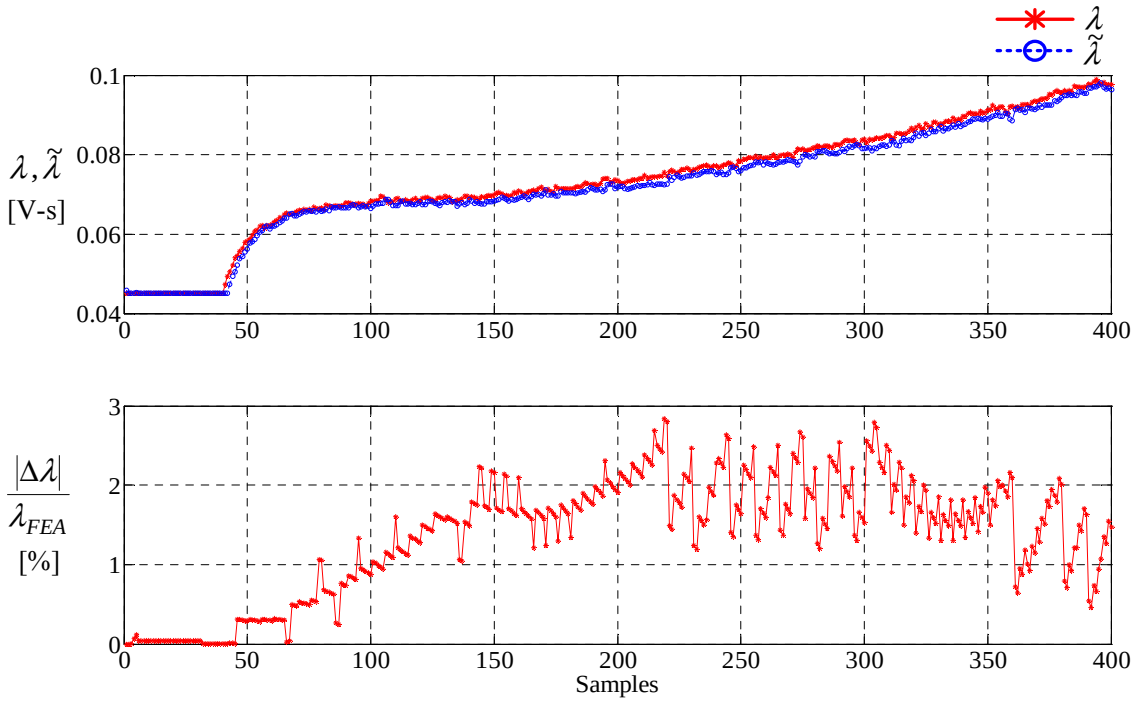

(a) Flux-linkage estimation

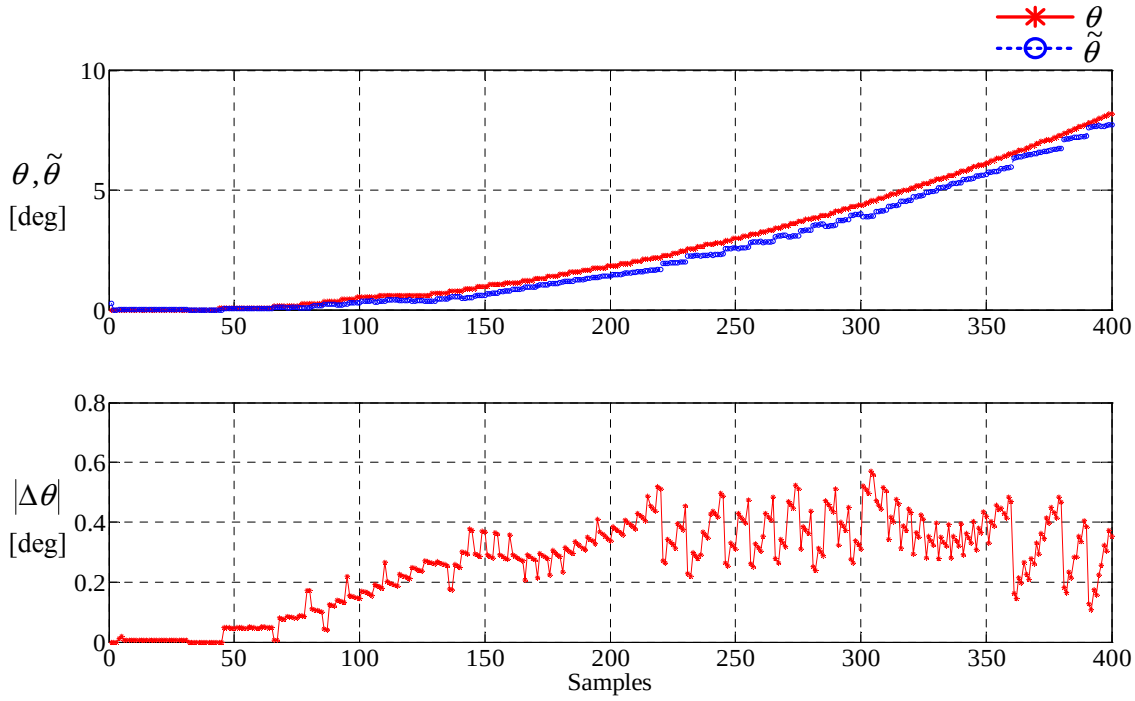

(b) Position estimation

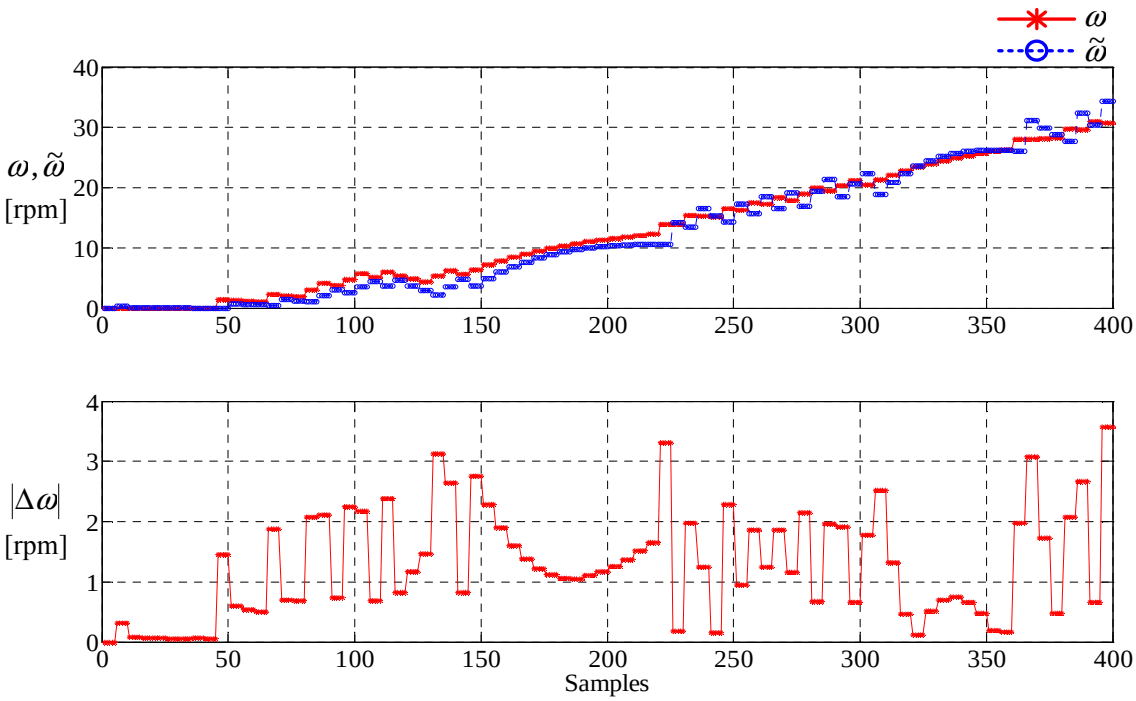

(c) Speed estimation

To verify the validity of the proposed position estimation scheme using Fourier series at high speed under no load, the phase current command of 3A is applied to the SRM at standstill and it is keeping up until the average speed during 400 PWM cycles is 1111 rpm. Fig 6.4 shows the estimated and actual values of flux-linkage, rotor position and speed. Fig 6.4(a) shows the estimated and actual flux-linkage and the absolute values of the percentage errors between them. From Table 6.1, the average flux-linkage error is approximately 2.37 % and the maximum flux-linkage error is approximately 16.82 %. Fig 6.4(b) shows the estimated and actual position and the position error. From Table 6.1, the average position error is approximately 0.53 deg and the maximum position error is approximately 1.64 deg. Fig 6.4(c) shows the estimated and actual speed and the average speed error. From Table 6.1, the average speed error is approximately 6.10 rpm and the maximum speed error is approximately 29.77 rpm. As the speed increases, the resolution of the estimated rotor position in a PWM period increases due to the decrease of the number of PWM pulses for a conduction angle and thus the position error slightly increases compared to the results at startup under no load. It can be also pointed out that the flux-linkage error increases around the unaligned position, causing the increase of the position and speed error. However, it is stabilized as the rotor is moving towards aligned position.

Fig 6.4 Experimental results using Fourier series at ω=1111rpm and I^*=3A under no load

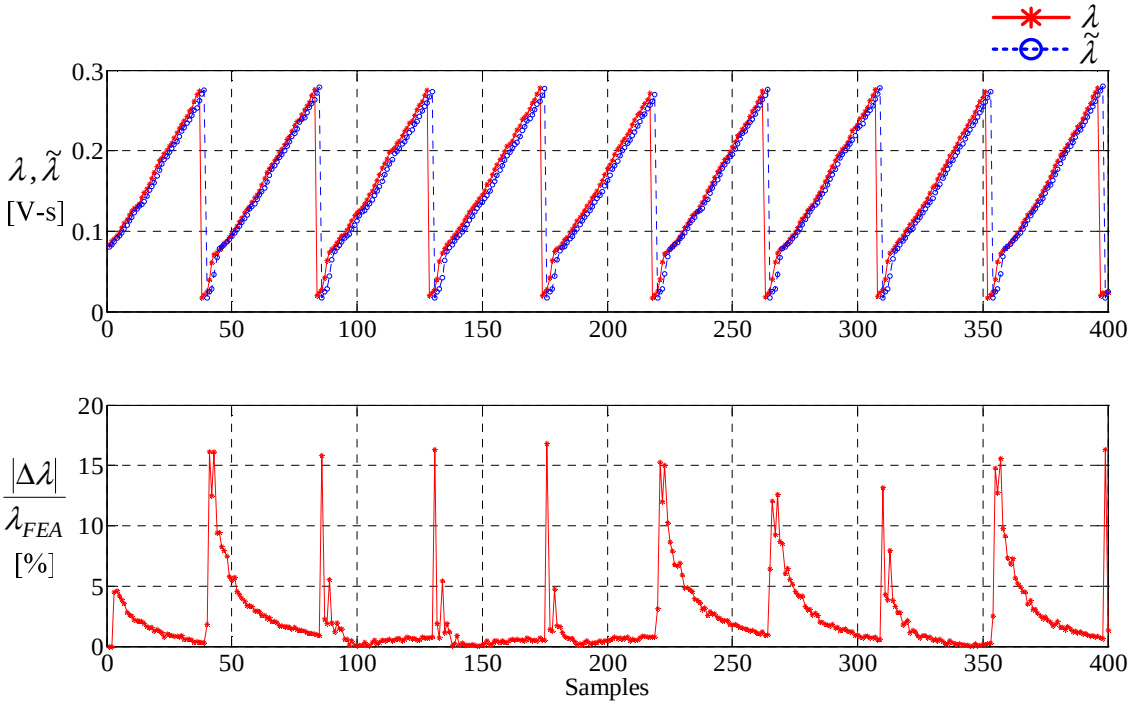

(a) Flux-linkage estimation

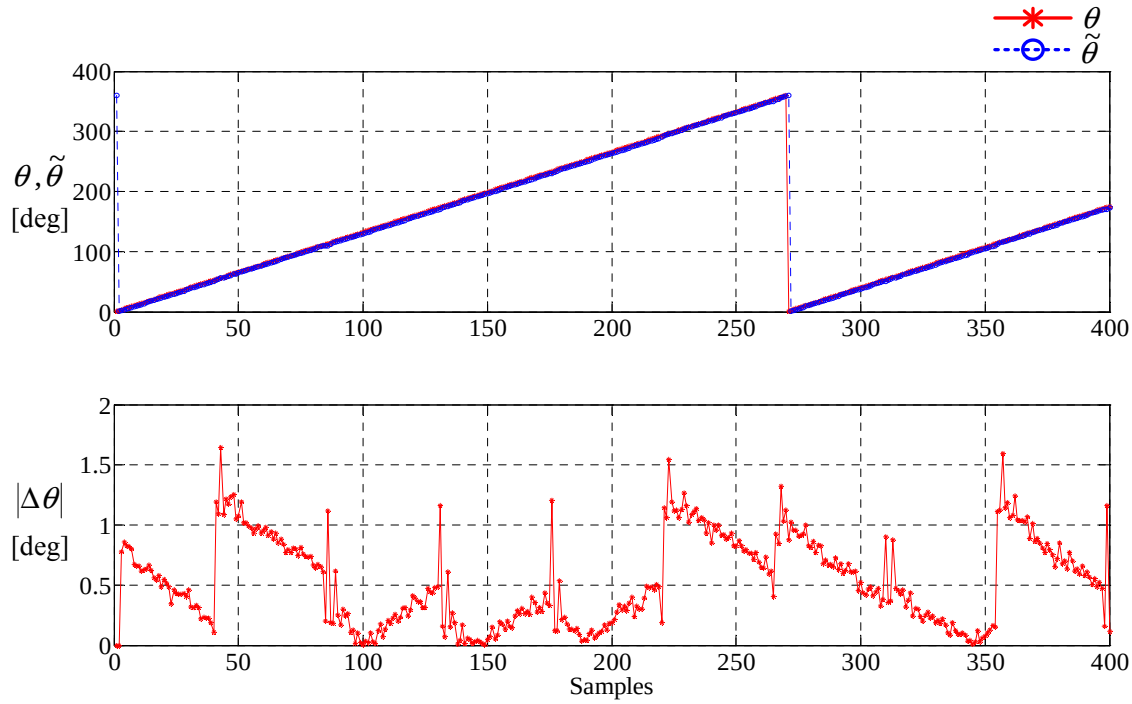

(b) Position estimation

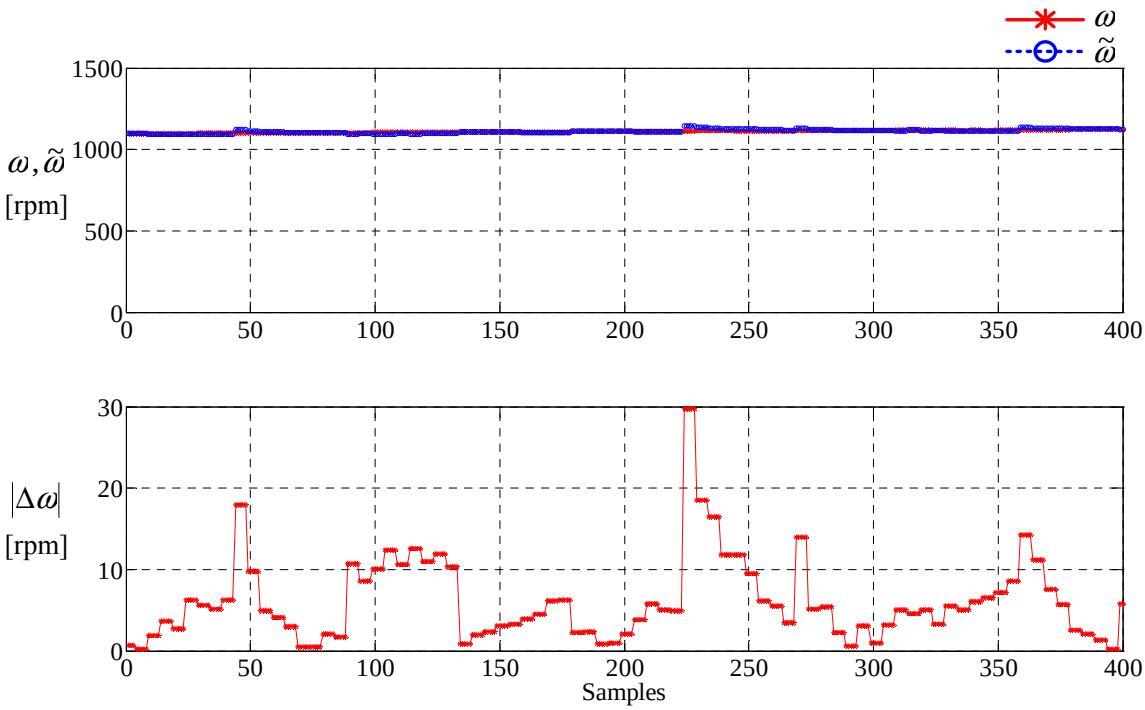

(c) Speed estimation

6.3.2 Load Test

In order to validate the performance of the proposed position estimation scheme using Fourier series in a more comprehensive operating condition, various experiments are performed at different phase current commands under various loads. The load generated form a separately excited DC generator is fed into the SRM coupled to its shaft and it is adjusted by changing a resistance of a rheostat. The SRM runs at 25%, 50%, 75%, and 100% of full load which is 4 N·m for the prototype SRM. Higher current commands more than 7A is applied to the SRM for the reliable startup since the SRM cannot recover from stalling at lower current less than 7A by its torque performance [81]. The SRM is initially at standstill with various loads when a phase current command is applied and it runs with regulating phase current. Note that no speed control loop is included. This test provides the results of the flux-linkage estimated from the incremental inductance estimated by the first switching harmonic of phase voltage and current using Fourier series, the rotor position estimated from the estimated flux-linkage and phase current by looking up a magnetization table, and the rotor speed estimated by the derivative of the estimated rotor position with respect to time. In general, the flux-linkage given by FEA is stored into a memory space of the DSP controller and the rotor position is estimated by the relationship between the

estimated flux-linkage and measured phase current. Therefore, the higher rate of change of flux-linkage with respect to rotor position at given phase current gives a better accuracy of the estimated rotor position. However, in the prototype two-phase 6/3 SRM, the flux-linkage is saturated from 6A. Hence even small variation of the estimated flux-linkage in saturated region causes to increase the position error. This is because the rate of change of flux-linkage with respect to rotor position in saturated region is lower than that in unsaturated region. Thus in experiments, to reduce the position error in saturated region, the flux-linkage profile linearly varying with respect to the rotor position from unsaturated to saturated region is stored into a DSP memory.

At the rate of 5 kHz, the estimated and actual values of flux-linkage, rotor position, and speed are obtained during 300 PWM cycles at different operating conditions such as transient startup as well as low and high speeds. The number of PWM cycles is determined by the available memory space of the DSP controller [84]. The average and maximum values of the results obtained during 300 PWM cycles are summarized in Table 6.2.

Table 6.2 Experimental results using Fourier series at different current commands under various loads

Torque [N·m]	Iref [A]	Average Speed [rpm]	Position Error [deg] $\lvert\Delta\theta\rvert$		Speed Error [rpm] $\lvert\Delta\omega\rvert$		Flux-linkage Error [%] $(\lvert\Delta\lambda\rvert/\lambda_{FEA})*100$	
			Average	Maximum	Average	Maximum	Average	Maximum
1	7	895	0.3483	1.1006	5.2576	18.0279	1.4143	14.7268
2	9	885	0.3044	1.1177	4.7058	16.4863	1.3372	14.7666
3	11	844	0.2960	1.1633	3.8047	13.5337	1.3420	12.4133
4	13	776	0.3931	1.1702	4.1952	14.9454	1.4352	13.1195

Fig 6.5 shows the performance of the position estimation scheme using Fourier series when applying the phase current command of 9A under half load, 2 N·m. Fig 6.5(a) shows the estimated and actual flux-linkage and the absolute percentage error between them. From Table 6.2, the average and maximum flux-linkage errors are approximately 1.33 % and 14.76 %, respectively. Fig 6.5(b) shows the estimated and actual rotor position and the position error between them at the bottom. From Table 6.2, the average and maximum position errors are approximately 0.30 deg and 1.11 deg, respectively. Fig 6.5(c) shows that the estimated and actual speed and the speed error between them. From Table 6.2, the average and maximum speed errors are approximately 4.70 rpm and 16.48 rpm, respectively. It is evident that the position

error decreases when the rotor is moving towards aligned position due to getting rid of the nonlinear effects of the saturation as shown in Fig 6.5(a).

Fig 6.5 Experimental results using Fourier series at ω=885rpm and I^*=9A under half load, 2 N·m

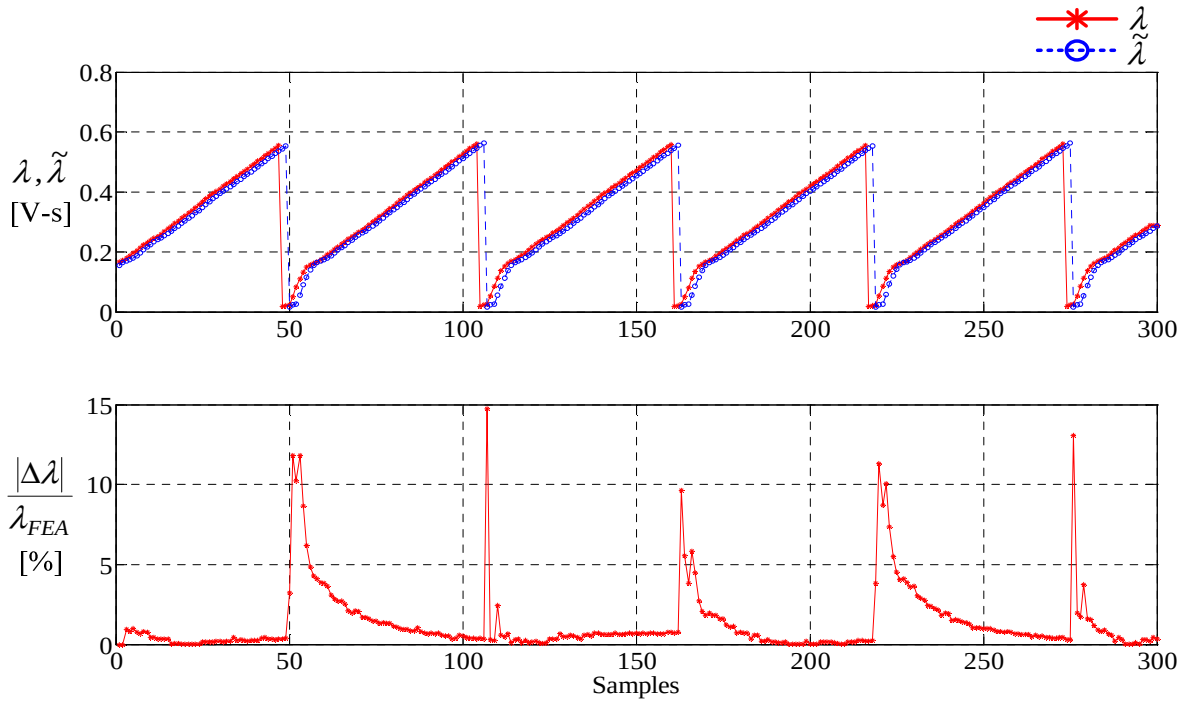

(a) Flux-linkage estimation

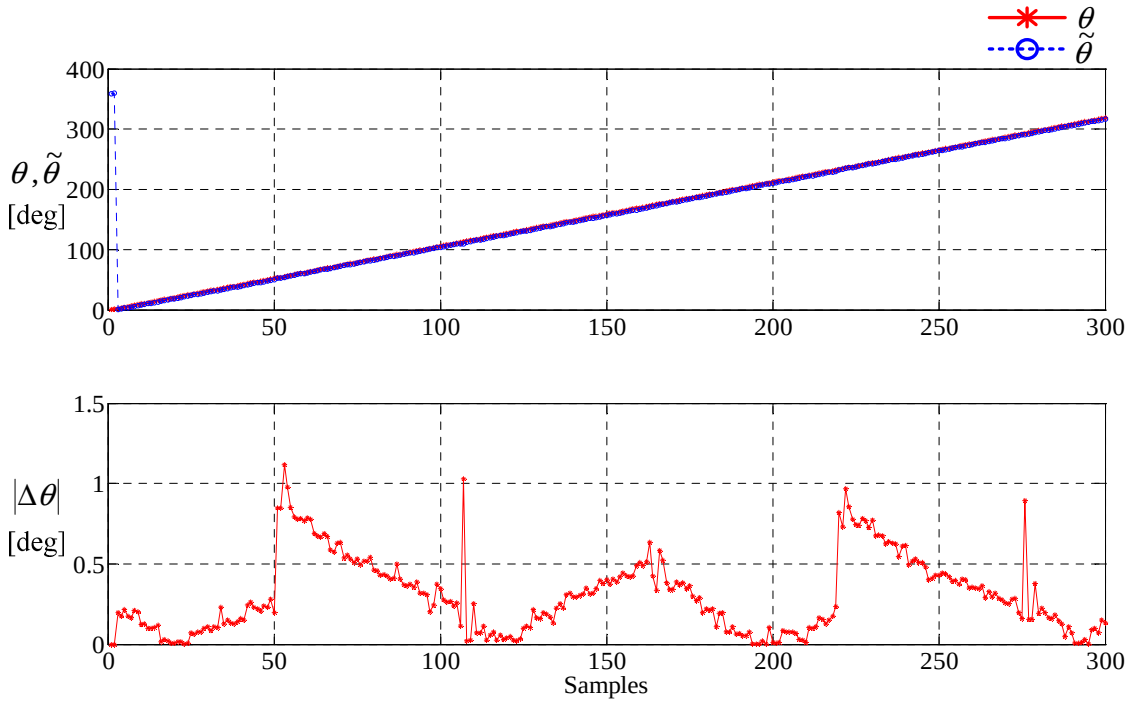

(b) Position estimation

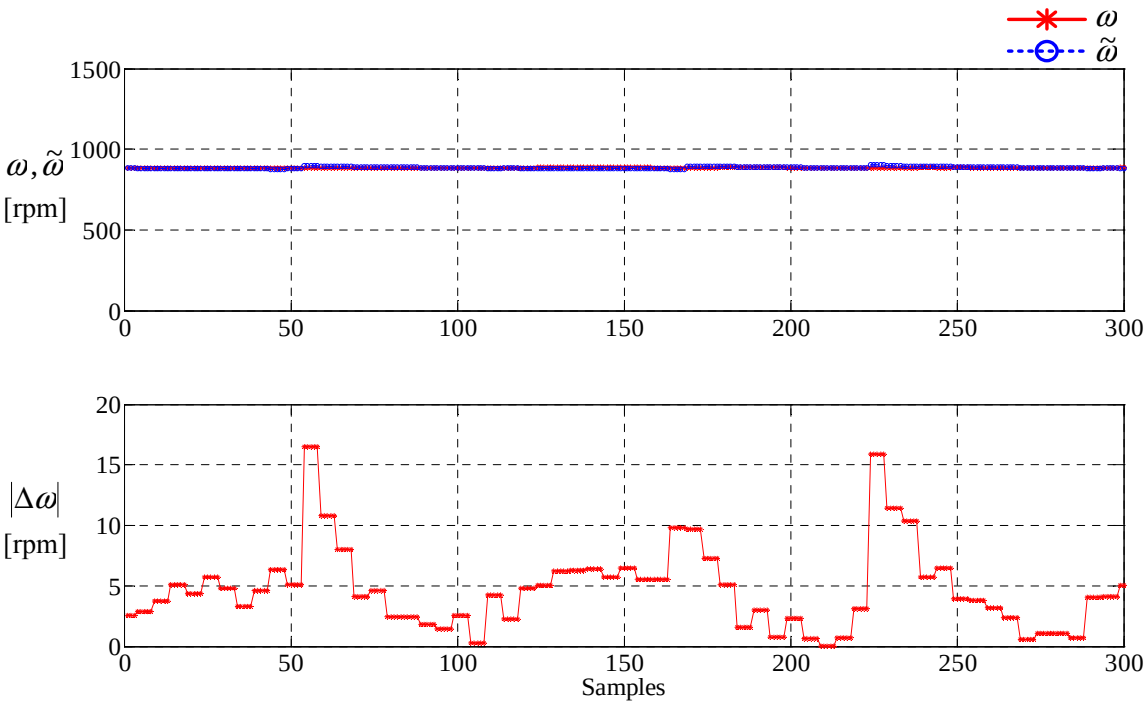

(c) Speed estimation

Fig 6.6 shows the estimated and actual values of flux-linkage, rotor position, and speed when applying the phase current command of 13A under full load. The SRM is initially at standstill and it runs until the average rotor speed during 300 PWM cycles reaches 776 rpm. Fig 6.6(a) shows that the estimated flux-linkage is compared with the actual flux-linkage given by FEA and the absolute values of the percentage errors between them are plotted as the error at the bottom. From Table 6.2, the average flux-linkage error is approximately 1.43 % and the maximum flux-linkage error is approximately 13.11 %. Based on the estimated flux-linkage and phase current, the rotor position is estimated every PWM cycle. Fig 6.6(b) shows the estimated and actual rotor position and the position error between them. From Table 6.2, the average position error is approximately 0.39 deg and the maximum position error is approximately 1.17 deg. Fig 6.6(c) shows the estimated and actual speed and the speed error between them. It can be seen from Table 6.2 that the average speed error is approximately 4.19 rpm and the maximum speed error is approximately 14.94 rpm. From Fig 6.6(a), the flux-linkage error increases around the unaligned position due to the higher rate of change of phase current around the unaligned position. It causes the increase of the position and speed error. However, the position error tends to decrease when the rotor is moving towards the aligned position as in Fig 6.5.

Fig 6.6 Experimental results using Fourier series at ω=776rpm and I^*=13A under full load, 4 N·m

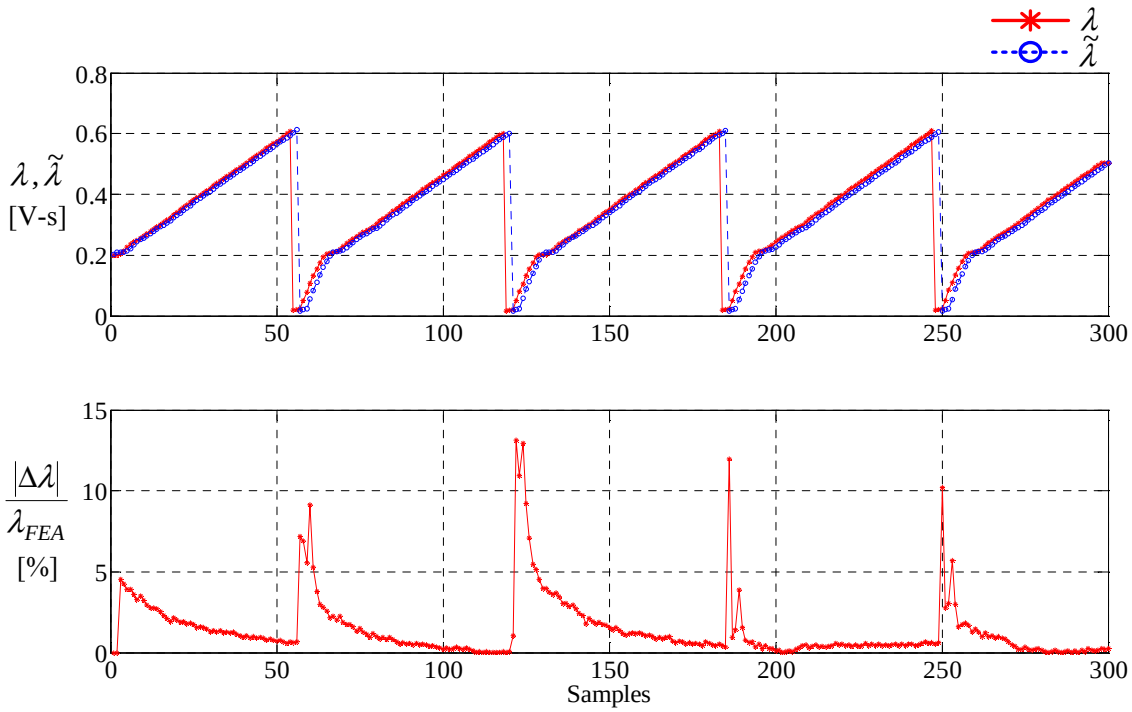

(a) Flux-linkage estimation

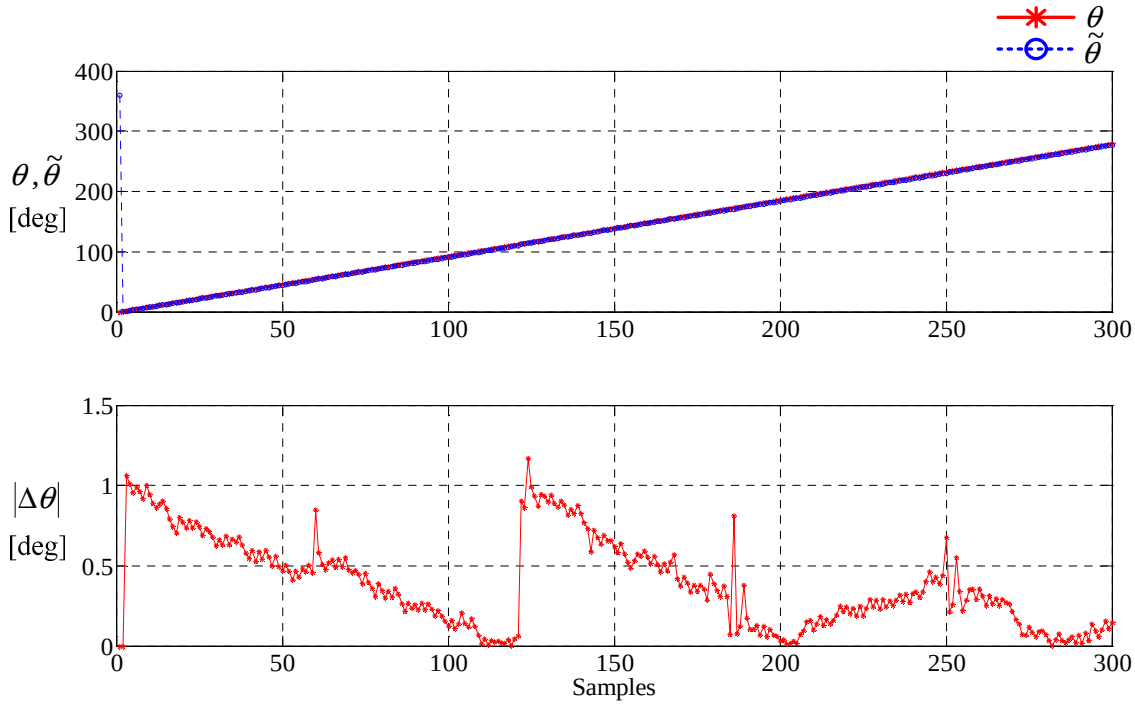

(b) Position estimation

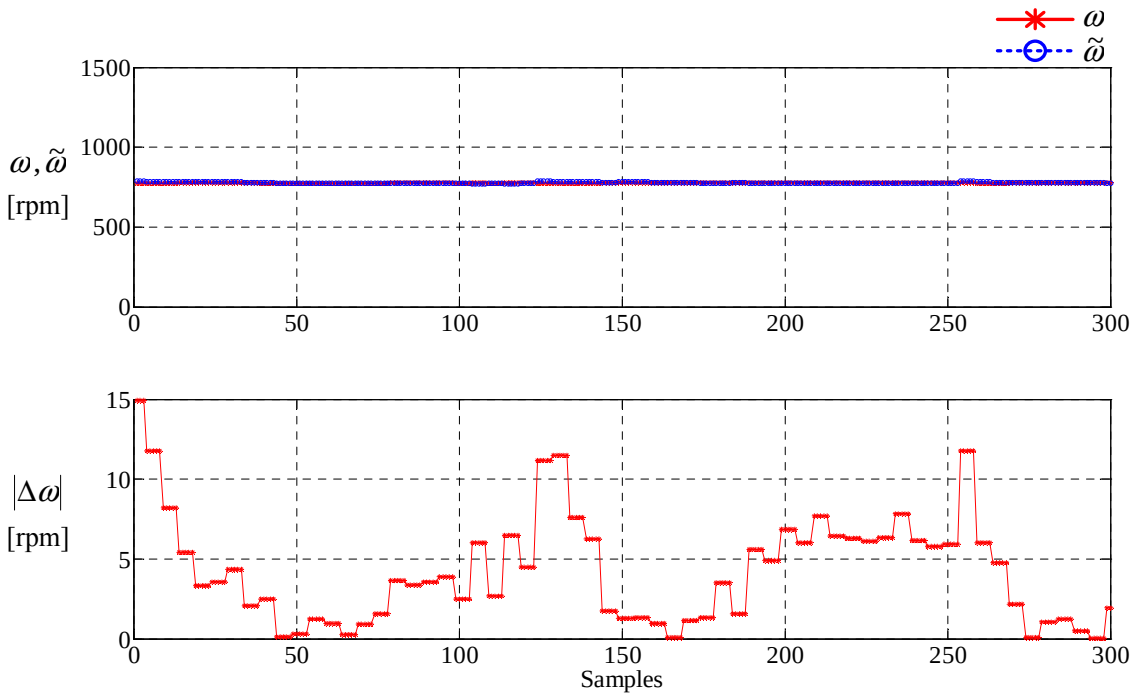

(c) Speed estimation

6.4 Experimental Evaluation of Fast Fourier Transform-Based Algorithm

The performance of the position estimation scheme using the first switching harmonic of phase voltage and current decomposed by FFT is verified at different current commands under various loads. For each current command, the estimated and actual values of flux-linkage, rotor position, and speed are presented. Note that no speed control loop is included and the current command is the only external input of experiments. The SRM is operated with regulating phase current from standstill with various loads.

As mentioned in the previous section, asymmetrical PWM method with a fixed frequency (set at 5 kHz) is employed for dynamic current control and an anti-windup functionality is included in the current control loop. The asymmetric bridge converter operating under hard chopping mode is employed to increase the rate of change of phase current in a PWM period. DC bus voltage and phase current are sampled at a sampling rate of 250 kHz and the sample size of FFT computation is 50 samples in a PWM period. From FFT computation of the sampled DC bus voltage with the duty cycle provided from the current control loop, real and imaginary parts of the first switching harmonic of phase voltage are calculated. In addition, from FFT

computation of the sampled phase current, real and imaginary parts of the first switching harmonic of phase current are calculated.

For FFT computation of the sampled data in a PWM period, twiddle factors, composed of $N/2$ samples containing half cycle of SIN function and $N/2$ samples containing half cycle of COS function, are stored into an initialized memory of the DSP. Based on real and imaginary parts of the first switching harmonics of phase voltage and current, the flux-linkage is estimated in a PWM period. Flux-linkage values given by FEA are stored into the two dimensional lookup table with phase current for row and rotor position for column. By using linear interpolation in the two-dimensional flux-linkage lookup table with the estimated flux-linkage and average phase current, the rotor position is estimated.

The rotor speed estimated by the derivative of the estimated rotor position is filtered out by using an exponentially weighted moving average filter (EWMAF), which is called the first order IIR filter, at the sample rate of 1 kHz and filter coefficient of 0.9, resulting in increasing the degree of filtering. The EWMAF is chosen because the most recent estimated speed is given more emphasis than older values as well as reflects better the state of the process in dynamic control systems. Different loads are applied to the SRM from startup by using a separately excited DC generator. The flow chart for experiments using FFT is represented in Fig 6.7.

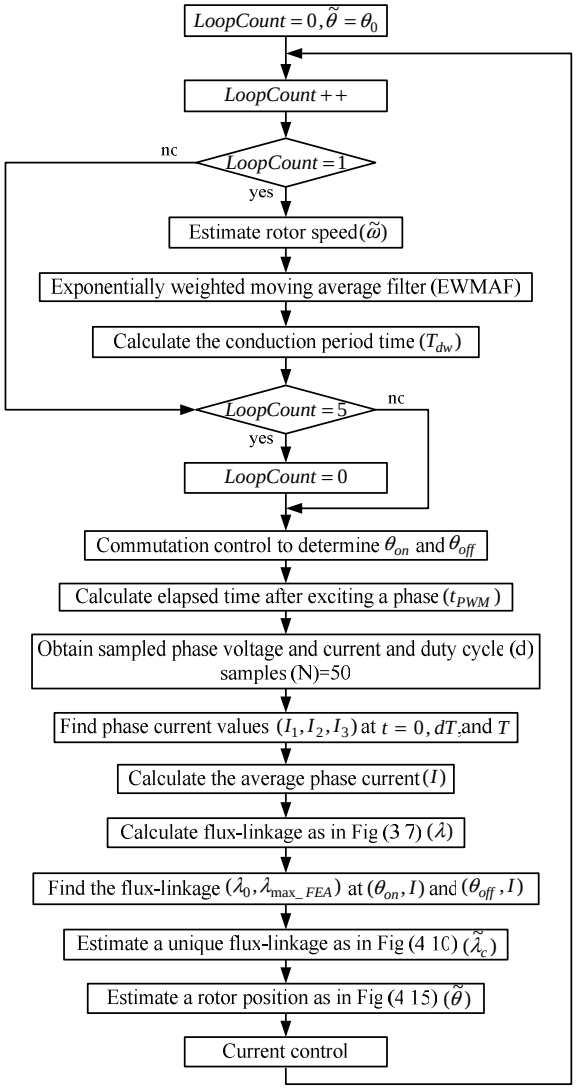

Fig 6.7 The flow chart for experiments using FFT

6.4.1 No Load Test

In order to validate the performance of the proposed position estimation scheme using FFT, various experiments are performed at different phase current commands under no load. As the experiments using Fourier series at the previous section, the SRM is initially at standstill with no load when a phase current command is applied to the SRM and it runs with regulating phase current. No speed control loop is included. The sample size for FFT computation conducted in a PWM period is 50 and the sampling frequency is set to 250 kHz, reducing the aliasing effect discussed in Chapter 2. Twiddle factors, $N/2$ samples containing half cycle of SIN function and $N/2$ samples containing half cycle of COS function, are stored into an initialized memory of

the DSP and these twiddle factors are used to calculate real and imaginary parts of the first switching harmonic of phase voltage and current. From these real and imaginary parts, the magnitude and phase angle of the first switching harmonic of phase voltage and current are calculated. This test also provides the estimated and actual values of flux-linkage, rotor position, and speed for a PWM period. At the rate of 5 kHz, the estimated and actual values of flux-linkage, rotor position, and speed are obtained during 400 PWM cycles at different operating conditions such as transient startup as well as low and high speed. The number of PWM cycles is determined by the available memory space of the DSP controller[84]. The average and maximum values of the results obtained during 400 PWM cycles are presented in the following Table 6.3.

Table 6.3 Experimental results using FFT at different current commands under no load

Iref [A]	Average Speed [rpm]	Position Error [deg] $\lvert\Delta\theta\rvert$		Speed Error [rpm] $\lvert\Delta\omega\rvert$		Flux-linkage Error [%] $(\lvert\Delta\lambda\rvert / \lambda_{FEA}) * 100$	
		Average	Maximum	Average	Maximum	Average	Maximum
2	Startup	0.4518	0.7184	1.4755	2.8809	2.6341	4.1716
	236	0.1881	0.4822	1.8480	6.3790	0.7363	5.5064
	314	0.2577	0.8943	3.2245	11.0724	1.0801	9.4785
	590	0.5922	1.2854	8.3459	27.1738	2.1589	11.0761
	774	0.6238	1.6743	10.7887	25.1936	2.3061	13.6797
3	Startup	0.4425	0.8671	1.5727	3.6999	2.3017	3.8532
	490	0.4068	1.2421	5.9109	19.4738	1.5823	11.0161
	676	0.6442	1.3548	11.0311	30.2657	2.3562	12.2106
	941	0.6094	2.0893	10.1536	30.9586	2.4360	17.0758
	1144	0.8561	1.9715	13.0675	24.5110	3.3168	18.3464
4	Startup	0.1976	0.7256	1.6048	5.1568	0.8927	2.3535
	705	0.6342	1.5586	9.9982	24.3159	2.3329	14.2513
	976	0.7128	1.5190	10.8604	25.1939	2.9084	15.8663
	1189	0.9549	1.8449	14.3880	25.3826	3.8394	16.5392
5	Startup	0.0875	0.4255	1.0851	3.3632	0.3692	1.3069
	724	0.6040	1.4314	10.1744	22.2554	2.1913	13.5979
	1085	0.8747	1.8458	15.2846	31.1438	3.1725	18.6625
6	Startup	0.5617	1.9575	3.4674	10.9815	1.5013	4.2524
	874	0.7247	1.6199	12.3772	33.4202	2.6855	15.4853
	1280	0.9641	2.0968	16.6907	37.5575	3.6249	18.8666

Fig 6.8 shows the estimated and actual values of flux-linkage, rotor position, and speed at startup when applying the phase current command of 3A under no load. These values are obtained every PWM period and the rotor position set to zero at the aligned position. The estimated and actual flux-linkage and the absolute value of percentage error between them are shown in Fig 6.8(a). From Table 6.3, the average and maximum flux-linkage errors are approximately 2.30 % and 3.85 %, respectively. Fig 6.8(b) shows the estimated and actual position error and the average position error. From Table 6.3, the average and maximum position errors are approximately 0.44 deg and 0.86 deg, respectively. Fig 6.8(c) shows the estimated and actual speed and the speed error between them. From Table 6.3, the average and maximum speed errors are approximately 1.57 rpm and 3.69 rpm, respectively. It can be observed that the proposed position estimation scheme works reliably at startup under no load.

Fig 6.8 Experimental results using FFT at startup and $I^{*}=3A$ under no load

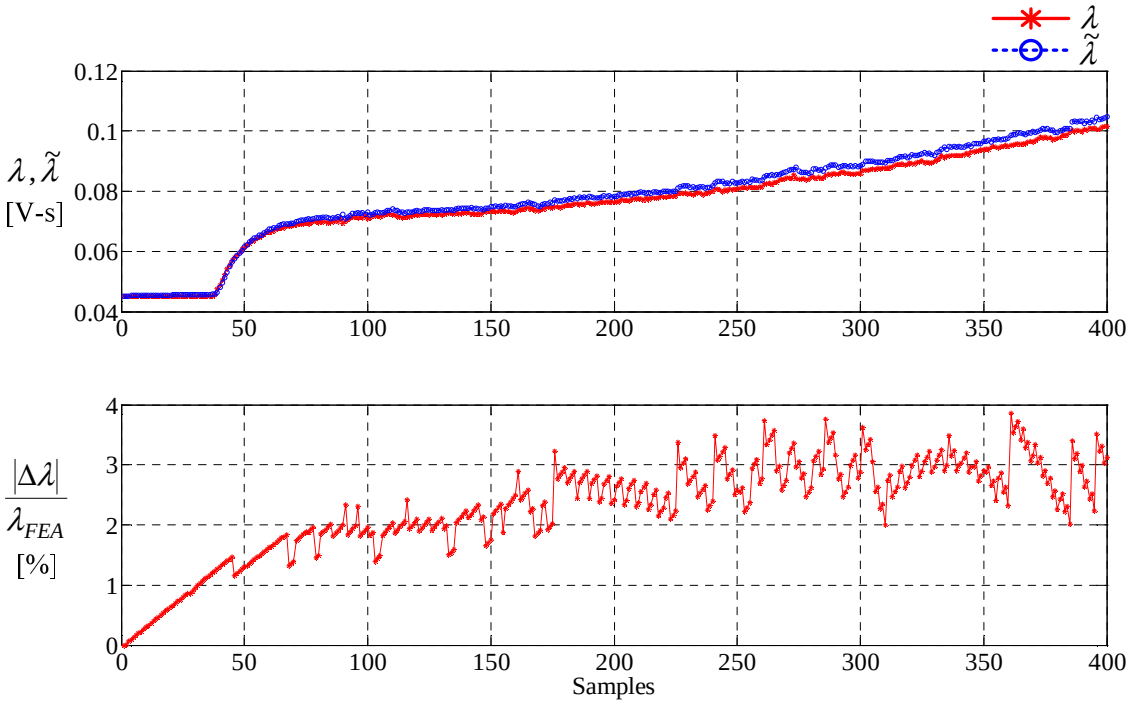

(a) Flux-linkage estimation

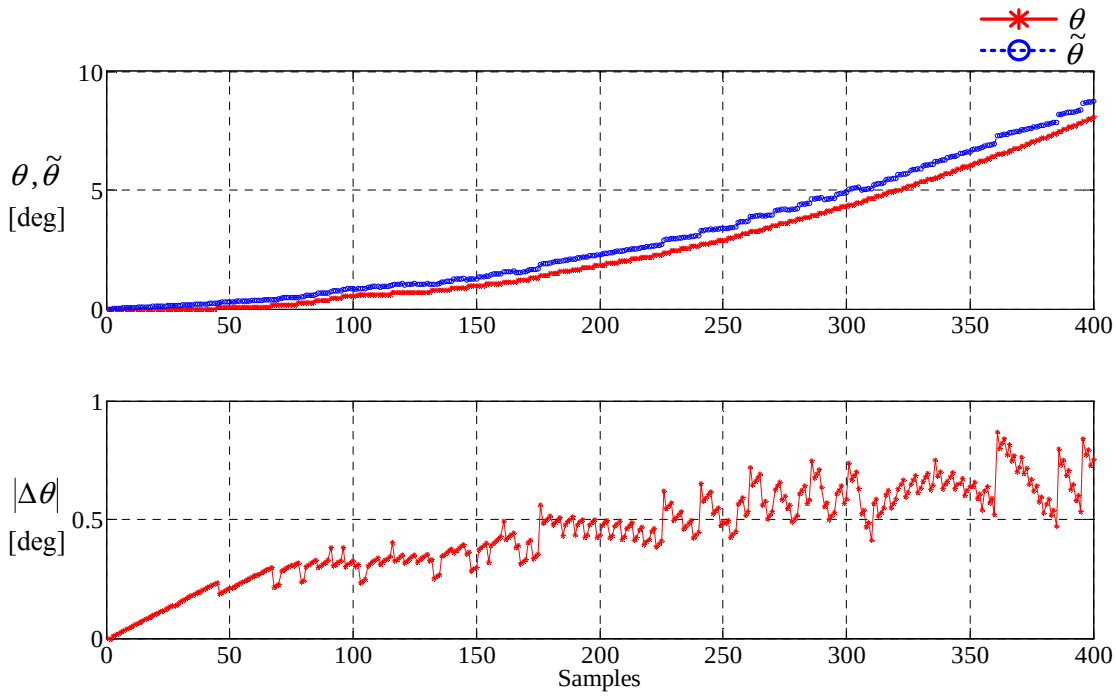

(b) Position estimation

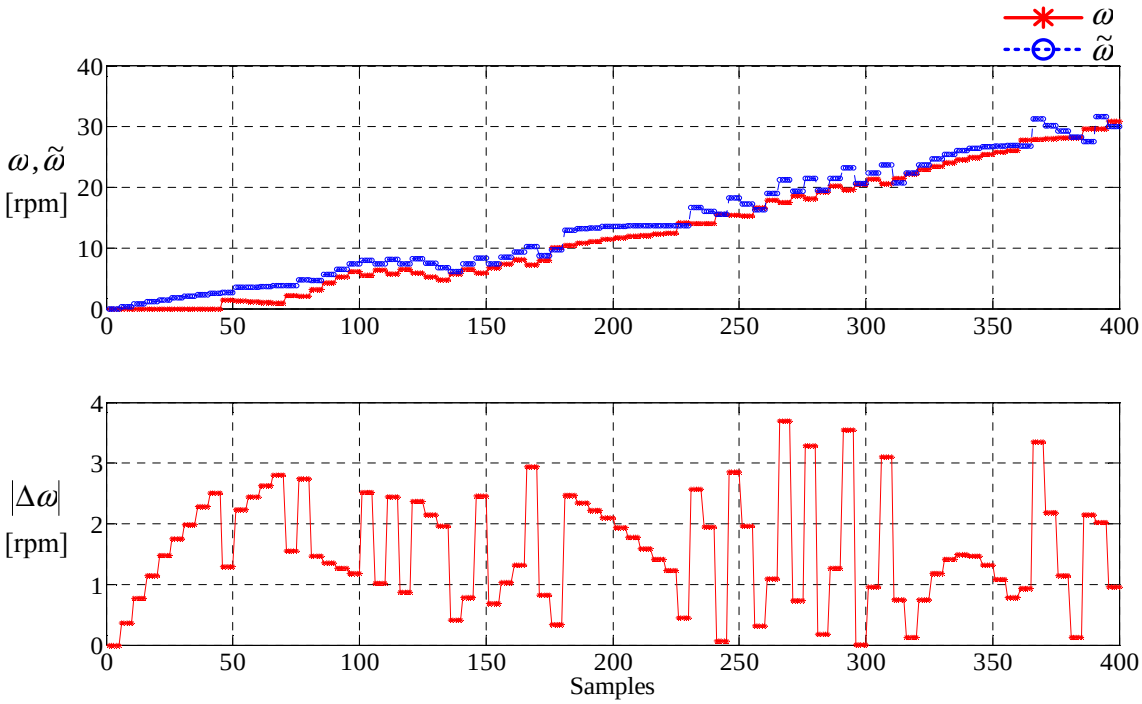

(c) Speed estimation

Fig 6.9 shows the estimated and actual values of flux-linkage, rotor position, and speed at high speed when applying the phase current command of 3A under no load. The SRM starts at standstill and it runs with regulating phase current until the average speed during 400 PWM cycles is 1144 rpm. Fig 6.9(a) shows the estimated and actual flux-linkage error and the absolute values of the percentage errors between them. From Table 6.3, the average and maximum flux-linkage error is approximately 3.31 % and 18.34 %, respectively. Fig 6.9(b) shows the estimated and actual position and the position error between them. From Table 6.3, the average and maximum position error is approximately 0.85 deg and 1.97 deg, respectively. From Fig 6.9(c) and Table 6.3, the average and maximum speed errors are approximately 13.06 rpm and 24.51 rpm, respectively. As the experimental results using Fourier series at high speed under no load, it has the characteristic that the position error slightly increases as the speed increases due to the low resolution at high speed, but it is reliably stabilized as the rotor is moving towards aligned position. Comparing these results with those in using Fourier series, it can be noted that they are slightly larger because phase current shifted due to an anti-aliasing LPF and the propagation delay time of devices linked to ADC channels of the DSP is sampled without any compensation for correcting the shifted phase current, while the shifted phase current is compensated by LLS fitting algorithm in using Fourier series.

Fig 6.9 Experimental results at ω=1144rpm and I^*=3A under no load

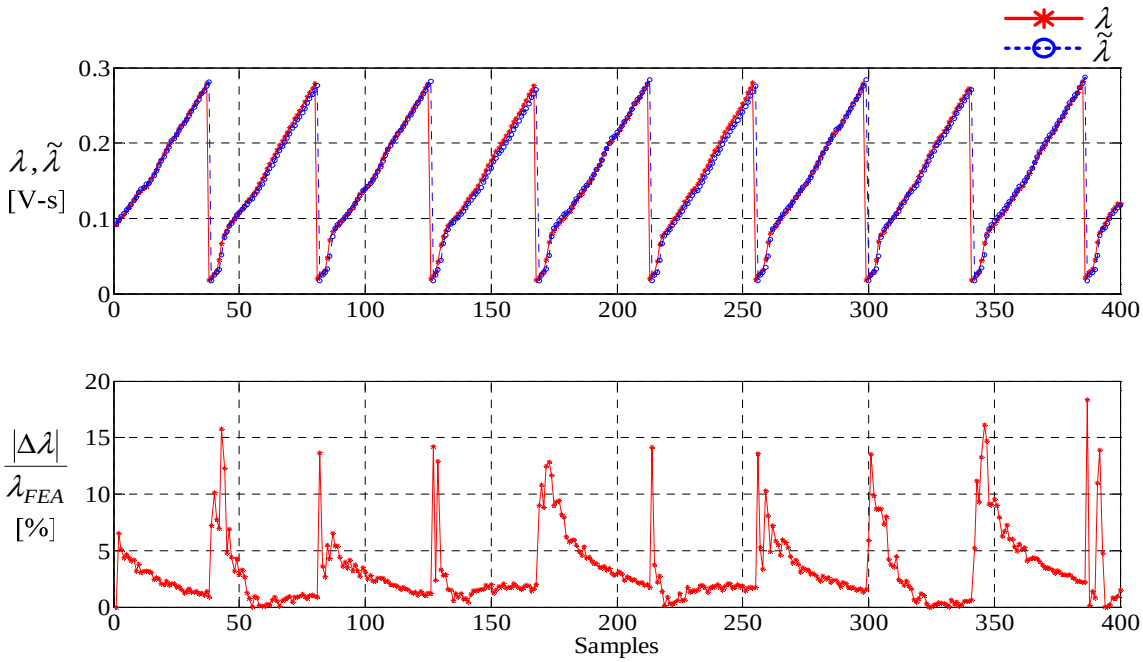

(a) Flux-linkage estimation

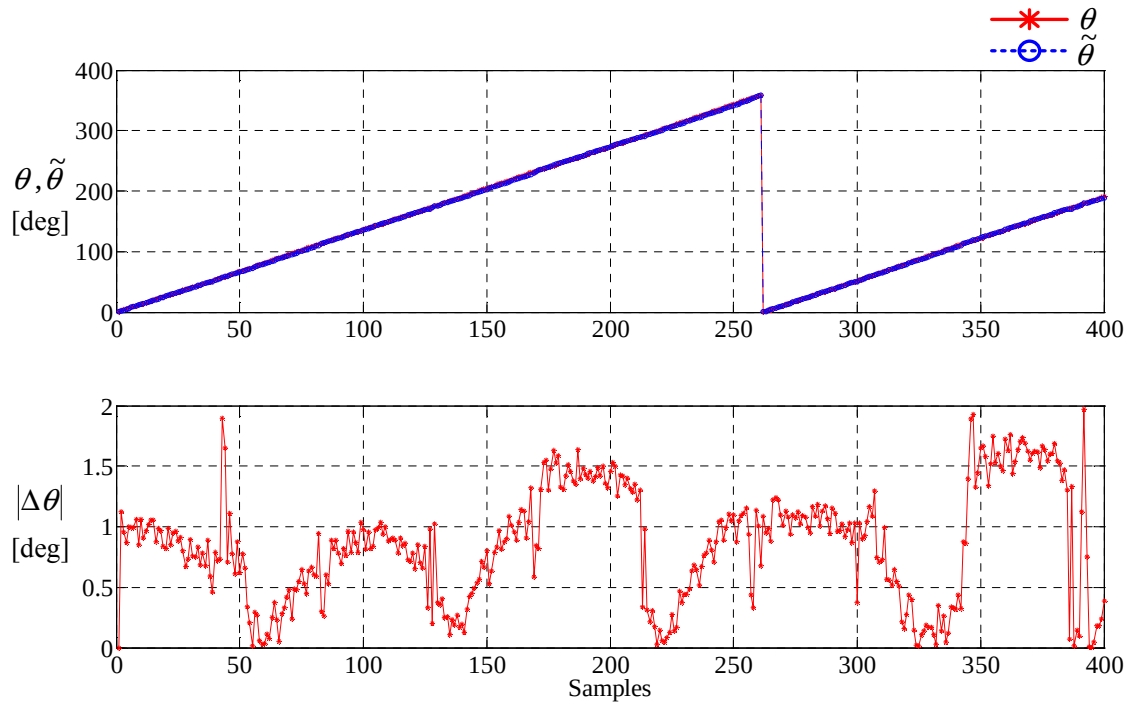

(b) Position estimation

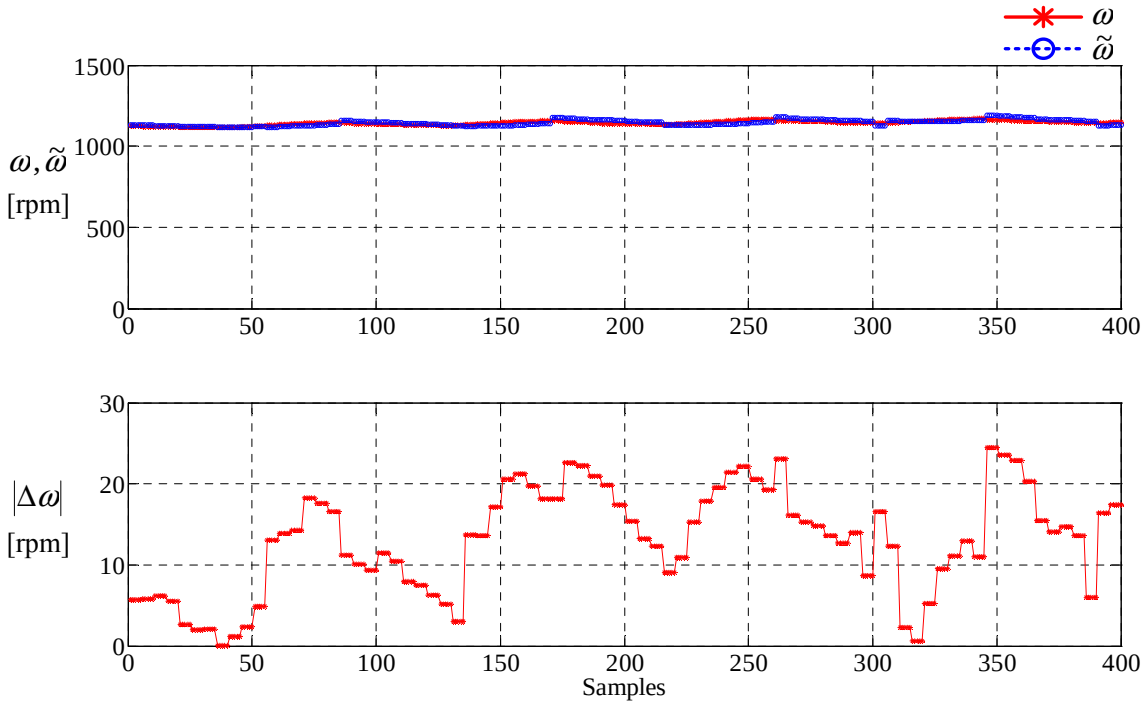

(c) Speed estimation

6.4.2 Load Test

To verify the validity of the proposed position estimation scheme using FFT by load conditions, comprehensive experiments are performed at different phase current commands under various loads. The load generated form a separately excited DC generator is 25%, 50%, 75%, and 100% of full load which is 4 N·m for the prototype. The SRM is at standstill with various loads when a phase current command is applied and it runs with regulating phase current. No speed control loop is included. As the experiments using Fourier series, higher current commands more than 7A is applied to the SRM in order to generate enough positive torque to move the SRM at standstill. This test provides the performance of the proposed position estimation scheme using FFT under various loads. As mentioned in section 6.3.2, the flux-linkage lookup table linearly varying with respect to rotor position is stored into the DSP memory to enhance the accuracy of the estimated rotor position around the aligned position. The estimated and actual values of flux-linkage, rotor position and speed are compared at the rate of 5 kHz and the results are summarized in Table 6.4. The results show that the proposed position algorithm using FFT exhibits a good performance at different currents under various loads.

Table 6.4 Experimental results using FFT at various current commands under various loads

Torque [N·m]	Iref [A]	Average Speed [rpm]	Position Error [deg] $\lvert\Delta\theta\rvert$		Speed Error [rpm] $\lvert\Delta\omega\rvert$		Flux-linkage Error [%] $(\lvert\Delta\lambda\rvert/\lambda_{FEA})*100$	
			Average	Maximum	Average	Maximum	Average	Maximum
1	7	864	0.6960	1.5221	11.2061	26.6586	2.5967	13.1478
2	9	889	0.8884	1.5678	14.4563	25.5034	2.9398	16.5401
3	11	853	0.8369	1.6458	11.1746	27.9180	2.8596	13.6750
4	13	819	0.7842	1.6916	9.6338	23.2913	2.5371	13.4636

Fig 6.10 shows the estimated and actual values of flux-linkage, rotor position, and speed when applying the phase current command of 9A under half load, 2 N·m. The SRM starts to run from standstill and it is keeping up until the average speed during 300 PWM cycles is 849 rpm. From Fig 6.10(a) and Table 6.4, the average and maximum flux-linkage errors are approximately 3.26 % and 16.30 %, respectively. Fig 6.10(b) and Table 6.4 show that the average and maximum position errors are approximately 0.90 deg and 1.74 deg, respectively. From Fig 6.10(c) and Table 6.4, the average and maximum speed errors are approximately 10.90 rpm and

23.63 rpm, respectively. It can be observed that the proposed estimation scheme works reliably even around the aligned position.

Fig 6.10 Experimental results using FFT at ω=889rpm and I^*=9A under half load, 2 N·m

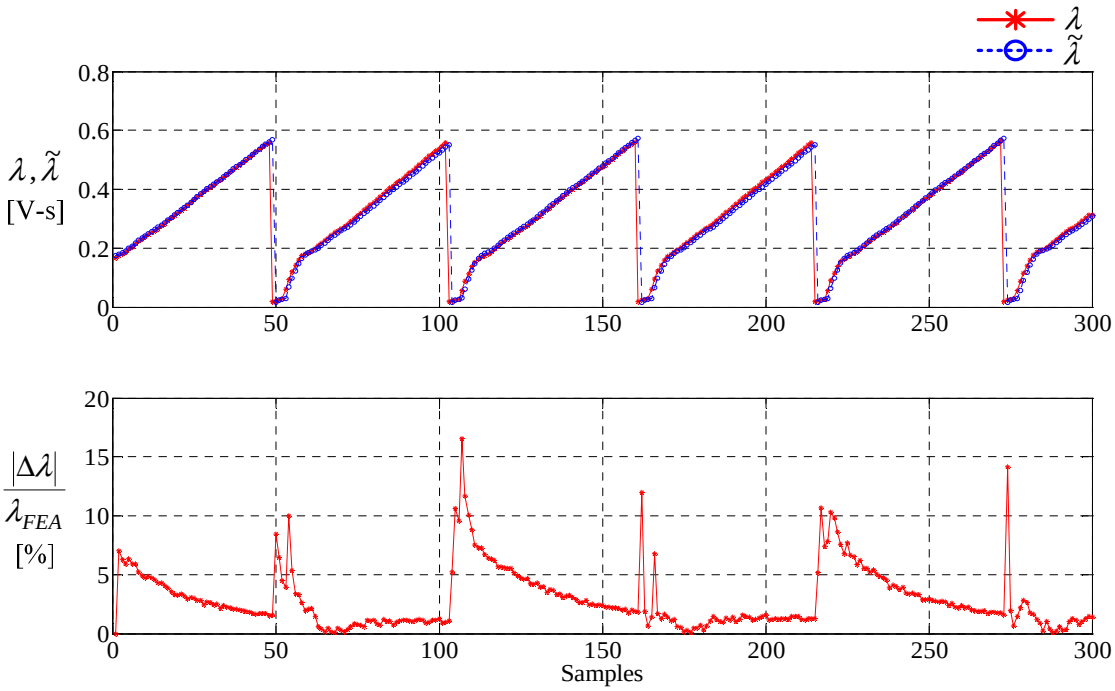

(a) Flux-linkage estimation

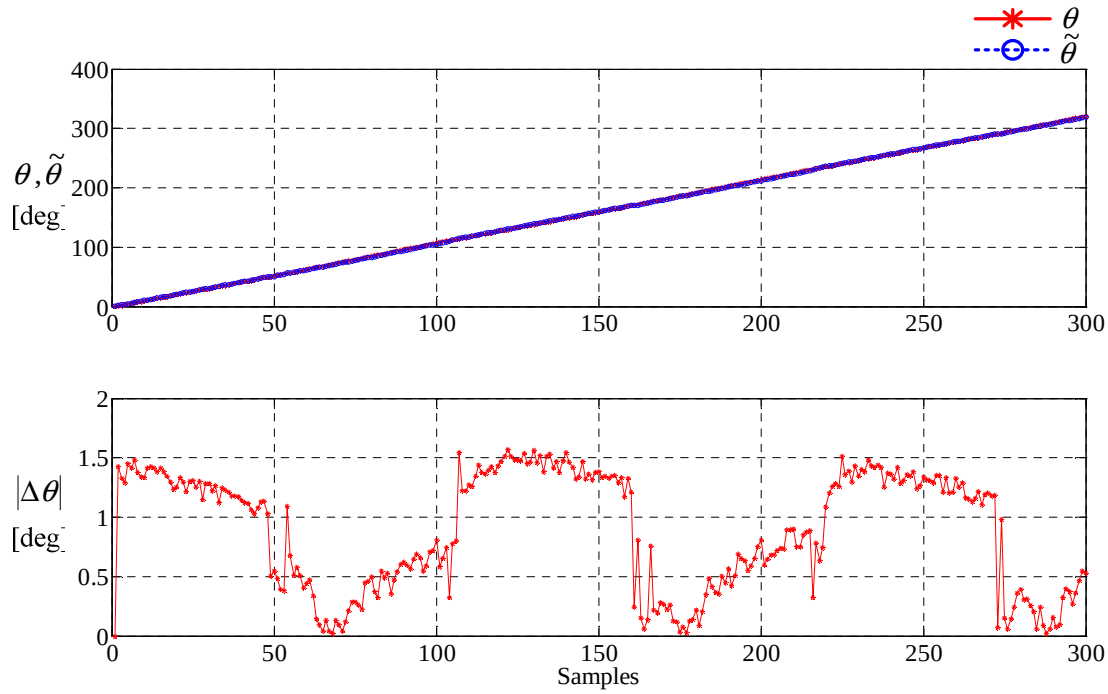

(b) Position estimation

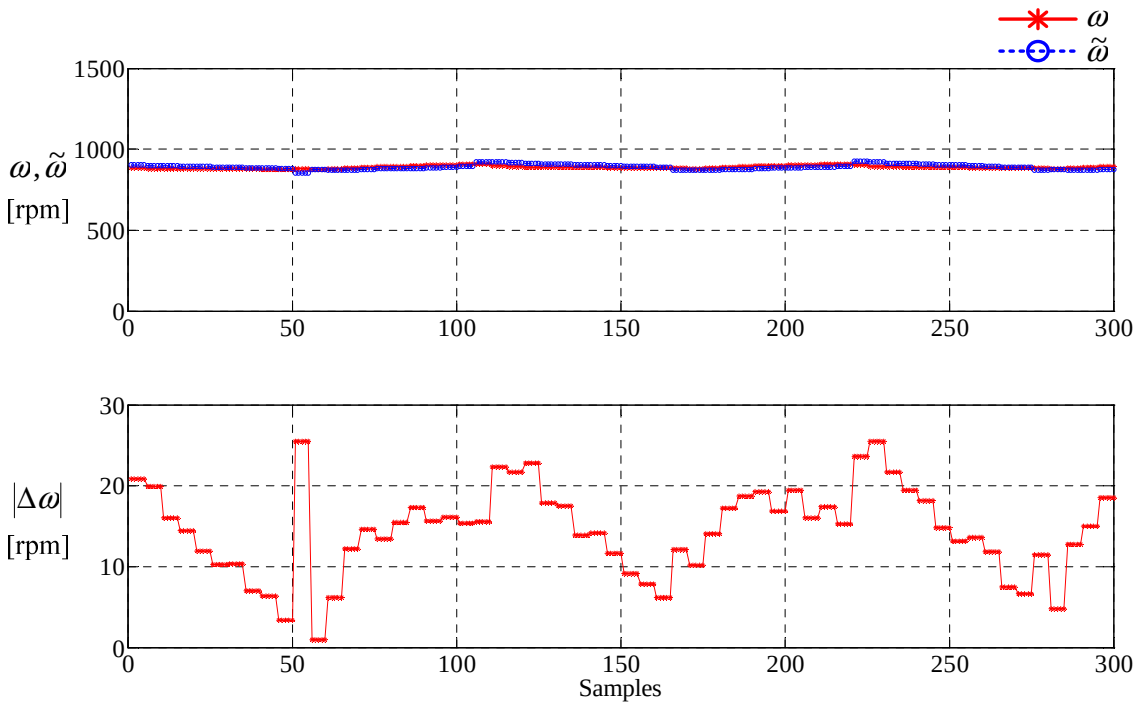

(c) Speed estimation

Fig 6.11 shows the estimated and actual values of flux-linkage, rotor position, and speed when applying the phase current command of 13A under full load. The SRM is initially at standstill and it runs with phase current regulation until the average speed during 300 PWM cycles reaches 819 rpm. Fig 6.11(a) shows the estimated and actual flux-linkage error and the absolute values of the percentage errors between. From Table 6.4, the average flux-linkage error is approximately 2.53 % and the maximum flux-linkage error is approximately 13.46 %. Fig 6.11(b) shows the estimated and actual rotor position and the position error between them. From Table 6.4, the average position error is approximately 0.78 deg and the maximum position error is approximately 1.69 deg. Fig 6.11(c) shows the estimated and actual speed and the speed error between them. From Table 6.4, the average speed error is approximately 9.63 rpm and the maximum speed error is approximately 23.29 rpm. The experimental results confirm the dynamic simulations results. The flux-linkage error increases around the unaligned and it cause the increase of the position and speed error. However, these errors decrease when the rotor is moving towards the aligned position. Comparing these results with those in using Fourier series under full load, it can be observed that they are slightly larger due to the sampling of the shifted

phase current at ADC channels of the DSP controller without compensation for correcting the shifted phase current, as discussed in the previous section.

Fig 6.11 Experimental results using FFT at ω=819rpm and I^*=13A under full load, 4 N·m

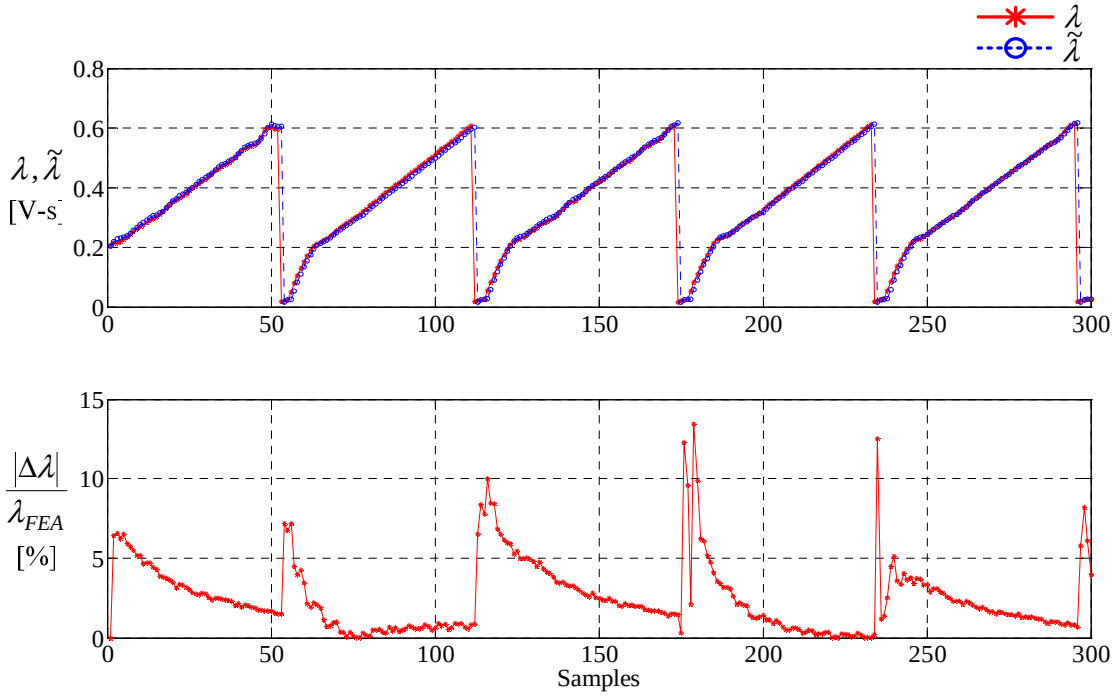

(a) Flux-linkage estimation

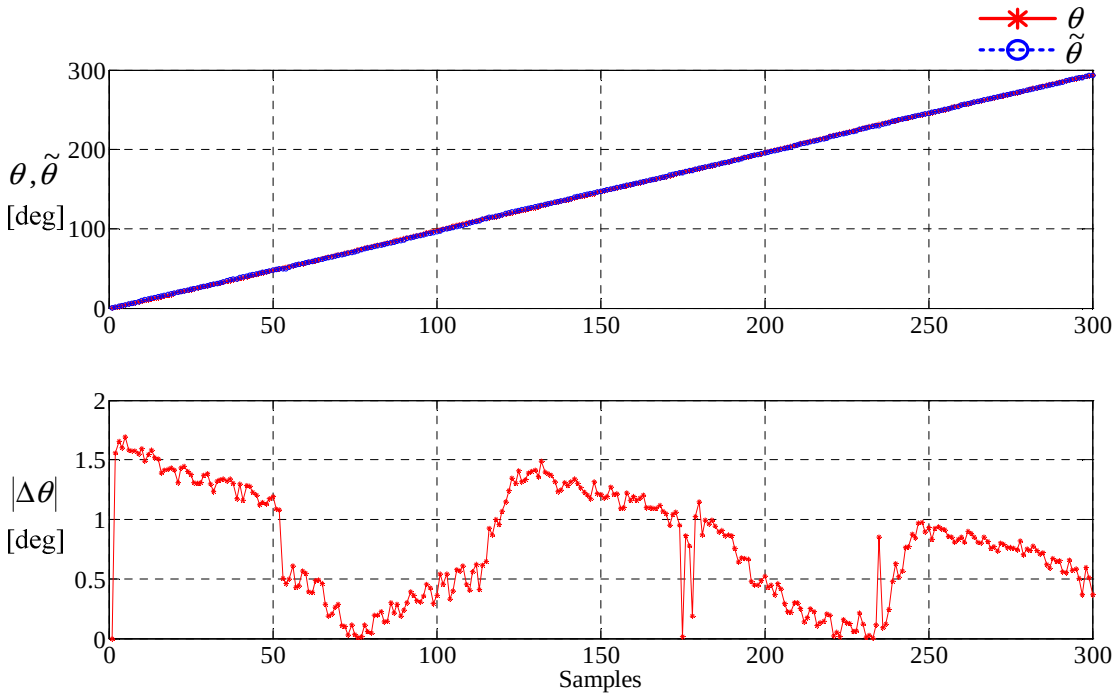

(b) Position estimation

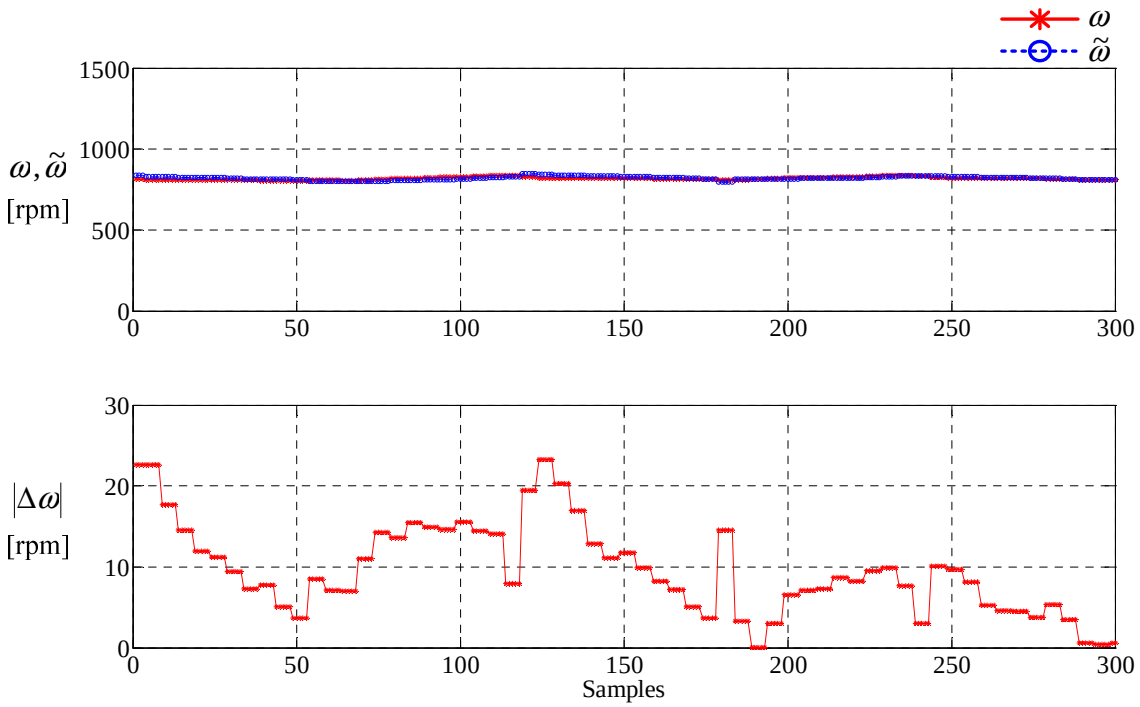

(c) Speed estimation

6.5 Analysis

In order to have a high performance practical position estimation scheme, it is essential to have reliable characteristics about the accuracy and resolution of the estimated rotor position. In this research, experimental verification of the proposed position estimation scheme using Fourier analysis has been carried out. The SRM has been started up from zero speed at different current commands under various loads and it has run with phase current regulation. The loads of 25%, 50%, 75%, 100% of the rated load, 4 N·m, have been applied to the SRM by switching a resistive load which is connected to a DC generator. The rotor position set to zero at the aligned position. Note that no speed control loop is included and each phase is excited with the fixed conduction angle regardless of current command and rotor speed.

The conduction angle of $60°$ is used so that there will be no overlap between two phases. Hence, the rotor speed range has the limitation, which is lower than 1,500 rpm in experiments. This is due to the tail current which flows into the negative inductance slope region after commutating the excited phase. It basically produces negative torque and forms the upper limit on the rotor speed which can be achieved using the sensorless operation. Each phase is turned ON at 50° (mechanical angle) from its unaligned position and turned OFF at 110° (mechanical

angle) from its aligned position. Phase voltage and current of the excited phase are used for rotor position estimation during its conduction period. Due to the lack of an available memory space of the DSP controller, the estimated and actual values of flux-linkage, rotor position, and speed during 400 or 300 PWM cycles have been stored and thereafter the average and maximum values of them have been obtained.

From the following tables to be discussed, when the actual rotor speed is lower than 1,000 rpm, it is referred as low speed, while it is higher than 1,000 rpm, then it is referred as high speed. On the other hand, at the current command of 2A, the rotor speed does not exceed 800 rpm in experiments since the positive torque generated during the conduction angle is not enough to increase the rotor speed. Thereby, it is referred as high speed when the rotor speed is higher than 700 rpm.

Table 6.5 shows the summary of the experimental results executed at different current commands under no load, where the average and maximum values of flux-linkage, rotor position, and speed obtained during 400 PWM cycles at transient startup and low and high speeds are presented.

Table 6.5 Comparison of experimental results under no load

Iref [A]	Speed [rpm]	**Fourier series**						**Fast Fourier Transform**					
		Position Error [deg]		Speed Error [rpm]		Flux-linkage Error [%]		Position Error [deg]		Speed Error [rpm]		Flux-linkage Error [%]	
		Avg.	Max.	Avg.	Max.	Avg.	Max.	Avg.	Max.	Avg.	Max.	Avg.	Max.
2	Startup	0.11	0.47	0.95	3.47	0.67	2.56	0.45	0.71	1.47	2.88	2.63	4.17
	Low	0.16	0.76	2.18	8.39	0.68	6.60	0.34	0.88	4.47	14.87	1.32	8.68
	High	0.41	2.01	4.19	18.36	1.93	16.27	0.62	1.67	10.78	25.19	2.30	13.67
3	Startup	0.26	0.57	1.26	3.57	1.37	2.84	0.44	0.86	1.57	3.69	2.30	3.85
	Low	0.34	1.25	3.77	15.53	1.60	11.92	0.55	1.56	9.03	26.89	2.12	13.43
	High	0.53	1.64	6.10	29.77	2.37	16.82	0.85	1.97	13.06	24.51	3.31	18.34
4	Startup	0.53	1.00	2.15	5.57	2.44	4.25	0.19	0.72	1.60	5.15	0.89	2.35
	Low	0.27	1.67	4.11	20.45	1.20	16.51	0.67	1.53	10.42	24.75	2.62	15.05
	High	0.41	1.68	6.53	21.77	2.05	17.38	0.95	1.84	14.38	25.38	3.83	16.53
5	Startup	0.75	1.28	2.91	6.49	2.97	5.19	0.08	0.42	1.08	3.36	0.36	1.30
	Low	0.30	0.81	4.43	18.48	1.25	11.31	0.60	1.43	10.17	22.25	2.19	13.59
	High	0.40	1.43	5.47	17.16	1.96	16.86	0.87	1.84	15.28	31.14	3.17	18.66
6	Startup	0.81	1.42	3.43	8.40	3.01	5.81	0.56	1.95	3.46	10.98	1.50	4.25
	Low	0.41	1.20	6.10	22.73	1.81	13.32	0.72	1.61	12.37	33.42	2.68	15.48
	High	0.54	1.90	6.83	23.61	2.71	18.63	0.96	2.09	16.69	37.55	3.62	18.86

Table 6.5 shows that the maximum errors of flux-linkage, rotor position and speed in experiments are approximately 18 %, 2 deg, and 38 rpm, respectively. The speed tolerance with the maximum speed error is approximately 3 %. Table 6.6 shows the summary of the experimental results executed at different current commands and under various loads, where the average and maximum values of flux-linkage, rotor position, and speed obtained during 300 PWM cycles are presented. From Table 6.6, the average actual rotor speed obtained during 300 PWM cycles is approximately 850 rpm. Table 6.6 shows that the maximum errors of flux-linkage, rotor position and speed in experiments are approximately 16 %, 2 deg, and 27 rpm, respectively. The speed tolerance with the maximum speed error is approximately 3 %.

Table 6.6 Comparison of experimental results under various loads

Torque [N·m]	Iref [A]	**Fourier series**						**Fast Fourier Transform**					
		Position Error [deg]		Speed Error [rpm]		Flux-linkage Error [%]		Position Error [deg]		Speed Error [rpm]		Flux-linkage Error [%]	
		Avg.	Max.	Avg.	Max.	Avg.	Max.	Avg.	Max.	Avg.	Max.	Avg.	Max.
1	7	0.34	1.10	5.25	18.02	1.41	14.72	0.69	1.52	11.20	26.65	2.59	13.14
2	9	0.30	1.11	4.70	16.48	1.33	14.76	0.88	1.56	14.45	25.50	2.93	16.54
3	11	0.29	1.16	3.80	13.53	1.34	12.41	0.84	1.64	11.17	27.91	2.85	13.67
4	13	0.39	1.17	4.19	14.94	1.43	13.11	0.78	1.69	9.63	23.29	2.53	13.46

It can be pointed out from Tables 6.5 and 6.6 that the position error in using Fourier series is smaller since the shifted phase current due to an anti-aliasing LPF and the propagation delay time of devices fed to DSP controller is compensated with a LLS fitting algorithm after sampling phase current. These results satisfactorily verify that the proposed position estimation algorithm works reliably under various loads in implementation and overcomes the disadvantages of requiring position sensors.

From the experiments, the maximum errors between the estimated and actual values of flux-linkage, rotor position, and speed arise around the unaligned position or right before phase commutation, which can be observed from Figs 6.3 to 6.6 and from Figs 6.8 to 6.11. This is because the rate of change of flux-linkage with respect to rotor position is lower around the unaligned position, thus the phase voltage applied to the winding is greater, and thereby the gradient of phase current is eventually higher, assuming the rotor speed is constant in operation. It produces a lot of high frequency components in the development of phase current using Fourier analysis and it is hard to represent phase current in a PWM period as only the fundamental switching frequency component. Consequently, the flux-linkage error around the

unaligned position is slightly larger than that around the aligned position, causing the position and speed error to increase.

On the other hand, in dynamic simulations, the error between estimated and actual rotor position is slightly larger right before phase current commutation and during phase changeover due to saturation effects. However, in experiments, it is reduced by using the flux-linkage profile linearly varying with respect to rotor position from phase excitation to commutation angle. Hence the accuracy of the estimated rotor position around the aligned region is improved.

The correlation between dynamic simulations and experiments of the proposed position estimation scheme using Fourier series is provided in Table 6.7 and 6.8.

Table 6.7 Comparison of experiments and simulations using Fourier series under no load

Iref [A]	Speed [rpm]	**Experiments**						**Simulations**					
		Position Error [deg]		Speed Error [rpm]		Flux-linkage Error [%]		Position Error [deg]		Speed Error [rpm]		Flux-linkage Error [%]	
		Avg.	Max.	Avg.	Max.	Avg.	Max.	Avg.	Max.	Avg.	Max.	Avg.	Max.
2	Startup	0.11	0.47	0.95	3.47	0.67	2.56	0.15	0.82	0.47	4.10	0.71	3.98
	Low	0.16	0.76	2.18	8.39	0.68	6.60	0.36	0.50	0.24	1.32	0.95	1.85
	High	0.41	2.01	4.19	18.36	1.93	16.27	0.57	0.70	0.26	1.62	1.47	3.20
3	Startup	0.26	0.57	1.26	3.57	1.37	2.84	0.11	0.82	0.34	3.64	0.51	3.98
	Low	0.34	1.25	3.77	15.53	1.60	11.92	0.61	1.03	0.59	6.10	1.55	5.41
	High	0.53	1.64	6.10	29.77	2.37	16.82	0.84	1.26	0.81	7.54	2.14	4.75
4	Startup	0.53	1.00	2.15	5.57	2.44	4.25	0.11	0.61	0.31	2.61	0.40	2.54
	Low	0.27	1.67	4.11	20.45	1.20	16.51	0.66	1.45	0.50	8.85	1.60	9.66
	High	0.41	1.68	6.53	21.77	2.05	17.38	0.86	1.61	0.93	12.00	2.05	11.45
5	Startup	0.75	1.28	2.91	6.49	2.97	5.19	0.09	0.37	0.38	1.99	0.37	1.78
	Low	0.30	0.81	4.43	18.48	1.25	11.31	0.60	1.75	1.50	15.52	1.49	11.43
	High	0.40	1.43	5.47	17.16	1.96	16.86	0.81	2.28	2.03	19.33	2.06	11.91
6	Startup	0.81	1.42	3.43	8.40	3.01	5.81	0.10	0.29	0.53	1.56	0.33	1.78
	Low	0.41	1.20	6.10	22.73	1.81	13.32	0.55	2.14	0.98	11.89	1.43	12.37
	High	0.54	1.90	6.83	23.61	2.71	18.63	0.78	2.74	1.58	17.94	2.02	16.07

Table 6.8 Comparison of experiments and simulations using Fourier series under various loads

Torque [N·m]	Iref [A]	**Experiments**						**Simulations**					
		Position Error [deg]		Speed Error [rpm]		Flux-linkage Error [%]		Position Error [deg]		Speed Error [rpm]		Flux-linkage Error [%]	
		Avg.	Max.	Avg.	Max.	Avg.	Max.	Avg.	Max.	Avg.	Max.	Avg.	Max.
1	7	0.34	1.10	5.25	18.02	1.41	14.72	0.46	1.45	2.16	11.64	1.51	11.93
2	9	0.30	1.11	4.70	16.48	1.33	14.76	0.48	1.27	3.60	14.38	1.40	11.22
3	11	0.29	1.16	3.80	13.53	1.34	12.41	0.47	1.61	2.57	18.28	1.30	15.22
4	13	0.39	1.17	4.19	14.94	1.43	13.11	0.43	1.64	2.17	16.14	1.12	13.65

It can be pointed out from Tables 6.7 and 6.8 that the flux-linkage error is large in experiments because the flux-linkage is estimated from phase current values indirectly estimated from sampled currents in a PWM period, even though sampled currents are compensated. On the other hand, in simulations, phase current values are directly calculated from the differential equation of (5.4) and the inductance given by FEA, which is represented as the actual inductance. Calculated phase current values in a PWM period are used for flux-linkage estimation and therefore, errors between the estimated and actual flux-linkage given by FEA are smaller.

Despite large flux-linkage error in experiments, the maximum position errors in experiments are slightly smaller than those in simulations at high current references where the nonlinear effects of saturation is incurred around the aligned position. The reduction of the rotor position errors in experiments is attributed as the rotor position is estimated from the flux-linkage lookup table eliminating the saturation effects, where the flux-linkage is linearly varying with respect to rotor position from phase excitation to commutation angle. It increases the rate of change of flux-linkage with respect to rotor position at a given phase current in saturated region and hence eventually increases the accuracy of the estimated rotor position around the aligned position at high current references.

However, even though the accuracy of the estimated rotor position is improved in experiments, the rotor speed error is larger compared to that in simulations. This is caused by the difference of the selection of filter coefficient of a EWMAF (exponentially weighted moving average filter), which filters out the estimated rotor speed. In simulations, the rotor position error is slightly larger than experiments and thereby the filter coefficient to filter out the estimated rotor speed is determined as the value close to 1, which is 0.95, in order to increase the degree of filtering and smooth the estimated rotor speed. On the other hand, in experiments, it is determined as the value less than the value of filter coefficient chosen in simulations because the rotor position error in experiments is smaller than simulations. Hence the selection of large filer coefficient close to 1 will reduce the rotor speed error in experiments.

Generally, when the filter coefficient is set to large value, the filtered signal, which is the estimated rotor speed in experiments, can be suffered from large lags and thereby it can severely degrade the stability margin of the closed speed loop system. Therefore, a compromise to achieve sufficient noise attenuation with minimum filtered signal lags has to be made when selecting an appropriate filter coefficient. Through a thorough analysis, it can be demonstrated

that the experimental results are very close to the simulation results and the performance of the proposed position estimation algorithm using Fourier series has satisfactory results, which leads to reliable operations at different operating conditions such as transient startup as well as low and high speeds under various loads without position sensors.

Table 6.9 and 6.10 show the correlation between dynamic simulations and experiments of the proposed position estimation scheme using FFT.

Table 6.9 Comparison of experiments and simulations using FFT under no load

Iref [A]	Speed [rpm]	**Experiments**						**Simulations**					
		Position Error [deg]		Speed Error [rpm]		Flux-linkage Error [%]		Position Error [deg]		Speed Error [rpm]		Flux-linkage Error [%]	
		Avg.	Max.	Avg.	Max.	Avg.	Max.	Avg.	Max.	Avg.	Max.	Avg.	Max.
2	Startup	0.45	0.71	1.47	2.88	2.63	4.17	0.01	0.02	0.06	0.16	0.22	2.35
	Low	0.34	0.88	4.47	14.87	1.32	8.68	0.21	0.23	0.10	0.67	0.60	1.50
	High	0.62	1.67	10.78	25.19	2.30	13.67	0.41	0.43	0.08	0.84	1.12	2.85
3	Startup	0.44	0.86	1.57	3.69	2.30	3.85	0.01	0.02	0.17	0.30	0.12	4.66
	Low	0.55	1.56	9.03	26.89	2.12	13.43	0.45	0.80	0.34	5.24	1.20	5.12
	High	0.85	1.97	13.06	24.51	3.31	18.34	0.67	0.91	0.47	6.26	1.78	4.49
4	Startup	0.19	0.72	1.60	5.15	0.89	2.35	0.01	0.02	0.29	0.50	0.08	1.45
	Low	0.67	1.53	10.42	24.75	2.62	15.05	0.50	1.50	0.51	9.69	1.30	9.62
	High	0.95	1.84	14.38	25.38	3.83	16.53	0.69	1.62	0.90	11.17	1.76	10.82
5	Startup	0.08	0.42	1.08	3.36	0.36	1.30	0.01	0.03	0.46	0.76	0.09	1.31
	Low	0.60	1.43	10.17	22.25	2.19	13.59	0.46	1.85	1.09	14.49	1.21	11.06
	High	0.87	1.84	15.28	31.14	3.17	18.66	0.64	2.18	1.17	16.58	1.70	11.66
6	Startup	0.56	1.95	3.46	10.98	1.50	4.25	0.01	0.02	0.69	1.35	0.10	1.92
	Low	0.72	1.61	12.37	33.42	2.68	15.48	0.40	2.15	0.99	10.81	1.18	12.38
	High	0.96	2.09	16.69	37.55	3.62	18.86	0.65	2.77	1.81	16.34	1.94	16.13

Table 6.10 Comparison of experiments and simulations using FFT under various loads

Torque [N·m]	Iref [A]	**Experiments**						**Simulations**					
		Position Error [deg]		Speed Error [rpm]		Flux-linkage Error [%]		Position Error [deg]		Speed Error [rpm]		Flux-linkage Error [%]	
		Avg.	Max.	Avg.	Max.	Avg.	Max.	Avg.	Max.	Avg.	Max.	Avg.	Max.
1	7	0.69	1.52	11.20	26.65	2.59	13.14	0.33	1.20	1.51	8.49	1.21	10.95
2	9	0.88	1.56	14.45	25.50	2.93	16.54	0.34	1.40	1.38	17.12	1.18	12.38
3	11	0.84	1.64	11.17	27.91	2.85	13.67	0.25	1.69	1.88	18.45	1.07	15.48
4	13	0.78	1.69	9.63	23.29	2.53	13.46	0.18	1.74	1.69	16.99	1.00	14.39

It can be pointed out from Tables 6.9 and 6.10 that maximum position errors in experiments are slightly smaller than in simulations at high current references since the rotor

position is estimated from the flux-linkage lookup table eliminating the saturation effects, where the flux-linkage is linearly varying with respect to rotor position from phase excitation to commutation angle. On the other hand, average rotor position errors in experiments are slightly larger than in simulations. This is because the shifted phase current due to an anti-aliasing LPF and the propagation delay time of devices linked to ADC channels of the DSP are sampled without any compensation for correcting the shifted phase current, while the shifted phase current is compensated by linear least squares (LLS) fitting algorithm in the position estimation scheme using Fourier series. Nevertheless, rotor position errors in experiments are less than 2 deg and the rotor position is therefore reliably estimated in a PWM period.

In spite of the accurate estimation of rotor position in experiments, the rotor speed error is larger compared to that in simulations. As the experiments using Fourier series, this is attributed to the different selection of filter coefficient to filter out the estimated rotor speed in experiments. When the filter coefficient is set to large value, the degree of filtering increases and the filtered signal is therefore to be smooth. In simulations, the filter coefficient is set to 0.95, while it is set to 0.9 in experiments. Hence the selection of large filer coefficient close to 1 will reduce the rotor speed error in experiments.

However, filtering out or smoothing the estimated rotor speed is good when the filter coefficient is set to large value, but this is achieved at the expense of large lags on the filtered signal, which is the estimated rotor speed. Therefore, a compromise to achieve sufficient noise attenuation with minimum filtered signal lags has to be made when selecting an appropriate filter coefficient. From a thorough analysis, it can be demonstrated that the experimental results are very close to the simulation results and the performance of the proposed position estimation method using FFT has satisfactory results, which leads to a reliable operation at different operating conditions such as transient startup as well as low and high speeds under various loads without position sensors.

6.6 Discussion

The experimental evaluation of the proposed position estimation algorithms based on Fourier series and FFT has been performed in this chapter. A comparison of performance of the proposed position estimation algorithms at different operating conditions, such as transient startup and low and high speeds, was given in the previous section. It is shown that the average

and maximum position error with Fourier series-based position estimation algorithm are smaller than what under the same phase current reference and load. This is because phase current shifted due to an anti-aliasing LPF and the propagation delay time of devices linked to ADC channels of the DSP is compensated by LLS fitting algorithm. On the other hand, in the FFT-based position estimation algorithm, the shifted phase current is sampled without any compensation and therefore the estimated flux-linkage estimated from phase voltage and current has large errors, resulting an increased error in the rotor position. In addition, the accuracy of the estimated rotor position depends on the sampling frequency and sample size for FFT computation. Increasing the sampling frequency and sample size with a faster and more powerful DSP controller could improve the estimation accuracy of the FFT-based position estimation algorithm, but it increases the drive cost.

In order to compare the computational burden for each algorithm in experiments, execution time to conduct each algorithm on the DSP controller is measured and given in Table 6.11. The proposed position estimation algorithms are performed using a 16-bit DSP controller of Texas Instruments, the TMS320F2808. The clock frequency of the DSP is 100 MHz and the machine cycle is 10 ns. Table 6.11 summarizes the execution time to compute the first switching harmonics of phase voltage and current and estimate the flux-linkage, rotor position, and speed for each algorithm for a switching frequency of 5 kHz.

Table 6.11 Comparison of computation time on DSP for each position estimation algorithm [unit: μs]

Items	Fourier series (sample size = 6)	Fast Fourier Transform (sample size = 50)
First switching harmonics computation	27.9	92.8
Flux-linkage estimation	11.8	11.8
Rotor position estimation	11.8	11.8
Rotor speed estimation	1.4	1.4

The Fourier series-based position estimation algorithm requires 27.9 μs to compute the first switching harmonics of phase voltage and current in a PWM period, while 92.8 μs is required in the FFT-based position estimation algorithm. From the comparison of computation time in Table 6.11, implementing the FFT-based position estimation algorithm on DSP controllers for SRM drives can be difficult due to the execution time required to extract the first switching harmonics of phase voltage and current in a PWM period. Hence the Fourier series-

based position estimation algorithm is better suited for low-cost and real-time drive systems due to its higher accuracy, lower execution time, and better performance than the FFT-based position estimation.

6.7 Conclusions

In this chapter, performance of the proposed position estimation method using Fourier analysis has been carried. Comprehensive sets of experiments have been performed on a DSP-based two-phase SRM drive system at different current commands under various loads. The SRM is operated from zero speed at different current commands under various loads. The loads of 25%, 50%, 75%, and 100% of the rated load, 4 N·m, are applied to the SRM by switching a resistive load which is connected to a DC generator. The proposed position estimation method leads to a reliable operation under different operating conditions such as transient startup as well as low and high speeds under various loads without position sensors. The following are believed to be main contributions of this chapter:

1) Position estimation by *Fourier series* development of phase voltage and current waveforms for a PWM cycle has been analyzed and experimentally validated at different current commands and under various loads.
2) Position estimation by *FFT* development of phase voltage and current waveforms for a PWM cycle has been analyzed and experimentally validated at different current commands and under various loads.
3) The correlation of experimental results obtained by using between Fourier series and FFT has confirmed the validity of the proposed position estimation method.
4) Excellent correlation between dynamic simulation and experimental results validates the proposed approach to position estimation in SRM drives.
5) A DSP-based control system embedded with TI TMS320F2808 has been realized to execute the proposed position estimation algorithms.
6) The proposed position estimation method has been experimentally demonstrated and verified under different operating conditions such as transient startup and low and high speeds.

Through these experiments, the proposed position estimation algorithm is capable of providing robust and accurate position estimation at startup and low and high speeds under various loads.

CHAPTER 7 LOW COST AND HIGH EFFICIENCY TWO-PHASE SRM DRIVE SYSTEM

7.1 Introduction

High efficiency drive systems are currently applied to home appliances and power tools. Also, the industry wants to move away from brushed and commutator-based machines for reasons of reliability, safety, longevity, and acoustic noise concerns. Hence the search for a simpler and lower cost brushless variable speed motor drive has intensified with three requirements - machine, power converter, and control algorithm.

Firstly, the machine should be a brushless motor being capable of high speeds and also easy to manufacture. Due to this factor, SRMs seems to be a preferable machine compared to other electric machines. Another key point to realizing low cost motor drives is to minimize the number of switching devices. One of cost effective solutions is using a single switch per phase converter topology. The last is a sensorless control without position sensors.

Variable speed motor drive systems mostly need to get rotor position information for operation and these sensors should be mounted on the shaft. However, these position sensors have several drawbacks. The critical problem is that sensor cable should be shielded to avoid signal attenuation or interference with an external noise. In order to overcome these disadvantages, a reliable position estimation scheme without position sensors is eventually necessary for low cost drive systems.

Hence, the proposed position estimation using Fourier analysis for a two-phase 6/3 SRM gives a solution to meet the requirements of a low cost drive system. However, in order to reduce drive costs, the classical asymmetric bridge converter with two switches and two diodes is costly due to increased number of switching devices.

Thus, in order to reduce the drive costs, the split AC converter which has the structure of single switch and single diode per phase can be one of the solutions and it is combined with the proposed position estimation method. Hence it is indispensable to analyze and verify the performance of the split AC converter. In this chapter, the comparison of the split AC converter to other well-known converters is described. Its performance is also numerically estimated and

experimentally compared with well-known asymmetric bridge converter with respect to cost, efficiency, and acoustic noise.

7.2 Comparisons of Converters

Converter design has been one of the main research aspects of SRM drives since performance and cost of the drive are highly affected by the converter configurations. A number of converter topologies suitable for SRM drives have been proposed in literature [21, 85] for given applications. There are several methodologies for converter classification but all of them give way to the classification by the number of power switching devices. Due to the high cost of power semiconductors and their drive circuits compared to other components in SRM drives, a large amount of effort has gone into developing SRM drive converters which utilize the fewest possible number of power switches. Among many converter topologies, five types of configurations which are shown in Fig 7.1 have been found to be feasible for the considered two-phase SRM drive. Both qualitative and quantitative comparisons are presented to find the most appropriate converter configuration in terms of converter efficiency, cost, and performance.

Fig 7.1 Converter topologies feasible for two-phase SRM drive

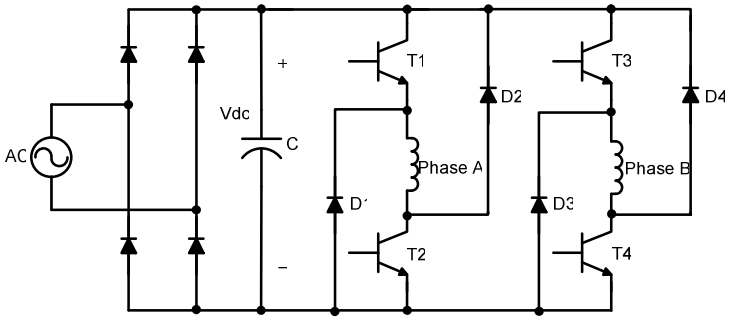

(a) Asymmetric bridge converter

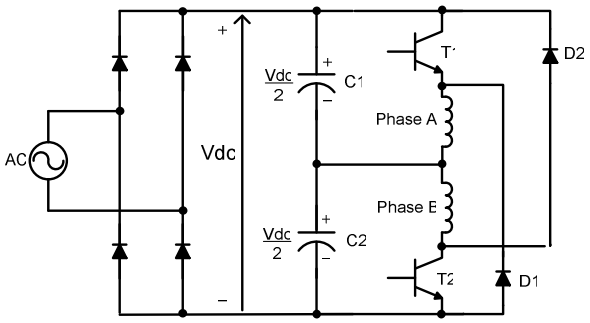

(b) Split DC link converter

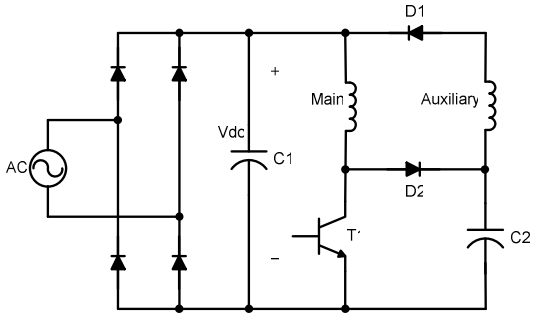

(c) Single controllable switch converter

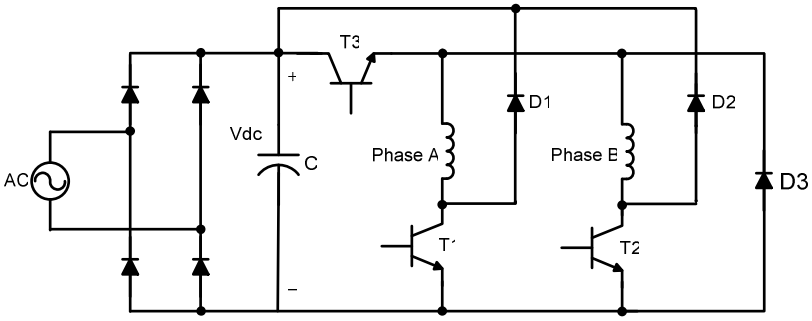

(d) N+1 converter

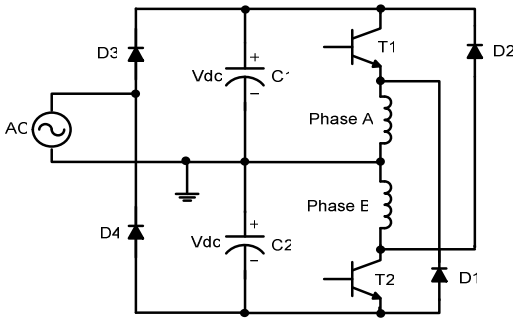

(e) Split AC supply converter

The VA (volt-ampere) rating of the converter is important in that it provides a useful measure of the actual power rating of the semiconductor switches that reflects the drive cost. The per-unit voltage stress (V) times per-unit current stress (I), multiplied by the number of total power switches (N) in the converter gives the converter VA rating (N×V×I). Based on this VA rating, the relative converter efficiency can be evaluated by comparing the converter power losses among each different configuration. The converter power losses can be estimated from each device switching and conduction losses by using derivation in Appendix C. The device switching loss is determined by maximum voltage and current stress and the device conduction

loss is determined by the average current and forward voltage drop from the datasheet under the assumption of the same conditions of control scheme, switching parameters, and torque-speed operation.

For easier comparison between the different converters, normalized power loss is used by setting the discrete IGBT switching loss 1p.u. In the case of hard chopping in the asymmetric converter, total IGBT switching loss is 4p.u. since it has four switches for a two-phase SRM. The rationale is applied to estimate power loss for the remaining converters. Note that the all other converters also have 4p.u. total IGBT loss. The reason is as follows: the N+1 has three switches; switch T3 in Fig 7.1(d) has twice the device switching losses due to the repeated switching operation for every phase.

The split DC and split AC converters have half the number of switches when compared to the asymmetric converter, hence the voltage and current stresses seen by the switch are [V_{dc}, 2I], and [$2V_{dc}$, I], respectively. Hence, they have the same converter rating (4VI) as the asymmetric converter resulting in the same total per-unit switching loss (4p.u). The single controllable converter also has a 4VI rating because of its voltage (2V) and current (2I) stress, thus having the same total IGBT switching loss (4p.u).

The per-unit conduction loss of the discrete IGBT and diode can be determined by measured average current and on-state voltage drop from the device datasheet, and was found to be 1.33p.u. and 0.99p.u., respectively, when compared to the discrete IGBT switching loss (1p.u.). Thus, the total IGBT and diode conduction losses in the asymmetric converter under hard chopping are 5.3p.u. and 3.96p.u., respectively. In the soft chopping mode, IGBT switching loss decreases due to the reduced number of switching and the IGBT conduction loss increases to 1.98p.u.. Table I shows the comparison of the total converter losses between different converter topologies based on the discrete per unit loss. Likewise, total IGBT and diode conduction losses for all converters can be determined.

Table 7.1 shows the comparison of converter losses among the above discussed converter topologies for two-phase SRM. It can noted from Table 7.1 that the split AC converter has the lowest power losses resulting in the highest converter efficiency due to its smaller VA rating and fewer number of power switches than any other converters.

Table 7.1 Comparison of converter losses among converter topologies for two-phase SRM drive

Type of Losses	Asymmetric		N+1	Split DC	Split AC	Single controllable switch
	Hard	Soft				
Convert VA Rating	4VI	4VI	3VI	4VI	4VI	4VI
IGBT Switching	4	2	4	4	4	4
IGBT Conduction	5.3	7.95	5.3	5.3	2.65	5.3
Diode Conduction	3.96	1.65	3.96	3.96	1.98	3.96
Total Converter	13.26	11.60	13.26	13.26	8.63	13.26

Another important factor for selecting converter topology is overall drive cost which is mainly determined by the number of power semiconductors, isolated gate drivers, passive components, sensors, and control circuits. Table 7.2 shows the overall comparison of the considered split AC converter with other converters in terms of performance, component count, efficiency and cost.

Table 7.2 Overall comparisons among converter topologies for two-phase SRM drive

Features	Asymmetric	N+1	Split DC	Split AC	Single controllable switch
Phase Independence	Yes	No	Partial	Partial	No
Commutation Time	Fast	Slow	Slow	Fast	Slow
Free Wheeling	Yes	Yes	No	No	Yes
Performance	Very Good	Fair	Fair	Good	Low
Number of Rectifier Diodes	4	4	4	2	4
Number of Switches	4	3	2	2	1
Number of Diodes	4	3	2	2	2
Number of Floating Power	5	2	2	2	1
Number of DC Capacitors	1	1	2	2	2
Cost	High	Medium	Low	Low	Lowest
Converter Efficiency	High	Medium	Medium	High	Medium

One of the key components other than power switching devices that affect the overall rive cost is the DC capacitor. As shown in Table 7.2 and Fig 7.1, the split AC and split DC converters require two DC link capacitors each, and the single controllable switch converter also requires two capacitors; one for the DC link and the other for energy recovery. Therefore, the cost of the split DC and split AC converters could double due to the additional cost of the DC link capacitors. The increased current ripple rating increases the capacitance requirement which adds to cost to the overall drive. However, the price reduction obtained by the reduced number of power semiconductor devices and their gate drive circuits still keeps the overall drive cost of the split DC and split AC converters lower than the conventional asymmetric converter. Employing appropriate control algorithms to minimize the current ripple can reduce the capacitor size [86]. When comparing the split AC and split DC converters, the cost of the split AC is lower due to its lowest number of rectifier diodes.

Although the single controllable switch converter is the least expensive, it is not desirable for our considered drive system due to its low performance and efficiency. The split AC converter has the same power rating as the asymmetric converter but utilizes fewer components and the total converter loss is the lowest among all converters, thus making the split AC converter the most inexpensive and highly efficient configuration. The classic asymmetric converter is less competitive because of its higher cost; however, due to its high performance and reliability it has been chosen for performance comparison with the split AC converter.

7.3 Experiments

7.3.1 Efficiency

In order to validate the considered drive system, comprehensive sets of experiments were performed on the experimental setup described in Chapter 6. The voltage and current can be measured using a differential probe and a current probe, respectively. The product of the instantaneous voltage and current to obtain the instantaneous power is computed in the oscilloscope. The average power can then be determined. The Appendix C describes how to calculate the power and efficiency. Experimental measurements were performed in order to compare them to estimations. It can be seen from the following tables that subsystem and system efficiencies for drive system are evaluated by measurement and estimation at various loads.

7.3.1.1 Rectifier Efficiency

Rectifier diode forward drop is 1 V given by datasheet and the mean value of DC link current is used for estimating power losses.

Table 7.3 Rectifier efficiency at various loads (3000 rpm)

Torque [N·m]	Estimations [%]			Measurements [%]		
	Split AC	Asymmetric	Error	Split AC	Asymmetric	Error
1	99.69	99.70	-0.01	98.43	99.30	-0.87
2	99.70	99.68	0.02	99.18	99.49	-0.31
3	99.68	99.67	0.01	98.03	99.50	-1.47
4.5	99.64	99.65	-0.01	98.63	98.39	0.24

Generally, the asymmetric drive system utilizes the full-bridge rectifier, but in case of the considered split AC drive system, the half bridge rectifier provides the DC bus voltage for each phase winding. The number of diodes for rectifying voltage at the considered split AC drive system is half the number of asymmetric drive system and it can be seen from Table 7.3 that the rectifier efficiency is high under the full load.

7.3.1.2 Converter Efficiency

Converter power losses dissipated from the switching transients and conduction can be derived analytically by using device characteristics from the datasheet and the measured peak and average currents with the assumption that diode and power switch forward voltage drops are assumed to be constant over various loads.

Table 7.4 Converter efficiency at various loads (3000 rpm)

Torque [N·m]	Estimations [%]			Measurements [%]		
	Split AC	Asymmetric	Error	Split AC	Asymmetric	Error
1	96.66	95.30	1.30	98.01	95.46	2.55
2	97.59	96.43	1.16	96.54	98.75	-2.21
3	97.90	97.01	0.89	96.23	97.20	-0.97
4.5	97.92	97.22	0.70	97.19	96.86	0.33

Although the total number of switching devices is different, two converters have the same switching losses since the voltage rating at the split AC drive system is doubled. However, it can be found from Table 7.4 that switching device's conduction losses and diode losses for the split AC drive system are half that of the asymmetric drive system and the total converter losses consequently are reduced compared to the asymmetric drive system under full load.

7.3.1.3 Machine Efficiency

The air gap power of SRM can be estimated by multiplying the electromagnetic torque and rotor speed. Table 7.5 shows the comparison of efficiency in the machine only for the asymmetric drive system and the considered split AC drive system at various loads while driving at 3000 rpm.

Table 7.5 Machine efficiency at various loads (3000 rpm)

Torque [N·m]	Estimations [%]			Measurements [%]		
	Split AC	Asymmetric	Error	Split AC	Asymmetric	Error
1	63.99	66.09	-2.10	64.55	67.01	-2.46
2	66.10	73.70	-7.60	69.14	71.65	-2.51
3	70.63	75.32	-4.69	74.76	76.18	-1.42
4.5	79.57	79.64	-0.07	81.11	82.45	-1.34

The difference in machine efficiency between two systems is 2.46% at low load and is decreased to 1.34% at full load. The machine efficiency at the split AC drive system is to a small extent lower than that of the asymmetric drive system at the full load, But it is always lower since in the free-wheel mode, the terminal voltage is equal to zero, resulting in lower current ripple and lower core loss with the use of soft chopping drive in the asymmetric drive system.

7.3.1.4 Overall Efficiency

Table 7.6 shows the comparison of efficiency in the system aspect including rectifier, converter, and motor efficiency between the asymmetric drive system and the considered split AC drive system at various loads while driving at 3000 rpm.

Table 7.6 System efficiency at various loads (3000 rpm)

Torque [N·m]	Estimations [%]			Measurements [%]		
	Split AC	Asymmetric	Error	Split AC	Asymmetric	Error
1	61.66	62.89	-1.23	62.27	63.52	-1.25
2	64.31	70.96	-6.65	66.21	70.39	-4.18
3	68.92	72.95	-4.06	70.52	73.67	-3.15
4.5	77.63	77.29	0.34	77.75	78.58	-0.83

The deviation between two systems is 1.3% at low load and is 3-4% or so at the middle load, but it is significantly decreased to 0.8% under full load. The split AC drive system produces the efficiency corresponding to that of the asymmetric drive system although the machine efficiency of the split AC drive system is lower than that of the asymmetric drive system. It was caused by

the higher efficiency of the rectifier and converter due to the reduction of switching losses and conduction losses of switching devices and diodes.

7.3.2 Acoustic Noise

The acoustic noise has been obtained from the real-time spectrum analyzer. In order to accurately measure the audible noise caused by vibrations in electrical machines, it usually is made in an anechoic chamber after calibrating the measuring equipments and measuring sound pressure at several points. However, an anechoic chamber is not available in the normal laboratory environment and, therefore, measurements can be made in an ordinary large room after measuring the ambient noise.

7.3.2.1 Sound Pressure Level

As for small motors, the sound pressure level from the test motor should be measured over a hypothetical hemisphere, centering on the motor and with a radius of 1 m [87] as shown in Fig 7.2.

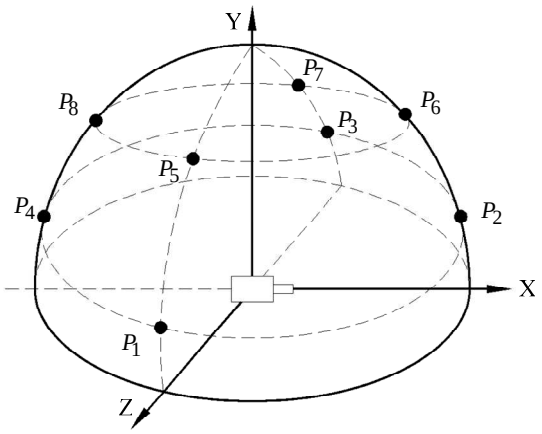

Fig 7.2 Locations for measuring the sound pressure level (radius=1m)

After measuring sound pressure levels of eight points with a microphone, each sound pressure level is averaged in decibels and it can be expressed as,

$$\overline{L}_p = 10\log\left\{\frac{1}{n}\left(\sum_{i=1}^{n} 10^{\frac{L_{p,i}}{10}}\right)\right\} \tag{7.1}$$

where $\overline{L}_p$ is the averaged sound pressure level in decibels and $L_{p,i}$ is the sound pressure at the *i*-th measurement point and n is the total number of measurement points.

Table 7.7 Measured sound pressure level (No Load)

Location of point	Split AC [dB]	Asymmetric [dB]
P1	40.00	41.30
P2	42.50	45.50
P3	42.40	41.80
P4	39.00	38.00
P5	41.20	39.70
P6	44.30	44.30
P7	42.80	42.50
P8	42.80	42.80
$\overline{L}_p$	42.15	42.54

Table 7.8 Measured sound pressure level (Full Load)

Location of point	Split AC [dB]	Asymmetric [dB]
P1	62.90	62.70
P2	63.00	63.70
P3	64.60	61.10
P4	60.80	62.30
P5	60.50	63.80
P6	59.40	61.80
P7	61.80	61.90
P8	64.20	62.30
$\overline{L}_p$	62.48	62.54

The ambient noise was 34.80 dB and it was below the measured acoustic noise from the tested two-phase SRM and no correction is required for the ambient noise. It can be seen from the Table 7.7 for no load and Table 7.8 for full load that the acoustic noise from the considered split AC drive system is slightly lower than the asymmetric drive system and it produces a reasonably quiet operation.

7.3.2.2 Frequency Spectrum

Fig 7.3 and 7.4 show that the frequency spectra of the acoustic noise are measured from the considered split AC drive system and the asymmetric drive system. The frequency spectra throughout eight locations of point were found to have very similar pattern and a measurement at P2 location is taken for illustration.

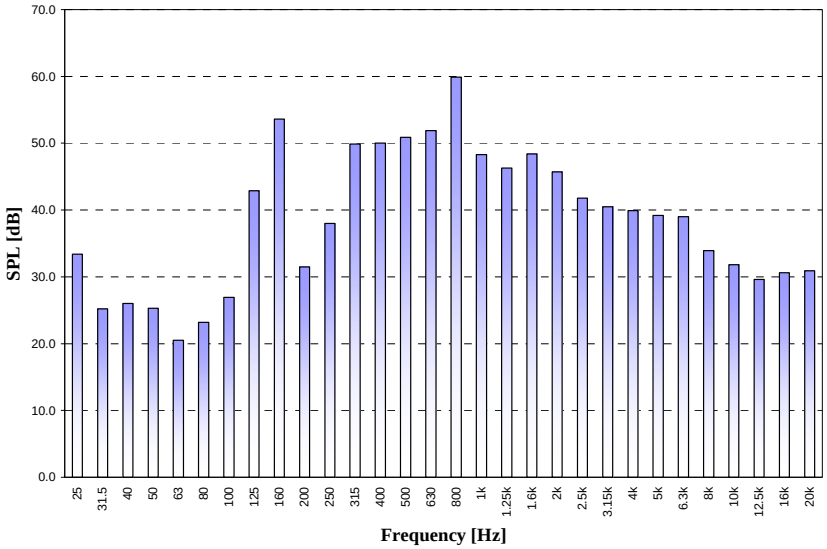

Fig 7.3 Frequency spectrum of acoustic noise at the split AC drive system at 3000 rpm under full load

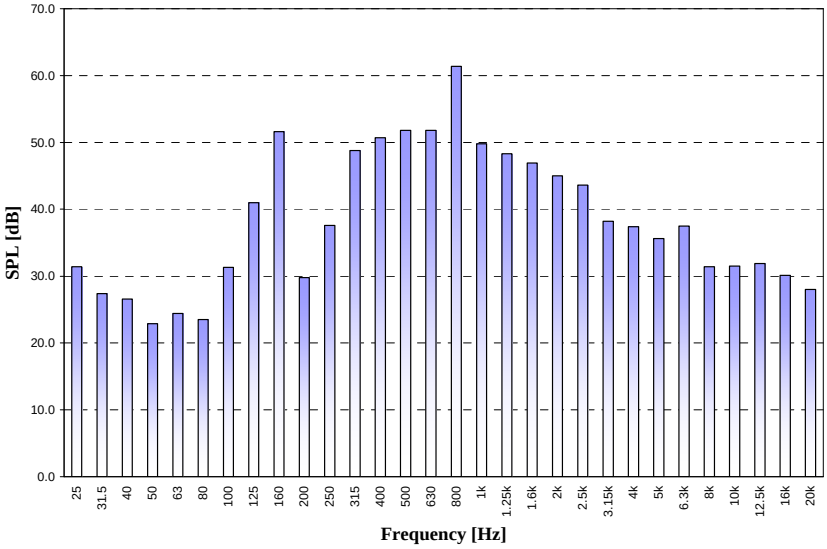

Fig 7.4 Frequency spectrum of acoustic noise at the asymmetric drive system at 3000 rpm under full load

The frequency component at 160 Hz is due to the frequency of the phase current at 3000 rpm and the noise level of the split AC drive system is close to that of the asymmetric drive system. The frequency spectra also show a frequency component at 10 kHz, which is the PWM frequency of the phase current. The noise level of the split AC drive system is 2 dB greater due to the hard chopping drive. The peak component at the frequency spectrum can be found at 800 Hz and this frequency coincides with five times the phase frequency. It is referred that vibration is maximum

when the natural frequency of the stator pole coincides with the odd times the phase frequency [88].

7.4 Conclusions

A split AC drive system for a novel two-phase flux-reversal-free-stator SRM has been proposed in this chapter and it has a single-switch-per-phase topology. The following are considered to be main contributions of this chapter:

1) The proposed drive system has been analyzed with theoretical comparisons to several types of converter topologies and its performance has been experimentally verified with comparisons to an asymmetric drive system in terms of efficiency and acoustic noise.
2) Although the machine efficiency in the proposed drive system is lower than the asymmetric drive system under the soft chopping PWM current control, the overall system efficiency is very close to the asymmetric drive system due to the better efficiency in rectifier and converter. Excellent correlation between estimation and measurement validates the efficiency of the proposed drive system.
3) The acoustic noise spectrum of the proposed drive system has lower average sound pressure level than the asymmetric drive system.

It is believed that the proposed split AC two-phase SRM drive system combined with the proposed position estimation scheme using Fourier analysis is a strong contender for low cost motor drive systems with single switch per phase having comparable efficiency and lower acoustic noise level as the asymmetric drive system.

CHAPTER 8 CONCLUSIONS

8.1 Discussion

The proposed position estimation method based on the first switching harmonics of phase voltage and current in SRM drives has been verified in simulations and experiments. In order to extract the first switching harmonics of phase voltage and current, Fourier series and FFT have been selected. A comparison of performance of the position estimation method using Fourier series and FFT was given in Chapters 5 and 6. The results show that the average and maximum position error with Fourier series-based position estimation algorithm is smaller under the same phase current reference and load. This is because phase current shifted due to an anti-aliasing LPF and the propagation delay time of devices linked to ADC channels of the DSP is compensated by LLS fitting algorithm.

On the other hand, in FFT-based position estimation algorithm, the shifted phase current is sampled without any compensation for correcting it and thereby the flux-linkage estimated from phase voltage and current has large errors, resulting in increasing the rotor position error. In addition, a sampling frequency and sample size for FFT computation determine the accuracy of the estimated rotor position. Increasing the sampling frequency and sample size with a higher speed DSP controller could improve the estimation accuracy of the FFT-based position estimation algorithm, but it increases the drive cost. Hence the Fourier series-based position estimation algorithm is better suited for low-cost and real-time drive systems due to its higher accuracy, lower execution time, and better performance than the FFT-based position estimation.

Practical aspects to be considered while implementing the proposed position estimation algorithms are discussed below:

1) *The slope of phase current in a PWM period:* To estimate the incremental inductance, the slope of the phase current during turn ON and turn OFF and the maximum and minimum current value during a PWM cycle are required in theory, assuming that the initial current value is known at the moment of PWM signal application. However, critical current values, viz. the maximum and minimum current value when using Fourier series cannot be accurately measured in implementation due to the switching noise generated in PWM operation. Hence they should be calculated through the slope of phase current during turn

ON and turn OFF, which can be measured in the PWM span so that switching noise is not generated. The slope of phase current can be calculated from the sampled current values at each of the three ADC trigger points during turn ON and turn OFF instant and the least squares algorithm.

2) *Hard chopping PWM strategy:* In the hard chopping strategy, both IGBT devices of a phase are driven by the same pulsed signal - two IGBT devices are switched on and switched off at the same time. Therefore a greater current ripple compared to the soft chopping strategy is present and thereby the gradient of phase current will be easier to measure, resulting in the increase of the accuracy of the estimated rotor position.
3) *Limitation of PWM duty cycle and current sensing time:* Digital signals transferred from one device to another device as well as analog signals to be sensed in the DSP incur some time delay. These may result in erroneous position estimation and shifting phase current waveforms in a PWM period. Hence to avoid these problem, delay time of gate drive circuit, the ringing in the current waveform at the instant of switching, delay time of ADC triggering signal in the DSP, delay time of sample and hold circuit in the DSP, and delay time of an anti-aliasing low pass filter should be taken into account. Furthermore, it should be noted that analog input signals are sensed with the delay time generated after ADC trigger signals in the DSP. In the developed drive system, if the ADC clock is 12.5 MHz, the sample and hold time is 160 ns with selection of the acquisition window width (ACQ_PS) of the DSP as 1 [89], and the cut-off frequency of an anti-aliasing LPF is 5 kHz, the total delay time generated after switching on or switching off power devices is approximately 24 μs and therefore the PWM duty cycle range is limited between 13% to 87% if the switching frequency is 5 kHz.

The proposed position estimation method in this research has a lot of advantages which include eliminating the position estimation error generated near zero speed if the motional back emf is neglected, external hardware circuitry required in high frequency signal injection methods, and resistance changes due to temperature changes in stator windings. However, it has a couple of disadvantages which are as follows:

1) It is difficult to work in single pulse operation mode, where the SRM operates at high speeds. At high speeds, the rate of rise of the phase current is very low and can at times become negative since the back emf is large and can at times be even larger than the supply voltage.

Therefore, the SRM operates with a single pulse of current in the stator windings and allows no time for chopping to take place.

2) It requires a prior knowledge about the magnetic characteristics of the SRM before getting into the implementation.

8.2 Conclusions

In this research, a novel position estimation method using the first switching harmonics of phase voltage and current through Fourier analysis has been presented to perform high accuracy position estimation for SRM. The first switching harmonic phase voltage and current in a PWM period are used to estimate the incremental inductance from which the flux-linkage can be estimated. From the estimated flux-linkage, the rotor position and speed are known in a PWM period. In order to validate the performance of the proposed position estimation scheme using Fourier analysis, it has been analyzed and comprehensive set of simulations and experiments have been accomplished and verified with a two-phase 6/3 SRM drive system, which consists of an asymmetric converter and a closed-loop PI current controller, at different conditions such as transient startup as well as low and high speeds under various loads. The average absolute differences of the percentage errors between the estimated and actual flux-linkage is approximately 3 % and the maximum flux-linkage error is approximately 18 %. The average estimated position error obtained from the estimated flux-linkage at measured phase current in a PWM period is approximately 1 deg and the maximum position error is approximately 2 deg. The average estimated speed tolerance to the actual speed is approximately 2 % and the maximum estimated speed tolerance is approximately 3 %. These experimental results have been correlated with dynamic simulations. It is evident that the proposed position estimation method using Fourier analysis is sufficiently accurate and works satisfactorily at various operating points such as startup and low and high speeds under various loads.

An automated method to measure the flux-linkage of the SRM using ac excitation has been proposed and it has eliminated errors from thermal resistance changes and eddy current effects. The measured flux-linkage has been compared with FEA results for validation of the proposed method. For flexible measurement environment and user-friendliness of the measurement system, a LabVIEW environment has been developed.

A split AC two-phase SRM drive system for low cost and high efficiency applications has been presented and numerically analyzed. Its performance has been verified with the comparisons of numerical estimations and experiments with respect to efficiency and acoustic noise. It is believed that this drive system combined with the proposed position estimation method using Fourier analysis is a strong contender to be a low cost motor drive system with single switch per phase.

8.3 Contributions

The following are believed to be original major contributions of this research and what is claimed are:

1) A novel position estimation algorithm using the first switching harmonics of phase voltage and current through Fourier analysis is presented, which has features of estimating rotor position
   a) irrespective of the motional back emf effect near zero speed,
   b) without external hardware circuitry such as a modulator and a demodulator in high frequency signal injection methods, and
   c) irrespective of resistance changes of the stator winding due to temperature changes or measurement error.
2) Position estimation by *Fourier series* development of phase voltage and current waveforms for a PWM cycle is proposed, analyzed, and validated through dynamic simulations and experiments under various loads.
3) Position estimation by *Fast Fourier Transform* development of phase voltage and current waveforms for a PWM cycle is proposed, analyzed, and validated through the dynamic simulations and experiments under various loads.
4) A DSP-based control system embedded with TI TMS320F2808 is realized to validate the performance of the proposed position estimation algorithms.
5) An accurate flux-linkage measurement method using 60 Hz AC power supply is presented and validated through comparing the results of experiments and FEA, which has features of eliminating the thermal effect of the stator resistance and the eddy current loss in the motor [90].

6) Low cost and high efficiency split AC drive system with lower acoustic noise is presented, analyzed, and validated through numerical estimation and experiments.

APPENDIX A. DERIVATION OF K_P AND K_I

Proportional and integral gains of a PI controller for a specific second-order system, which is common in this research, were derived from design specifications given by the system bandwidth ω_B and the damping ratio ζ. For a given second-order system transfer functions $G_c(s)$ is represented as,

$$G_c(s) = \frac{2\zeta\omega_n s + \omega_n^2}{s^2 + 2\zeta\omega_n s + \omega_n^2} \tag{A.1}$$

where,

$$\begin{aligned} 2\zeta\omega_n &= K_1 K_p \\ \omega_n^2 &= K_1 K_p K_i \end{aligned} \tag{A.2}$$

K_1 is a specific system constant and K_p and K_i are the proportional and integral gains of a PI controller, respectively. The system bandwidth ω_B is the frequency at which the magnitude of $G_c(j\omega)$ drops to $1/\sqrt{2}$ of its zero-frequency value. Thus we have,

$$\left|G_c(j\omega)\right|_{\omega=\omega_B} = \sqrt{\frac{\left(\omega_n^2\right)^2 + \left(2\zeta\ \omega_n\omega_B\right)^2}{\left(-\omega_B^2 + \omega_n^2\right)^2 + \left(2\zeta\ \omega_n\omega_B\right)^2}} = \frac{1}{\sqrt{2}} \tag{A.3}$$

By rearranging (A.3), we have,

$$\omega_B^4 - 2\left(1 + 2\zeta^2\right)\omega_n^2\omega_B^2 - \omega_n^4 = 0 \tag{A.4}$$

This equation leads to,

$$\omega_B^2 = \left(1 + 2\zeta^2\right)\omega_n^2 \pm \sqrt{\left(1 + 2\zeta^2\right)^2 + 1}\cdot\omega_n^2 \tag{A.5}$$

Since ω_B is a positive real value for any ζ, the plus sign should be chosen in (A.5). Therefore the bandwidth ω_B of the second order system is determined as,

$$\omega_B = \sqrt{\left(1 + 2\zeta^2\right) + \sqrt{\left(1 + 2\zeta^2\right)^2 + 1}}\cdot\omega_n \tag{A.6}$$

By rearranging (A.2) for the controller gains K_p and K_i, we have,

$$K_p = \frac{2\zeta\ \omega_n}{K_1}$$
$$K_i = \frac{\omega_n^2}{K_1 K_p} = \frac{\omega_n^2}{K_1 \dfrac{2\zeta\ \omega_n}{K_1}} = \frac{\omega_n}{2\zeta} \tag{A.7}$$

Substituting (A.6) into (A.7) yields,

$$K_p = \frac{2\zeta\ \omega_B}{\sqrt{\left(1+2\zeta^2\right)+\sqrt{\left(1+2\zeta^2\right)^2+1}}} \cdot \frac{1}{K_1}$$
$$K_i = \frac{\omega_B}{2\zeta\ \sqrt{\left(1+2\zeta^2\right)+\sqrt{\left(1+2\zeta^2\right)^2+1}}} \tag{A.8}$$

Hence, for a given set of bandwidth ω_B and damping ratio ζ , a proportional gain K_p and an integral gain K_i are calculated algebraically above. Based on (A.8), a proportional gain K_{pv} and an integral gain K_{iv} for the velocity loop controller are given as,

$$K_{pv} = \frac{2\zeta_v \omega_v}{\sqrt{\left(1+2\zeta_v^2\right)+\sqrt{\left(1+2\zeta_v^2\right)^2+1}}} \cdot \frac{J \cdot H_t}{H_v}$$
$$K_{iv} = \frac{\omega_v}{2\zeta_v \sqrt{\left(1+2\zeta_v^2\right)+\sqrt{\left(1+2\zeta_v^2\right)^2+1}}} \tag{A.9}$$

Based on (A.9), a proportional gain K_{pc} and an integral gain K_{ic} for the current loop controller are given as,

$$K_{pc} = \frac{2\zeta_c \omega_c}{\sqrt{\left(1+2\zeta_c^2\right)+\sqrt{\left(1+2\zeta_c^2\right)^2+1}}} \cdot \frac{L(\theta)}{H_c K_r}$$
$$K_{ic} = \frac{\omega_c}{2\zeta_c \sqrt{\left(1+2\zeta_c^2\right)+\sqrt{\left(1+2\zeta_c^2\right)^2+1}}} \tag{A.10}$$

APPENDIX B. SPECIFICATIONS OF TWO-PHASE SRM DRIVE SSYTEM

Number of stator poles	6
Number of rotor poles	3
Stator pole arc [deg]	36
Rotor pole arc [deg]	72
Minimum inductance at 2A [mH]	6
Maximum inductance at 2A [mH]	103
Air gap length [mm]	max: 0.7, min: 0.3
Number of turns [turns/phase]	110
Stack length [mm]	85
Rated voltage [VAC]	230
Rated torque [Nm]	4
Rated speed [rpm]	3,000
Rated current [A]	13
Inertia coefficient [Nm/rad/s]	0.0007
Friction coefficient [kg-m^2]	0.0003
Speed feedback gain [V/rad/s]	$3/140\pi$
Current feedback gain [V/A]	3/20
Torque feedback gain [V/Nm]	3/4.5

APPENDIX C. CALCULATIONS OF POWER EFFICIENCY

C.1 Calculation of the Converter Losses

The estimation of IGBT switching, IGBT conduction, and diode conduction losses during the whole current commutation period are converter losses are given as follows. The IGBT switching losses are given by,

$$\begin{aligned} P_{sw\_on} &= (0.5 \cdot V_{pk} \cdot I_{pk} \cdot t_{on} \cdot f_{sw}) \cdot t_{dwell} \cdot f_{com} \\ P_{sw\_off} &= (0.5 \cdot V_{pk} \cdot I_{pk} \cdot t_{off} \cdot f_{sw}) \cdot t_{dwell} \cdot f_{com} \end{aligned} \tag{C.1}$$

where V_{pk}, I_{pk}, t_{on}, t_{off}, t_{dwell}, f_{sw}, f_{com} are peak voltage stress, peak current stress, switch-on time delay, switch-off time delay, current dwell time, switching frequency, and commutation frequency, respectively. The IGBT or diode conduction losses are given by,

$$P_{cond} = \frac{1}{T_{com}} \int_0^{T_{com}} V_{on} \cdot i_{on} dt \approx V_{on} \cdot I_{on} \cdot \frac{t_{on}}{T_{sw}} \cdot \frac{t_{dwell}}{T_{com}} \tag{C.2}$$

where V_{on}, i_{on}, T_{com} are IGBT or diode on-state voltage drop, IGBT or diode instantaneous on-state current, and current commutation time, respectively.

C.2 Calculation of the Output Power of SRM

The losses of DC generator including the copper losses, mechanical losses, core losses, stray losses, and brush contact losses can be calculated in advance and based on these losses, the output power of SRM can calculated.

1) Copper losses (in case of separately excited field)

$$P_{copper} = I_a^2 \cdot R_a \tag{C.3}$$

The change in resistance of the armature due to temperature and skin effect has to be considered in order to calculate the accurate copper losses in the DC generator. Improper value of resistance can lead to reduce the input power of DC generator, resulting in reduction of the output of the tested drive system. Temperature measurements are made right after driving and resistor values for copper at any temperature other than the standard temperature (usually specified at 20 Celsius) are measured through the following formula [76].

$$R = R_{ref.}[1+\alpha\cdot(T-T_{ref})] \tag{C.4}$$

where R is resistance at temperature "T", R_{ref} is resistance at reference temperature T_{ref}, α is 0.004041, meaning the temperature coefficient of resistance for copper, T and is temperature in degree Celsius. Skin effect can be neglected since the frequency of DC generator at the rated speed is 100 Hz and the AC/DC resistance ratio is unity.

2) Mechanical losses & core losses

These two losses can be calculated while driving a DC generator as a DC motor at no load. The output power of DC motor is ideally zero and all of the input power turns into losses.

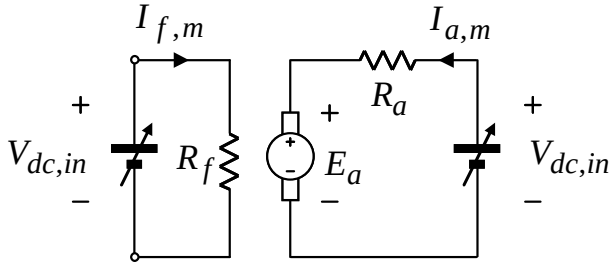

Fig C.1 Circuitry for measuring mechanical and core losses

The copper losses in the field and the armature circuits at no load are given as,

$$P_{copper,m} = I_{f,m}^2\cdot R_f + I_{a,m}^2\cdot R_a \tag{C.5}$$

The remaining portion of the input power must be rotational losses of the motor, which is the summation of mechanical losses and core losses. Hence, the rotational losses with respect to speed are expressed as,

$$\begin{aligned} P_{mech} + P_{core} &= P_{in,m} - P_{copper,m} \\ &= V_{dc,in}\cdot(I_{a,m} + I_{f,m}) - P_{copper,m} \end{aligned} \tag{C.6}$$

3) Stray losses

It is noted that the stray losses is miscellaneous losses associated with mainly electromagnetic radiation and they can be assumed generally to be 0.5 percent of the full load power.

$$P_{stray} = 0.005\times P_{out,Gen} \tag{C.7}$$

4) Brush contact losses [91]

There is an electric power loss in the brushes that make with the commutator. The potential difference occurs between the commutator surface and the brush material close to the brush contact surface. This potential difference varies nonlinearly with current density and the

total potential difference across brushes is 1.8 V under the full load in this machine and it causes the reduction of 1~2 % of the machine and overall system efficiency.

$$P_{brush} = V_{brush} \times I_a \tag{C.8}$$

5) Output power of DC generator

It equals to the load voltage multiplied by the load current in DC generator.

$$P_{out,Gen} = V_L \cdot I_L \tag{C.9}$$

6) Output power of SRM

Consequently, based on the beforehand calculated losses and the output power, the total input power of DC generator correspond to the output power of the tested drive system.

$$P_{out,SRM} = P_{in,Gen} = (C.3) + (C.6) + (C.7) + (C.8) + (C.9) \tag{C.10}$$

7) Rectifier efficiency

It can be found from Fig 6.1 that the rectifier efficiency is given as,

$$\eta_{rec} = \frac{P_{in,dc}}{P_{in,sys}} \tag{C.11}$$

8) Converter efficiency

It can be found from Fig 6.1 that the converter efficiency is given as,

$$\eta_{conv} = \frac{P_{in,SRM}}{P_{in,dc}} \tag{C.12}$$

9) Machine efficiency

It can be found from Fig 6.1 that the machine efficiency is given as,

$$\eta_{SRM} = \frac{P_{out,SRM}}{P_{in,SRM}} \tag{C.13}$$

10) System efficiency

It can be found from Fig 6.1 that the overall system efficiency is given as,

$$\eta_{sys} = \frac{P_{out,SRM}}{P_{in,sys}} = \eta_{rec} \cdot \eta_{conv} \cdot \eta_{SRM} \tag{C.14}$$

REFERENCES

[1] R. Krishnan, "Whither motor drives: A case study in switched reluctance motor drives," in *Electrical Machines and Systems, 2007. ICEMS. International Conference on*, 2007, pp. 472-480.

[2] P. P. Acarnley, R. J. Hill, and C. W. Hooper, "Detection of rotor position in stepping and switched reluctance motors by monitoring of current waveforms," *IEEE Trans on .Industrial Electronics*, vol. IE-32, pp. 215-222, 1985.

[3] S. K. Panda and G. A. J. Amaratunga, "Waveform detection technique for indirect rotor-position sensing of switched-reluctance motor drives. II. Experimental results," *Electric Power Applications, IEE Proceedings B [see also IEE Proceedings-Electric Power Applications]*, vol. 140, pp. 89-96, 1993.

[4] S. K. Panda and G. A. J. Amaratunga, "Waveform detection technique for indirect rotor-position sensing of switched-reluctance motor drives. I. Analysis," *Electric Power Applications, IEE Proceedings B [see also IEE Proceedings-Electric Power Applications]*, vol. 140, pp. 80-88, 1993.

[5] S. K. Panda, C. Keng Young, and L. Kai Sang, "Indirect rotor position sensing for variable reluctance motors," in *Industry Applications Society Annual Meeting, 1994., Conference Record of the 1994 IEEE*, 1994, pp. 644-648 vol.1.

[6] S. K. Panda, K. C. Leong, W. T. J. Lau, and K. S. A. L. K. S. Lock, "Further developments in indirect-rotor position sensing of variable-reluctance motors using waveform-detection technique," in *Industrial Electronics, Control, and Instrumentation, 1993. Proceedings of the IECON '93., International Conference on*, 1993, pp. 1009-1014 vol.2.

[7] F. R. Salmasi and M. Ehsani, "A novel approach to auto-calibrating sensorless switched reluctance motor drive," in *IECON '03. The 29th Annual Conference of the IEEE*, 2003, pp. 2471-2476 Vol.3.

[8] H. Gao, B. Fahimi, F. R. Salmasi, and M. Ehsani, "Sensorless control of the switched reluctance motor drive based on the stiff system control concept and signature detection," 2001, pp. 490-495 vol.1.

[9] F. R. Salmasi, B. Fahimi, H. Gao, and M. Ehsani, "Sensorless control of switched reluctance motor drive based on BEMF calculation," in *Applied Power Electronics Conference and Exposition, 2002. APEC 2002. Seventeenth Annual IEEE*, 2002, pp. 293-298 vol.1.

[10] G. Suresh, B. Fahimi, K. M. Rahman, and M. Ehsani, "Inductance based position encoding for sensorless SRM drives," in *PESC 99. IEEE 30th Annual*, 1999, pp. 832-837 vol.2.

[11] G. Hongwei, F. R. Salmasi, and M. Ehsani, "Inductance model-based sensorless control of the switched reluctance motor drive at low speed," *Power Electronics, IEEE Transactions on*, vol. 19, pp. 1568-1573, 2004.

[12] B. Fahimi and R. B. Sepe, Jr., "Development of 4-quadrant sensorless control of SRM drives over the entire speed range," in *37th IAS Annual Meeting. Conference Record of the 2002 IEEE*, 2002, pp. 1625-1632 vol.3.

[13] B. Fahimi and A. Emadi, "Robust position sensorless control of switched reluctance motor drives over the entire speed range," in *PESC 02. 2002 IEEE 33rd Annual*, 2002, pp. 282-288 vol.1.

[14] B. Fahimi, A. Emadi, and R. B. Sepe, Jr., "Four-quadrant position sensorless control in SRM drives over the entire speed range," *Power Electronics, IEEE Transactions on*, vol. 20, pp. 154-163, 2005.

[15] F. R. Salmasi and B. Fahimi, "Modeling switched-reluctance Machines by decomposition of double magnetic saliencies," *Magnetics, IEEE Transactions on*, vol. 40, pp. 1556-1561, 2004.

[16] B. Fahimi, G. Suresh, J. Mahdavi, and M. Ehsami, "A new approach to model switched reluctance motor drive application to dynamic performance prediction, control and design," in *Power Electronics Specialists Conference, 1998. PESC 98 Record. 29th Annual IEEE*, 1998, pp. 2097-2102 vol.2.

[17] B. G. Hedland, "A method and a device for sensorless control of a reluctance motor," 1986.

[18] J. P. Lyons, S. R. MacMinn, and M. A. Preston, "Flux-current methods for SRM rotor position estimation," in *Industry Applications Society Annual Meeting, Conference Record of the 1991 IEEE*, 1991, pp. 482-487 vol.1.

[19] D. Panda and V. Ramanarayanan, "Sensorless control of switched reluctance motor drive with self-measured flux-linkage characteristics," in *PESC 00. 2000 IEEE 31st Annual*, 2000, pp. 1569-1574 vol.3.

[20] G. Gallegos-Lopez, P. C. Kjaer, and T. J. E. Miller, "A new sensorless method for switched reluctance motor drives," *Industry Applications, IEEE Transactions on*, vol. 34, pp. 832-840, 1998.

[21] R. Krishnan, *Switched Reluctance Motor Drives*: CRC press, 2001.

[22] A. Lumsdaine and J. H. Lang, "State observers for variable-reluctance motors," *Industrial Electronics, IEEE Transactions on*, vol. 37, pp. 133-142, 1990.

[23] I. Husain, S. Sodhi, and M. Ehsani, "A sliding mode observer based controller for switched reluctance motor drives," in *Industry Applications Society Annual Meeting, Conference Record of the 1994 IEEE*, 1994, pp. 635-643 vol.1.

[24] R. A. McCann, M. S. Islam, and I. Husain, "Application of a sliding-mode observer for position and speed estimation in switched reluctance motor drives," *Industry Applications, IEEE Transactions on*, vol. 37, pp. 51-58, 2001.

[25] S. A. Hossain, I. Husain, H. Klode, B. Lequesne, A. M. Omekanda, and S. Gopalakrishnan, "Four-quadrant and zero-speed sensorless control of a switched reluctance motor," *Industry Applications, IEEE Transactions on*, vol. 39, pp. 1343-1349, 2003.

[26] I. Husain and M. Ehsani, "Rotor position sensing in switched reluctance motor drives by measuring mutually induced voltages," *Industry Applications, IEEE Transactions on*, vol. 30, pp. 665-672, 1994.

[27] M. Bin-Yen, F. Wu-Shiung, L. Tian-Hua, and C.-G. Chen, "Design and implementation of a sensorless switched reluctance drive system," *Aerospace and Electronic Systems, IEEE Transactions on*, vol. 34, pp. 1193-1207, 1998.

[28] L. Tian-Hua and C. Yih-Hua, "Implementation of a microprocessor-based sensorless switched reluctance drive," in *Industrial Electronics Society, 2000. IECON 2000. 26th Annual Confjerence of the IEEE*, 2000, pp. 375-380 vol.1.

[29] G. R. Dunlop and J. D. Marvelly, "Evaluation of a self-commutated switched reluctance motor," in *Proc. of Int. Conf. on Electric Machines and Drives*, 1987, pp. 317-320.

[30] W. D. Harris and J. H. Lang, "A simple motion estimator for variable-reluctance motors," *Industry Applications, IEEE Transactions on*, vol. 26, pp. 237-243, 1990.

[31] S. R. MacMinn, W. J. Rzesos, P. M. Szczesny, and T. M. Jahns, "Application of sensor integration techniques to switched reluctance motor drives," *Industry Applications, IEEE Transactions on*, vol. 28, pp. 1339-1344, 1992.

[32] N. H. Mvungi, M. A. Lahoud, and J. M. Stephenson, "A new sensorless position detector for SR drives," in *Power Electronics and Variable-Speed Drives, Fourth International Conference on*, 1990, pp. 249-252.

[33] N. H. Mvungi, "Switched reluctance motor commutation using its magnetisation characteristics," in *Virtual Environments, Human-Computer Interfaces and Measurement Systems, 2004 IEEE Symposium on*, 2004, pp. 113-118.

[34] H. J. Guo, W. B. Lee, T. Watanabe, and O. Ichinokura, "An improved sensorless driving method of switched reluctance motors using impressed voltage pulse," in *Power Conversion Conference, 2002. PCC Osaka 2002. Proceedings of the*, 2002, pp. 977-980 vol.3.

[35] H. J. Guo, M. Takahashi, T. Watanabe, and O. Ichinokura, "A new sensorless drive method of Switched Reluctance Motors based on motor's magnetic characteristics," *Magnetics, IEEE Transactions on*, vol. 37, pp. 2831-2833, 2001.

[36] E. Kayikci, M. C. Harke, and R. D. Lorenz, "Load invariant sensorless control of a SRM drive using high frequency signal injection," in *Industry Applications Conference, 2004. 39th IAS Annual Meeting. Conference Record of the 2004 IEEE*, 2004, pp. 1632-1637 vol.3.

[37] M. W. Degner and R. D. Lorenz, "Using multiple saliencies for the estimation of flux, position, and velocity in AC machines," *Industry Applications, IEEE Transactions on*, vol. 34, pp. 1097-1104, 1998.

[38] P. Laurent, M. Gabsi, and B. Multon, "Sensorless rotor position analysis using resonant method for switched reluctance motor," in *Industry Applications Society Annual Meeting, Conference Record of the 1993 IEEE*, 1993, pp. 687-694 vol.1.

[39] M. Ehsani, I. Husain, and A. B. Kulkarni, "Elimination of discrete position sensor and current sensor in switched reluctance motor drives," *Industry Applications, IEEE Transactions on*, vol. 28, pp. 128-135, 1992.

[40] M. Ehsani, I. Husain, and K. R. Ramani, "Low cost sensorless switched reluctance motor drives for automotive applications," in *Electronic Applications in Transportation, IEEE Workshop on*, 1990, pp. 96-101.

[41] M. Ehsani, I. Husain, and A. B. Kulkarni, "Elimination of discrete position sensor and current sensor in switched reluctance motor drives," in *Industry Applications Society Annual Meeting, Conference Record of the 1990 IEEE*, 1990, pp. 518-524 vol.1.

[42] Y. J. Wang, Y. Y. Sun, C. C. Huang, and M. C. Tsai, "Rotor position detection of switched reluctance motors using FM technique," in *Control Applications, Proceedings of the 1999 IEEE International Conference on*, 1999, pp. 939-944 vol. 2.

[43] M. Ehsani, I. Husain, S. Mahajan, and K. R. Ramani, "New modulation encoding techniques for indirect rotor position sensing in switched reluctance motors," *Industry Applications, IEEE Transactions on*, vol. 30, pp. 85-91, 1994.

[44] G. Suresh, B. Fahimi, and M. Ehsani, "Improvement of the accuracy and speed range in sensorless control of switched reluctance motors," in *APEC '98. IEEE Thirteenth Annual*, 1998, pp. 771-777 vol.2.

[45] G. Suresh, B. Fahimi, K. M. Rahman, M. Ehsani, and I. Panahi, "Four-quadrant sensorless SRM drive with high accuracy at all speeds," in *APEC '99. IEEE Fourteenth Annual*, 1999, pp. 1226-1231 vol.2.

[46] G. Suresh, B. Fahimi, K. M. Rahman, and M. Ehsani, "Analysis of amplitude modulation methods for sensorless SRM drives," in *IECON '98. Proceedings of the 24th Annual Conference of the IEEE*, 1998, pp. 917-922 vol.2.

[47] G. Suresh, K. M. Rahman, B. Fahimi, and M. Ehsani, "Self-tuning sensorless SRM drives for low cost mass production," in *33rd IAS Annual Meeting. Conference Record of the 1998 IEEE*, 1998, pp. 593-600 vol.1.

[48] P. Bishop, A. Khalil, and I. Husain, "Low level amplitude modulation based sensorless operation of a switched reluctance motor," in *PESC 04. 2004 IEEE 35th Annual*, 2004, pp. 3347-3352 Vol.5.

[49] A. Brosse, G. Henneberger, M. Schniedermeyer, R. D. Lorenz, and N. Nagel, "Sensorless control of a SRM at low speeds and standstill based on signal power evaluation," in *Industrial Electronics Society, 1998. IECON '98. Proceedings of the 24th Annual Conference of the IEEE*, 1998, pp. 1538-1543 vol.3.

[50] A. Bellini, F. Filippetti, G. Franceschini, C. Tassoni, and P. Vas, "Position sensorless control of a SRM drive using ANN-techniques," in *33rd IAS Annual Meeting. Conference of the 1998 IEEE*, 1998, pp. 709-714 vol.1.

[51] D. S. Reay, Y. Dessouky, and B. W. Williams, "The use of neural networks to enhance sensorless position detection in switched reluctance motors," in *Systems, Man, and Cybernetics, IEEE International Conference on*, 1998, pp. 1774-1778 vol.2.

[52] D. S. Reay and B. W. Williams, "Sensorless position detection using neural networks for the control of switched reluctance motors," in *Control Applications, Proceedings of the 1999 IEEE International Conference on*, 1999, pp. 1073-1077 vol. 2.

[53] E. Mese and D. A. Torrey, "An approach for sensorless position estimation for switched reluctance motors using artifical neural networks," *Power Electronics, IEEE Transactions on*, vol. 17, pp. 66-75, 2002.

[54] C. Hudson, N. S. Lobo, and R. Krishnan, "Sensorless control of single switch based switched reluctance motor drive using neural network," in *30th Annual Conference of IEEE*, 2004, pp. 2349-2354 Vol. 3.

[55] C. A. Hudson, N. S. Lobo, and R. Krishnan, "Sensorless Control of Single Switch-Based Switched Reluctance Motor Drive Using Neural Network," *Industrial Electronics, IEEE Transactions on*, vol. 55, pp. 321-329, 2008.

[56] A. Cheok and N. Ertugrul, "A model free fuzzy logic based rotor position sensorless switched reluctance motor drives," in *31st IAS Annual Meeting, Conference Record of the 1996 IEEE*, 1996, pp. 76-83 vol.1.

[57] A. Cheok and N. Ertugrul, "High robustness and reliability of a fuzzy logic based angle estimation algorithm for practical switched reluctance motor drives," in *PESC 98. IEEE 29th Annual*, 1998, pp. 1302-1308 vol.2.

[58] A. D. Cheok and N. Ertugrul, "High robustness and reliability of fuzzy logic based position estimation for sensorless switched reluctance motor drives," *Power Electronics, IEEE Transactions on,* vol. 15, pp. 319-334, 2000.

[59] N. Ertugrul and A. D. Cheok, "Indirect angle estimation in switched reluctance motor drive using fuzzy logic based motor model," *Power Electronics, IEEE Transactions on,* vol. 15, pp. 1029-1044, 2000.

[60] C. Eyguesier, K. J. Tseng, F. Yan, and S. Cao, "A basic algorithm of sensorless rotor position detection using fuzzy logic for the switched reluctance motor drives," in *ISIE '99. Proceedings of the IEEE International Symposium on*, 1999, pp. 684-688 vol.2.

[61] W. Zhongfang, A. D. Cheok, and W. Lim Khiang, "Sensorless rotor position estimation algorithm for switched reluctance motors using fuzzy logic," in *PESC. 2001 IEEE 32nd Annual*, 2001, pp. 1701-1706 vol. 3.

[62] A. D. Cheok and W. Zhongfang, "Fuzzy logic rotor position estimation based switched reluctance motor DSP drive with accuracy enhancement," *Power Electronics, IEEE Transactions on,* vol. 20, pp. 908-921, 2005.

[63] S. Paramasivam, S. Vijayan, M. Vasudevan, R. A. A. R. Arumugam, and R. A. K. R. Krishnan, "Real-Time Verification of AI Based Rotor Position Estimation Techniques for a 6/4 Pole Switched Reluctance Motor Drive," *Magnetics, IEEE Transactions on,* vol. 43, pp. 3209-3222, 2007.

[64] M. Wellner and R. Krishnan, "Position estimation in switched reluctance motor drives by fourier transformation," Property of Virginia Tech 2003.

[65] H. H. Moghbelli, M. Moallem, and C. M. Ong, "Operational characteristics of switched reluctance motor drives," in *Industrial Electronics, Proceedings of the IEEE International Symposium on*, 1992, pp. 643-647 vol.2.

[66] H. H. Moghbelli, G. E. Adams, and R. G. Hoft, "Prediction of the instantaneous and steady state torque of the switched reluctance motor using the finite element method (FEM)," in *Industry Applications Society Annual Meeting, 1988., Conference Record of the 1988 IEEE*, 1988, pp. 59-70 vol.1.

[67] A. M. Omekanda, C. Broche, and M. Renglet, "Calculation of the electromagnetic parameters of a switched reluctance motor using an improved FEM-BIEM-application to different models for the torque calculation," *Industry Applications, IEEE Transactions on,* vol. 33, pp. 914-918, 1997.

[68] S. S. Murthy, B. Singh, and V. K. Sharma, "Finite element analysis to achieve optimum geometry of switched reluctance motor," in *TENCON '98. 1998 IEEE Region 10 International Conference on Global Connectivity in Energy, Computer, Communication and Control*, 1998, pp. 414-418 vol.2.

[69] R. Krishnan and P. Materu, "Measurement and instrumentation of a switched reluctance motor," in *Industry Applications Society Annual Meeting, Conference Record of the 1989 IEEE*, 1989, pp. 116-121 vol.1.

[70] V. Ramanarayanan, L. Venkatesha, and D. Panda, "Flux-linkage characteristics of switched reluctance motor," in *Power Electronics, Drives and Energy Systems for Industrial Growth, Proceedings of the 1996 International Conference on*, 1996, pp. 281-285 vol.1.

[71] V. N. Walivadekar, S. K. Pillai, S. S. Sadistap, and R. Bhandhari, "PC based data acquisition system for measurement of switched reluctance motor (SRM)," in *Power Electronics, Drives and Energy Systems for Industrial Growth, Proceedings of the 1996 International Conference on*, 1996, pp. 957-963 vol.2.

[72] V. K. Sharma, S. S. Murthy, and B. Singh, "An improved method for the determination of saturation characteristics of switched reluctance motors," *Instrumentation and Measurement, IEEE Transactions on*, vol. 48, pp. 995-1000, 1999.

[73] A. D. Cheok and N. Ertugrul, "Computer-based automated test measurement system for determining magnetization characteristics of switched reluctance motors," *Instrumentation and Measurement, IEEE Transactions on*, vol. 50, pp. 690-696, 2001.

[74] A. C. Worley and J. M. Stephenson, "Eddy current behaviour in saturating laminations with impressed flux waveforms," in *Electrical Machines and Drives, Sixth International Conference on*, 1993, pp. 229-233.

[75] J. Faiz and M. B. B. Sharifian, "Core losses estimation in a multiple teeth per stator pole switched reluctance motor," *Magnetics, IEEE Transactions on*, vol. 30, pp. 189-195, 1994.

[76] T. R. Kuphaldt, "All about Circuits - Chap 12. The physics of conductors and insulators - Temperature coefficient of resistance," 2003.

[77] H. Wei, H. Wei, and M. Cheng, "Inductance characteristics of 3-phase flux-switching permanent magnet machine with doubly-salient structure," in *Power Electronics and Motion Control Conference, 2006. IPEMC '06. CES/IEEE 5th International*, 2006, pp. 1-5.

[78] A. Ganji, A. Ganji, P. Guillaume, R. Pintelon, and P. A. L. P. Lataire, "Induction motor dynamic and static inductance identification using a broadband excitation technique," *Energy Conversion, IEEE Transaction on*, vol. 13, pp. 15-20, 1998.

[79] H. Keunsoo, L. Cheewoo, K. Jaehyuck, R. A. K. R. Krishnan, and A. S.-G. O. Seok-Gyu Oh, "Design and Development of Low-Cost and High-Efficiency Variable-Speed Drive System With Switched Reluctance Motor," *Industry Applications, IEEE Transactions on*, vol. 43, pp. 703-713, 2007.

[80] O. Seok-Gyu and R. Krishnan, "Two Phase SRM With Flux Reversal Free Stator: Concept, Analysis, Design and Experimental Verification," in *41st IAS Annual Meeting. Conference Record of the 2006 IEEE*, 2006, pp. 1155-1162.

[81] S. G. Oh and R. Krishnan, "Two-Phase SRM With Flux-Reversal-Free Stator: Concept, Analysis, Design, and Experimental Verification," *Industry Applications, IEEE Transactions on*, vol. 43, pp. 1247-1257, 2007.

[82] W. Chi-Yao and C. Pollock, "Analysis and reduction of vibration and acoustic noise in the switched reluctance drive," *Industry Applications, IEEE Transactions on*, vol. 31, pp. 91-98, 1995.

[83] H. K. Bae, H. K. Bae, and R. Krishnan, "A study of current controllers and development of a novel current controller for high performance SRM drives," in *Industry Applications Conference, 1996. Thirty-First IAS Annual Meeting, IAS '96., Conference Record of the 1996 IEEE*, 1996, pp. 68-75 vol.1.

[84] *TMS320F2809, F2808, F2806, F2802, F2801, C2802, C2801, and F2801x DSPs (Rev. J) Data Manual*: Texas Instruments, 2003.

[85] R. Krishnan, P. Sung-Yeul, and H. Keunsoo, "Theory and operation of a four-quadrant switched reluctance motor drive with a single controllable switch-the lowest cost four-quadrant brushless motor drive," *Industry Applications, IEEE Transactions on*, vol. 41, pp. 1047-1055, 2005.

[86] H. Keunsoo, L. Cheewoo, K. Jaehyuck, R. Krishnan, and O. Seok-Gyu, "Design and Development of Brushless Variable Speed Motor Drive for Low Cost and High Efficiency," in *41st IAS Annual Meeting. Conference Record of the 2006 IEEE*, 2006, pp. 1649-1656.

[87] S. J. Yang, *Low-Noise Electrical Motors*: Clarendon, 1981.

[88] P. Vijayraghavan and R. Krishnan, "Noise in electric machines: a review," *Industry Applications, IEEE Transactions on*, vol. 35, pp. 1007-1013, 1999.

[89] *TMS320x280x,2801x,2804x DSP Analog-toDigital converter*: Texas Instruments, 2005.

[90] H. Keunsoo, O. Seok-Gyu, B. MacCleery, and R. Krishnan, "An automated reconfigurable FPGA-based magnetic characterization of switched reluctance machines," in *ISIE 2005. Proceedings of the IEEE International Symposium on*, 2005, pp. 839-844 vol. 2.

[91] G. R. Slemon and A. Straughen, *Electric Machine*: Addison Wesley, 1980.